

The Cryo-V

Final report

DSE Group 10



DELFT UNIVERSITY
OF TECHNOLOGY

 TU Delft

The dawn of the hydrogen age of aviation ...

The Cryo-V

Final Report

by

DSE Group 10

June 30, 2020

Group Members:

Last Name	First Name	Student Number
Aalders	Jaime	4650166
Daugulis	Edgars	4662350
van Dalen	Sander	4657640
Francotte	Thibaut	4656172
Laar	Yuri	4659031
Megill	Liam	4563999
Shi	Minan	4649192
de Vilder	Sietse	4551729
Vossen	Frans	4666631
Wu	Zimai	4649915

Supporting Staff:

Dr. ir.	Feijia Yin	TU Delft, <i>Tutor</i>
Dr. ir.	Roberto Merino-Martinez	TU Delft, <i>Tutor</i>
Prof. dr. ir.	Sybrand van der Zwaag	TU Delft, <i>Coach</i>
Ir.	Eva Smeets	TU Delft, <i>Coach</i>

Preface

In 1949, a peculiar aircraft took to the skies over the United Kingdom. People turned to look up as it passed overhead in excitement and awe. Gone was the familiar drone of propellers: This aircraft had a roar of power from its brand new turbojet engines. The first flight of the de Havilland Comet marked the beginning of the jet age.

Today, we stand at a similar crossroads. With advancements in electric propulsion and fuel cell technology, it is time to usher in a new, cleaner and greener age of aviation: *the hydrogen age*.

Before you are the final results of the "Silent and Climate-Neutral Medium-Range Airliner" project of the Spring Design Synthesis Exercise (DSE) 2020. Ten weeks of research, innovation and design have culminated in the Cryo-V, a design that we are all very proud of. From the very first planning sessions to the final, converged design, the first 3D printed model and a VR walk around the aircraft, it has been an amazing experience for us all.

The global COVID-19 pandemic has put a whole different dimension on the DSE. Since the beginning of the year, we have seen the aviation industry go from strength to almost the brink of collapse. Although movements like *Flygskam* have tried, before 2020 it did not seem likely that the world would stop flying. But aviation is a fundamental part of the modern world, and the industry will undoubtedly bounce back quickly.

In this respect, the recovery from the pandemic is an opportunity to drastically improve the status quo. As an industry, we need to make sure that we do not recover from one crisis only to immediately enter another one: climate effects have not been put on hold during the pandemic. As this project shows, we are able to make aircraft quieter, cleaner and greener, so what are we waiting for? It is, therefore, very heartening to see the major aerospace players and governments invest in hydrogen and alternative fuels. Sustainable aviation is necessary realism, not simply a figment of an idealistic world.

The pandemic also had an affect on the DSE itself. Ten weeks ago, we all met online for the first time. At the time of writing, we still have not met each other in person. Doing the DSE in this uncertain time has certainly been an interesting experience for all of us. Whether the fact that we were not sitting next to each other all day at the Fellowship affected the outcome of the project we will never know, but it is safe to say that we managed to find a good rhythm and limit the effects of remote work effectively. Here's to many more virtual drinks, questionable t-shirt designs and terrible Skribbl.io drawings!

We would like to especially thank our tutors Roberto and Feijia and our coaches Sybrand and Eva for their guidance and support throughout the project. The results and our DSE experience, objectively more important, would not have been the same without you! We would also like to thank Roelof Vos and Pieter-Jan Proesmans for their help with the Flying-V configuration. Finally, thanks goes out to all other staff members, friends and family who have supported us in the past weeks, especially given the circumstances.

The status quo in aviation is changing, and it is exciting to be part of it. We very much hope that this is not the end and that the Cryo-V can inspire future development to make the world a quieter, greener and better place. Welcome to the hydrogen age!

- DSE Group 10

Contents

Preface	i	6.5 Battery Sizing	35
Nomenclature	iv	6.6 Distributed Electric Propulsion Design	36
List of Tables	vii	6.7 Fuel System Design	39
List of Figures	viii	6.8 Aircraft Systems Power	42
Executive Overview	xi	6.9 Material Selection and Mass Budgets	42
1 Introduction	1	6.10 Recommendations	44
2 Concept Selection Review	2	7 Structural Design	45
2.1 Functional Analysis	2	7.1 Functional analysis	45
2.2 Requirements Review	2	7.2 Assumptions	46
2.3 Project Considerations	3	7.3 Methods	46
2.4 Design Options	5	7.4 Verification	49
2.5 Design Trade-Off and Selection	6	7.5 Validation	50
3 Design Methodology	11	7.6 Structural Characteristics Determination	50
3.1 Project Design and Development Logic	11	7.7 Material Characteristics	55
3.2 Sustainable Development Plan	13	7.8 Compliance and Recommendations	56
4 Design Integration	16	8 Stability and Controllability Design	58
4.1 Design Disciplines	16	8.1 Longitudinal Stability and Controllability	58
4.2 Code Structure	16	8.2 Lateral-Directional Stability and Controllability	63
4.3 Recommendations	17	8.3 Landing Gear Design	70
5 Aerodynamic Design	18	8.4 Recommendations	74
5.1 Functional Analysis	18	9 Aircraft Configuration	75
5.2 Airfoil Design	18	9.1 Final Sizing and Configuration	75
5.3 Wing Design	20	9.2 Aircraft System Characteristics	78
5.4 Wing Characteristics	24	9.3 System Integration	79
5.5 Verification and Validation	25	9.4 Sensitivity Analysis	80
5.6 Recommendations	26	9.5 Manufacturing, Assembly, and Production Plan	84
6 Propulsion Design	27	10 Aircraft Performance Analysis	85
6.1 Functional Analysis	27	10.1 Weight Analysis	85
6.2 Design Overview	28	10.2 Flight Characteristics	86
6.3 Fuel Cell Design	29	10.3 Emission Characteristics	88
6.4 Turbofan Design	32	10.4 Noise Characteristics	91

10.5 Resource Allocation and Budget Review	99	13 Economic Analysis	113
11 Operations and Logistics	100	13.1 Cost Breakdown	113
11.1 Airport Operations	100	13.2 Market Analysis.	115
11.2 LH ₂ Logistics	101	13.3 Return on Investment and Operational Profit	116
11.3 End-of-Life Procedures.	102	14 Risk Analysis	119
11.4 RAMS aspect	103	14.1 Technical Risk Management	119
12 Life Cycle Assessment	106	15 Compliance With Requirements	122
12.1 Goal and Scope	106	15.1 Feasibility Analysis	122
12.2 Inventory Analysis and Impact Assessment.	107	15.2 Compliance Matrix	123
12.3 Interpretation	108	16 Conclusion and Recommendations	124
12.4 Verification and Validation	111	16.1 Conclusion	124
		16.2 Recommendations	125
		Bibliography	126

Nomenclature

Symbols

α	Angle of attack	deg	ρ_c	Air density at cruise condition	kg/m ³
α_s	Stall angle of attack	deg	σ_n	Tensile stress	MPa
α_t	Twist angle of aft wing	deg	σ_v	Crab angle	deg
α_{0L}	Zero lift angle of attack	deg	$\sigma_{bending}$	Bending stress	MPa
α_{LG}	Angle of attack of aircraft body on ground	deg	σ_{cr}	Critical buckling stress	MPa
\bar{x}	x position with respect to the mean aerodynamic chord	—	$\sigma_{fatigue}$	Maximum fatigue stress	MPa
\bar{x}_{CoG}	x position with respect to mean aerodynamic chord	%MAC	σ_{max}	Maximum stress	MPa
$\bar{x}_{n.p.}$	x position of neutral point	m	σ_{min}	Minimum stress	MPa
β	Prandtl-Glauert compressibility correction factor	—	σ_{total}	Total von Mises stress	MPa
β	Sideslip angle	deg	τ	Control surface effectiveness	—
$\ddot{\theta}_{req}$	Angular acceleration	deg/s ²	τ	Shear stress	MPa
$\Delta\bar{g}_f$	Gibbs free energy	kJ/mol	τ_r	Rudder effectiveness	—
δ_a	Maximum aileron deflection	deg	$\tau_{torsion}$	Torsional stress	MPa
δ_f	Flap angle	deg	A	Aspect ratio	—
Δp	Pressure difference between ceiling and cabin altitude	Pa	a	Aircraft longitudinal acceleration	m/s ²
\dot{m}	Mass flow in combustion chamber	kg/s	A_m	Area enclosed by cross-section	m ²
\dot{m}_{fuel}	Fuel flow rate	kg/s	A_{tt}	Noise attenuation from shielding	dB
\dot{W}_{turb}	Output power of turbine	W	b	Stringer pitch	m
η	Airfoil efficiency factor	—	b_2	Span of the aft wing	m
η_t	Energy absorption efficiency	—	c_r	Root chord	m
η_{cc}	Combustion chamber efficiency	—	C_{D_i}	Lift induced drag coefficient	—
η_{cell}	Fuel cell efficiency	—	C_{D_y}	Aircraft side drag coefficient	—
η_{fan}	Ducted fan efficiency	—	$C_{L_{\delta a}^*}$	Rolling moment coefficient	—
$\frac{d\varepsilon}{d\alpha}$	Wing downwash derivative	—	C_{L_0}	Lift coefficient at zero angle of attack	—
λ	Wing taper ratio	—	C_{L_α}	Slope of the lift curve	deg ⁻¹
Λ_1	Fuselage wing leading edge sweep	deg	$C_{L_{aft}}$	Lift Coefficient of the aft wing	—
Λ_2	Aft wing leading edge sweep	deg	$C_{L_{fus}}$	Lift Coefficient of the fuselage lifting body	—
λ_2	Taper ratio of the aft wing	—	$C_{L_{max}}$	Maximum lift coefficient	—
$\Lambda_{0.5c}$	Half chord sweep angle of wing	deg	C_{L_p}	Roll damping coefficient	—
Λ_{LE}	Sweep angle of leading edge of wing	deg	C_{LDes}	Designed Lift Coefficient	—
μ	Dynamic friction force coefficient	—	C_{M_0}	Zero lift pitching moment coefficient	—
μ_{H_2}/μ_{O_2}	Hydrogen/Oxygen utilisation	—	C_{M_α}	Pitching moment coefficient	—
ν	Poissons ratio	—	C_{n_β}	Stability coefficient	—
ω	Rotational velocity	RPM	$C_{p,gas}$	Gas pressure coefficient	—
ϕ_{H_2}	Hydrogen equivalence ration	—	$C_{y\beta}$	Lift curve slope of vertical tail	—
ρ_0	Air density at sea level	kg/m ³	D	Aircraft drag	N
			D	Diameter of fan	m
			D	Wheel diameter	m
			D_{fan}	Diameter of ducted fan	m
			$dx_{a,b}$	Longitudinal distance; $x_b - x_a$	m
			$dz_{a,b}$	Vertical distance; $z_b - z_a$	m
			E	Modulus of elasticity (Youngs modulus)	GPa
			e	Oswald efficiency factor	—
			F	Faraday constant	C/mol

F_w	Force generated by crosswind	N	Q	Discharged volume	m^3/s
F_x	Aircraft runway friction force	N	Q	First moment of area	m^3
h_{cg}	Height of the centre gravity	m	Q	Motor torque	Nm
I	Total current	A	Q_d	Directivity factor	–
$I_{x'x'}$	Moment of inertia parallel to chord in beam coordinate system	m^4	q_{eff}	Effective dynamic pressure	Pa
$I_{x'y'}$	Product moment of inertia in beam coordinate system	m^4	R	Gas constant	J/mol · K
$I_{y'y'}$	Moment of inertia perpendicular to chord in beam coordinate system	m^4	R	Radius of pressure vessel segment	m
I_{yy}	Lateral mass moment of inertia	kgm^2	r	Distance to observer	m
J	Advance ratio	–	R_σ	Stress ratio	–
j	Pressure vessel sizing safety factor	–	S	Rated motor power	kW
K_c	Buckling coefficient	–	S	Wing area	m^2
K_{al}	Maximum allowable stress	MPa	S_1	Area of fuselage wing	m^2
L^*	Roll moment	–	S_2	Area of aft wing	m^2
L_p	Sound pressure level	dB	S_f	Flap surface area	m^2
l_{cabin}	Length of the longer wall of cabin	m	S_t	Maximum allowable tire deflection	in
$l_{f_{nlg}}$	Load fraction on nose gear	–	S_c	Conformal surface area of fan	m^2
LHV_{fuel}	Lower heating value	J/kg	S_{ref}	Total wing surface area	m^2
M_F	Fuel mass	kg	S_{vert}	Vertical tail area	m^2
M_{ac}	Moment force around the wing aerodynamic center	Nm	SF	Safety factor	–
M_{FS}	Fuel system mass	kg	T	Aircraft thrust	N
M_{H_2O}	Mass of water produced	kg	T	Temperature	K
m_{H_2}	Molecular weight of hydrogen	g/mol	T	Torsion load	Nm
M_{MLG}	Moment around the main landing gear	Nm	t	Pressure vessel thickness	mm
m_{O_2}	Molecular weight of oxygen	g/mol	T_N	Net engine Thrust	N
M_{PL}	Mass of payload	kg	t_w	Fuel tank wall thickness	m
M_{PS}	Propulsion system mass	kg	t_{skin}	Skin thickness	mm
$M_{x'}$	Bending moment around chord in beam coordinates	Nm	t_{spar}	Spar thickness	mm
N	Fresnel number	–	U	Total voltage	V
N	Normal force on the ground	N	V	Fuel cell voltage	V
N	Number of noise sources	dB	V	Shear load	N
N_g	Landing gear load factor	–	V	Tail volume coefficient	–
$N_{elecSys}$	Number of separated electrical systems	–	v	Weld efficiency	–
N_{mw}	Number of main wheels	–	V_c	Cruising speed	m/s
N_{side}	Fresnel numbers of side edges	–	V_r	Take-off rotation speed	m/s
P	Aircraft operating pressure	Pa	V_∞	Incoming flow velocity	m/s
P	Aircraft roll rate	deg/s	V_{appr}	Approach speed	m/s
P	Shaft power	kW	V_{bypass}	Bypass flow velocity	m/s
p	Partial pressure	Pa	V_{exit}	Exit velocity in turbofan	m/s
p_d	Maximum allowable pressure	Pa	V_{jet}	Jet velocity	m/s
p_∞	Atmospheric static pressure	Pa	V_s	Stall speed	m/s
P_{bat}	Battery Power	W	W	Weight of aircraft	N
p_{jet}	Jet static pressure	Pa	w_{cabin}	Width of the cabin	m
p_{nw}	Static load on nose wheel	–	x'	Chord-wise positioning in beam coordinate system	m
PWL	Sound power level	dB	y'	Span-wise positioning in beam coordinate system	m
			Y_e	Moment arm of engine	m
			y_{mlg}	Lateral position of main landing gear	m

Abbreviations

AC	Aerodynamic Centre	LTO	Landing and Take-Off
AC	Alternating Current	MAAMF	Mylar, Aluminium, Aluminium, Mylar, Fabric
AIC	Aircraft Induced Cloudiness	MAC	Mean Aerodynamic Chord
AMC	Aviation Mega-City	MDF	Multidisciplinary Feasible
ANOPP	Aircraft Noise Prediction Program	MLG	Main Landing Gear
AoA	Angle of Attack	MLI	Multi-Layer Insulation
APU	Auxiliary Power Unit	MNS	Mission Need Statement
AR	Aspect ratio	MOI	Moment of Inertia
BLI	Boundary Layer Ingestion	MRA	Medium Range Aircraft
BWB	Blended Wing Body	MTOW	Maximum Take-Off Weight
CFD	Computational Fluid Dynamics	MTTF	Mean Time to Failure
CFRP	Carbon Fibre Reinforced Polymers	MTTR	Mean Time to Repair
CoG	Center of Gravity	NACA	National Advisory Committee for Aeronautics
CONV	Power Converter	NO _x	Nitrogen Oxides
CS-25	Certification Specifications for Large Aircraft	OASPL	Overall Sound Pressure Level
DEP	Distributed Electric Propulsion	OEW	Operating Empty Weight
DSE	Design Synthesis Exercise	OPR	Overall Pressure Ratio
EI	Environmental Impacts	PEM	Proton Exchange Membrane
EMF	Electromotive Force	PEMFC	Proton-Exchange Fuel Cell
EoL	End-of-Life	PENL	Effective Perceived Noise Level
EPNL	Effective Perceived Noise Level	PKM	Passenger Kilometre
FAR	Fuel to Air Ratio	PNL	Perceived Noise Level
FC	Fuel Cell	POS	Project Objective Statement
FEM	Finite Element Modelling	PWL	Sound Power Level
HHV	Higher Heating Value	RAMS	Reliability, Availability, Maintainability and Safety
HLD	High Lift Devices	ROI	Return on Investment
ICAO	International Civil Aviation Organization	S&C	Stability and Controllability
IFSD	In-Flight Shutdown	SC	Secondary City
ISA	International Standard Atmosphere	SDLM	Strontium-Doped Lanthanum Manganite
ISO	International Organisation for Standardisation	SMR	Steam Methane Reforming
L _{Amax}	Maximum Sound Pressure Level	SOEC	Solid Oxide Electrolysis Cell
LCA	Life Cycle Assessment	SOFC	Solid Oxide Fuel Cell
LCN	Load Classification Number	SPL	Sound Pressure Level
LH ₂	Liquid Hydrogen	TSFC	Thrust Specific Fuel Consumption
LPC/HPC	Low/High Pressure Compressor	W&B	Weight and Balance
LPT/HPT	Low/High Pressure Turbine	XDSM	Extended Design Structure Matrix
		XLR	Extra Long Range

List of Tables

1	Total emissions of the Cryo-V, including a comparison to the Airbus A320	xvi	8.1	Elevator subsystem requirements	60
2	LAmox noise levels of the Airbus A320 and the Cryo-V, with and without noise reduction applied	xvi	8.2	Elevator final characteristics and planform	62
3	Emission and noise reduction of the Cryo-V, including the requirements from Flightpath 2050	xviii	8.3	Validation of the elevator analysis compared to the Airbus A320	63
2.1	Stakeholder requirements	3	8.4	Aileron subsystem requirements	64
2.2	Key requirements	3	8.5	Aileron final characteristics and planform	65
2.3	Driving and potential critical requirements - system requirements	4	8.6	Validation of the aileron analysis compared to the Fokker 100A, Boeing 777-200 and the Airbus A320	66
5.1	Wing subsystem requirements	18	8.7	Vertical tail computation V&V using the Airbus A320 and Boeing 777 aircraft	68
5.2	Characteristics of the analysed airfoils, including both fuselage wing airfoils and the aft wing airfoil	20	8.8	Landing gear subsystem requirements	70
5.3	Verification results of the DATCOM wing planform calculations using the XFLR5 software	26	8.9	Landing gear subsystem final values	73
6.1	Propulsion subsystem requirements	27	8.10	System test: A320 actual landing gear positions and computed positions	74
6.2	Cryo-V mission thrust setting profile	29	10.1	Class II+ mass group results, including contingency margins	85
6.3	Fuel cell characteristic parameters of the initial and corrected models	32	10.2	Class II+ operational empty weight breakdown	86
6.4	Model data and GSP 11 verification of the turbofan (per engine)	34	10.3	Total emissions of the Cryo-V, including a comparison to the Airbus A320	89
6.5	Turbofan design characteristics, evaluated per engine	36	10.4	EPNL noise requirements and reference noise levels	91
6.6	Propulsion and fuel system material selection	43	10.5	LAmox noise requirements and reference noise levels	92
6.7	Propulsion system overview	43	10.6	Engine noise reductions achievable due to shielding for the Cryo-V	95
7.1	Structure subsystem requirements	45	10.7	Cryo-V final noise levels, including a comparison to the Airbus A320	97
7.2	System test inputs for structural design verification	50	10.8	Engine shielding method verification	98
7.3	System tests: stress deviation from manually computed values in percentage	50	11.1	Cryo-V maintenance checks	104
7.4	Structural analysis validation input parameters	51	12.1	Structural material breakdown of the Cryo-V	108
7.5	Structural analysis validation results	51	12.2	Inventory analysis for the Airbus A320	112
7.6	Half span positions and masses of the different weight-elements considered in the load cases	52	13.1	Development costs per kg in USD 2020	114
7.7	Cross-section design parameters	53	13.2	Manufacturing costs per kg in USD 2020	114
7.8	Considered materials for structures & landing gear	55	13.3	Cryo-V operating cost in USD	116
7.9	Summary of the structural design results	56	13.4	Cost detail of dominant aircraft in the market	118
			14.1	Summary of main technical risks	120
			15.1	Requirement compliance matrix	123

List of Figures

1	Render of the Cryo-V	xi	6.15	Cross-sectional view of the hydrogen delivery lines	41
2	Cryo-V SOFC integrated turbofan	xiii	6.16	Electrical block diagram	42
3	Top view of the Cryo-V configuration	xv	7.1	Overview of the structural analysis coordinate system	48
2.1	Cryo-V flight profile	5	7.2	Applied loading on the wing in spanwise direction	52
2.2	Morphological box path selection	6	7.3	Bending loads on the wing in spanwise direction	52
3.1	Top level steps of the DSE project	11	7.4	Internal torque on the wing in spanwise direction	53
4.1	Cryo-V Extended Design Structure Matrix (XDSM)	17	7.5	Maximum von Mises stress in the skin, measured in beam direction	53
5.1	The original and redesigned fuselage airfoil	19	7.6	Maximum von Mises stress in the spars, measured in beam direction	54
5.2	Pressure distributions of the original and redesigned fuselage airfoil	19	7.7	Pressure vessel radii in mm	54
5.3	Supercritical airfoil of the aft wing, sc20414	20	8.1	Simplified view of the Cryo-V stability centre	59
5.4	Projection view of the half wing planform	21	8.2	X-plot and CoG plot of the Cryo-V	60
5.5	Geometry of the aft wing	21	8.3	Forces and moments during take-off rotation	61
5.6	Effect of the AR and sweep angle on $C_{L_{\alpha}}$	25	8.4	Control surface effectiveness graph	62
5.7	Lift-to-drag ratio at cruise condition	25	8.5	Aft wing control surfaces planform	62
5.8	Original plots of $C_{L_{max}}/C_{l_{max}}$ vs. Λ_{LE}	25	8.6	Free Body Diagram of an Aircraft with Engine Failure	67
5.9	Interpolated plots of $C_{L_{max}}/C_{l_{max}}$ vs. Λ_{LE}	25	8.7	Vertical tail final dimensions	70
6.1	Propulsion system configuration during "cruise mode"	28	8.8	Tire pressure	72
6.2	Fuel cell characteristic curve comparison	31	8.9	British tire dimensions	72
6.3	Performance of model calculation of engine fuel consumption	34	9.2	Cross-section of Cryo-V cabin	75
6.4	Internal architecture of the Cryo-V turbofan	35	9.1	Topview of the Cryo-V configuration	76
6.5	External architecture of Cryo-V turbofan	35	9.3	Cross-section of the cargo hold and LD3-45 dimensions	76
6.6	Shaft rotational speed during operation	35	9.4	Landing gear positioning and CoG range	77
6.7	Compressor map of fan core	35	9.5	Propulsion system layout	77
6.8	Compressor map of LPC	36	9.6	Aft wing control surfaces	78
6.9	Compressor map of HPC	36	9.7	Cryo-V side view and dimensions	78
6.10	Thrust per turbofan during climb at take-off mode	36	9.8	Fuel system block diagram of the Cryo-V	78
6.11	Electric motor and fan efficiency maps	37	9.9	Auxiliary electric power block diagram of the Cryo-V	78
6.12	Mean storage density as a function of tank pressure for maximum saturation conditions	40	9.10	Hydraulic system block diagram of the Cryo-V	79
6.13	Liquid hydrogen volume fraction as shown for different tank venting pressures	40	9.11	Cabin environmental control block diagram of the Cryo-V	79
6.14	Cryogenic hydrogen tank wall design	41			

9.12 External environment control block diagram of the Cryo-V	79	10.11 Representation of the engine shielding effect for the Cryo-V	94
9.13 Communication flow and data handling block diagram of the Cryo-V	79	10.12 Budget breakdown and contingencies of the Cryo-V	99
9.14 Hardware block diagram of the Cryo-V	80	11.1 Gate position layout of the Cryo-V	101
9.15 Software block diagram of the Cryo-V	80	11.2 Turnaround timeline for the Cryo-V	101
9.16 Optimisation for different response variables using opt MTOW as a benchmark	81	11.3 Range of the Airbus A320 and Cryo-V, departing from Amsterdam, for maximum payload (200 pax).	101
9.17 Cruise speed and cabin sweep sensitivity analyses	82	12.1 Comparison of the climate change environmental impact between the Airbus A320 and the Cryo-V	109
9.18 Range and cruise altitude sensitivity analyses	83	12.2 Environmental impact of the material usage of the Cryo-V and A320, including a material breakdown	110
9.19 Distributed propulsion thrust fraction and aft wing sweep angle sensitivity analyses	83	12.3 Environmental impact of the Cryo-V, not showing aluminium	110
9.20 Production plan flow diagram of the Cryo-V	84	12.4 Fuel production EI comparison between the Airbus A320 and the Cryo-V	111
10.1 Cryo-V MTOW breakdown, in % of MTOW	85	12.5 Environmental impacts verification and validation for the Airbus A320, using comparative studies	112
10.2 Payload/Range diagram of the Cryo-V	86	13.1 Cost breakdown for Cryo-V design and production	113
10.3 Climb rate and gradients Cryo-V vs Airbus A320	87	13.2 Production cost breakdown pie chart	114
10.4 Climb time and distance Cryo-V vs Airbus A320	87	13.3 Medium range aircraft market share and forecast	115
10.5 EINO _x in g/kg for the Cryo-V turbofans during nominal climb performance	88	13.4 Return on Investment for the Cryo-V	117
10.6 Emission profile of the Cryo-V during various flight phases	89	13.5 SWOT diagram of Cryo-V for market	118
10.7 Radiative NO _x forcing factor and induced cloudiness versus altitude	90	14.1 Risk map	121
10.8 Location of noise assessment points	92	14.2 Post-mitigation risk map	121
10.9 LA _{max} (dBA) as a function of take-off thrust (N)	93		
10.10 Noise source ranking of the A319 at approach and take-off	93		



Executive Overview

This report concerns the final preliminary design of a carbon-neutral and silent medium range aircraft: the Cryo-V. It is the culmination of 10 weeks of work by 10 students as part of the Design Synthesis Exercise at the Delft University of Technology faculty of Aerospace Engineering. This report is preceded by the the Project Plan [1], Baseline Report [2] and the Midterm Report [3].

The Challenge

Since the dawn of commercial aviation, the focus of development within the aviation industry has been to improve the efficiency of aircraft. Although a more efficient aircraft is also more sustainable, improvements are less impactful and noise emissions remain high. As the climate reaches a point of no return, the industry requires fundamentally new design drivers to meet the challenges created by rising global temperatures, dwindling oil supplies and worsening air quality.

The Cryo-V project is wholly driven by the need to reduce the aviation industry's impact on the environment. This design philosophy not only includes reducing greenhouse gas emissions, but also tackling air quality and noise emissions. It presents a paradigm shift in the status quo and aims to inspire the development of other projects to help make the aviation industry a leader in sustainable technology. The Mission Need and Project Objective Statements for the project are set as [3],

Mission Need Statement

The aviation industry has a need for sustainable aircraft with reduced greenhouse gases and noise emissions, in order to meet international sustainability agreements.

Project Objective Statement

Design a climate-neutral, medium-range passenger airliner by 10 students in 10 weeks that meets the Flightpath 2050 goals of reducing NO_x by 90%, CO_2 by 75% and perceived noise by 65% compared to technology levels in the year 2000.

The Cryo-V

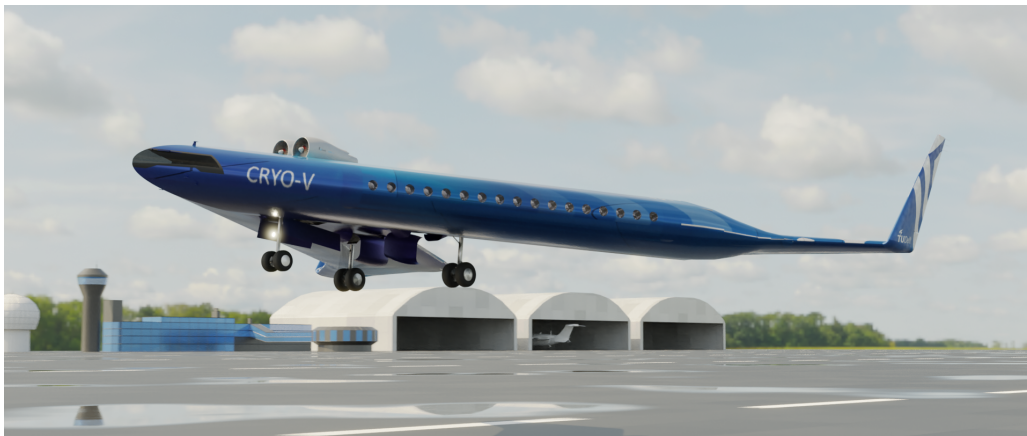


Figure 1: Render of the Cryo-V

Centred around a revolutionary, cryogenic hydrogen hybrid-electric distributed propulsion system, the Cryo-V is designed to match or improve the operational performance of the Airbus A320 whilst meeting the Flightpath 2050 [4] sustainability goals. The Cryo-V also makes use of a lifting-body configuration inspired by the Delft University of Technology Flying-V [5] to provide unparalleled aerodynamic efficiency. Furthermore, with a theoretical entry into service in 2034, the Cryo-V is designed to be able to enter service without the need for major airport infrastructure changes.

Requirements, Concept Selection and Initial Design Review

The Cryo-V requirements are categorised into operations and sustainability, split into social, economic and environmental sustainability. At the beginning of the project, the stakeholder requirements were analysed and a requirements discovery tree was established to create a complete list [2]. The driving and critical requirements could then be identified, shown in Table 2.3, which were given particular attention during the design phases.

Based on the requirements, a detailed concept discovery was performed and a set of feasible concepts were chosen for further investigation. These concepts included unconventional aircraft configurations, such as the Blended Wing Body (BWB) [6, 7] and Prandtl box wing [8], as well as alternative propulsion systems, including biofuel, full electric and fuel cell designs. The feasible design space was described by placing all concepts in a design option tree.

During a trade-off in the midterm phase, all options were further investigated and expanded. The trade-off methodology consisted of analysing each subsystem individually as well as the interaction and integration of the subsystems to obtain a final set of feasible concepts. This analysis greatly reduced the feasible design space and removed all non-hybrid configurations due to non-compliance with weight and emissions requirements. The final trade-off was performed with the following six configuration options (in order of final score) [3],

Final Trade-Off Concepts

1. **Hybrid LH₂ combustion / fuel cell Flying-V aircraft**
2. Hybrid LH₂ combustion / fuel cell BWB aircraft
3. Hybrid biofuel combustion / LH₂ fuel cell Flying-V aircraft
4. Hybrid biofuel combustion / LH₂ fuel cell BWB aircraft
5. Hybrid LH₂ combustion / fuel cell discrete BWB aircraft
6. Hybrid biofuel combustion / LH₂ fuel cell discrete BWB aircraft

The final trade-off showed that the Flying-V planform was optimal for operational and aerodynamic performance and had the lowest risk level of the concepts considered. This is in part due to the improved accessibility for loading and maintenance compared to BWB or discrete BWB [3] designs. Although both hybrid systems could meet all requirements, the single fuel hybrid was chosen predominantly for efficiency and safety. The risk of running out of biofuel and thus losing a significant portion of the propulsion system and carrying unnecessary extra fuel were driving factors in the trade-off.

A class I estimation was performed on the chosen configuration in the Midterm Phase [3]. Here, it was found that the fuel weight could be decreased by 21 tonnes compared to the Airbus A320 for a maximum range flight, but that the required internal volume substantially limited the design. The results of the class I estimation are used in the class II design described in this report.

Design Integration

The Cryo-V analysis and optimisation is based on Multidisciplinary Feasible (MDF) architecture and includes convergence iteration, optimiser and sensitivity modules. The Cryo-V can be optimised for different response variables, such as the Maximum Take-Off Weight (MTOW), NO_x emissions or noise, and, although not implemented in this phase, could be configured to make use of objective

functions. Given the unconventional planform and propulsion design of the Cryo-V, the sizing and design integration method implements elements of traditional class I and II sizing as well as extra, more detailed elements. Ten analysis functions are included in the iteration, which fall into one of the four design disciplines aerodynamics, propulsion, structures and stability & control.

Aerodynamic Design

Unlike conventional aircraft, the Cryo-V merges the wing and fuselage, which improves aerodynamic efficiency but also introduces restrictions on the planform design. The planform is split into the fuselage wing, which houses the cabin, cargo and fuel; and the aft wing, which supports all control surfaces. The differences in geometry, such as sweep angle, thickness-to-chord ratio and airfoil, result in a more complex planform design and optimisation. The required internal volume places a restriction on the minimum fuselage wing area, where the minimum aft wing area is set by the size of the control surfaces. The combination of these constraints leads to a limited design space.

The airfoil is selected according to the design lift coefficient $C_{L_{Des}}$ and the internal volume requirement. The fuselage wing uses a NACA 64A-237 airfoil, modified to create a positive moment coefficient. The aft wing uses the supercritical airfoil SC20414 to operate most efficiently at $C_{L_{Des}}$ whilst also being able to operate in the low transonic region.

After optimisation, the total wing area is 376.0 m², split into 319.4 m² for the fuselage wing and 56.6 m² for the aft wing. The aft wing is twisted downward with 10° for better stall performance and therefore produces less lift during cruise. However, the Cryo-V nevertheless achieves a maximum lift-to-drag ratio of 24 at an angle of attack of 9°. During cruise, the lift-to-drag ratio is around 20, significantly higher than that of the Airbus A320 at 16.3 [9].

Propulsion Subsystem Design

An innovative, new hybrid LH₂ propulsion system is developed specifically for use in the Cryo-V. High-temperature Solid Oxide Fuel Cells (SOFCs) provide electric power to 8 Distributed Electric Propulsion (DEP) units, which are designed to reduce noise emissions, improve aerodynamic efficiency and safety compared to conventional propulsion designs. The high operating temperature and airflow required by the SOFCs are maintained by hydrogen combustion in two turbofans, that have the added benefit of providing a boost in thrust during take-off and climb. In cruise, the main turbofan fans are powered electrically to reduce the emissions. To make most efficient use of space, the SOFCs are integrated into the turbofans and the upper surface of the wing directly below. This also allows the hot SOFC exhaust air to be used to drive the turbofan turbines, improving efficiency.

Figure 2 shows the Cryo-V turbofan design. The SOFCs are shown in yellow, the combustion chamber in red. During take-off, hydrogen combustion in the turbofans produces 54% of the total thrust. During cruise, the turbofan fans are powered by an electric motor and the thrust is split almost equally over all ten fans. The Cryo-V has a total system efficiency of 38%, a 7% increase to the Airbus A320 [9, 10].

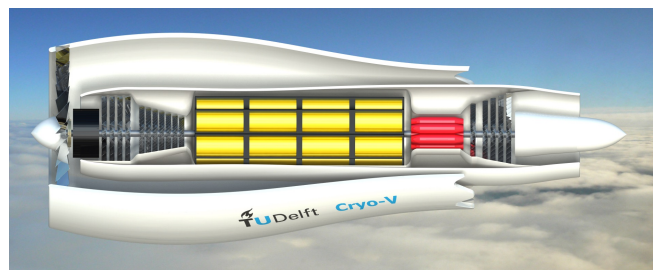


Figure 2: Cryo-V SOFC integrated turbofan

The cryogenic hydrogen is stored in six AA2219 tanks, insulated using closed-cell polyurethane. In contrast to gaseous hydrogen, the cryogenic tanks work at a low pressure of 3 bar and feature pressure relief valves that ensure the pressure remains below the design maximum pressure of 4.5 bar. The hydrogen is transported out of the tanks and through the aircraft in gaseous form and heated to operating temperature by the turbofan exhaust air. To improve efficiency further, the cryogenic temperatures could also be used to cool electric cables and motors.

Structural Design

The load-bearing structure is sized for a maximum load factor of 2.5 in bending, shear and torsional stress, accounting for plate buckling. The load-bearing design has a required AA2024-T6 skin thickness of 4 mm for the fuselage wing and 3 mm for the aft wing with 150 and 100 stringers respectively. Even considering the effect of the high sweep angle due to the distributed mass over the span, shear and bending loads are reasonable, and, combined with a significant cross-sectional area needed to accommodate the payload and fuel, the stress amplitude remains much lower than the AA2024-T6 fatigue stress. Based on the analysis presented on this report, 100 000 load cycles can easily be achieved by the load-bearing structure.

The pressure vessel inside the fuselage wing, because of its flattened shape, requires a larger thickness than conventional aircraft, since the pressurisation stress is a function of the local radius of curvature. The vessel is sized using the difference between the operational ceiling and cabin altitude pressures, the largest radius of the vessel, a safety factor of 1.5 [11] and the fatigue stress of the vessel material. This analysis resulted in a required thickness of 2 mm for AA2024-T6.

The landing gear is designed using methods presented by Roskam [12]. The wheel count, shock absorber and tires are sized for maximum landing weight, which for the Cryo-V is the same as the MTOW. The positioning of the landing gear is calculated for both longitudinal tip-back and lateral tip-over requirements. The resulting design is a tricycle landing gear with two wheels per strut for both the main and nose landing gears. The main wheel diameter is 1.14 m, the nose wheel diameter 0.91 m. Due to the high angle of rotation and the highly swept wings, the main landing gear is higher compared to conventional aircraft, at 2.3 m.

Stability and Control Subsystem Design

The unconventional configuration of the Cryo-V presents a challenge for stability and control (S&C). For the S&C analysis of the Cryo-V, the aft wing of the aircraft is considered as the horizontal stabiliser to make a traditional sizing of the aft wing possible. In certain flight conditions, the aft wing therefore must produce negative lift, made possible by elevons and the negative twist angle of the aft wing. During cruise, however, the aft wing is designed to produce positive lift for increased efficiency. For lateral stability, the winglets of the aircraft also function as a vertical tail with a rudder, and the required size is analysed for crosswind, engine failure, stall and directional stability.

The analysis of the control surfaces shows that the elevator is the critical factor for the design for rotation of the aircraft during take-off. Due to the limited span of the aft wing, the elevator and aileron are combined into an elevon to maximise the available control surface area. The final ratios are an elevon to chord ratio of 0.4 and a rudder to winglet chord ratio of 0.2. The winglet area is 36.9 m² with a height of 7.44 m.

Aircraft Configuration and Characteristics

Figure 3 shows the final internal configuration of the Cryo-V. A single aisle 3x3 configuration is used to make most efficient use of the space inside the fuselage. Four LD3-45 cargo containers can be placed behind the passengers in two separate cargo containers. The fuel is placed in six separate tanks in the trailing edge and behind the cargo for redundancy and safety. This configuration enables the total area to be used more efficiently than for conventional aircraft. The cabin area of the Cryo-V, including the cockpit, cargo hold and fuel, makes up about 80% of the total wing area, in comparison to 40% for the Airbus A320 fuselage [13].

A sensitivity analysis is performed on the results to analyse the influence of the input and design parameters on the final design. The Cryo-V design is characterised using five main parameters, the MTOW, approach and lateral noise, NO_x emissions and manufacturing cost. The analysis shows that the NO_x emissions are very sensitive to changes in input parameters. The MTOW and manufacturing

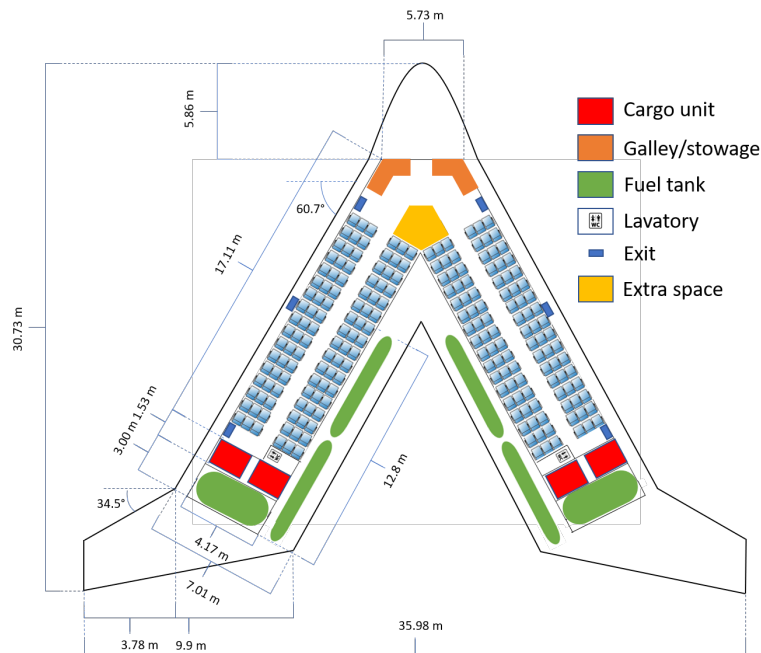


Figure 3: Top view of the Cryo-V configuration

cost are also sensitive to changes, although are nevertheless stable within their contingency margins. The cruise altitude and speed as well as the sweep of both the fuselage and aft wings are found to have a large influence on the design and should be monitored carefully for any changes in future design optimisation. Furthermore, the choice of optimisation parameter is found to have an effect on the final design and should also be improved into an optimisation function.

The Cryo-V is optimised for a Mach 0.78 cruise at FL400, but is also capable of Mach 0.76 cruise at FL300 for short-range missions. At FL400, the Cryo-V can reach a maximum payload range of 6150 km as well as a ferry range of 9100 km. The Cryo-V achieves a maximum sea level climb rate of 3730 ft/min and outperforms the Airbus A320 over the majority of the climb. The Extra Long-Range (XLR) version of the Cryo-V, which replaces the cargo containers with fuel tanks, can achieve a maximum payload range of 8280 km and can also cruise at a higher speed. The Cryo-V therefore closely matches or outperforms the Airbus A320 in all flight performance conditions analysed.

Project Design and Development Logic

The Design Synthesis Exercise (DSE) covers the conceptual design of the Cryo-V. After completion of the DSE, further, more detailed analyses, such as Computational Fluid Dynamics (CFD) and Finite Element Modelling (FEM), should be performed as part of the preliminary design. The detailed and part designs then follow, after which prototype production and certification starts. Following a successful certification and flight-test campaign, full-scale production can begin. The process is expected to take 13 years, resulting in an introduction into service earliest in 2034.

Operations and Logistics

To be competitive with the Airbus A320, the Cryo-V must be able to operate at type 4C airports. This requirement limits the maximum span, landing gear and turnaround time. The span and landing gear requirements are taken into account in the design process. The required turnaround time of 45 minutes is met. Although refuelling takes comparatively longer for the Cryo-V than for the Airbus A320, the aircraft can be boarded more efficiently due to the split fuselage. The cargo loading time is also reduced due to the smaller cargo capacity.

The major logistical challenge with the Cryo-V is the use of Cryogenic Hydrogen (LH₂). LH₂ has a high boil-off rate, so production close to the airport is a necessity. Optimally, LH₂ would be produced on-site at each airport using electrolysis with renewable electric power or obtained using pipelines. However, short-range LH₂ tanker trucks are a short term solution until infrastructure is in place, especially since a significant number of major hub airports are already located within 60 km of an LH₂ plant [14]. A full tank of the Cryo-V takes approximately the capacity of a tanker truck.

Finally, the Reliability, Availability, Maintainability and Safety aspects (RAMS) are considered. The aircraft has an estimated operational reliability of 99.54% and an availability of 95.61%. This is slightly lower than the Airbus A320 due to the LH₂ propulsion system, however, it is expected that this will increase as experience is gained with LH₂ storage and propulsion. The maintenance schedule will take the traditional "ABCD" check approach.

Sustainability Analysis

Emissions - The use of LH₂ both for combustion and in a fuel cell completely eliminates CO₂ emissions during operation of the Cryo-V. Combustion of LH₂ in the turbofans, especially in high thrust conditions during take-off and climb, does produce NO_x, but this effect is limited during cruise due to the low fuel to air ratio required. In total, the Cryo-V produces 8.200 kg of NO_x for a maximum range flight, a 90.8% reduction compared to the Airbus A320.

Since fuel cells produce water as a by-product, the effects of water vapour emissions at altitude are also investigated. Although the Cryo-V produces 33.1% more H₂O than the Airbus A320, the climate impact caused by Aircraft Induced Cloudiness (AIC) is on average 38% lower due to cruise flight at FL400 [15]. Therefore, the Cryo-V has a 17% lower net climate impact related to water vapour emissions, even though more water vapour is produced.

The climate impact of the Cryo-V is, therefore, significantly lower than for the Airbus A320 and all emission reduction requirements are met, as shown in Table 1.

Table 1: Total emissions of the Cryo-V, including a comparison to the Airbus A320

	LTO Cycle (kg)	Cruise (g/s)	Total - Max Range (kg)	Comparison with A320
NO _x	7.839	0.0135	8.200	-90.8%
H ₂ O	3538	1212	35 816	+33.1%
CO ₂	0	0	0	-100%

Noise - The dominant noise source for the Cryo-V is found to originate from the engines for the lateral and flyover measurement points and from the landing gear during approach. Three mitigation strategies are implemented in the iterative design process: reducing gross thrust, reducing approach speed, and positioning the engines for effective shielding. The thrust depends primarily on aerodynamic performance and can be significantly reduced compared to the A320, whereas the approach speed is similar. By placing the engines on top of the wing, an engine noise attenuation of 24.2 dBA, 8.1 dBA and 17.9 dBA can be achieved for approach, lateral and flyover certification positions respectively. These effects alone, however, do not meet the requirements, as shown in Table 2.

Table 2: LAmax noise levels of the Airbus A320 and the Cryo-V, with and without noise reduction applied

	A320	Requirements	Cryo-V		Comparison with A320
			Excl.	Incl.	
Approach (dBA)	86.1	71.1	72.7	69.8	-16.3
Lateral (dBA)	86.4	71.4	72.2	70.1	-16.3
Flyover (dBA)	71.7	56.7	58.3	50.4	-21.3

Further noise reduction is achieved by applying noise reduction technologies, including swept stators, over rotor acoustic treatment, chevrons, electric engine phase control and landing gear hub caps. Using these technologies, it is possible to meet the noise requirements of 15 dBA reduction for all measurement points.

Environmental Impacts - Assessing the environmental impact of the Cryo-V includes analysing its entire life cycle to identify processes that have large Environmental Impacts (EI). These EIs include, among others, climate change, land use, resource use, ionising radiation and water scarcity, which are quantified and compared to the A320 by means of a simplified formal Life Cycle Assessment (LCA). This includes a *goal and scope* definition of the LCA introducing the functional unit; an *inventory analysis* identifying and measuring material in and outflows; an *impact assessment* converting the material flows to EIs; and an *interpretation* combining the results and comparing them to the A320.

This LCA identifies a reduction in climate change EI for the overall life cycle, with the flight operational cycle being reduced significantly, almost entirely to zero. Furthermore, the material usage process in the manufacturing cycle presents a large EI reduction compared to the A320, due to the elimination of composite materials. Then, different hydrogen fuel production methods are analysed to ensure no significant increase in EI compared to conventional kerosene fuel production. This analysis shows a significant increase in EI when producing hydrogen with nonrenewable energy, but a small increase when using electrolysis with renewable energy. Finally, it is noted that other EIs than climate change should be investigated in more detail, since due to the significant reduction in the flight operational cycle, climate change no longer shadows other EIs, where the water scarcity EI is witnessed to increase.

End-of-Life (EoL) solutions are not included in the LCA due to the small amount of accurately defined data for the used materials. However, a preliminary EoL study shows that in past years most of the non-valuable waste consists of composites and cabin interior material. From this study and because the Cryo-V does not use composites, it is estimated that more than 90% of the material weight can be either recycled or reused for the Cryo-V.

Economic Analysis

The Cryo-V cost is divided into two parts: recurring cost and non-recurring cost. Non-recurring cost predominantly consists of the development cost of the aircraft, estimated at 2.858 billion EUR. Recurring cost, predominantly production cost, is estimated at 98.8 million EUR. The estimated Cryo-V price is, therefore, 117.6 million EUR, 30% higher than the Airbus A320.

Market research shows that with high aviation growth numbers of 4.3% [16] and governmental incentives for more sustainable aircraft, the Cryo-V is in a very good market position. This is reflected by the expected return of investment (ROI) for the Cryo-V at around 17%, which is the highest ROI value of the Airbus A320. Based on analysis, the market share of the Cryo-V could reach up to 20%.

Technical Risks

Risk analysis is an integral part of design projects. Risks can often not be totally mitigated, but they can be reduced to acceptable levels. The risks for the Cryo-V project can be subdivided in different categories: production, operational, external/market and design risks. The most critical production risk is that production cost is higher than budgeted since this significantly influences the commercial success of the aircraft. This risk is mitigated by selecting a sufficient contingency margin. The most critical operations risk is a hydrogen explosion due to tank leakage or improper refuelling. Foam insulation, a venting system and pressure valves minimise this risk. External risks are not deemed critical. Finally, a number of design risks can be identified, where incorrect assumptions or requirements can lead to unsuccessful certification, minimised using verification and validation. It is important to note that risk management is a continuous process and needs to be regularly updated.

Requirement compliance

The Cryo-V meets all gas emission and noise requirements, as shown in Table 3. No CO₂ is produced and NO_x emissions are reduced by 90.8%. Noise requirements are also met, resulting in a substantially quieter aircraft than the Airbus A320 in all flight phases.

Table 3: Emission and noise reduction of the Cryo-V, including the requirements from Flightpath 2050

		A320	Requirement [4]	Cryo-V
Noise ¹				
Lateral/Full power reference noise	(dBA)	86.4	71.4	69.8
Approach reference noise	(dBA)	86.1	71.1	70.1
Flyover reference noise	(dBA)	71.7	56.7	50.4
Gas Emissions [10, 17]				
CO ₂ during flight	(kg)	68 996	35 816	0
NO _x during flight	(kg)	89.23	8.923	8.200

All requirements except for the cargo volume, cruise altitude and reliability have been partially or fully satisfied. All non-compliant or partially-compliant requirements are described and motivated in detail in Chapter 15, and are deemed not critical to reach the project objective statement.

Conclusion

Clean and silent aviation is not idealistic, it is necessary realism. The Cryo-V conceptual design proves that it is possible to meet the ambitious goals set by Flightpath 2050 using hydrogen propulsion. For medium-range aircraft, it is found that fuel cells must be combined with hydrogen combustion for high-thrust conditions, such as during take-off and climb. Combustion of bio- or synfuels is likely not possible due to higher EINO_x.

Hydrogen propulsion and noise reduction are both tied to unconventional aircraft configurations. The large wing of the Cryo-V, for example, is beneficial for noise shielding, improves fuel performance and optimises hydrogen storage, which would not be possible with current configurations. New configurations can also be designed for modified operational procedures, such as an increased approach angle, which would be beneficial for noise reduction.

It is hoped that the Cryo-V design helps inspire the development of technologies that will help aviation and the environment co-exist. It is recommended that further research is conducted into the propulsion system and noise reduction techniques presented in this report, since these are not limited to use on the Cryo-V. We also suggest that close interaction is sought between airports, hydrogen suppliers and local governments to prepare for a hydrogen supply chain and ecosystem. We firmly believe that the future is hydrogen-powered and it is our duty to ensure that designs such as the Cryo-V become the new status quo. The Cryo-V is ready for the future, are you?

¹URL <https://www.easa.europa.eu/easa-and-you/environment/easa-certification-noise-levels> [cited 05 May 2020]

Introduction

For many decades, humanity has carelessly exploited Earth's natural resources without considering their scarcity and the consequences on the environment. Now, Earth is warming up at an alarming rate ¹. The aviation industry is currently responsible for 2% of the total CO₂ emissions and, with an average annual industry growth of 4.3% [16], is only set to grow further. Additionally, aircraft noise emissions are becoming an increasing problem. It has been proven that noise emissions can cause community annoyance, sleep disturbance and even mental and physical health problems [18–20]. The global population growth of 1.1% per year ² inevitably leads to more people living in direct vicinity to airports, who will experience an increase in aircraft noise if no measures are taken.

Considering these problems, ACARE (Advisory Council for Aviation Research and Innovation in Europe) has developed the Flightpath 2050 goals [4], which set high standards for the year 2050 regarding sustainability in aviation. To achieve these goals, a completely new approach in aircraft design is required. This Design Synthesis Exercise (DSE) aims to investigate the challenges and possibilities this presents. The mission need and objective statements for the project are provided below.

Mission Need Statement (MNS)

The aviation industry has a need for sustainable aircraft with reduced greenhouse gas and noise emissions, in order to meet international sustainability agreements [1].

Project Objective Statement (POS)

Design a climate-neutral, medium-range passenger airliner by 10 students in 10 weeks that meets the Flightpath 2050 goals of reducing NO_x by 90%, CO₂ by 75% and perceived noise by 65% compared to technology levels in the year 2000 [1].

The aim of this report is to present the results of the DSE, including the approach and final design of the Cryo-V, a cryogenic hydrogen hybrid combustion-electric aircraft. Chapter 2 presents an overview of the concept selection phase, including a functional analysis, classification of requirements and the final concept selection process. Chapter 3 describes the design and development methodology until entry into service. Chapter 4 provides an overview of the integration process and Chapters 5-8 present the design and sizing of each subsystem. In Chapter 9, the final aircraft configuration is presented. Chapter 10 analyses the performance of the final design regarding weight, flight characteristics, emissions and noise. The operations and logistics are described in Chapter 11, followed by the life cycle assessment in Chapter 12, which considers the environment impact of the manufacturing process and materials used. In Chapter 13, the cost and predicted return of investment of the Cryo-V is analysed. Chapter 14 provides an overview of the risks associated with the project. Chapter 15 analyses compliance of the final design with requirements. Finally, Chapter 16 provides a conclusion and recommendations for further work.

¹URL <https://www.ncdc.noaa.gov/sotc/global/201913> [cited 19 June 2020]

²URL <https://ourworldindata.org/world-population-growth> [cited 19 June 2020]

Concept Selection Review

Multiple concepts were considered during earlier stages of the project before deciding on the final design. This chapter summarises the design activities involved in concept selection before the detailed design phase. First, the aircraft functional analysis is performed and described in Section 2.1. A review of the project requirements is presented in Section 2.2 followed by a discussion of the main project considerations in Section 2.3. Finally, the design options and the trade-off process are introduced in Section 2.4 and Section 2.5, respectively.

2.1. Functional Analysis

In order not to miss any critical requirements, it is important to analyse all functions of the aircraft during its life cycle. This is done using a Functional Flow Diagram, which presents all functions the system must perform from design to end of life in a chronological order. The functional flow diagram is shown on pages nine and ten. Next to that, a functional breakdown structure is set up (see page eight) which gathers all functions of the functional flow diagram in their respective top-level functions along with additional functions which should be performed at all times.

2.2. Requirements Review

The Cryo-V design is subject to many requirements created to satisfy the goals of the project as specified by the customer and by the MNS/POS. The stakeholder requirements are identified as being the top level requirements, from which the subsystem requirements follow. Table 2.1 shows the stakeholder requirements given to the team by the customer. *MRA* stands for "Medium Range Aircraft" and is an abbreviation of the original project title.

The stakeholder requirements cover the performance, sustainability and cost of the product. Compliance with these requirements is crucial for the aircraft to be competitive. To present a clear overview of these requirements, key, driving and potential critical requirements are identified. *Key requirements* are considered most important to the customer and are defined on a more global level. These are presented in Table 2.2. The *driving requirements*, considered to be crucial for the engineering design and which affect the sizing and design of the aircraft the most, are presented in Table 2.3. This table also shows the *potential critical requirements*, which are considered the most challenging to meet, as analysed in the Midterm Report [3]. It should be noted that the remaining requirements in Table 2.3 serve to present a complete requirement coverage, but are not considered to drive the design to the same extent as the driving requirements. Requirement compliance is discussed in Chapter 15, with a requirement compliance matrix shown in Table 15.1.

2.3. Project Considerations

Table 2.1: Stakeholder requirements [3]

Stakeholder Requirements	
MRA.SH.1	The aircraft shall have a minimum range of 6150 km.
MRA.SH.2	The aircraft shall have a minimum endurance of 6 h.
MRA.SH.3	The aircraft shall have a minimum cruise speed of 830 km/h.
MRA.SH.4	The aircraft shall have a cruise altitude of 30 000 ft.
MRA.SH.5	The aircraft shall have a maximum take-off distance of 2100 m.
MRA.SH.6	The aircraft shall have a maximum landing distance of 1500 m.
MRA.SH.7	The aircraft shall follow the same regulations as the Airbus A320 (CS-25).
MRA.SH.8	The aircraft shall have the same reliability as the Airbus A320.
MRA.SH.9	The aircraft shall have no additional maintenance than the Airbus A320.
MRA.SH.10	The aircraft shall be quieter than the Airbus A320.
MRA.SH.11	The aircraft shall be at least 75% recyclable/reprocessable.
MRA.SH.12	The aircraft shall have a lower environmental impact than the Airbus A320.
MRA.SH.13	The aircraft shall have a capacity of 200 passengers.
MRA.SH.14	The aircraft shall have a maximum take-off weight of at most 78 000 kgf.
MRA.SH.15	The aircraft shall cost less than 100 million EUR.

Table 2.2: Key requirements [3]

Key Requirements	
MRA.SYS.PERF	The aircraft shall have the customer requested performance.
MRA.SYS.REG	The aircraft shall comply with CS-25 safety and reliability regulations.
MRA.SYS.COST	The aircraft shall have a competitive cost to the Airbus A320.
MRA.SYS.SUST	The aircraft shall comply with sustainability goals stated in Flightpath 2050; including social, economic and environmental sustainability.

2.3. Project Considerations

The mission need and project objective statements in the introduction show the importance of developing a design that not only reduces greenhouse gas emissions, but also focuses on other key aspects of sustainability, such as noise emissions, and economic competitiveness. The Airbus A320 is taken as a baseline for the project, against which performance and sustainability are compared. The mission profile that the Cryo-V is designed to meet, shown in Figure 2.1, is similar to a typical profile for medium range airliners. Furthermore, the Cryo-V must be certified to EASA CS-25 standards [21].

2.3.1. Sustainability Considerations

To ensure this project adheres to sustainability requirements, it is important to understand the specific meaning of sustainability and how the Cryo-V contributes to the global sustainability movement. The sustainability considerations are presented in this section and their implementation in the design

¹URL https://www.skybrary.aero/index.php/ICAO_Aerodrome_Reference_Code [cited 01 May 2020]

²URL <https://bit.ly/3cpbdV1> [cited 01 May 2020]

³URL <https://www.airbus.com/newsroom/news/en/2008/03/new-service-package-will-extend-a320-039-s-life.html> [cited 01 May 2020]

⁴URL <https://www.icao.int/MID/Documents/2017/Aviation%20Data%20and%20Analysis%20Seminar/PPT3%20-%20Airlines%20Operating%20costs%20and%20productivity.pdf> [cited 01 May 2020]

⁵URL <https://www.easa.europa.eu/easa-and-you/environment/easa-certification-noise-levels> [cited 05 May 2020]

2.3. Project Considerations

Table 2.3: Driving and potential critical requirements - system requirements [3]

Performance Requirements	
MRA.SYS.PERF.1.1	The aircraft shall have a minimum range of 6150 km.
MRA.SYS.PERF.1.3	The aircraft shall have a minimum cruise speed of 830 kph.
MRA.SYS.PERF.1.4	The aircraft shall have a cruise altitude of 30 000 ft.
MRA.SYS.PERF.1.5	The aircraft shall have a minimum endurance of 6 h under standard conditions.
MRA.SYS.PERF.4	The aircraft shall be stable in all flight conditions.
MRA.SYS.PERF.7.1	The aircraft shall obtain an initial maximum climb rate at sea level at standard conditions of 3000 ft/min. ¹
MRA.SYS.PERF.10.6	The aircraft shall have a maximum take-off distance of 2100 m at sea level at standard atmospheric conditions on a concrete runway.
MRA.SYS.PERF.11.6	The aircraft shall have a maximum landing distance of 1500 m at sea level at standard atmospheric conditions on a concrete runway.
Aircraft Sizing Requirements	
MRA.SYS.OP.1.6	The aircraft shall be designed for a load factor of 2.5. [21]
MRA.SYS.OP.1.7	The aircraft shall be designed to withstand gust loads specified by CS25.
MRA.SYS.OP.2.2	The aircraft shall have a cargo volume of 25 m ³ . [17]
MRA.SYS.OP.2.4	The aircraft shall have a capacity of 200 passengers.
MRA.SYS.OP.3.1	The aircraft shall be able to operate from a type 4C Aerodome. ²
MRA.SYS.PERF.10.10	The aircraft shall have a maximum take-off weight of at most 78 000 kgf.
Regulation Requirements	
MRA.SYS.OP.REG.1.1	The aircraft shall be certified to EASA CS25 standard.
MRA.SYS.PERF.12.7	The aircraft shall qualify for an ETOPS-180 min rating.
Operation Requirements	
MRA.SYS.OP.1.1	The aircraft shall have an operational reliability of 99.6%. ²
MRA.SYS.OP.1.2	The aircraft shall perform at least 60 000 cycles or 120 000 flight hours. ³
MRA.SYS.OP.7.1	The aircraft shall be integrate-able in the global infrastructure.
Cost Requirements	
MRA.SYS.OP.COST.1.2	The aircraft's maintenance costs shall on average be less than 800 USD per flight hour. ⁴
MRA.SYS.OP.COST.1.3	The aircraft's operational costs shall on average be less than 2800 USD per flight hour. ⁵
MRA.SYS.OP.COST.1.4	The aircraft's production cost shall be less than 95 million EUR.
Sustainability Requirements	
MRA.SYS.SUST.1.0	The aircraft shall have a cumulative noise reduction of 45 EPNdB for all three certification levels. [4]
MRA.SYS.SUST.1.1	Lateral/full power reference noise shall be lower than 76.4 EPNdB. [22] ⁵
MRA.SYS.SUST.1.2	Approach reference noise shall be lower than 80.5 EPNdB. [22] ⁶
MRA.SYS.SUST.1.3	Flyover reference noise shall be lower than 68.5 EPNdB. [22] ⁶
MRA.SYS.SUST.4.0	The aircraft shall comply with gas emission reductions as stated in Flightpath 2050.
MRA.SYS.SUST.4.1	The aircraft shall emit at most 17 249 kg CO ₂ during flight. [10, 17]
MRA.SYS.SUST.4.2	The aircraft shall emit at most 8.923 kg NO _x during flight. [10, 17]
MRA.SYS.SUST.5.0	The aircraft shall have a lower environmental impact than the Airbus A320.
MRA.SYS.SUST.5.1	The entire life cycle shall have a lower environmental impact on climate change than 98 g CO ₂ eq PKM. [23]
MRA.SYS.SUST.5.6	The aircraft shall be at least 75% recyclable.

Driving Requirement
Potential Critical Requirement

process is discussed in Section 3.2.

Sustainability has experienced a rapid increase in importance in recent years. It is commonly expressed as *"meeting the needs of the present without compromising the ability of future generation to*

2.4. Design Options

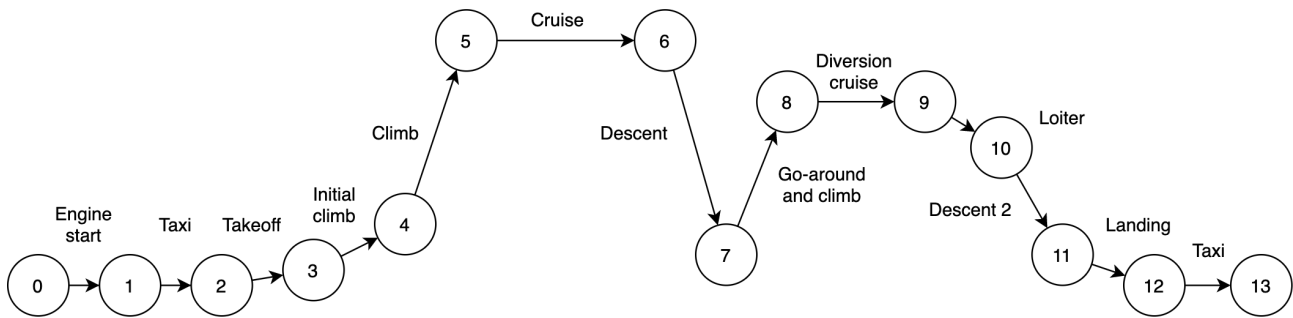


Figure 2.1: Cryo-V flight profile

meet their own needs”⁶, which clearly shows its broad scope. To present more specific sustainability goals, the European Union released Flightpath 2050 [4] containing specific goals related to aviation. These goals are best categorised by means of the *Trinity Concept*, categorising Flightpath 2050 into: *Social Sustainability*, *Economic Sustainability* and *Environmental Sustainability* goals. By incorporating the comparison of this project to the Airbus A320, the following sustainability project objectives are derived:

Social Sustainability

Provide an aircraft that contributes to an efficient transport system, that provides customer services and significantly reduces noise pollution with respect to the Airbus A320 [3].

An efficient transport system relates to a vehicle operating safely, affordably, quickly, smoothly, seamlessly, predictably and without interruption [4].

Economic Sustainability

Provide an aircraft that adheres to providing a resilient transport chain and incorporates measures to stay up to date with ongoing research and contributing to implementing innovative products or services in the project’s organisational system [3].

A resilient transport chain relates to a vehicle operating seamlessly, safely, securely, cost effectively, quickly, reliably and resiliently without negatively impacting the environment [4].

Environmental Sustainability

Provide an aircraft that mitigates the engine emissions to satisfy the Flightpath 2050 CO₂ and NO_x goals and has a significant lower environmental impact than current aircraft [3].

2.4. Design Options

Due to the challenging design goals, a wide range of conventional and unconventional design options are considered. Different airframe configurations are considered together with multiple potential energy sources, since the use of a specific energy source directly impacts the emissions produced. After preliminary research, three main airframe designs are chosen: the Prandtl/box wing [8], blended wing body (BWB) [6, 7] and Flying-V⁷ configurations. All concepts have potential to improve the aerodynamic efficiency of the aircraft. The conventional airframe configuration is also considered if combined with noise reduction technologies. However, due to its weaker aerodynamic efficiency, the conventional aircraft is also used as a baseline for the trade-off process.

⁶URL <https://academicimpact.un.org/content/sustainability> [cited 21 June 2020]

⁷URL <https://www.tudelft.nl/en/ae/flying-v/> [cited 20 June 2020]

For the different energy sources, the options considered are biofuels, liquid hydrogen, synthetic fuels and batteries. Furthermore, different energy conversion methods are considered for liquid hydrogen and synthetic fuels: either combustion or using fuel cells. Hybrid options that use a combination of the energy sources and conversion methods are viable design solutions as well. Use of kerosene as a fuel is not considered since it would be impossible to reach the sustainability requirements.

2.5. Design Trade-Off and Selection

A trade-off for different design options is performed before arriving at the final design. The trade-off method is explained in Subsection 2.5.1, followed by the final trade-off results in Subsection 2.5.2.

2.5.1. Trade-Off Method

To reach the final design from the options considered, it is essential to use a robust trade-off method. Since it is necessary to combine airframe designs with multiple energy source options, the trade-off is performed on multiple levels. Three trade-off levels (system-level, integration-level and configuration-level) are performed to reach a final trade-off selection. At the system-level, the trade-off is performed to assess airframe design, energy storage & conversion, propulsion system and engine placement options separately. The latter two are important parameters, as these affect both propulsion efficiency and noise. Trade-offs are performed using weighted criteria. The most significant criteria are emission reduction, noise reduction and aircraft performance, while also considering risk and cost of the design options.

The optimal scenario would be to choose the design combining the highest scoring options from all of the system-level trade-offs. However, some combinations of design options are not feasible and at the integration-level these are eliminated. Two integrations are evaluated in more detail during the integration-level: propulsion system & engine placement and airframe design & energy storage.

At the configuration-level, system-level options are linked together using the feasible integrations generated at the integration-level. Each set of linked options is called a path and is given a weighted score, which is a sum of all its system- and integration-level components. Paths are presented in a morphological box, an excerpt of which is shown in Figure 2.2, where the system-level trade-offs are listed in the first column on the left and all design options within each system are listed in the corresponding rows. For example, the blue path represents a design combined with all of the highest scoring options of each system, while the red path differs from the blue one by using the second highest scoring option of energy trade-off.

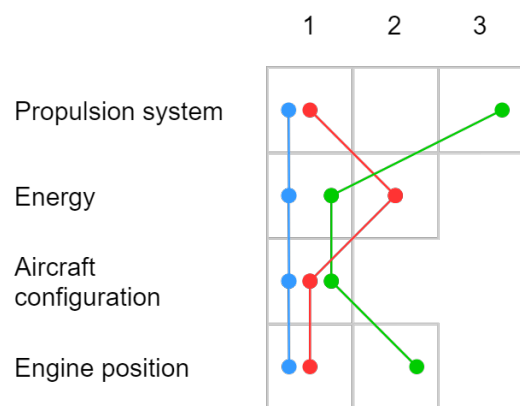


Figure 2.2: Morphological box path selection

2.5.2. Final Design Selection

The final trade-off analyses the six highest-scoring paths from the morphological box. However, as explained in detail in the Midterm Report [3], a number of initial highest-scoring paths are eliminated, including the full use of alcohol fuel cells, biofuels and hydrogen. A preliminary analysis concluded that due to their low energy density, alcohol and hydrogen fuel cells on their own would be too heavy. It can also be shown that a maximum of 20% of the total energy could be provided by combustion due to the limit of NO_x emissions [3]. Therefore, only hybrid options could be considered for the final trade-off.

Liquid hydrogen fuel cells are used in all six hybrid options due to the elimination of NO_x and CO₂ emissions during their use. The fuel cells are combined with the combustion of either hydrogen or

2.5. Design Trade-Off and Selection

biofuel. The Prandtl-wing configuration could be eliminated due to its low capability of storing large volume of fuel on board. The final design options are listed below in order of final score. It should be noted that the discrete BWB differs from the BWB, as it has a clearly defined fuselage (such as the Airbus MAVERIC⁸ and Rockwell B-1 Lancer⁹). For the BWB, the fuselage is entirely integrated in the wing (as for the Boeing - NASA X-48¹⁰).

Final Trade-Off Concepts

1. **Hybrid LH₂ combustion / fuel cell Flying-V aircraft**
2. Hybrid LH₂ combustion / fuel cell BWB aircraft
3. Hybrid biofuel combustion / LH₂ fuel cell Flying-V aircraft
4. Hybrid biofuel combustion / LH₂ fuel cell BWB aircraft
5. Hybrid LH₂ combustion / fuel cell discrete BWB aircraft
6. Hybrid biofuel combustion / LH₂ fuel cell discrete BWB aircraft

These six final designs are compared using weighted criteria. The most significant factors are emission and noise reduction, followed by aircraft performance and, finally, cost and design risk. The final design chosen is LH₂ fuel cells & LH₂ combustion with Flying-V configuration. This is also the inspiration for the aircraft and project name: the Cryo-V.

The chosen design scores the highest due to several reasons. Firstly, biofuel hybrid options score lower due to CO₂ production and the use of two different fuels has disadvantages for safety and operations [3]. Secondly, the Flying-V configuration scores higher than the BWB due to a slightly larger noise reduction, based on preliminary estimates [3]. However, most importantly, the BWB is found to have higher development risk and cost. These two factors are analysed quantitatively by considering production, maintenance, development, operational costs and similar risk factors including also certification and RAMS aspects. Maintenance is easier for the Flying-V configuration due to similar accessibility to the wings and fuselage as for conventional aircraft. Operations of BWB aircraft is more complicated due to its larger wing body.

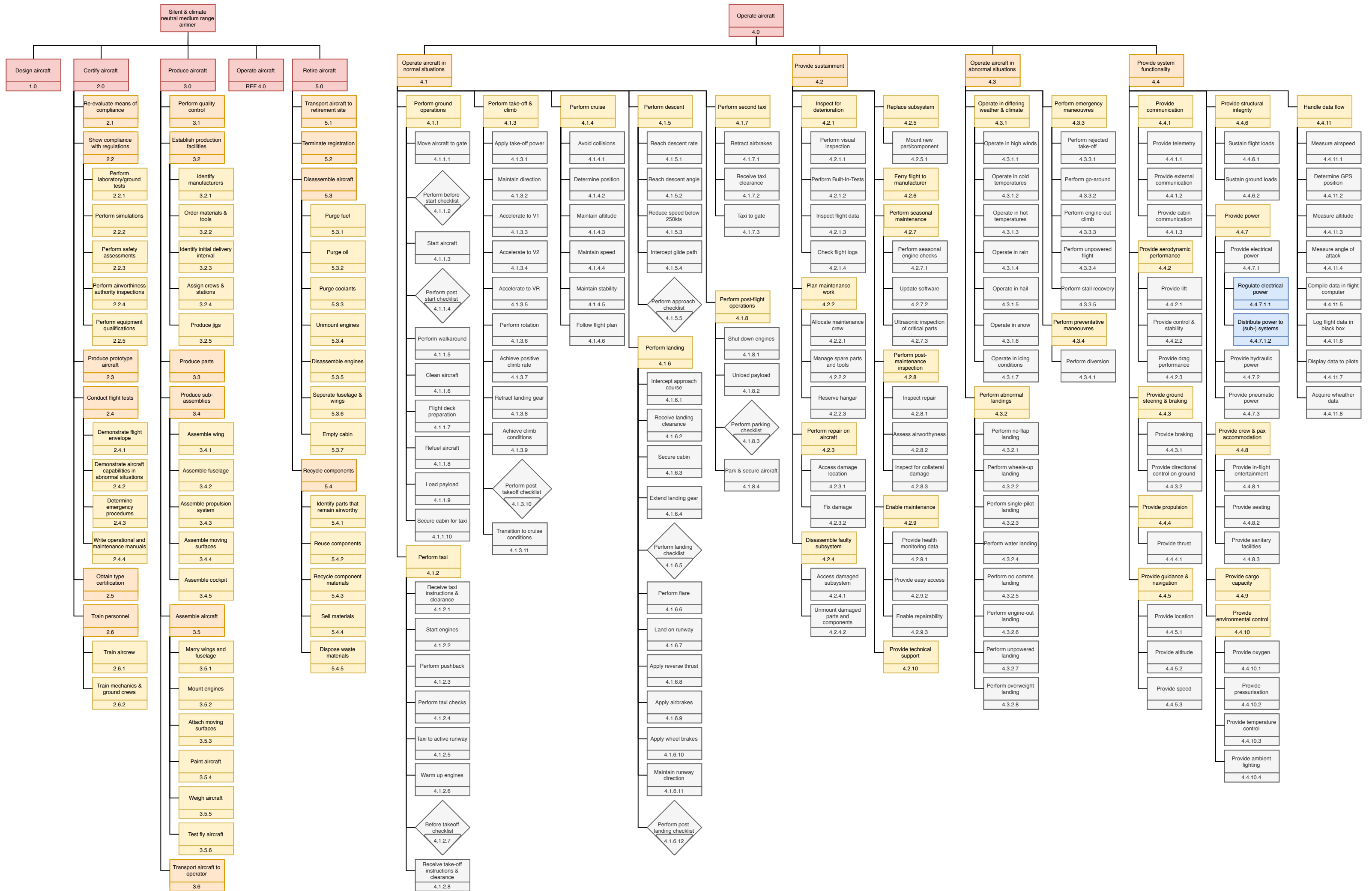
2.5.3. Class I Sizing Results

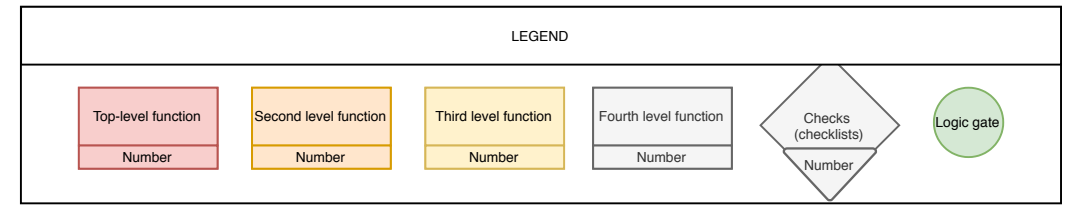
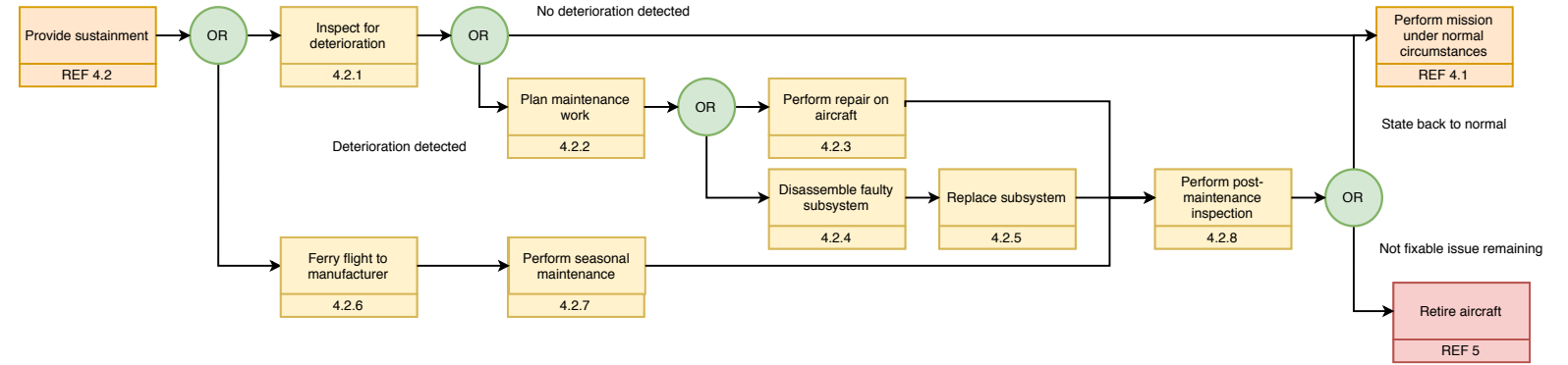
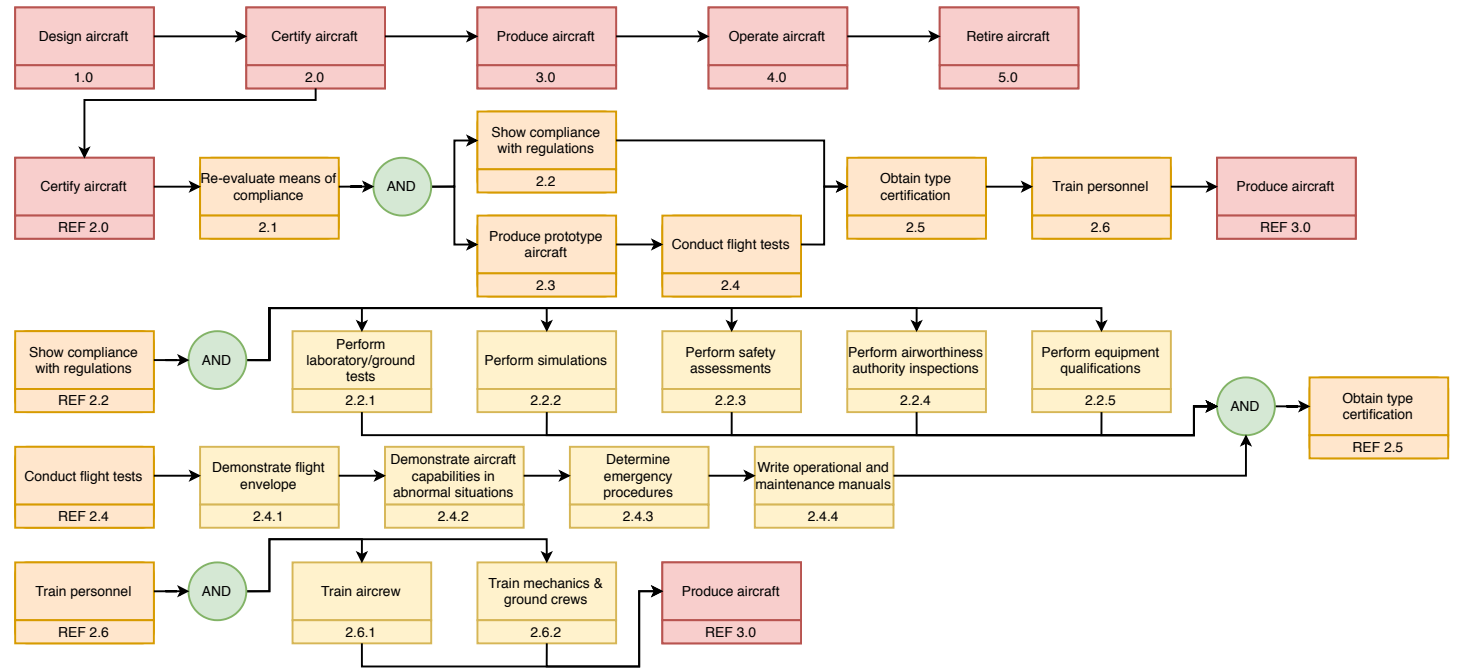
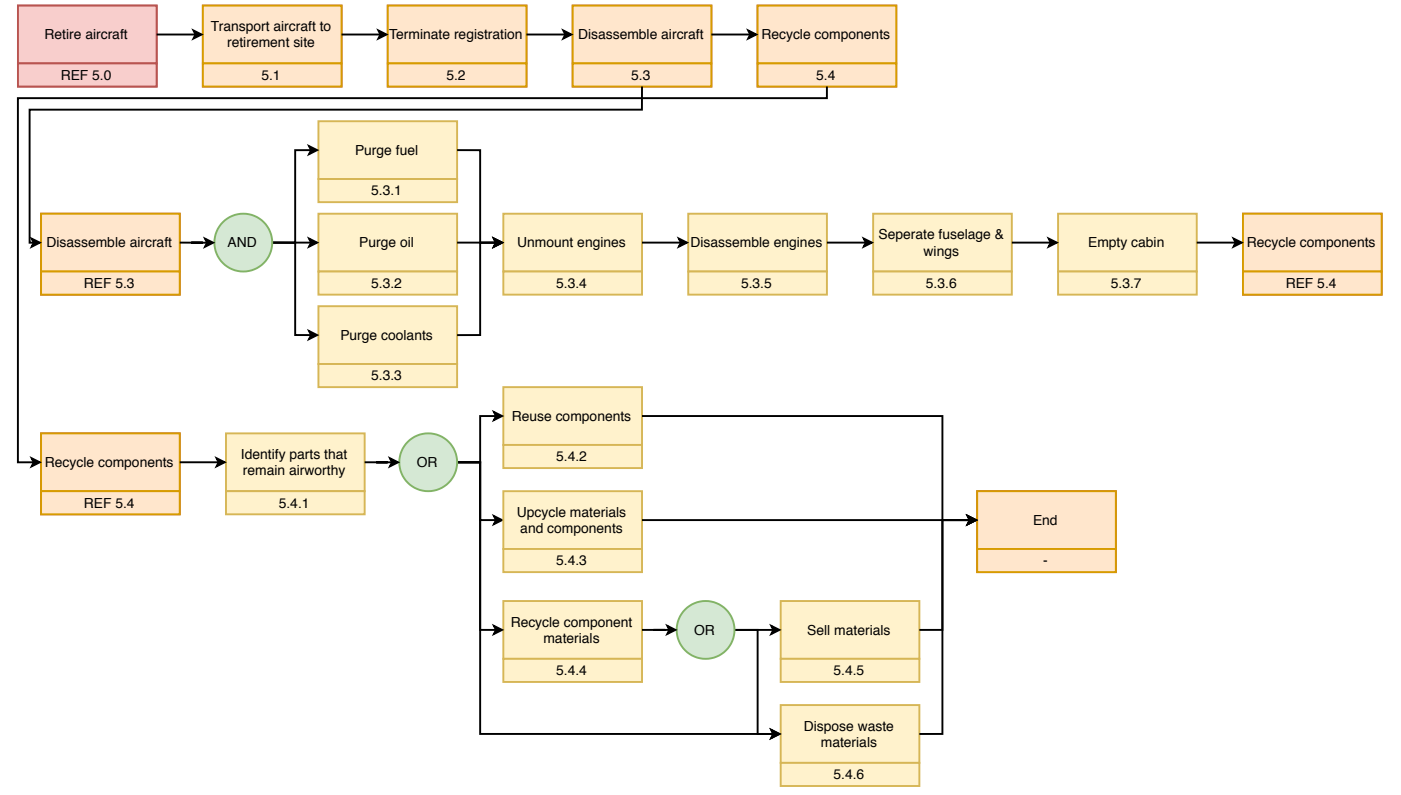
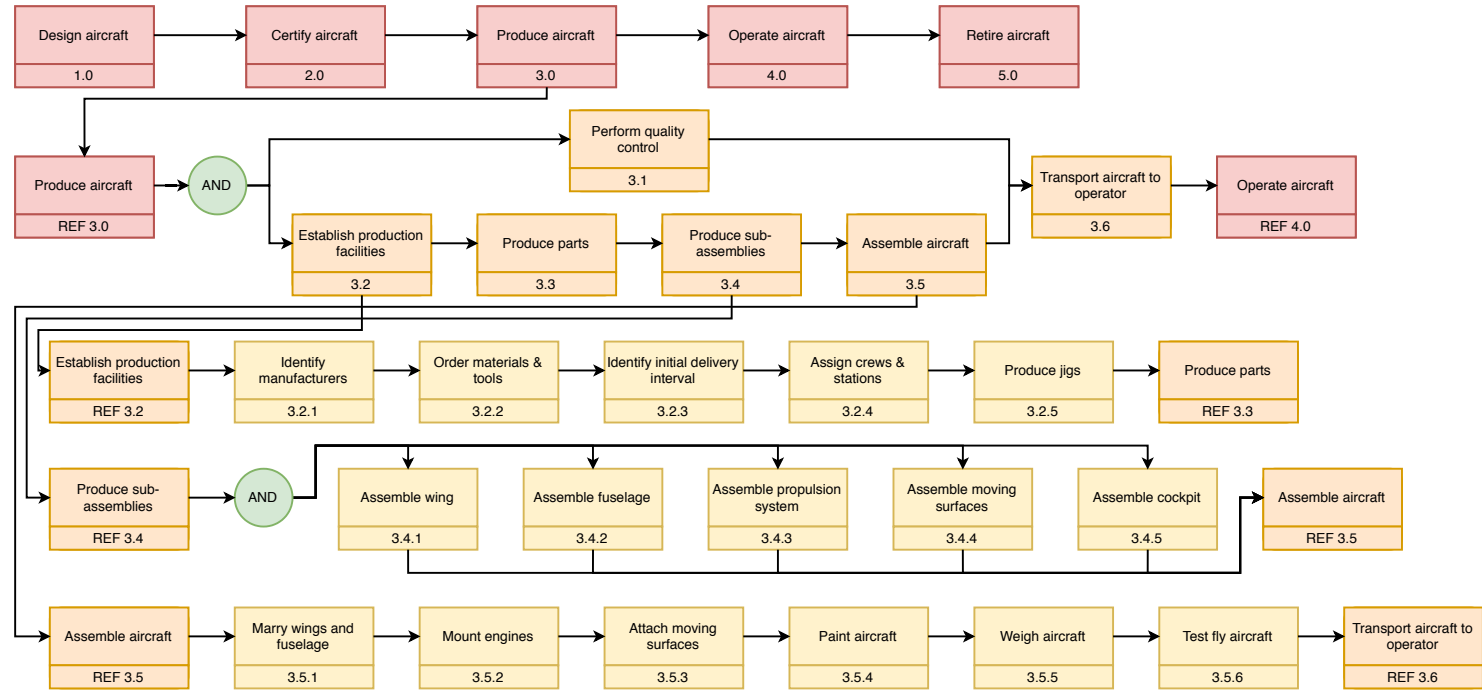
Class I sizing is performed to understand the main design parameters of Cryo-V and ensure that design is realistic. The Operational Empty Weight (OEW) is estimated around 38 tonnes and the Maximum Take-Off Weight (MTOW) around 63 tonnes, 5 and 15 tonnes lighter, respectively, than for the Airbus A320. Furthermore, the estimated fuel mass on board is only three tonnes, which is 5% of MTOW and 21 tonnes less than for the Airbus A320. This low fuel weight makes the range very sensitive to the amount of fuel carried: a small amount of extra fuel has a significant effect on the maximum range. On the other hand, a disadvantage is that the relative landing weight is higher than for the Airbus A320, which leads to a stronger and heavier landing gear.

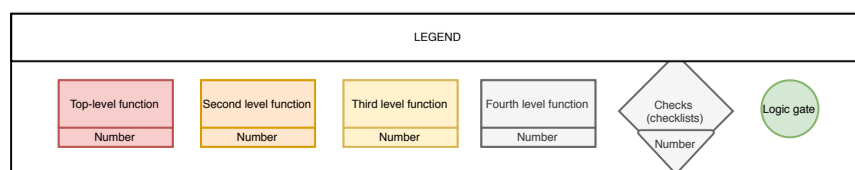
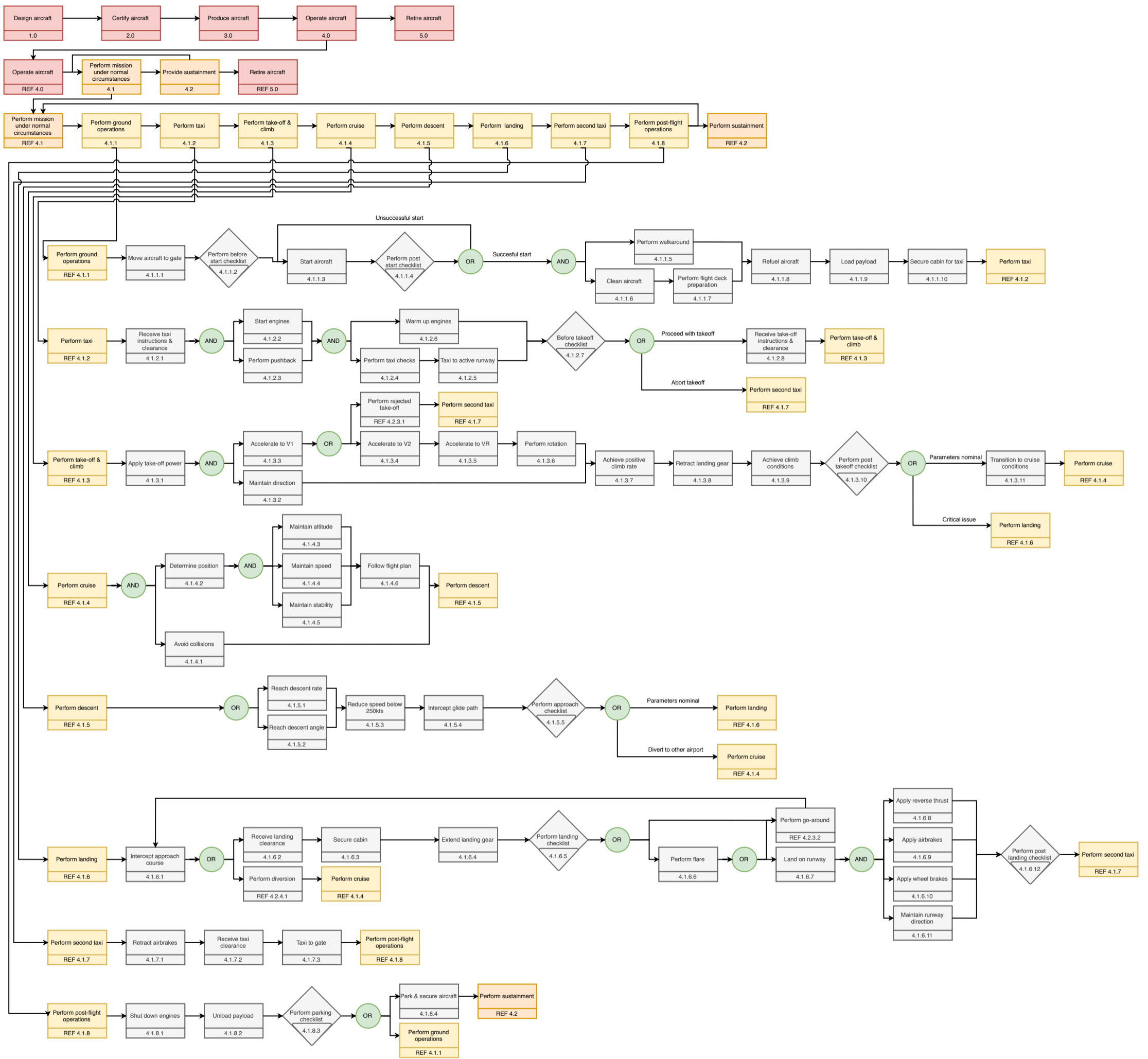
⁸URL <https://www.airbus.com/newsroom/press-releases/en/2020/02/airbus-reveals-its-blended-wing-aircraft-demonstrator.html> [cited 28 May 2020]

⁹URL <https://www.boeing.com/defense/b-1b-bomber/> [cited 28 May 2020]

¹⁰URL https://www.nasa.gov/topics/aeronautics/features/X-48_research_ends.html [cited 28 May 2020]







Design Methodology

This chapter describes the approach towards a sustainable design reaching entry into service. In 3.1 each design, certification and production phase is described and their corresponding timeline is given. 3.2 presents how sustainability is implemented in the entire process.

3.1. Project Design and Development Logic

Before the Cryo-V can be introduced in the aircraft industry it has to go through the complete design, certification and production process. The complete design process of an aircraft includes a conceptual, preliminary and detailed design phase. The expected duration of each of these phases is described in Subsection 3.1.2. The DSE only covers the conceptual design phase. The tasks in these phases are based on the design procedures described by Anderson and Raymer [24, 25]. The design phases, certification procedure and final production process are each explained in Subsection 3.1.1. A logical flow diagram of the subsequent phases and a Gantt chart with the initially estimated time required for each of these phases and their coherent tasks is provided in page 14.

3.1.1. Design and Development Phases

The complete design process consists of the conceptual design, preliminary design and detailed design. Each of these give a more detailed design of the prior phase and can only start as soon as the prior phase has finished.

Conceptual Design - After requirements have been given by the stakeholder, the conceptual design phase can be started. The scope of the DSE is within this phase, where the top level steps taken are shown in Figure 3.1. After a final concept is selected based on the requirements the specific design process can start. Initially the size, shape, weight and performance of the design are determined in an iterative process. The fundamental aspects of the design are then used to give an initial layout of the aircraft configuration. At this point of the design process, the configuration is flexible and will be optimised in the next phase, the preliminary design. Although the DSE project thoroughly covers the conceptual design, new problems or better ideas are expected to emerge when design elements are investigated in further detail. Additionally it is also an iterative process where the design team should adjust it's design based on the stakeholder's feedback. The time required for extra research and stakeholder's approval is substantially longer than the given time of the DSE project.

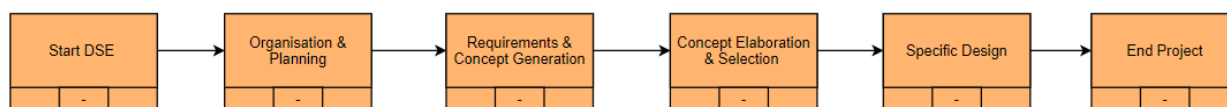


Figure 3.1: Top level steps of the DSE project

Preliminary Design - After the conceptual design has been produced, it can be analysed in further detail. In this phase structural and control system analysis will initially take place to eliminate possi-

ble flaws in the configuration, as shown in the flowchart provided on page 14. Next, computational fluid dynamic analysis and wind tunnel testing will be performed to uncover possible aerodynamic or stability problems. Additionally acoustic testing will be performed to validate the noise reduction technologies implemented, and possibly reveal new noise sources. After the design has been optimised based on all these analyses, a full-scale development proposal is produced [25]. This is a crucial moment since it will determine whether the available budget will be exceeded and whether production will be feasible. At this stage it is decided whether the design team will continue with the detailed design or the project will be stopped.

Detailed Design - As shown on page 14, the detailed design consists of three stages: the assembly design, system design and part design. The assembly design covers the integration and interface of the different subsystems and components. The system design covers each subsystem in more detail and the part design covers each individual component to as much detail as the sizing and positioning of fasteners. During the part design phase the manufacturing facility, including assembly line and each tool and jig for manufacturing are also designed. During the whole detailed design process every step is verified and each phase is validated to ensure that the design is still in line with the given requirements. At the end of the detailed design phase a go/no moment is introduced to determine whether production is feasible or the project should be stopped.

Certification - After the prototype aircraft and the simulator have been built in the detailed design phase, the testing for certification can start. First, the certification organisation must be familiarised with the technical information provided by the design team after which a certification programme can be developed. Various ground tests are performed to show compliance with regulations and at the same time flight tests are performed, as specified in the flowchart provided on page 14. After all the testing has been done, the certification organisation determines whether the aircraft can obtain type certification or requires modifications in the design. If the design needs modifications the management team determines whether redesign is feasible or the project should be aborted. If type certification is reached, the ground personnel can be trained to start the production process. Simultaneously the aircrew will be introduced to the aircraft and be prepared for first flight.

Production - Once the certification is approved, the Cryo-V is ready to be produced. The whole aircraft is broken down into different groups, fuselage group, aft wing group, propulsion group, etc., which are further broken into individual component parts for massive production. Although most of the manufacturing process is similar to that of the conventional aircraft as they share common components, there is still a major difference in the propulsion system, due to the usage of fuel cells and storage of liquid hydrogen. Therefore, the production of the propulsion system has to be carried out by an individual department, either from the conventional engine manufacturers or from a specially founded department of the Cryo-V group. A production, assembly and integration plan diagram is included in Section 9.5.

3.1.2. Expected Timeline

The Gantt chart shown on page 14 gives an initial prediction of the duration and starting date of each phase and corresponding tasks. The estimated duration of each design phase is based on the published design timeline of the Boeing 777 [26]. This timeline is chosen as reference since it is the most detailed timeline published. However this timeline is assumed to be representative for different aircraft such as the Airbus A320. In this publication the conceptual and preliminary design phase is given as a whole with a duration of 4 years.

Design Phases - The Cryo-V is expected to have a conceptual design phase of 1 year, where an iterative process with the stakeholders and more detailed research on encountered problems is taken into account. The preliminary design phase is expected to last 3 years. The tasks of the preliminary design phase have also been given an initial duration estimate but these can vary substantially throughout the process since unexpected problems may arise or more iterations are required. The detailed design of the Boeing 777 including production of the prototype aircraft lasted 4 years [26].

However, the Cryo-V is expected to have a longer system and part design phase since it is an unconventional aircraft configuration. The hybrid propulsion system namely will require many new components which require more time to develop. Therefore the detailed design phase is initially expected to have a duration of roughly 7 years.

Certification - Although modern aircraft, such as the A350 can have a certification process of only 14 months¹, the Cryo-V certification is expected to have a duration of 3 years. This is because the Cryo-V contains many new technologies to be introduced to the market, such as the hybrid propulsion system, which require more testing time than current technologies. Furthermore aircrew as well as ground crew must be prepared for the new aircraft type which requires a longer training process than for conventional aircraft.

Production - The production time of Airbus A320 from its first part being manufactured to its delivery to airlines is about 1 year [27], and such duration is also considered suitable for Cryo-V. The propulsion systems of Cryo-V need to be produced unconventionally and thus a new production department and production lines will be founded.

3.2. Sustainable Development Plan

Following the sustainability considerations discussed in Subsection 2.3.1 this section presents how they are implemented in the design process.

3.2.1. Social Sustainability

To comply with the set social sustainability project objective, the Cryo-V needs to contribute to an efficient transport system, provide customer services and significantly reduce noise pollution [3].

Contributing to an **efficient transport system** entails dealing with operational safety. It needs to be ensured the aircraft complies with CS-25 safety regulations [21], that an extensive risk identification, and mitigation plan is present and that structural maintenance and repair is implemented efficiently. This directly leads to an aircraft that is predictable and efficient in its operation, that mitigates technical issues and thereby minimising undesirable long passenger delays and costs.

Therefore, all mentioned elements are incorporated in the design process, where Section 11.4 presents the reliability, availability, maintainability, and safety considerations of the Cryo-V and Chapter 14 presents an extensive risk analysis, including their mitigation strategies.

Furthermore, **customer services** entails providing the passengers sufficient room to travel comfortably, providing passenger utilities, including lavatories, food and drinks, and ensuring cabin environmental control. This contributes to minimise the impact travelling has on the human body. The project deals with these considerations by complying with seat pitch regulations and including passenger utilities in the cabin, presented in Chapter 9.

Finally, **noise pollution** is dealt with throughout the subsystems design by including noise prediction methodologies and ensuring compliance to the established noise requirements for the final aircraft configuration. The final noise characteristics are presented in Section 10.4, giving an elaborate noise breakdown analysis.

3.2.2. Economic Sustainability

To comply with the set economic sustainability project objective, the Cryo-V needs to contribute to a resilient transport chain as well as support and implement innovation [3].

To contribute to a **resilient transport chain** the Cryo-V needs to be economically feasible and com-

¹URL <https://www.airbus.com/aircraft/how-is-an-aircraft-built/test-programme-and-certification.html> [cited 18 June 2020]

petitive on the market, next to being safe, reliable and resilient, and an efficient transport system. To ensure this, an economic analysis is conducted in Chapter 13, including a cost breakdown analysis, market analysis, and a return of investment and operational profit analysis.

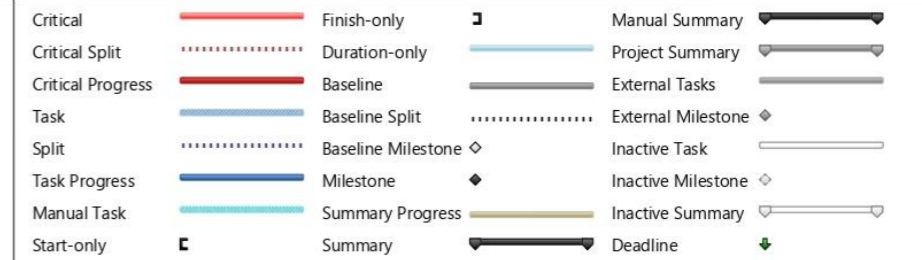
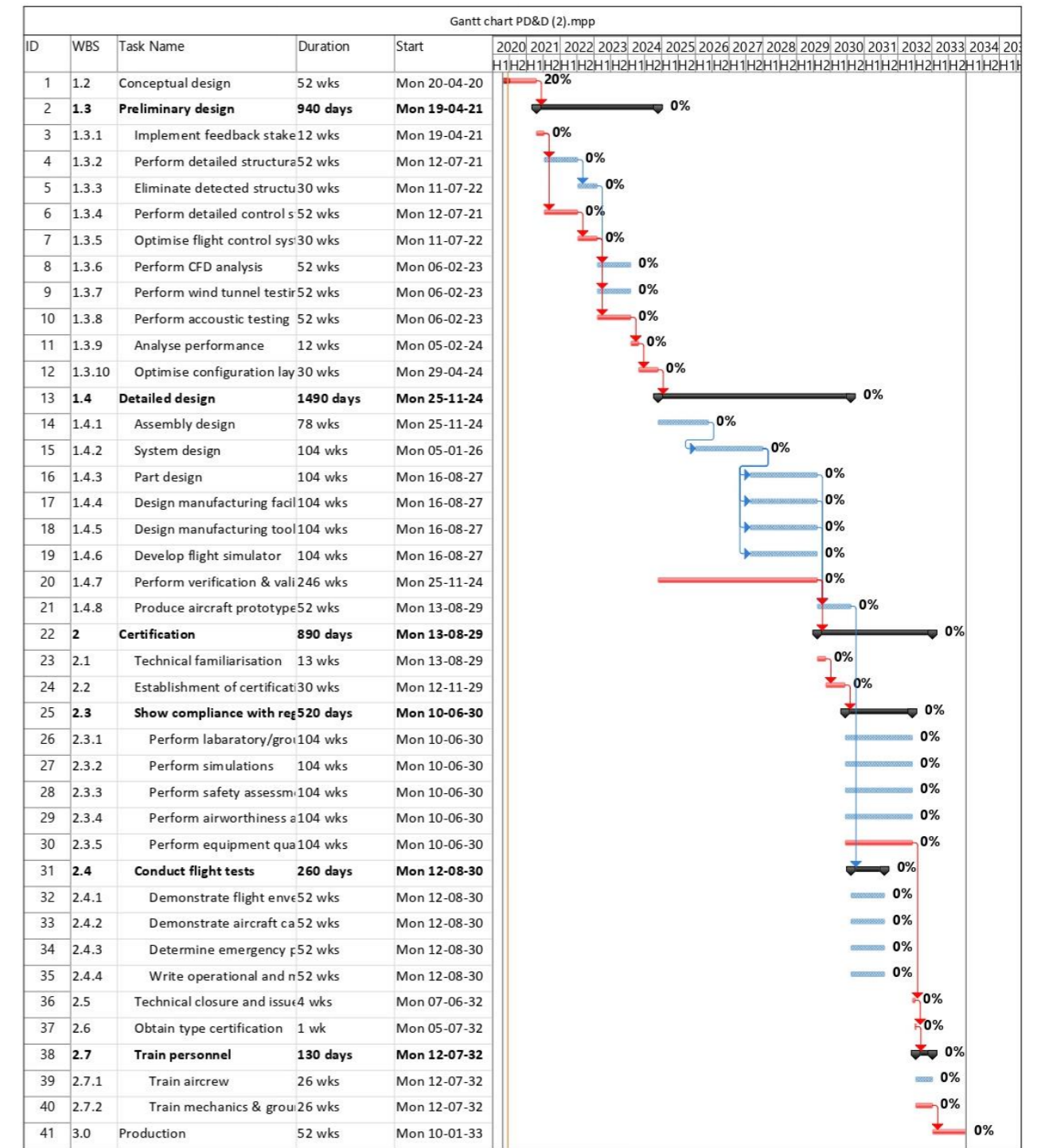
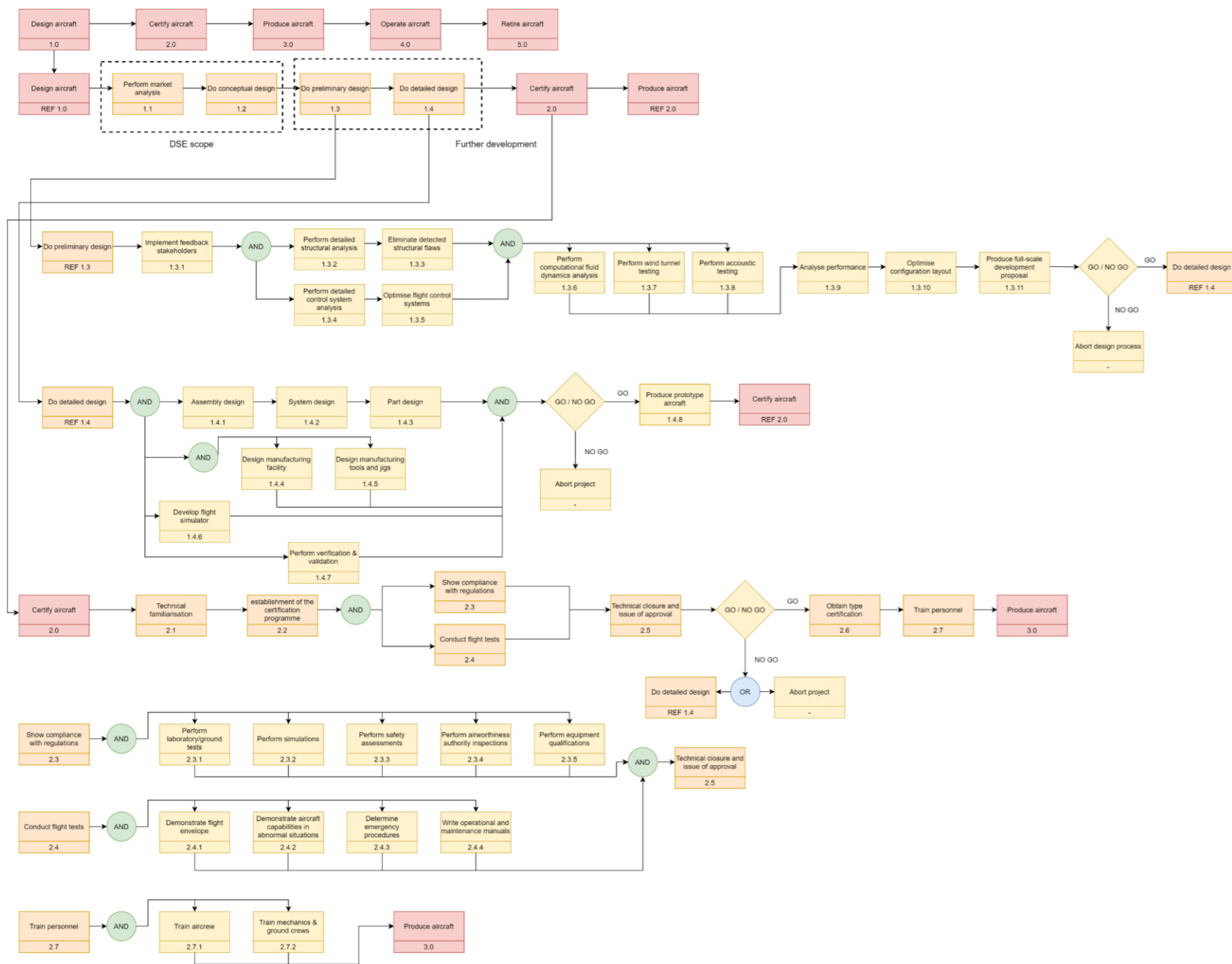
Furthermore, contributing measurements taken to stay up to date with ongoing research and contributing to implement **innovative** products is provided throughout the subsystems design and design option selection. Careful consideration is attributed to obtain an accurate overview of current technology research that can be implemented in the design to reach the requested challenging requirements contributing to the innovative mindset present in Flightpath 2050.

3.2.3. Environmental Sustainability

To comply with the set environmental sustainability project objective, the Cryo-V needs to mitigate engine emissions and have a significant lower environmental impact than conventional aircraft [3].

To ensure reduction in **engine emissions**, careful consideration is attributed to the design option analysis presented in the Midterm Report [3]. Furthermore, emission prediction tools are created and integrated in the design iteration to assess the resulting emissions and ensuring compliance to the requirements. The final emission characteristics are discussed elaborately in Section 10.3, covering the NO_x emission, H₂O emission and climate effects.

Finally, the **environmental impact** of the Cryo-V entails an investigation of the life cycles and the corresponding environmental impacts, including climate change, land use, resource use and water scarcity. This analysis is done by means of a simplified formal life cycle assessment, including the manufacturing cycle, flight operational cycle and the fuel production cycle, presented in Chapter 12. Here, environmental impacts are quantified by converting material in and outflows to ReCiPe Midpoint categories [28], which is an integral part of the conducted life cycle assessment.



4

Design Integration

This chapter describes the integration of the design disciplines into one analysis and optimisation framework. Section 4.1 provides an overview of the design disciplines used in the analysis and Section 4.2 describes the process and structure of the program. Finally, Section 4.3 offers recommendations for future work.

4.1. Design Disciplines

Due to the unconventional planform and propulsion design of the Cryo-V, the sizing and design integration method implements elements of traditional class I and II sizing as well as extra, more detailed or adapted elements. Some aspects, such as the propulsion system, are analysed in more detail than would otherwise be expected for class II, since their feasibility is not certain and must be analysed. However, the general approach resembles a class II sizing method and follows the class I sizing, described in the Baseline Report [2].

Full integration of the class I method is not possible due to design changes, for example the new propulsion system; and model assumptions that are no longer valid, for example that electric power is limiting for propulsion. Instead, the class I output variables, such as the wing area S or maximum take-off weight MTOW, are used as initial design variables for the class II method. The thrust loading diagram, an element of class I, is, however, used in the class II method for the calculation of maximum thrust and for verification purposes.

The class II sizing is performed as an iteration for convergence of MTOW to within 1% and features ten analysis functions: internal layout design, planform design, propulsion design, vertical tail design, landing gear design, structural design, cost analysis, noise analysis, weight & balance analysis and stability & control analysis. The elements of the analysis functions are described in the following design chapters. An optimiser is also written, which can perform an optimisation for any response variable, such as MTOW or NO_x emissions. This is a useful addition to determine the minimum possible value for each variable. Finally, a sensitivity analysis varies the input design variables to the optimiser to analyse the influence of each variable on the results. The output of the sensitivity analysis can be used to refine the input variables for the optimiser and therefore obtain the most optimal design.

4.2. Code Structure

The Cryo-V analysis and optimisation Python code is based on Multidisciplinary Feasible (MDF) architecture [29]. The complete code is presented in Figure 4.1 as an extended design structure matrix (XDSM) [30]. The grey lines symbolise a connection of data, the thinner, black line the process.

The design code can be started at the iteration, optimiser or sensitivity module level. Each iteration is performed on a Python `class`, initiated with input parameters from the optimiser and a global `dictionary` with constants. Logically, the optimiser creates a list and the sensitivity analysis an array of classes. Each class and its variables can be analysed and plotted upon completion.

4.3. Recommendations

Design variables, such as wing area or maximum lift coefficient, are stored in the design vector \mathbf{x} . Response variables, such as NO_x or noise emissions, are stored in the response vector \mathbf{y} . The superscript (0) denotes the initial values of the variables and * the final, optimised variables. The superscript t denotes a target value, which is a copy of the response variable to be used as an input to all analyses to ensure consistency of the design.

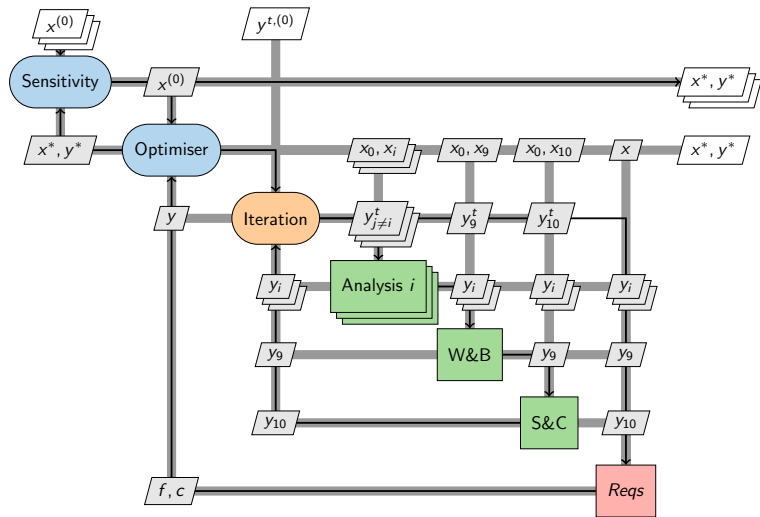


Figure 4.1: Cryo-V Extended Design Structure Matrix (XDSM)

The objective function is denoted by f . The optimiser is designed to only optimise for a single parameter but could be improved by using a dedicated objective function. Figure 9.16 shows the value this would add to the process and final design. Finally, \mathbf{c} is the design constraint vector that ensures all considered designs meet the requirements. Within Python, all design, response and constraint values are stored in the `dictionary` of each iteration `class` and are locally updated after each iteration.

Within the iteration, all analyses except for weight & balance (W&B) and stability & control (S&C) are run in parallel. The W&B and S&C analyses are run in series after the other analysis functions since the enclosed functions depend on the updated design and response variables. Each analysis can also be run outside the iteration for verification and validation.

The requirements function is run after convergence of the iteration function to ensure that the design is feasible. For each requirement, a True/False marker for compliance is added to the constraint vector \mathbf{c} , which is read by the optimiser. The optimiser systematically varies the input parameters to obtain compliant results and filters those with False markers. If no compliant results are found, the optimiser raises an error and requests new initial design variables.

The sensitivity analysis varies the input design and target variables within their contingency ranges to analyse the effect of these parameters on the outcome. The result of these analyses are described in Section 9.4. It is important to note that not all parameters can be varied to their contingency limits due to model constraints. This effect is also described in Section 9.4.

4.3. Recommendations

Multiple improvements can be made to the code structure to improve efficiency. The average time to completion has been reduced from 8.2 s to 0.7 s on a personal computer, which was a very useful improvement. However, the optimiser is programmed to run through set lists of design variables in a certain order and can therefore not make decisions to ignore unfeasible or less optimal design spaces.

Therefore, the optimiser could be improved by calculating the derivatives of the optimising parameter during the optimisation process. This would allow the optimiser to obtain an optimised result in far fewer cycles. Failed constraints could also be coupled with possible solutions, for example too high noise with reducing the approach speed. This would increase the efficiency of the optimiser further and could also be part of a machine learning algorithm.

5

Aerodynamic Design

In order to make the Cryo-V aircraft fly, it should be equipped with wings providing adequate aerodynamic characteristics. This chapter presents the design of those wings starting with the airfoil selection in Section 5.2, the wing design method in Section 5.3, the resulting wing characteristics in Section 5.4 concluding with verification and validation for the method in Section 5.5.

5.1. Functional Analysis

The airfoil provides a shape that is capable of producing lift. The main goal of the design is to maximise the lift-to-drag ratio, while fulfilling all design constraints. The Cryo-V has two lifting surfaces - the fuselage wing and the aft wing. One of the constraints is the thickness of the fuselage wing: the cabin has to fit in. Other constraints regard aerodynamic and stability concerns. The planform is an essential element of any aircraft as it is the subsystem which provides lift, and make the aircraft possible to fly. For the Flying-V configuration of the Cryo-V, the wing will also need to comply with other less conventional functions. The wing requirements are shown in Table 5.1.

Table 5.1: Wing subsystem requirements

Airfoil Requirements	
MRA.SYS.Foil.1.1	The cabin shall fit inside the fuselage airfoil.
MRA.SYS.Foil.1.2	The fuselage airfoil shall have a thickness over chord ratio of 0.37.
MRA.SYS.Foil.1.3	Both airfoils shall have a stall angle higher than 15 degrees.
MRA.SYS.Foil.1.4	The aft wing airfoil shall be able to function in the low transonic regime.
MRA.SYS.Foil.1.5	The fuselage airfoil shall have a zero angle of attack moment coefficient of 0.05.
Wing Requirements	
MRA.SYS.Planform.1.1	The cabin shall fit inside the fuselage wing.
MRA.SYS.Planform.1.2	The total span of the planform shall not exceed 36 m.
MRA.SYS.Planform.1.3	The aft wing shall provide enough area to mount control surfaces and winglets.
MRA.SYS.Planform.1.4	The wing shall provide enough lift to counteract the weight of the aircraft at all stages of flight.

 Second iteration requirement

5.2. Airfoil Design

The choice of airfoil is one of the starting points of more detailed aircraft design. It influences the aerodynamic and stability characteristics of the aircraft, influencing almost all aspects of the design.

5.2.1. Airfoil Characteristics

The fuselage and aft wing have different airfoils due to different thickness requirements and different perceived Mach numbers.

Fuselage Lifting Surface Airfoil - It was decided to initially only consider NACA airfoils for the fuselage wing; very few airfoils with the desired thickness to chord ratio were available and NACA airfoils allow for relatively easy modification. The airfoil initially selected is the NACA 64A-237 airfoil as shown in Figure 5.1a. It has the desired 37% thickness to chord ratio and has its $C_{L_{Des}}$, Design Lift Coefficient, at the cruise C_L of the Cryo-V. A comparison was made between different locations of maximum thickness (30, 40 and 50 %). 40 % results in the most efficient airfoil, with the right critical Mach number.

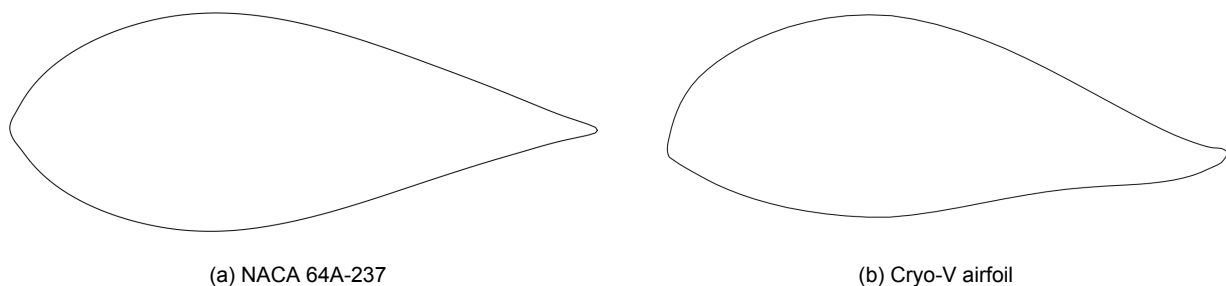


Figure 5.1: The original and redesigned fuselage airfoil

After the first iteration one additional requirement was introduced: the airfoil shall have a positive C_{M_0} of 0.05, to be able to rotate the aircraft at take-off. To achieve this, the pressure distribution of the original airfoil was changed until the desired characteristics were found. Mainly pressure at the bottom-rear side of the airfoil was decreased to create this moment (Figure 5.2). This results in the backside of the airfoil achieving a positive camber. The downside of this design is a decrease in the maximum lift over drag. This is deemed acceptable to satisfy the requirements. This airfoil is named the Cryo-V airfoil (see figure 5.1b).

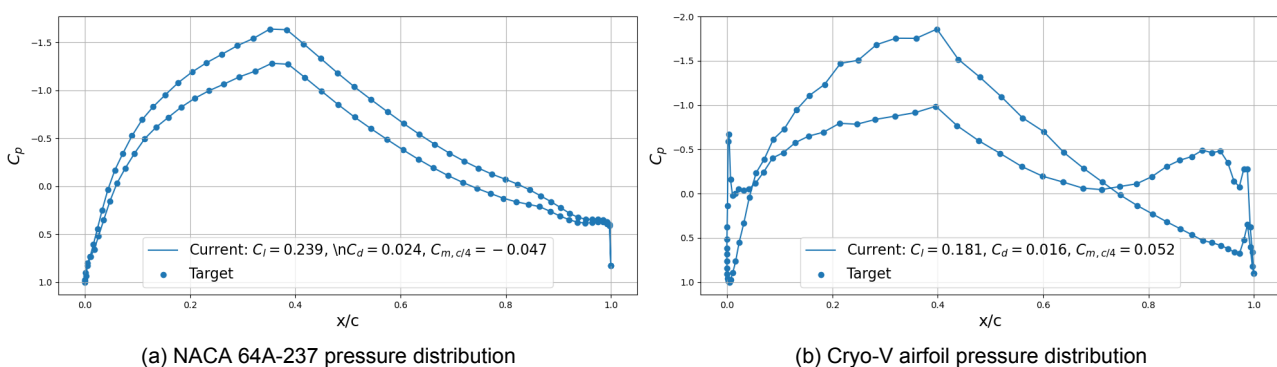


Figure 5.2: Pressure distributions of the original and redesigned fuselage airfoil

Aft Wing Airfoil - The aft wing has a smaller sweep angle and the airfoil should be able to operate in the low transonic region (Mach 0.675). A supercritical airfoil is therefore selected. The airfoil that performs best around the $C_{L_{Des}}$ is the sc20414 airfoil (Figure 5.3), selected from the University of Illinois airfoil database, also used by the TU Delft faculty of Aerospace Engineering¹. It gives the highest lift over drag and has a relatively high stall angle and $C_{L_{\alpha}}$ compared to other supercritical airfoils.

¹URL <https://brightspace.tudelft.nl/d21/1e/content/214652/viewContent/1474325/View> [cited 24 June 2020]

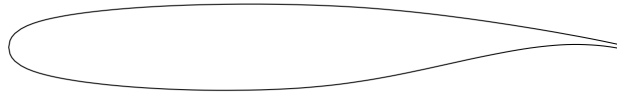


Figure 5.3: Supercritical airfoil of the aft wing, sc20414

5.2.2. Airfoil Selection Method

The first step in airfoil selection is the determination of the design lift coefficient $C_{L_{Des}}$. The $C_{L_{Des}}$ determines at which lift coefficient the chosen airfoil should be the most efficient or is a starting point for designing a new non-standard airfoil. Aircraft $C_{L_{Des}}$ is calculated with formula 5.1 and related to the airfoil $C_{l_{Des}}$ with Equation 5.2.

$$C_{L_{Des}} = 1.1 \cdot \frac{1}{q} \cdot \left\{ \frac{1}{2} \left[\left(\frac{W}{S} \right)_{\text{start cruise}} + \left(\frac{W}{S} \right)_{\text{end cruise}} \right] \right\} \quad (5.1)$$

$$L = qSC_{L_{Des}} \cong q_{eff}SC_{l_{Des}} \quad (5.2)$$

The next step is comparing a number of airfoils which operate efficiently at the $C_{L_{Des}}$ for favourable characteristics. As no stability parameters have been established yet, the airfoil which produces the least drag at $C_{L_{Des}}$ is selected for iteration 1. Javafoil in combination with an airfoil database is used to analyse the airfoils. In further iterations stability and stall characteristics are taken into account. Here Javafoil's design airfoil function is used to design an airfoil for a certain pressure distribution.

Final Airfoil Characteristics - All airfoil characteristics are shown in Table 5.2.

Table 5.2: Characteristics of the analysed airfoils, including both fuselage wing airfoils and the aft wing airfoil

		NACA 64A-237	Cryo-V Airfoil	SC20414
$C_{L\alpha}$	(deg ⁻¹)	0.138	0.128	0.121
$C_{L_{max}}$	(-)	2.3	2.5	2.5
α_{stall}	(deg)	20	23	17
C_{M_0}	(-)	-0.048	0.045	-0.089

5.3. Wing Design

In this section, the design of the wing planform is discussed. Firstly, the geometry of the planform is defined and determined in Subsection 5.3.1, then, the aerodynamic considerations are discussed in Subsection 5.3.2.

5.3.1. Geometry Definition

The main goal of geometric design of the wing planform is to define a unique planform by using the least number of parameters. Two of these parameters are the cabin width w_{cabin} and cabin length l_{cabin} that were determined in the Midterm Report [3], as the fuselage wing needs to allow the cockpit, cabin, cargo compartment and fuel tanks to fit in, and their dimensions, thus, provide a minimum restriction on the sizing of the fuselage wing. The remaining four parameters are the sweep angles of the leading edges of both the fuselage wing Λ_1 and the aft wing Λ_2 , and the taper ratio λ_2 and span b_2 of the aft wing, which are variable and their final values are determined by the optimiser.

A projection view of the planform is shown in Figure 5.4, in which the fuselage wing and the aft wing are separated by the dashed line K_1K_2 . In the 3D geometry of the planform, the surface of the fuselage wing is connected to the aft wing by spline. According to the cabin sizing, the cabin has a constant

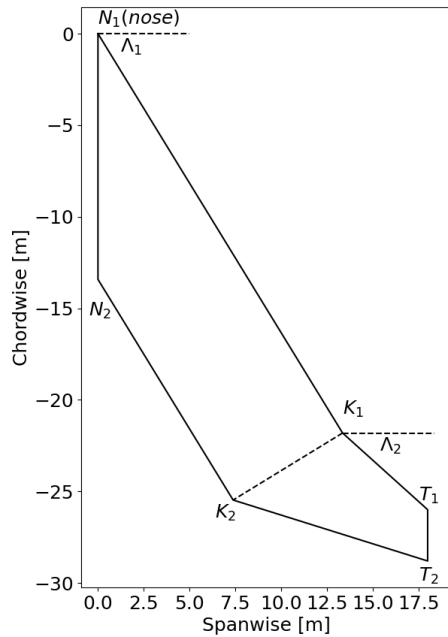


Figure 5.4: Projection view of the half wing planform

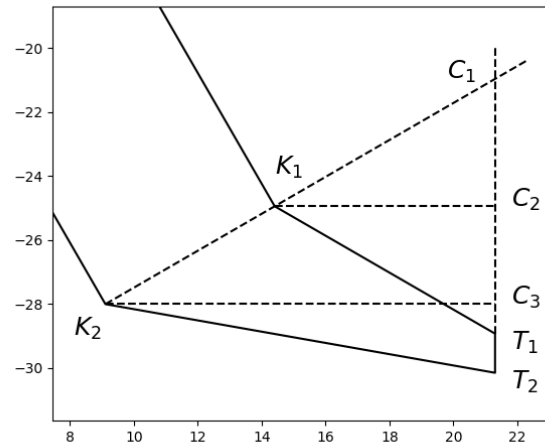


Figure 5.5: Geometry of the aft wing

width, so the length of the swept chord of the fuselage wing (length of K_1K_2) is set to constant as well, and its value is calculated by the w_{cabin} multiplied by a factor of the ratio of chord to cabin, whose initial value is 1.7 determined from the original Flying-V², and varies slightly with the optimisation. This makes the fuselage wing a right trapezoid. Due to the clearance between the outer cabin wall and the leading edge of the planform, the whole cabin has to be shifted towards the trailing edge a bit in order to fit inside the planform, which thus makes the length of the trailing edge greater than l_{cabin} to prevent the back of the cabin extending into the aft wing. The clearance is determined by the cabin layout design and is returned as a ratio of it to the swept chord length K_1K_2 . In addition, due to the large area of cabin and the factor of chord-to-cabin ratio, the area of the fuselage wing is already big enough that results in a low wing loading and may introduce more drag according to findings in the Midterm Report [3], hence it is decided that the dimension of the fuselage wing will be kept at its minimum value. This decision makes the shape of the fuselage wing fixed, and the only variable to it is its sweep angle Λ_1 .

Different from a fixed-shape fuselage wing, the aft wing morphs freely and is defined by its taper ratio λ_2 , sweep angle Λ_2 and span b_2 , while its root chord is bounded by the swept chord K_1K_2 of the fuselage wing. The restrictions are that the span must be long enough in order to provide the control surfaces mounted on the trailing edge of the aft wing with enough area; and the taper ratio also must have a certain minimum value resulting in the tip chord being long enough for the winglet as well as the rudder mounted on it.

5.3.2. Aerodynamic Estimation

The purpose of this section is to determine the aerodynamic coefficients for a certain well defined planform; then modify its geometry if necessary according to the feedback from its performance and requirements from other departments. To determine the aerodynamic characteristics resultant of the geometric considerations described in Subsection 5.3.1 the DATCOM method [31] was applied. Two critical situations are analyzed, the take-off where the maximum lift coefficient C_{Lmax} is critical and cruise where the weight should be balanced by lift calculated from the lift coefficient $(\alpha - \alpha_{0L}) \cdot C_{L\alpha}$. Since the whole Cryo-V is divided into fuselage wing and aft wing, two separated analysis has to be

²URL <https://www.tudelft.nl/en/ae/flying-v/technology/> [cited 15 June 2020]

done on them, respectively. Firstly, $C_{L\alpha}$ is estimated for both wings at both conditions; then $C_{L_{max}}$ is estimated as well as the stall angles for both wings at take-off condition. The maximum lift coefficient at take-off is then determined at the minimum stall angles of both wings.

Lift - The equation of DATCOM [31] used to estimate $C_{L\alpha}$ is

$$C_{L\alpha} = \frac{2\pi A}{2 + \sqrt{4 + \left(\frac{A\beta}{\eta}\right)^2 \cdot \left(1 + \frac{\tan^2 \Lambda_{0.5c}}{\beta^2}\right)}} \quad (5.3)$$

where A is the aspect ratio, β the Prandtl-Glauert compressibility correction factor calculated by $\beta = \sqrt{1 - M^2}$, η the airfoil efficiency factor that is 0.95 [31] and $\Lambda_{0.5c}$ the sweep angle measured at half chord length. The $\Lambda_{0.5c}$ of the fuselage wing is equal to Λ_1 as the fuselage wing has a taper ratio of 1. For the aft wing, its $\Lambda_{0.5c}$ can be calculated by finding its slope, which is equal to $(k_{K_1T_1} + k_{K_2T_2})/2$; in Figure 5.5, $k_{K_1T_1}$ of the leading edge can be calculated from the its sweep angle as $\tan(180^\circ - \Lambda_2)$, and $k_{K_2T_2}$ of the trailing edge can be computed by the coordinates of K_2 and T_2 that have been determined in Subsection 5.3.1. Therefore, $C_{L\alpha}$ is only related to the geometry of the planform i.e. aspect ratio and half-chord sweep angle, and the Mach number, and is not affected by which type of airfoil is used. This method is accurate for Mach numbers in range from 0 to 0.8, so it is reliable for the design of the Cryo-V, whose maximum Mach number at cruise is 0.78. $C_{L\alpha}$ is then estimated for both wings at take-off condition using Mach number of 0.2 and at cruise condition the Mach number is a variable that changes along the design with a final value of 0.78. It is then sufficient to calculate and check the angle of attack required for cruise condition by

$$W = L = \frac{1}{2} \rho_c V_c^2 \cdot \left(S_1 (\alpha - \alpha_{0L,1}) C_{L\alpha,1} + S_2 (\alpha - \alpha_{0L,2}) C_{L\alpha,2} \right) \quad (5.4)$$

where ρ_c is the air density at cruise condition, V_c the cruising speed, S_1 and S_2 the area of fuselage wing and aft wing, respectively.

To estimate $C_{L_{max}}$ and the stall angle of attack α_s , several plots of curves from [31] and [25] are needed. In order to automatically find certain values from these plots with different input values, these plots are interpolated with splines and their data are stored in Python codes. Before the estimation, it is necessary to determine whether the input planform is of high aspect ratio or low aspect ratio as different methods will be applied for different cases, and this is distinguished by

$$A > \frac{4}{(C_1 + 1) \cos(\Lambda_{LE})} \quad (5.5)$$

where the coefficient C_1 is a function of taper ratio, Λ_{LE} is the sweep angle of the leading edge. If the aspect ratio of the planform satisfies Equation 5.5, it is considered of high aspect ratio, otherwise is of low aspect ratio.

For high aspect ratio, $C_{L_{max}}$ and α_s are estimated by

$$C_{L_{max}} = \frac{C_{L_{max}}}{C_{l_{max}}} C_{l_{max}} + \Delta C_{L_{max}} \quad (5.6a)$$

$$\alpha_s = \frac{C_{L_{max}}}{C_{L\alpha}} + \alpha_{0L} + \Delta \alpha_{C_{L_{max}}} \quad (5.6b)$$

where $C_{l_{max}}$ is the maximum lift coefficient of the 2D airfoil measured at take-off condition and α_{0L} the zero-lift angle of attack of the airfoil. The ratio $\frac{C_{L_{max}}}{C_{l_{max}}}$ is a function of Λ_{LE} and Δ_y calculated by interpolation of original plots. Δ_y is the leading edge sharpness parameter that is equal to the vertical distance as percentage of chord between two points on the upper surface of the airfoil that are at 0.0015c and 0.06c from the leading edge. The term $\Delta C_{L_{max}}$ accounts for Mach number greater than

0.2, so it is neglected for take-off condition of low Mach. The zero-lift angle of attack α_{0L} is a characteristics of the airfoil and is thus kept constant unless a new airfoil is selected. The term $\Delta\alpha_{C_{L_{max}}}$ accounts for the non-linear part of the lift curve, near to which the stall happens, and is a function of Λ_{LE} and Δ_y again calculated by interpolation of original plots.

For low aspect ratio, $C_{L_{max}}$ and α_s are estimated by

$$C_{L_{max}} = (C_{L_{max}})_{base} + \Delta C_{L_{max}} \quad (5.7a)$$

$$\alpha_s = (\alpha_{C_{L_{max}}})_{base} + \Delta\alpha_{C_{L_{max}}} \quad (5.7b)$$

where $(C_{L_{max}})_{base}$ ranges from 0.5 to 1.4 and is a function of Δ_y , Λ_{LE} , aspect ratio, taper ratio and Mach number; the term $\Delta C_{L_{max}}$ accounts for the compressibility effects that ranges from -0.1 to 0.35 and is a function of Mach number, taper ratio, aspect ratio and Λ_{LE} ; $(\alpha_{C_{L_{max}}})_{base}$ and $\Delta\alpha_{C_{L_{max}}}$ are two different functions respectively of Mach number, aspect ratio, taper ratio and Λ_{LE} . All the four functions above are estimated by interpolations from the original plots.

Finally the maximum lift coefficient $C_{L_{max}}$ of the whole Cryo-V at take-off can be calculated by using the smaller α_s of the fuselage wing and the aft wing with their corresponding $C_{L_{\alpha}}$ and α_{0L}

$$C_{L_{max}} = \frac{C_{L_{fus}} \cdot S_1 + C_{L_{aft}} \cdot S_2}{S_1 + S_2} = \frac{C_{L_{fus}} + C_{L_{aft}} \cdot \frac{S_2}{S_1}}{1 + \frac{S_2}{S_1}} \quad (5.8a)$$

$$C_{L_{fus}} = C_{L_{\alpha_{fus}}} \cdot (\alpha_s - \alpha_{0L_{fus}}) \quad (5.8b)$$

$$C_{L_{aft}} = C_{L_{\alpha_{aft}}} \cdot (\alpha_s - \alpha_t - \alpha_{0L_{aft}}) \quad (5.8c)$$

where α_t is the twist angle of the aft wing, positive value corresponding to twist downward. It was found in the preliminary estimation that the aft wing stalls before the fuselage wing while α_s of the fuselage wing is twice larger than that of the aft wing, so in order to obtain higher $C_{L_{max}}$, the whole aft wing is twisted downward to increase α_s .

Drag - The drag of the Cryo-V consists of two parts, the parasite drag C_{D_0} resulted from the friction of wing group and exposed propulsion group, and the lift induced drag. C_{D_0} is estimated as [31],

$$C_{D_0} = \frac{1}{S_{ref}} \sum C_{D_c} A_c + C_{D_{misc}} \quad (5.9)$$

where S_c is the wetted area, C_{D_c} the skin friction coefficients, 0.003 and 0.06 for the wing and propulsion respectively, and the last term $C_{D_{misc}}$ accounts for the winglet and adds 10% drag [31] to the wing group. The wetted engine area is computed by variables of length and diameter of cylindrical engines returned by propulsion department and thus optimisable during iterations. The lift induced drag coefficient C_{D_i} is computed by

$$C_{D_i} = \frac{C_L^2}{\pi A e} \quad (5.10)$$

where e is the Oswald efficiency factor and is estimated as 1.41³. Thus the overall drag coefficient can be calculated by $C_D = C_{D_0} + C_{D_i}$, which is a function of wing area and C_L , so it can be called and optimised in the programme.

To further quantify the aerodynamic characteristics of the design, particularly for stability and control considerations, the designs Mean Aerodynamic Chord (MAC) and aerodynamic centres positions were determined.

³URL https://www.fzt.haw-hamburg.de/pers/Scholz/ewade/2007/EWADE2007_Torenbeek.pdf [cited 17 June 2020]

The MAC was computed by, for both fuselage and aft wing, assuming a simple trapezoidal geometry and computing the MAC both of these individual planforms. Then by applying the following equation⁴: $(c_{mac1} \cdot S_1 + c_{mac2} \cdot S_2) / S_{tot}$, it is possible to determine the total MAC of the aircraft. This same method was then used to determine the y- locations of the MAC for the total planform, for which the x- location could be found using the wings sweep location.

The position of the aerodynamic centres are then determined by assuming that their positions to be on the quarter chord of the MAC.

5.4. Wing Characteristics

One major issue exposed during design is the low $C_{L_{max}}$ of the whole aircraft at take-off condition. This can be analysed by first examining how $C_{L_{max}}$ is calculated by

$$C_{L_{max}} = \frac{C_{L_{fus}} \cdot S_1 + C_{L_{aft}} \cdot S_2}{S_1 + S_2} = \frac{C_{L_{fus}} + C_{L_{aft}} \cdot \frac{S_2}{S_1}}{1 + \frac{S_2}{S_1}} \quad (5.11)$$

which shows that the $C_{L_{max}}$ of the whole aircraft can be considered as a weighted average of C_L of the fuselage wing and aft wing, while the weights are the area of the fuselage wing S_1 and aft wing S_2 . This implies that in order to obtain a higher $C_{L_{max}}$, the area ratio S_2/S_1 should be increased if $C_{L_{aft}} > C_{L_{fus}}$, or decreased if $C_{L_{aft}} < C_{L_{fus}}$, and obviously the higher both $C_{L_{fus}}$ and $C_{L_{aft}}$ the better. Since C_L is independent of S , it is convenient to analyse these two factors separately.

In this case of take-off condition, C_L of both fuselage wing and aft wing is calculated by

$$C_L = C_{L_\alpha} \cdot (\alpha_s - \alpha_{0L}) \quad (5.12)$$

where α_s is the stall angle of the aft wing, as the aft wing always stalls before the fuselage wing. In addition, since all control surfaces are mounted on the aft wing, the whole aircraft would be trapped in the deep stall once the stall of the aft wing happens. Thus it is beneficial to increase the stall angle and C_{L_α} . The stall angle can be increased by adding a downward twist angle to the whole aft wing, but this angle has to be designed wisely as too much twist would cause a large negative lift on the ground, and high pitch angle during cruise.

The lift curve slope C_{L_α} , as discussed in Subsection 5.3.2, is mainly dominated by the geometry of the planform. In Figure 5.6, the relation among the C_{L_α} , aspect ratio and sweep angle is shown. It clearly illustrates the positive effect of high aspect ratio and low sweep angle on C_{L_α} . The fuselage wing is classified as of low AR in Subsection 5.3.2, and its high sweep angle makes this even worse, which results in an AR of the fuselage wing around 1.0 during iterations, and Figure 5.6 shows that at low-AR interval, a small change in AR would dramatically increase C_{L_α} . However, due to the minimum length of the cabin and restriction on the total span of Cryo-V, not much improvement can be done to the fuselage wing's geometry. For the aft wing, it is supposed to have a much smaller sweep angle than the fuselage wing and a slender shape of higher AR with low taper ratio, which would have enormous positive effect on its C_{L_α} . However, as all the control surfaces, as well as the winglet mounted on the tip, they introduce some limitations to the geometry of the aft wing, so it is another trade-off to make during optimisation.

Another available improvement is to increase the stall angle of the stall angle of the aft wing that is calculated by

$$\alpha_s = \frac{C_{L_{max}}}{C_{L_\alpha}} + \alpha_{0L} + \Delta\alpha_{C_{L_{max}}} \quad (5.13)$$

The first term shows that higher $C_{L_{max}}$ would be obviously helpful, which is strongly affected by the sweep angle of the planform combined with the leading edge sharpness parameter as shown in Figure 5.8, as well as $C_{l_{max}}$ of the 2D airfoil. The second term in Equation 5.13 can be improved by

⁴URL https://www.fzt.haw-hamburg.de/pers/Scholz/HOOU/AircraftDesign_7_WingDesign.pdf [cited 15 June 2020]

5.5. Verification and Validation

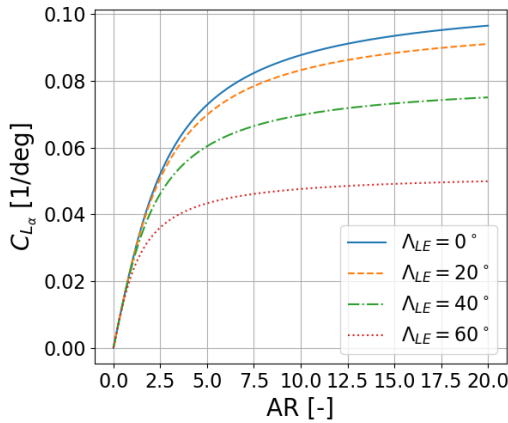


Figure 5.6: Effect of the AR and sweep angle on $C_{L\alpha}$

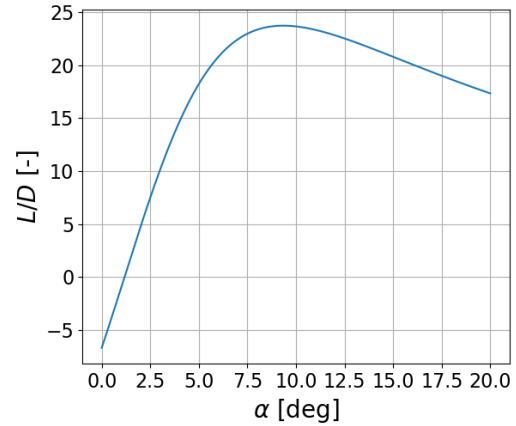


Figure 5.7: Lift-to-drag ratio at cruise condition

decreasing the camber of the airfoil, while the third term favours higher sweep angle and thinner airfoil. As Δ_y of the chosen airfoil for the aft wing is 3.6 that is a bit high as shown in Figure 5.8, there is a conflict in whether higher sweep angle should be applied because now the first term in Equation 5.13 favours lower sweep angle while the third term favours higher value. Thus, the best value of sweep angle has to be determined in iterations.

The final optimised design yields a $C_{L_{max}}$ at take-off condition equal to 0.88. This is lower than that of the original Flying-V which as $C_{L_{max}}$ around 1.05⁵, but considering that Cryo-V has a much lower MTOW than Flying-V, this $C_{L_{max}}$ is sufficient for landing with an approaching speed of 72 m/s. The lift-to-drag ratio is shown in Figure 5.7. It shows that the Cryo-V can reach a maximum L/D of about 24, and at cruise condition where the angle of attack is around 6°, the L/D ratio is about 20.

5.5. Verification and Validation

It is important to verify and validate the codes before its outputs can be used reliably by other departments. Unit tests are performed to check the outputs of member functions of the codes. As mentioned in Subsection 5.3.1, a lot of interpolated plots of curves are needed for automatic calculation, and thus it is vital to check whether they return reliable values. For plots that contain multiple regular curves for example as shown in Figure 5.8, it is not efficient to interpolate each curve. Instead, a general

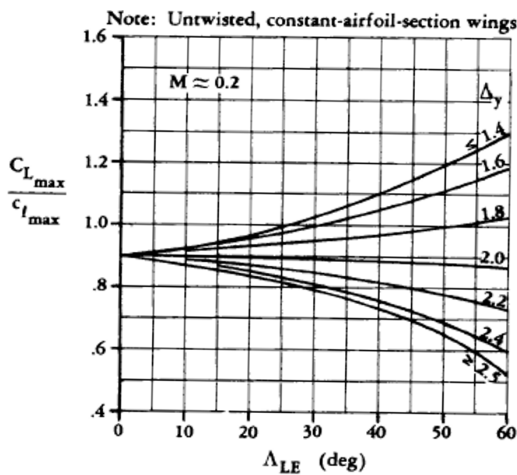


Figure 5.8: Original plots of $\frac{C_{L_{max}}}{C_{l_{max}}}$ vs. Λ_{LE} [25]

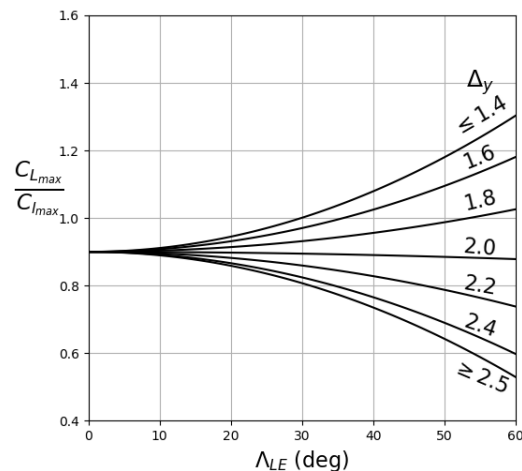


Figure 5.9: Interpolated plots of $\frac{C_{L_{max}}}{C_{l_{max}}}$ vs. Λ_{LE}

formula is tested with different coefficients to fit the curve, and for example curves, an expression of

⁵Information from Dr. Roelof Vos

5.6. Recommendations

$0.9 + k \cdot x^2$ is used. Corresponding coefficients k are found and interpolated to expand these curves and results are shown in Figure 5.9. All interpolations are checked by overlapping their plots to the original plots, and coefficients are modified to minimise errors. The remaining parts of the codes are mainly implementations of equations discussed in Subsections 5.3.1 and 5.3.2 and it is easy to verify whether variables are called correctly. Figure 5.4 is used as sanity check to verify the geometry does not violate physical constraints, such as trailing edge crossing with leading edge.

The software XFLR5⁶ is used to validate $C_{L\alpha}$ obtained by DATCOM as low values of $C_{L\alpha}$ is one of the main reasons of low $C_{L_{max}}$. The planform geometry used for validation is the initial one used in the preliminary design as presented in the Midterm Report [3], as the goal is to validate codes instead of the final geometry of design. The airfoil used for aft wing is SC20414 and for the fuselage wing is NACA64237 for validation, but NACA63A-237 for the final design, due to a re-selection of airfoil in the later design stage. The results of $C_{L\alpha}$ and C_{L_0} are shown in Table 5.3.

Table 5.3: Verification results of the DATCOM wing planform calculations using the XFLR5 software

	Code	XFLR5	Difference
Fuselage Wing			
$C_{L\alpha}$ (deg ⁻¹)	0.03498	0.03393	3%
C_{L_0} (-)	0.058	0.058	0%
Aft Wing			
$C_{L\alpha}$ (deg ⁻¹)	0.07852	0.07533	4.1%
C_{L_0} (-)	0.224	0.226	0.9%

5.6. Recommendations

As discussed in this chapter, the airfoil selection is assisted by the software JavaFoil, aerodynamic properties of the planform are estimated by using DATCOM method and validated by the software XFLR5. The drawback of these two software is that they cannot precisely predict the viscous flow and the stall angle. This results in the estimation of stall angle discussed in Subsection 5.3.2 underestimated, because the stall angle of the high-AR aft wing directly depends on the stall angle of the airfoil, which is then the limitation to the maximum lift coefficient of the whole Cryo-V. Therefore, in next design phase, it is recommended to perform Computational Fluid Dynamics (CFD) analyses or wind tunnel test on the scaled model of the Cryo-V in order to obtain more reliable data to aid the optimisation.

⁶URL <http://www.xflr5.tech/xflr5.htm> [cited 29 June 2020]

Propulsion Design

This chapter describes the design of the propulsion, electric and fuel subsystems of the Cryo-V. A functional analysis is performed in Section 6.1, followed by an overview of the propulsion design in Section 6.2. Sections 6.3 - 6.8 describe the fuel cell, turbofan, battery, distributed electric propulsion, fuel system and aircraft power systems design respectively. Finally, material selection and the mass budget is provided in Section 6.9.

6.1. Functional Analysis

The propulsion subsystem is responsible for providing propulsive and electric power for the aircraft and its subsystems. The main functions of the subsystem are presented below, from which a set of requirements are derived.

1. **Provide thrust** The propulsion subsystem shall provide enough thrust during all flight phases including take-off, climb, cruise, descend, landing and loiter.
2. **Provide power to aircraft systems** The propulsion subsystem shall produce enough power for all aircraft subsystems during operations.
3. **Energy storage and distribution** The fuel subsystem design shall be reliable and accommodate enough fuel to satisfy endurance and range requirements.
4. **Limit emission production** The production of greenhouse gas emissions produced during operations shall be limited.
5. **Limit noise production** Perceived noise emissions from the propulsion subsystem shall be limited.

Table 6.1: Propulsion subsystem requirements

Performance Requirements	
MRA.SYS.PROP.1.1	The propulsion system shall produce a minimum of 125.4 kN total thrust during take-off.
MRA.SYS.PROP.1.2	The propulsion system shall produce a minimum of 31.2 kN total thrust during cruise at altitude of 40 000 ft.
MRA.SYS.PROP.1.3	The propulsion system shall produce a minimum of 38.2 kN of thrust during cruise at altitude of 30 000 ft.
MRA.SYS.PROP.1.4	The propulsion system shall produce at least 420 kW of electric power for aircraft systems.
MRA.SYS.PROP.1.5	The aircraft shall carry at least 4.1 tons of liquid hydrogen on board.
MRA.SYS.PROP.1.6	The fuel system shall be able to produce fuel flow of 325 g/s when running at maximum power.
MRA.SYS.PROP.1.7	The propulsion system shall emit less than 17 249 kg of CO ₂ per maximum range flight.
MRA.SYS.PROP.1.8	The propulsion system shall emit less than 8.923 kg of NO _x per maximum range flight.
MRA.SYS.PROP.1.9	The propulsion system shall allow for the implementation of noise reduction technologies.

6.2. Design Overview

In a preliminary study in the midterm phase of the project, it was determined that fuel cells were the only feasible solution for meeting the greenhouse gas emission requirements. However, due to the lower specific weight of fuel cells, an aircraft powered solely by fuel cells was deemed not to be viable. Instead, in the detailed design phase, a refined hybrid system that combines combustion with fuel cells is developed.

To minimise the weight and environmental impact, Solid Oxide Fuel Cells (SOFCs) are used. SOFCs operate between 600 °C and 1000 °C [32], unlike low-temperature fuel cells such as Proton-Exchange Fuel Cells (PEMFCs), do not require rare earth metals and are less susceptible to hydrogen impurities. Moreover, SOFCs have the potential to be more efficient when combined with a gas turbine, a use case demonstrated in static power generation [32, 33] but never before in mobile applications [34].

The ingenuity of the Cryo-V propulsion subsystem is to combine SOFCs with hydrogen-combustion turbofans, which not only provide the required SOFC operating temperature but also extra thrust during take-off and climb. This system not only eliminates all CO₂ emissions, but reduces the required SOFC weight and results in a feasible design. Moreover, since for hydrogen combustion the required fuel to air ratio is lower than for conventional fuels, the design produces much less NO_x emissions, allowing the turbofans to be used during cruise. The increased pressure inside the core of the turbofan is an added benefit, since this also increases the efficiency of the SOFCs. Due to the slow response of the fuel cells to changes in power, a battery is included to receive any excess power. The battery is also used for start-up and emergency heating of the fuel cells in case of turbofan failure. A schematic of the propulsion subsystem is shown in Figure 6.1.

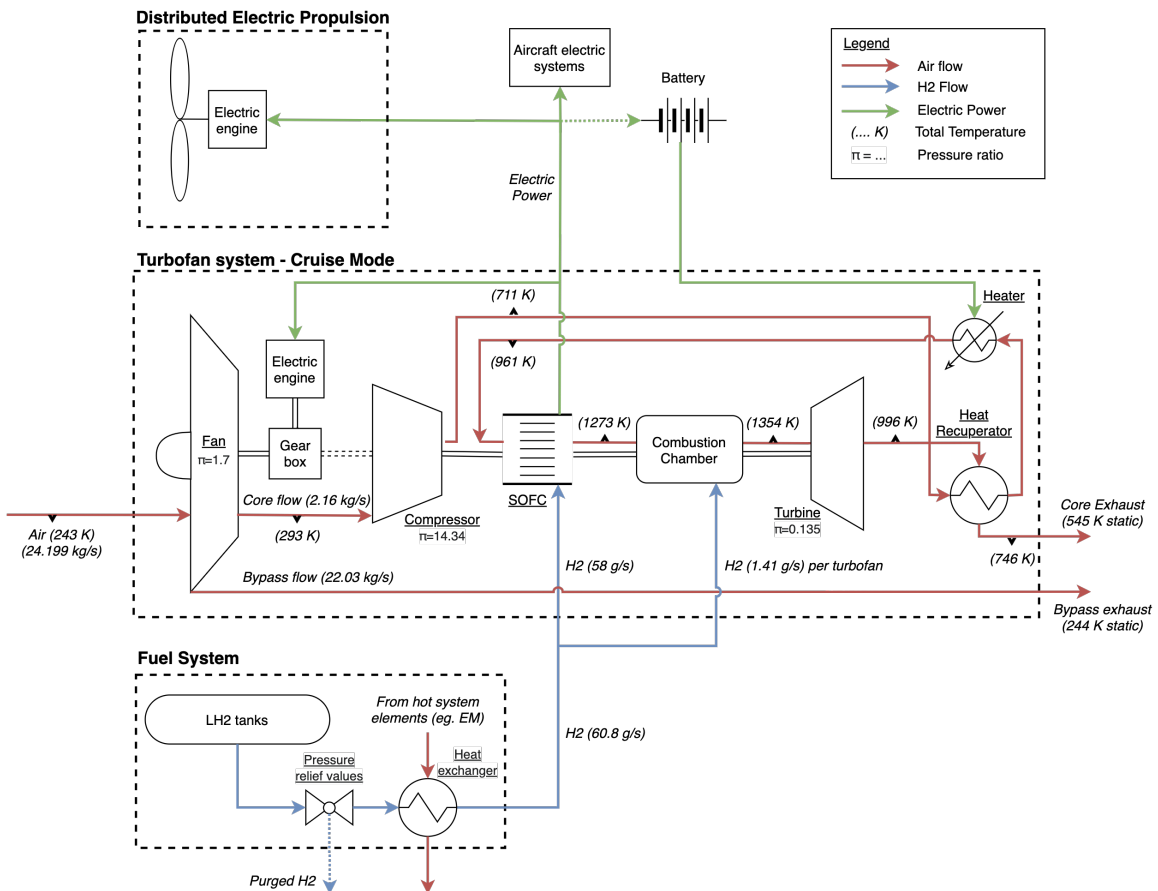


Figure 6.1: Propulsion system configuration during "cruise mode"

Since limiting noise is also a primary goal of the propulsion subsystem, distributed electric propulsion is used. A total of eight electric fans are placed on top of the wing of the aircraft for better noise

6.3. Fuel Cell Design

shielding and performance, given their position in the boundary layer of the aircraft. Although fewer or more electric fans are feasible, eight is chosen for weight reduction reasons; the difference in noise emissions is found to be negligible. The distributed electric propulsion is complemented by two turbofans, placed centrally on top of the wing. Although a single turbofan would be lighter and quieter, two turbofans are used for redundancy, since the working of the turbofan is closely coupled to the fuel cells. In case one turbofan fails, the second can support 77% of the fuel cells.

Table 6.2 describes the mission thrust/power profile based on the mission profile shown in Figure 2.1. The fuel cells are designed to provide all propulsive power during cruise and can therefore be run at a 100% power level during take-off and climb, with the remaining thrust provided by the turbofans. The Cryo-V is designed to cruise at both FL300 (100% thrust setting) and FL400 (75% thrust setting). The turbofans are marked with an asterisk since the combustion process does not produce thrust during cruise and descent, instead the main fan is powered electrically. This is described in more detail in Subsection 6.4.1. During approach, the fuel cells remain at a moderate power level due to their slow power response in case of a required go-around or climb. All excess power from the fuel cells is used to recharge the battery, which can provide a short-term boost as the fuel cells power up, shown by "as req" in Table 6.2. After landing, the fuel cells are switched off and the battery, supported if necessary by the turbofans, is used for taxiing.

Table 6.2: Cryo-V mission thrust setting profile

	Phases (from Figure 2.1)												
	0 -> 1	1 -> 2	2 -> 3	3 -> 4	4 -> 5	5 -> 6	6 -> 7	7 -> 8	8 -> 9	9 -> 10	10 -> 11	11 -> 12	12 -> 13
Fuel Cell	start	0->100%	100%	100%	100%	75%/100%	50%	50->100%	75%/100%	60%	50%	50%	50->0%
Turbofan	start	as req	100%	85%	70%	0%*	0%*	100%	0%*	0%*	0%*	10%	as req
Battery	as req	as req	0%	0%	0%	0%	0%	as req	0%	0%	0%	0%	100%

6.3. Fuel Cell Design

This section covers the preliminary selection and design of the fuel cells for use in the Cryo-V. First, the fundamental design of fuel cells is provided, followed by verification and validation of the model.

6.3.1. Fundamental Design

Hydrogen fuel cells are governed by the fundamental reaction,



In the case of solid-oxide fuel cells, as considered in the Cryo-V design, oxygen ions from the air are moved from the cathode to the anode, where they are combined with hydrogen ions to form water. The amount of useful energy that can be converted to electric power in the fuel cell is encapsulated by the Gibbs free energy $\Delta\bar{g}_f$. In SOFCs, work can also be extracted from volume and pressure changes, which combined with the Gibbs free energy is known as exergy. This extra work, in the form of hot exhaust air, is taken into account in the turbofan design; in this section, only the electrochemical work is analysed.

As with all thermodynamic processes, the reaction process in the fuel cell has both reversible and irreversible components. For a theoretical, reversible fuel cell, the total Electromotive Force (EMF), or voltage, is calculated using the Nernst equation [32],

$$E_{nernst} = \frac{-\Delta\bar{g}_f}{2F} + \frac{RT}{2F} \ln\left(\frac{p_{H_2}p_{O_2}^{0.5}}{p_{H_2O}}\right) + \frac{RT}{4F} \ln\left(\frac{P}{P^0}\right) \quad (6.2)$$

where F is the Faraday constant, T is the temperature in Kelvin, R is the gas constant, p_{H_2} , p_{H_2O} , p_{O_2} are the partial pressures of hydrogen and water vapour at the anode and oxygen at the cathode, P is the operating pressure, and P^0 is standard pressure (101 325 Pa). The Gibbs free energy $\Delta\bar{g}_f$ reduces with increasing temperature, but it is clear that the other elements of the Nernst equation increase both with temperature and pressure.

Irreversibilities, or overvoltages, reduce the reversible, Nernst voltage and can be broadly categorised into activation, fuel crossover, ohmic and concentration overvoltages, explained briefly below [32].

- **Activation** - Activation overvoltages are caused by the slow speed of the reactions taking place. The activation effect is seen by the non-linear drop at very low current, but is less important for high-temperature fuel cells.
- **Fuel crossover** - Fuel crossover overvoltages are caused by the diffusion of hydrogen from the anode through the electrolyte to the cathode, where it can react with the oxygen without producing current. For high-temperature fuel cells, this overvoltage is very small compared to the other three and is therefore ignored in the model.
- **Ohmic** - Ohmic overvoltages are due to the resistance to the flow of ions within the electrolyte and electrodes. This overvoltage is particularly important for high-temperature fuel cells.
- **Concentration** - The concentration changes locally within the fuel cell as the reactants are used. Near the entry of the reactants, the concentration is largest and decreases towards the exit, resulting in a lower voltage and current. This effect cannot be accurately modelled analytically for all fuel cells, but can be estimated based on test results from similar cells.

Taking the overvoltages into account, the voltage in a fuel cell can be expressed by the characteristic curve described by Equation 6.3 [32, 35], which forms the basis for the fuel cell model. Each overvoltage is a function of the current density i . It should be noted that this is a simplified, single-dimension model that provides reasonable results for low current densities in high temperature fuel cells. A more refined estimation of the fuel cell characteristics can be obtained by CFD analysis, for example using COMSOL [35–37]. However, this analysis is outside the scope of this project.

$$V = E_{nernst} - \eta_{act} - \eta_{ohmic} - \eta_{conc} = E_{nernst} - A \ln\left(\frac{i}{i_0}\right) - ir + \frac{RT}{2F} \ln\left(1 - \frac{i}{i_1}\right) \quad (6.3)$$

A , i_0 , i_1 and r are characteristic parameters of the fuel cell. The fuel cell design is performed by choosing a required voltage and then determining the corresponding current density. The multiplication of both parameters provides the power density of the cell. The cell efficiency can then be calculated based on the Higher Heating Value (HHV) of 1.48 V [32],

$$\eta_{cell} = \mu_{H_2} \frac{V}{1.48} \quad (6.4)$$

where μ_{H_2} is the hydrogen utilisation, assumed to be 95% [32]. Knowing the total voltage U and current I that each fuel cell system must deliver as well as an estimate for the electrode area, the number of cells can be calculated,

$$N_{cells} = \left[\frac{U}{V_{FC}} \right] \cdot \left[\frac{I}{I_{FC}} \right] \cdot N_{elecSys} \quad (6.5)$$

where $N_{elecSys}$ is the number of separate electrical systems. The mass flow of hydrogen, used to calculate the fuel mass and as an input for the turbofan calculations, can be calculated [38],

$$\dot{m}_{H_2FC} = \frac{I_{FC}}{2\mu_{H_2}F} m_{H_2} N_{cells} \quad (6.6)$$

$$\dot{m}_{airFC} = \frac{I_{FC}}{4\mu_{O_2}F} m_{O_2} N_{cells} \cdot \frac{1}{p_{O_2}} \tag{6.7}$$

where m is the molecular weight. Whilst it would be possible to calculate the mass of the fuel cell stacks based on the number of cells, no data is available about the balance of plant masses. Therefore, the mass of the fuel cells is calculated using a specific mass of 2.5 kW/kg¹.

6.3.2. Fuel Cell Model Verification and Validation

As mentioned previously, the analytical fuel cell model used in the Cryo-V design is simplified and is not universally valid. Fuel cells can generally only be accurately modelled using CFD analyses, which are outside the scope of this project. However, the analytical model input parameters can be amended such that the model matches similar fuel cells. This locally increases the accuracy of the analytical model. It is recommended that future work focuses on creating an accurate fuel cell model.

Only a limited amount of data is available for SOFCs. Unfortunately, no useful data could be obtained for a 1000 °C fuel cell. Therefore, data was used from an 821 °C SOFC at 1 atm. As shown by Leonide [35] and Larminie [32], increasing the operating temperature of a SOFC leads to a reduction in ohmic overvoltage and therefore a lower slope of the current density curve. However, a higher operating temperature also decreases the Gibbs free energy of formation and therefore the reversible EMF. The change specifically in Gibbs free energy of formation reduces the EMF by 0.06 V. However, the reduction of maximum EMF is small compared to the increase in the current density slope. These effects are visible in Figure 6.2b. It is therefore assumed that using a lower temperature fuel cell to calibrate the analytical model results in the specific power being underestimated. Although not ideal, an underestimation is better for the preliminary design than an overestimation.

The data used for calibration is shown in Figure 6.2a. The initial model, using data from an example in [32] is comparable to Figure 6.2b and shows a far higher ohmic overvoltage, resulting in a larger slope. The analytical model is corrected using Leonide [35] to obtain a corrected model for 1094 K and 1 atm. The effect of increased temperature and pressure is shown by the position of the corrected model at 1273 K and 15 atm. As mentioned in the previous paragraph, it is expected that the actual cell would have a smaller slope and a slightly lower initial cell voltage. The characteristic parameters of the initial and corrected models are provided in Table 6.3.

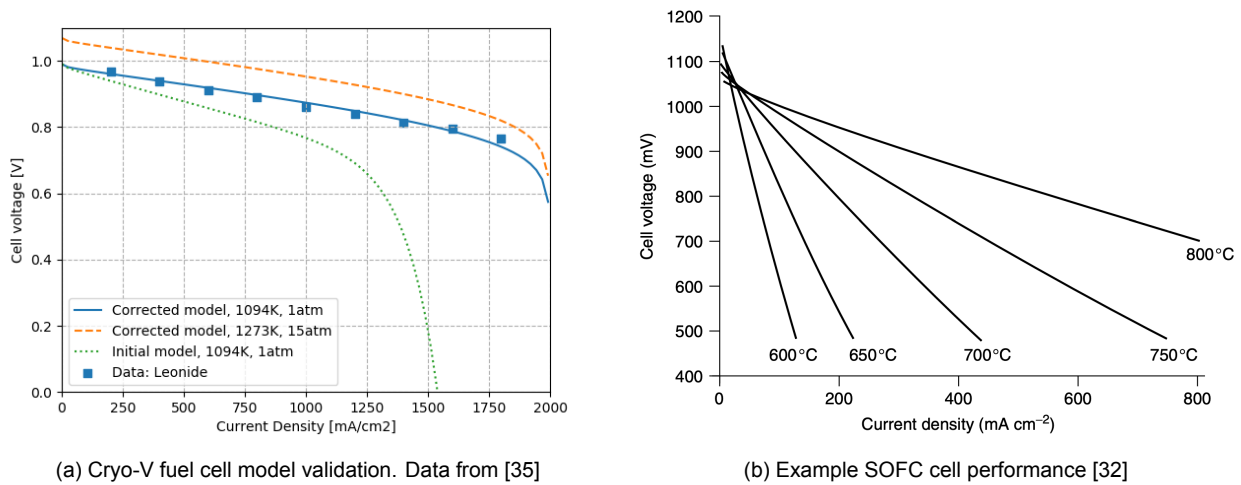


Figure 6.2: Fuel cell characteristic curve comparison

¹URL <https://ntts-prod.s3.amazonaws.com/t2p/prod/t2media/tops/pdf/LEW-TOPS-120.pdf> [cited 19 June 2020]

Table 6.3: Fuel cell characteristic parameters of the initial and corrected models

	Initial Model	Corrected Model
A (V)	0.02	0.02
i_0 (mA/cm ²)	0.01	0.01
i_1 (mA/cm ²)	1580	2000
r (kΩ cm ²)	2.0×10^{-4}	0.7×10^{-4}
Difference	> 13%	1.14%

6.4. Turbofan Design

The Cryo-V turbofans are modelled as ideal Brayton thermodynamic cycles. In this cycle, gas is first compressed, combusted and then expanded. The energy that is harvested by the turbines during expansion of the gas is used to drive the compressor stages and produce a net thrust. Because of the constant combustion under high pressure, turbofans usually achieve higher efficiencies than internal combustion engines. To further increase efficiency, the Cryo-V turbofans use the exhaust heat of the SOFCs and are equipped with a jet exhaust heat recuperation system, which combined with the fuel cells increases the core gas temperature by approximately 500 K in total [39].

6.4.1. Take-Off Mode & Cruise Mode

The main reason the Cryo-V is equipped with turbofans is the high concentration of thrust required during take-off, which cannot be covered by the other components. The design condition for the turbofans is thus take-off, where a thrust of 34.751 kN is required per engine. The required fuel consumption is calculated by optimising design parameters such as pressure bypass ratios. As described in Section 6.2, the turbofans also provide a secondary function of supplying the fuel cells with high pressure and temperature air to increase efficiency.

During cruise, no thrust requirement is set for the turbofans. However, because they are nevertheless functioning to compress air for the fuel cells, a small amount of thrust is generated anyway, 2.332 kN per engine. To further reduce fuel consumption for combustion, the fan of the turbofans is driven by an electric motor in cruise mode. This way, the turbines only have to power the compressor stages, which they do partly by using the waste heat of the fuel cells. However, a small amount of fuel needs to be combusted during cruise to make sure that the compressor can be run at the intended setting. During the design, these modes are referred to as "take-off mode" and "cruise mode".

6.4.2. Combustion of Hydrogen

The combustion performance of the Cryo-V turbofans is investigated to ensure no drastic design adaptations are necessary given the combustion of H₂ rather than conventional fuels. H₂ combustion is very stable and ignites at volume fractions 4-75% of H₂ in the fuel-air mixture. However, a modified combustion chamber design is required since H₂ occupies 29% of the combustion chamber volume during stoichiometric combustion, compared to 1-2% for kerosene combustion. Typically, less than half of the stoichiometric Fuel to Air Ratio (FAR) is used in lean combustion². This limits the combustion temperature and reduces NO_x formation to near zero. The FAR is predominantly optimised for NO_x emissions, documented in Section 10.3. An initial estimate for the FAR is,

$$FAR_{H_2} = \frac{FAR_{stoich}}{0.5} = \frac{1}{0.5 \cdot 34} = 0.01471 \quad [kg/kg] \quad (6.8)$$

²URL https://www1.eere.energy.gov/hydrogenandfuelcells/tech_validation/pdfs/fcm03r0.pdf [cited 17 June 2020]

6.4.3. Calculations

Calculations are performed using a custom thermodynamic model in Python. Compression and expansion are modelled using Equations 6.9 and 6.10 respectively [40]. The subscript 0 denotes stagnation conditions, which include the effects of decelerating the incoming flow to zero velocity.

$$T_{0,i+1} = T_{0,i} \left[1 + \frac{1}{\eta_{is,comp}} \cdot \left(\Pi^{\left(\frac{K_{air}-1}{K_{air}} \right)} - 1 \right) \right] \quad (6.9)$$

$$p_{0,i+1} = p_{0,i} \left[1 - \frac{1}{\eta_{is,turb}} \cdot \left(1 - \left(\frac{T_{0,i+1}}{T_{0,i}} \right)^{\left(\frac{K_{gas}}{K_{gas}-1} \right)} \right) \right] \quad (6.10)$$

The combustion process is modelled according to the heat balance shown in Equation 6.11. The output power of the turbine is calculated using the characteristics of the passing flow, described by Equation 6.12. The net engine thrust is the combination of the total acceleration of the flow and the pressure differences at the nozzle, expressed in Equation 6.13.

$$\dot{m}_{fuel} \cdot LHV_{fuel} \cdot \eta_{cc} = \dot{m}_{core} \cdot C_{p,gas} \cdot (T_{0,4} - T_{0,3}) \quad (6.11)$$

$$\dot{W}_{turb} = \dot{m}_{core} \cdot C_{p,gas} \cdot (T_{0,i} - T_{0,i+1}) \quad (6.12)$$

$$T_N = \dot{m}_{core} \cdot (V_{jet} - V_{\infty}) + \dot{m}_{bypass} \cdot (V_{bypass} - V_{\infty}) + A_{core} \cdot (p_{jet} - p_{\infty}) + A_{bypass} \cdot (p_{bypass} - p_{\infty}) \quad (6.13)$$

The turbofan model checks whether the flow is choked in order to calculate the correct exhaust pressure and velocity. During cruise, the bypass flow is designed to be choked for optimal thrust production, while the core flow remains unchoked due to the high temperature. The model iterates the parameters based on a required net thrust until the fuel consumption converges. In a final optimisation, all design parameters, such as the compression and bypass ratios, are varied to find the minimum fuel consumption whilst still meeting all requirements.

6.4.4. Model assumptions

The following assumptions are used in the Cryo-V turbofan model [40]:

- The working fluid of the cycle is considered as an ideal gas, and its composition does not change over time.
- Specific heats of the fluid are modelled in two steps, before combustion (subscript *air*) and after combustion (subscript *gas*). On both sides of this step, specific heat C_p and the ratio of specific heats K is constant:
 $C_{p,air} = 1000 \text{ J}/(\text{kg} \cdot \text{K})$, $C_{p,gas} = 1150 \text{ J}/(\text{kg} \cdot \text{K})$, $K_{air} = 1.4$, $K_{gas} = 1.33$
- Changes in kinetic and potential energy of the flow between inlet and outlet of certain components are neglected.
- The thermodynamic cycle is adiabatic, i.e. no heat transfer with the environment exist.
- Massflow is constant along stations in the turbofan core, for a certain moment in time, as $\dot{m}_{fuel}/\dot{m}_{core}$ is a negligible number ($\ll 0.1$)
- Mechanical losses in all transmissions are modelled as 1% ($\eta = 0.99$)
- Isentropic efficiency of components are estimated as follows:
 $\eta_{inlet} = 0.98$, $\eta_{nozzle} = 0.93$, $\eta_{fan} = 0.93$, $\eta_{comp/turb} = 0.88$, $\eta_{combustion} = 0.99$
- Rotational speed N is always equal for components mounted on the same shaft. In detailed design, this implies an iterative process where compressor and turbine components are "matched", is required. The model however does not include this iteration, but rather provides a first estimation on component performance.
- Atmospheric conditions are modelled according to ISA models.

6.4.5. Model Verification & Validation

For verification of the thermodynamic model, GSP 11 [41] is used, which is a gas turbine and turbofan analysis tool for iterative design. It is useful for the exact matching of different turbo-machinery components. Because the thermodynamic model does not include compressor and turbine maps and instead is based purely on assumptions, it is expected that verification with GSP 11 will reveal the accuracy of the model and also serves as a tool for improving it.

The Cryo-V turbofan is set up within GSP 11 such that the total pressure, temperature, and engine thrust can be compared to the predictions of the thermodynamic model. In Table 6.4, output values of GSP 11 and the thermodynamic model are presented for comparison. It is concluded that accurate results for take-off mode are obtained by the thermodynamic model. However, during cruise mode, larger differences exist. This is due to the limited capabilities of GSP 11 to model heat exchangers and external heat sources. It is thus recommended that future research is done on the thermodynamic properties of turbofan-fuel cell integration. For inclusion in the class II iteration, however, the thermodynamic model is fully verified as no drastic deviations are present.

Table 6.4: Model data and GSP 11 verification of the turbofan (per engine)

		Thermodynamic Model	GSP 11	Difference
Take-Off Condition				
Thrust	(kN)	33.494	33.623	0.39%
Combustion inlet temp.	(K)	767	778	1.43%
Combustion inlet pressure	(bar)	24.318	25.072	3.1%
Cruise Condition				
Thrust	(kN)	3.413	3.675	7.7%
Combustion inlet temp.	(K)	1273	1043	-18.1%
Combustion inlet pressure	(bar)	5.341	4.471	-16.3%

Validation is performed by using the ICAO engine emissions database. Engine characteristics and rated engine thrust are extracted from the database and used in the thermodynamic turbofan model. The rated engine thrust is set as a design requirement, allowing the fuel consumption during take-off to be approximated. The results are plotted in Figure 6.3. The ratio between calculated and actual fuel flow is used because it is a normalised value. The average and maximum deviations are 6.29% and 24% respectively. Since the database consists of engines with a large range of bypass ratios, efficiencies, pressure ratios and fuel consumptions, the deviations are considered small and are most likely due to the assumptions made. For the preliminary design of the Cryo-V, the thermodynamic model can therefore be assumed to be valid, although in future work the model should be updated and refined with more accurate assumptions.

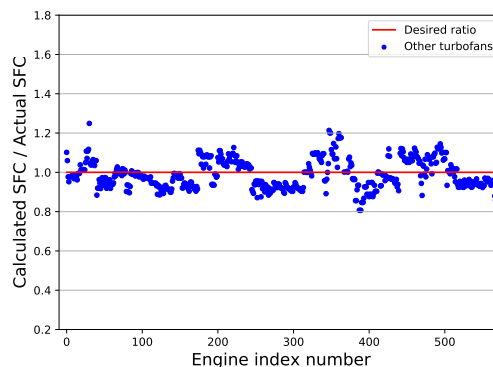


Figure 6.3: Performance of model calculation of engine fuel consumption

6.4.6. Final Turbofan Design

Figure 6.4 shows the internal architecture of the Cryo-V turbofan design. From left to right are depicted the fan, gearbox, electric motor, Low Pressure Compressor (LPC), High Pressure Compressor (HPC), fuel cells (yellow), combustion chamber (red), HPT, LPT and exhaust nozzle. The external architecture and front view are shown in Figure 6.5. Chevrons are included at the bypass nozzle, which act as noise reduction, as described in Subsection 10.4.3.

Using GSP 11, the matching of the compressor and turbine is done in more detail, and it is verified that the thermodynamic model is accurate enough for the current design phase. For the final design, rotational speeds and pressure ratios for different components are expressed for a range of operational conditional conditions. The range of operational conditions is defined as follows: Take-off at maximum thrust, throttle back to 85% until 3000 ft, and climb to 40 000 ft at 70% while gradually lowering fuel consumption to cruise conditions. In Figure 6.6, shaft rotational speed is plotted for the low pressure (N_1) and high pressure (N_2) shafts with respect to flight altitude. In Figures 6.7, 6.8 and 6.9, compressor maps are shown for the fan core, LPC and HPC, during take-off mode. Effect of the electric motors that assist during cruise is not included in the figures. In these multidimensional maps, pressure ratio, rotational speed, and corrected flow are related. Take-off and Cruise are indicated, as well as the climb connecting them. These maps act as extra verification that compressing components neither surge nor stall during any operational condition. In Figure 6.10, thrust per turbofan during the range of operational points is shown. Final characteristics of the turbofan system are provided in Table 6.5.

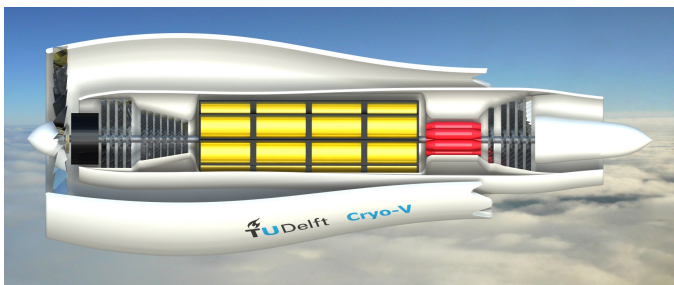


Figure 6.4: Internal architecture of the Cryo-V turbofan

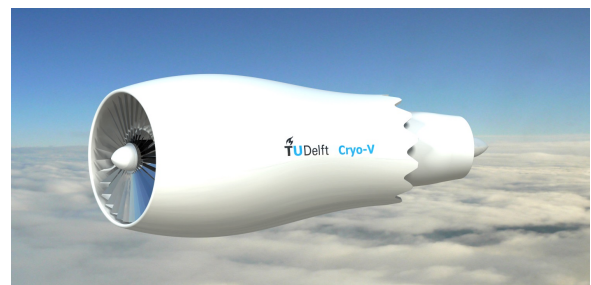


Figure 6.5: External architecture of Cryo-V turbofan

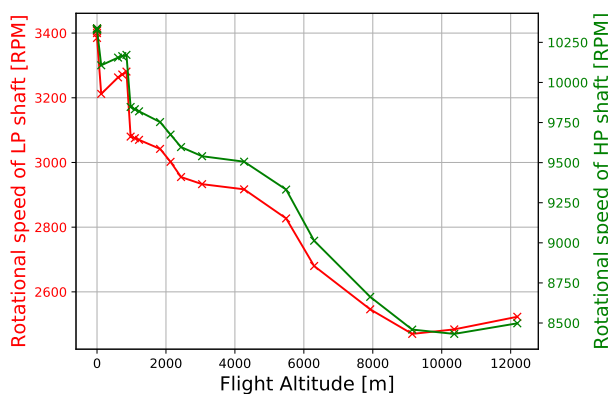


Figure 6.6: Shaft rotational speed during operation

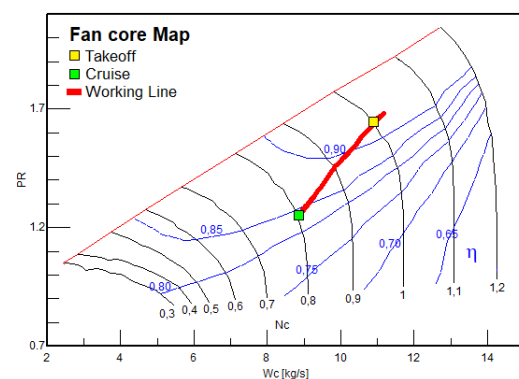


Figure 6.7: Compressor map of fan core

6.5. Battery Sizing

To ensure that the fuel cells are always provided with airflow of ideal temperature and to provide hot air when the turbofans are idle during taxiing, electric heaters are included along with a battery pack. The batteries are sized for the power required to heat the fuel cell airflow, assuming electric heating efficiency of 100%. The batteries do not necessarily have to be designed for energy capacity,

6.6. Distributed Electric Propulsion Design

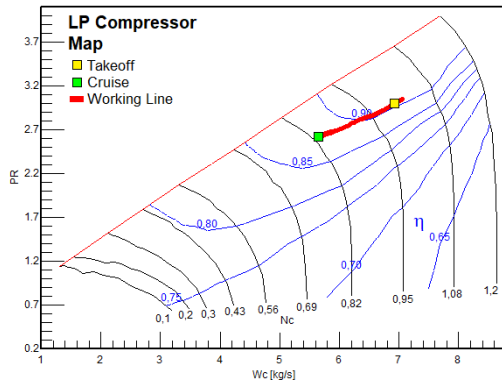


Figure 6.8: Compressor map of LPC

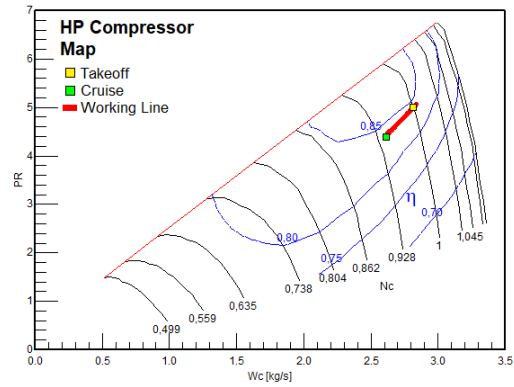


Figure 6.9: Compressor map of HPC

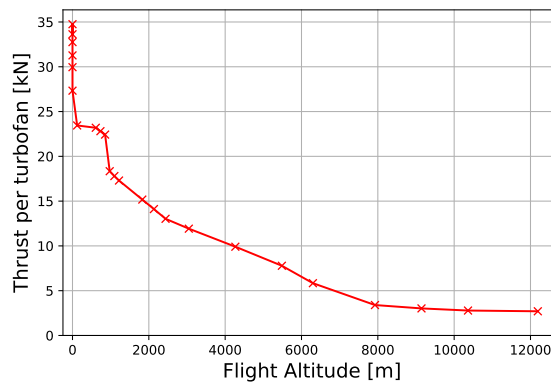


Figure 6.10: Thrust per turbofan during climb at take-off mode

Table 6.5: Turbofan design characteristics, evaluated per engine

	Value	Unit		Value	Unit
Take-Off Characteristics			Cruise Characteristics		
Max thrust	33.494	kN	Thrust	2.332	kN
OPR	15	-	OPR	14.34	-
Bypass ratio	8	-	Bypass ratio	10.21	-
Total massflow	97.9	kg/s	Total massflow	24.2	kg/s
Fuel consumption	128.5	g/s	Fuel consumption	4.00	g/s
			Cruise EM power	1603	kW

because they are recharged as soon as the fuel cells are running, making the system self-sustaining. The required battery power is calculated with Equation 6.14:

$$P_{bat} = \Delta T \cdot C_{p,air} \cdot \dot{m}_{airFC} \quad (6.14)$$

The heater should heat up the air by 500K working on a mass flow of 2.083 kg/s. The designed battery provides a power of 1.38 MW. Assuming specific power of near future batteries to be around 5 kW/kg [42], the total battery mass is found to be 278 kg.

6.6. Distributed Electric Propulsion Design

This section analyses the distributed electric propulsion (DEP) units used for the Cryo-V. The eight DEP units are situated on top of the wing of the aircraft and provide 78% of thrust during cruise and

47% of thrust during take-off. Distributed propulsion is used to meet the noise requirements whilst also increasing redundancy and therefore safety of the aircraft. Ducted fans are used to provide more thrust at high altitudes by using a higher fan pressure ratio than could be achieved by propellers. The duct further increases the efficiency of the fan whilst also increasing shielding.

6.6.1. DEP System Components and Efficiencies

The main function of the DEP system is to convert electric power from the fuel cells to thrust. Multiple components are involved in the power conversion, as shown in Figure 6.1. The major components analysed in this section are the electric motor controller, electric motor, gearbox and fan.

The motor controller and gearbox efficiencies are assumed by investigating existing designs and future trends. Motor controller efficiency is estimated at 97% since current motor controllers can reach efficiencies of around 95% [43], but this could improve to 99.8% using technologies like cryogenic cooling [43]. Gearbox efficiency is estimated to be 98%, a standard value verified by Stuckl [43].

For simplicity, the Cryo-V iteration assumes an electric motor efficiency of 95% [43, 44]. However, electric motor is designed for certain rotational speeds and torques, and motor efficiency can change depending on the operational conditions and flight phase. To investigate the relationship between motor efficiency and power setting, an efficiency map is created by evaluating torque and rotational velocity, shown in Figure 6.11a. The diagram is made by estimating the electric losses using the loss factor constants described by Zamboni [45] for a 250 kW motor. The blue lines indicate lines of constant power normalised with the maximum power; the black lines indicate lines of constant motor efficiency. The maximum power setting for the DEP electric motors is at FL300 cruise, while for take-off around 50% of maximum power is required due to the turbofan thrust. Due to the lower drag at FL400, the electric motors only need to be run at a 80% power setting. The map is validated using analyses of similar 250 kW [45] and 30 kW [46] motors, which show similar pattern of efficiencies and share a peak at 95%.

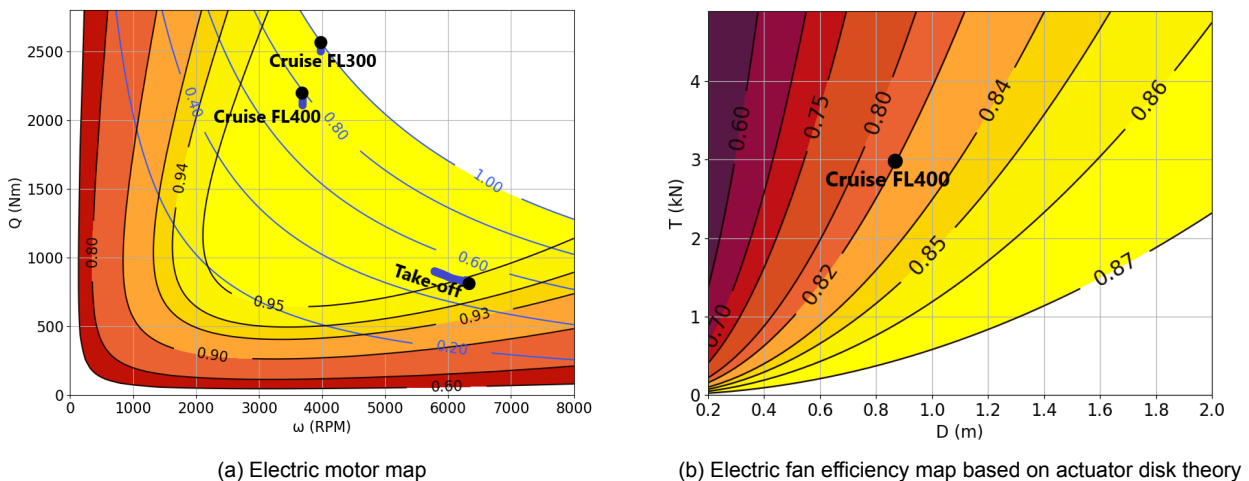


Figure 6.11: Electric motor and fan efficiency maps

6.6.2. Ducted Fan Efficiency and Thrust

Ducted fan efficiency is estimated and used as a tool in the sizing process. Estimation is performed using the actuator disk theory as described by Equation 6.15 [47]. This theory provides an estimate of propeller efficiency without requiring the specific blade design. However, it does not include some of the energy losses and the influence of the duct.

$$\eta_{fan} = \frac{2}{1 + \sqrt{1 + \frac{T}{\frac{1}{2}\rho\frac{\pi}{4}D_{fan}^2V_{\infty}^2}}} \quad (6.15)$$

Efficiency depends on fan diameter D_{fan} , thrust provided T and flow conditions, such as density ρ and free stream velocity V_{∞} . The theory uses the following assumptions³:

- Rotation imparted to the flow is neglected
- The flow outside propeller streamtube has a constant stagnation pressure
- The blade shape, number of blades and effect of a duct are not taken into account
- The pressure changes discontinuously across the actuator disk

Furthermore, the theory assumes steady and incompressible flow, which is only valid during take-off; and viscous losses are not taken into account. Hence, Equation 6.15 represents the theoretical maximum efficiency that a fan can achieve. To correct for the energy losses not taken into account, a multiplying factor of 0.88 is commonly applied, lowering the efficiency and accounting for the 10-15% overestimation [43, 45]. However, the duct around propeller is likely to increase the efficiency.

The thrust setting and diameter can be plotted to find the optimal diameter of the fan to reach the highest efficiency, providing it can satisfy thrust requirements. Figure 6.11b shows the electric fan efficiency map as represented by actuator disk theory. Since the efficiency depends on flow conditions, the efficiency map is made for cruise conditions at FL400 and the efficiency lines are representative of Equation 6.15. As stated before, actuator disk theory shows the theoretical maximum efficiency, hence the factor of 0.88 is applied also to the diagram.

As shown in Figure 6.11b, higher diameter fans are more efficient, however, using many smaller fans can decrease noise emissions compared with less, larger and more powerful fans as discussed in Subsection 10.4.3. Moreover, to avoid supersonic blade tip speeds, smaller diameters allow higher rotational velocity. Finally, the aircraft span and total mass of the distributed propulsion units are limiting for the design. The lightest propulsion subsystem occurs for eight DEP units.

After an iterative process, 0.84 m diameter is chosen. For this diameter, the cruise efficiency is estimated at 82%. The take-off efficiency is considerably lower, at 66%, mainly due to the low speeds at which fan needs to operate while still producing high amounts of thrust.

Thrust of Electric Fans - Another important parameter in fan sizing is the thrust that can be achieved. Thrust is limited by the diameter of the fan, rotational velocity, fan pressure ratio and flow conditions. In turn, the rotational velocity is limited by design tip speed of the fan blades. Design tip speed is limited by noise constraints to be 0.85 Mach at low altitude as explained in Subsection 10.4.3, and it is important not to overcome Mach 1 to prevent wave drag and the formation of shock waves. Rotational velocity of the propeller shaft affects motor performance and is variable during flight, since design tip velocity depends on aircraft speed.

Thrust is calculated by estimating mass flow and velocity difference by using actuator disk theory [48],

$$T = \rho\pi\frac{D_{fan}^2}{4}\frac{V_{exit} + V_{\infty}}{2}(V_{exit} - V_{\infty}) \quad (6.16)$$

6.6.3. Validation of Efficiencies and Recommendations

To validate fan efficiency, multiple models from literature are considered. A study by van den Dungen [47] investigates the F568 propeller and leads to take-off and cruise efficiencies of 65% and 85%

³URL <https://web.mit.edu/16.unified/www/FALL/thermodynamics/notes/node86.html> [cited 16 June 2020]

respectively. This propeller was used for the ATR72-600 aircraft and it has a considerably larger diameter of 3.93 m. However, it has no duct and it is, therefore, reasonable to assume that cruise efficiency is not significantly higher than the efficiency of Cryo-V ducted fans. Another study [49] achieves an efficiency of 80% for a 70 cm ducted fan at 1.5 kN thrust. A simple ducted fan model analysed in [50] achieves the best efficiency of 91% for a hub-to-tip ratio of 0.3. Therefore, the estimated peak efficiency is in a range of values obtained by other designs.

Further analysis of the fan can be done by estimating the thrust and power coefficients as described by Equations 6.18 and 6.19. Both coefficients depend on the advance ratio J , which is calculated in Equation 6.17.

$$J = \frac{V_{\infty}}{\omega D} \quad (6.17)$$

$$C_T = \frac{T}{\rho \omega^2 D^4} \quad (6.18)$$

$$C_P = \frac{P}{\rho \omega^3 D^5} \quad (6.19)$$

Low advance ratio propellers tend to have lower efficiency. Torenbeek [51] estimates that for low advance ratio (0.6) four blade propeller, efficiency can be in the range of 40-70%. A NASA study [52] experimentally finds ducted fan efficiency of 58% when operating at $J=0.6$ advance ratio, which is close to the advance ratio during take-off for Cryo-V design ($J=0.7$) and efficiency differs by 8%.

A recommendation for the next design phase is to estimate the thrust, power and also efficiency by using a blade element theory method as described in [47]. In this method, the propeller is discretised into many blade elements which are analysed in terms of the local thrust, drag and lift forces produced. This way also torque, power and efficiency can be calculated more accurately compared to actuator disk theory method, however, this method can only be performed when the specific blade shape is known.

6.7. Fuel System Design

The fuel system stores enough fuel for each mission as well as ensuring that the required fuel flow for the fuel cells and combustors is provided. This section first presents the fuel tank design, followed by the fuel distribution system. The reliability and safety of these systems is crucial and is also discussed in detail.

6.7.1. Fuel Tank Design

Liquid hydrogen is stored at cryogenic temperatures of 20 K. During the midterm phase [3], the preliminary fuel storage system estimation resulted in the decision to store two hydrogen tanks behind the cabin in each of the fuselage wings. However, by utilising aircraft volume more efficiently, two longer slender tanks in the trailing edge of both fuselage wings are also used, as shown in the cabin layout diagram in Figure 9.1.

In order to find the required tank volumes more accurately, the required mass flows for fuel cells and combustor are estimated, shown in Figure 6.1 for "cruise mode". Based on the maximum fuel flow required for take-off as described by requirement **MRA.SYS.PROP.1.6**, the total mass of the fuel needed can be calculated by taking the duration of different flight phases into account. Furthermore, allowance for boil-off losses and additional fuel for loiter must be included. These two aspects together are estimated to increase the required mass by 6%. For volume estimation, an additional margin for venting is included [53], since part of the hydrogen inside of the tank will be in gaseous form. Safety pressure valves are also installed to prevent the tank from bursting if the pressure suddenly increases rapidly.

Based on a preliminary hydrogen mass estimation, the tank operating pressure and required thicknesses can be obtained. As shown in Figure 6.12, the lower pressure corresponds to higher liquid hydrogen density, however, since for venting purposes some of the hydrogen is in gaseous form, higher pressure is needed. The tank pressure is chosen as 3 bar with a maximum allowable venting pressure of 4.5 bar, for which the structure of the tank is designed. As shown in Figure 6.13 [53], this corresponds to a LH₂ volume fraction of around 92%.

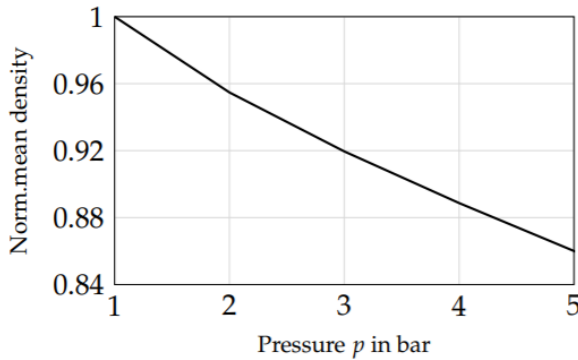


Figure 6.12: Mean storage density as a function of tank pressure for maximum saturation conditions [53]

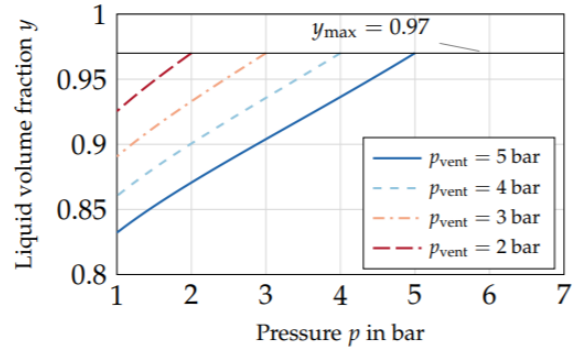


Figure 6.13: Liquid hydrogen volume fraction as shown for different tank venting pressures [53]

After the tank operating pressures are obtained, the structure of the tank can be designed. For the inner sheet, AA 2219 is used. The inner wall material must be resistant to embrittlement, and ductility and fracture resistance at cryogenic temperatures must be high [54]. AA 2219 is also used as the tank wall material in other liquid hydrogen tank designs for passenger aircraft [55]. Knowing the tank dimensions, the required pressure and material properties, it is possible to calculate the wall thickness, as shown in Equation 6.20 [53]. Here, p_d is the maximum allowable design pressure including the safety margin, SF is the safety factor, assumed at 1.5, and K_{al} is the maximum allowable stress for aluminium at cryogenic temperatures, found to be 172.4 MPa [53]. Finally, D_i is the tank diameter and ν the weld efficiency, assumed to be 0.8 [56].

$$t_w = \frac{p_d D_i}{\nu(2K_{al}/SF - p_d)} \quad (6.20)$$

One of the most critical aspects of the liquid hydrogen tank design is to achieve strong insulation. Insulation prevents hydrogen leakage and keeps the tank temperature low. Therefore, insulation materials must be lightweight, provide low thermal conductivity and low hydrogen permeability. The two most commonly used designs are Multi-Layer Insulation (MLI) and insulation using foam material. A trade-off is performed between foam insulation and MLI with an additional vacuum layer. As investigated by Verstraete [56], the MLI insulation with a vacuum jacket has lower thermal conductivity than foams, however, the foam materials are more weight efficient, which also can result in thinner insulation since the vacuum jacket is not required. Furthermore, for a vacuum layer it is of utmost importance to maintain the vacuum, which can be costly and increase the inner tank wall thickness, resulting in a higher tank mass [56].

Closed-cell polyurethane foam is, therefore, used as an insulation material. Brewer [55] estimates an insulation thickness of 9.14 cm [54], which is also chosen for the Cryo-V design. It is inside the range of insulation thicknesses (7.5 cm - 13 cm) estimated for different designs [57]. Closed-cell polyurethane foam is implemented together with a glass fibre protective layer, which has a low density of 67.9 kg/m³ [55, 58], which allows for insulation of large volume tanks. The insulation and tank wall are displayed in Figure 6.14. A MAAMF vapour barrier is a multilayer sandwich structure as explained by [56], where letters M, A and F stand for mylar, aluminium and fabric layers respectively. The total thickness of the MAAMF layer is from 0.01 mm to 0.02 mm [56]. Finally, the glass fibre fairing prevents external damage to the tank and is estimated to be 1.57 cm thick, as analysed by [53]. A recommendation

for the next design phase is to investigate the thermal properties of the chosen insulation design in more detail. This way, estimation of the tank mass can be performed more accurately. Different tank shapes can also be assessed [59], since that could allow for more efficient utilisation of space in the aircraft.

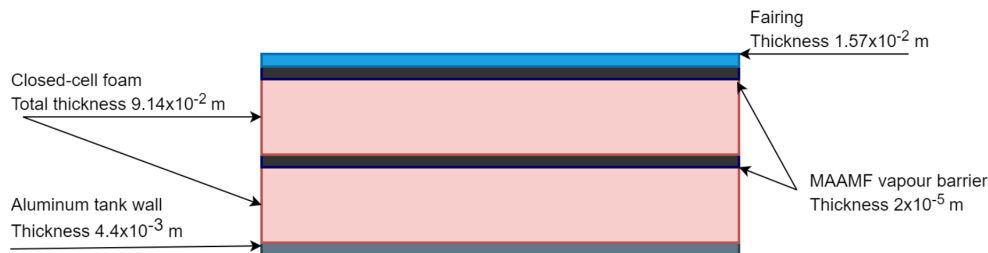


Figure 6.14: Cryogenic hydrogen tank wall design (not to scale)

6.7.2. Fuel Distribution

The hydrogen tanks are designed for a specific boil-off rate, such that hydrogen can be provided to the fuel cells and combustor in gaseous state. Hence, the tank pressure is regulated and a boost pump is used to obtain the pressure required for in the delivery lines. The delivery lines are steel, insulated using closed-cell polyurethane. Steel is chosen because the delivery lines require high strength and the weight is not critical, given that the pipes are small compared to the tank. The Cryo-V uses an inner wall with a thickness of 0.41 mm [55] and an insulation thickness of 3.8 cm [54]. Brewer designs the pipe for mass flow of 0.351 kg/s [37, 55], resulting in a pipe diameter of 2.54 cm [54]. Considering the required mass flow of 325 g/s, while accounting for a situation when only one tank delivers hydrogen to the system, the diameter of pipes is calculated to be 2.5 cm. A graphical view of delivery lines is shown in Figure 6.15.

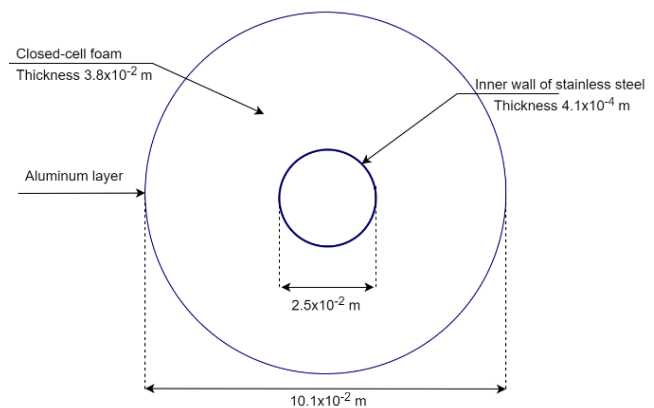


Figure 6.15: Cross-sectional view of the hydrogen delivery lines

Since the mass flow required for cruise and take-off differs, the pressure and temperature of the hydrogen flow must be controlled. Boost pumps can be used to increase or decrease the pressure in the delivery lines and the venting pressure can be changed if the boil-off rate must be increased. A heat exchanger is used along the delivery lines to regulate the temperature of the hydrogen before it enters the fuel cell. Alternatively, the delivery lines can be used to cool down other aircraft components, shown in Figure 6.1. In these sections, the insulation thickness can be lowered.

Since the mass flow required for cruise and take-off differs, the pressure and temperature of the hydrogen flow must be controlled. Boost pumps can be used to increase or decrease the pressure in the delivery lines and the venting pressure can be changed if the boil-off rate must be increased. A heat exchanger is used along the delivery lines to regulate the temperature of the hydrogen before it enters the fuel cell. Alternatively, the delivery lines can be used to cool down other aircraft components, shown in Figure 6.1. In these sections, the insulation thickness can be lowered.

6.7.3. Fuel System Mass Estimation

The total mass of the six fuel tanks together is 3800 kg. The ratio between fuel tank mass and fuel mass is 0.9, slightly lower than the ratio of 1.1 assumed previously in Midterm Report [3]. A single tank mass is estimated to be approximately 70% of the hydrogen mass if an optimal cylindrical shape is used [53, 57], but assumes only a single tank. When six tanks are used, the mass fraction increases since the total tank surface area is higher for the same fuel mass.

The delivery line masses are significantly lower, around 50 kg in total. For the estimation of the total fuel system mass, Brewer [55] uses a contingency allowance of 1.07 to account for boil-off, trapped fuel and equipment. For the Cryo-V, 14% is used to account for pressure relief valves, boost pumps and heat exchangers. The total fuel system mass is 4400 kg.

6.8. Aircraft Systems Power

The main aircraft systems considered for non-propulsive power management are the electric actuators, air conditioning, ice protection and various other, smaller items. Semi-empirical methods [43] are used to estimate the power required for these systems, which depend on aircraft volume, span, actuator size and other characteristics.

The total estimated power required for the aircraft systems is 0.42 MW. For validation purposes, the ratio of aircraft systems power and cruise power is used. The Cryo-V requires 5% of cruise power at an altitude of 30 000 ft, similar to mission profiles for smaller electric aircraft [43]. For commercial aircraft, the majority of systems power is provided by an Auxiliary Power Unit (APU). The Airbus A320 requires up to 90 kW of ground power, part of the systems power required [17]. The Pratt & Whitney APS5000 APU, designed for the Boeing 787 Dreamliner, can provide up to 450 kW⁴, which is similar to the total non-propulsive electrical power required by the Cryo-V.

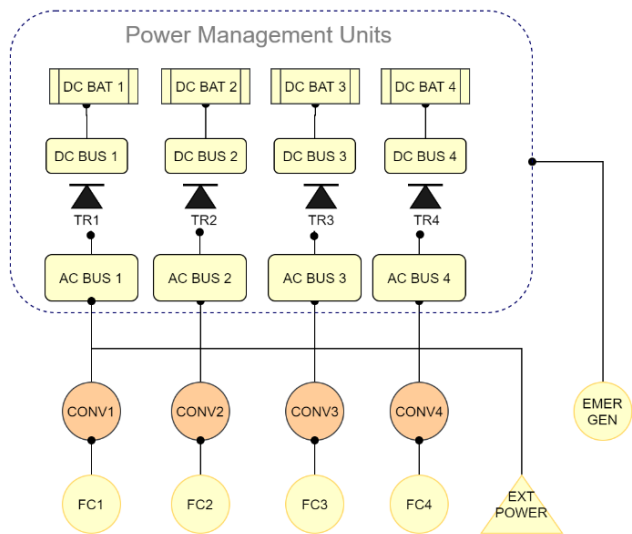


Figure 6.16: Electrical block diagram

Electrical Block Diagram - The main electrical components of the aircraft are shown in Figure 6.16. The electrical power distribution is adapted from the electrical system of the Airbus A320 [60]. The main differences are that electrical power for the aircraft systems is fully delivered by the four fuel cell modules. The electrical power from the fuel cells is delivered to the AC buses through converters (CONV) to be further distributed to the aircraft systems such as avionics, environment control, cabin equipment and others, as explained in Figure 9.9. It should be noted that Figure 6.16 shows a simplified electrical systems architecture of the main components and that the system will consist of more components such as essential shed buses, transmitters, power switching lines and others. The detailed design for these components will be performed during future development phases.

6.9. Material Selection and Mass Budgets

This section presents an overview of the materials used for the propulsion and fuel systems as well as their mass breakdown.

6.9.1. Material Selection

The materials are selected to keep the environmental impact of the propulsion system as low as possible. The use of SOFCs means that limited rare earth metals are required, as would be the case for low-temperature fuel cells. Instead, zirconia cermet (using nickel), yttria and Strontium-Doped Lanthanum Manganite (SDLM) are used [32] with a steel structure and interconnect to withstand the high temperatures. The turbofan and DEP mass breakdown is based on [61] and makes use of aluminium, titanium and nickel. Further analysis is required for the electric motor and battery materials.

⁴URL <https://www.pwc.ca/en/products-and-services/products/auxiliary-power-units> [cited 16 June 2020]

6.9. Material Selection and Mass Budgets

Table 6.6: Propulsion and fuel system material selection

Components	Material	Mass (kg)
DEP and TF nacelle & structure, fuel tank structure	Aluminium	4094
Fan blades, LPC	Titanium	329
Fuel cell structure, interconnect, anode support	Steel	3756
LPC, HPT, LPT	Nickel	174
Fuel cell anode material	Zirconia Cermet	751
Fuel cell electrolyte	Yttria	47
Fuel cell cathode material	SDLM	141
Fuel tank insulation	Polyurethane	1106
Electric motor, battery, cable insulation	Others	1076

6.9.2. Mass and Power Budgets

To summarise the propulsion system characteristics, the mass and power budgets are estimated. Table 6.7 shows the mass, total power produced and thrust produced by the main system components.

Table 6.7: Propulsion system overview

		Turbofans		DEP		Fuel Cells		Battery	
Number	(-)	2		8		-		1	
Diameter	(m)	0.91		0.84		-		-	
Total Mass	(kg)	1297		1892		5491		604	
		Take-Off	Cruise	Take-Off	Cruise	Take-Off	Cruise	Take-Off	Cruise
Total Efficiency	(%)	-	58	59	75	64	64	99	99
Total Power	(MW)	6.2	1.6	4.6	6.8	13.7	11.5	1.38	1.38
Total Thrust	(kN)	67.0	6.8	58.4	24.4	-	-	-	-

For the turbofans during take-off, no efficiency is expressed. Instead, Thrust Specific Fuel Consumption (TSFC) is calculated and standardised for fuel energy density. TSFC is found to be 0.545 MJ/(kN s), which is 38% higher compared to the Airbus A320 [10], explained by the smaller amounts of thrust being produced by the Cryo-V turbofans. The fuel cell mass is estimated using power density as explained in Section 6.3, whilst turbofan and DEP masses use empirical relations and the total thrust. The DEP mass consists of the propeller, duct and pylon masses together with electric component masses. Propeller and electric component masses are estimated using semi-empirical relations [43, 45]; the duct and pylon masses are considered as nacelles and use the Torenbeek weight estimation [51]. Turbofan total mass is found using the semi-empirical relation based on take-off thrust by Raymer and Jenkinson [62].

Total Propulsion System Mass - The total propulsion system mass, without the fuel system, is 9409 kg, 13.1% of MTOW. The fuel system adds another 4384 kg to a total of 13 793 kg. To validate this result, a Raymer estimation is used [25]. Raymer states that for conventional aircraft, the propulsion system usually weighs 8% of the MTOW. The Cryo-V propulsion system is heavier due to several reasons. Firstly, the fuel cell mass is around 5500 kg, a significant weight component of the aircraft. Furthermore, due to the use of distributed electric propulsion, the nacelle weight is higher. Finally, the Cryo-V is significantly lighter than reference aircraft due to a more efficient aerodynamic design and lower fuel mass due to use of hydrogen. These aspects, therefore, result in the propulsion system mass having a larger fraction of MTOW.

6.10. Recommendations

The propulsion system design methods have their limitations, and recommendations for future work are provided. A simplified analytical fuel cell model is used at the current stage, but CFD analyses are recommended to model the fuel cell performance more accurately. In addition, more research shall be focused on assessing the thermodynamic cycle of an integrated fuel cell - turbofan system. As shown in Figure 6.1, a heat recuperation system is implemented in the propulsion system. However, this component is modelled based on assumptions, and in future work a detailed analysis on this heat exchanging system should be performed.

The effect of Boundary Layer Ingestion (BLI) is not investigated in this report and it is highly recommended that future work focuses on analysing the benefits of BLI. A design which takes the highest possible advantage of this phenomenon would have increased aerodynamic and propulsive efficiency. To achieve the most efficient use of BLI, the engines might need to be integrated to greater extent into the wing or even placed behind it. These aspects might affect the available space for tank placement and noise shielding shall be assessed as well. For analysis of electric fan performance it is recommended that blade element method is used as explained in Subsection 6.6.3.

Finally, an accurate boil-off model and precise assessment of hydrogen tank insulation properties shall be considered in the next design phases. This step in design is also required to prepare for successful aircraft operations such as refuelling.

Structural Design

The structure of the Cryo-V is designed to carry all loads encountered during its lifetime and house all components. First, the functions of the structure are explored in Section 7.1, followed in Section 7.2 by the assumptions taken for the structural model and the methods built upon these in Section 7.3. Next, the verification and validation processes are described in Section 7.4 and Section 7.5 respectively, followed by the application of the methods on the Cryo-V aircraft in Section 7.6. The chapter is concluded by a description of considered materials in Section 7.7 and recommendations for future structural analysis in Section 7.8.

7.1. Functional analysis

A functional analysis is conducted to determine the requirements specific to the aircraft structure. For the Cryo-V, the wing and fuselage structures are merged, which presents an extra challenge. The structural considerations are provided below, followed by the structural requirements in Table 7.1.

- | | |
|--|--|
| 1. Allow pressurisation | The airframe should allow pressurisation of the passenger cabin segment to a viable environment for humans |
| 2. Provide structural integrity | The wing structure is to sustain and transfer flight loads, ground loads and weight on the whole life-cycle of the aircraft. |
| 3. Support all components | The structure is to join all other subsystems together, providing the necessary stiffness. |
| 4. Enable maintenance | The structure must allow access and maintainability different sub-systems and components. |

Table 7.1: Structure subsystem requirements

Structural Requirements	
MRA.SYS.STRUCT.1.1	The cabin shall be pressurised at an altitude of 40 000ft at an equivalent pressure altitude of 7800 ft.
MRA.SYS.STRUCT.1.2	The cabin shall sustain at least 60 000 pressurisation cycles.
MRA.SYS.STRUCT.1.3	The structure shall sustain a maximum load factor of 2.5 g.
MRA.SYS.STRUCT.1.4	The structure shall sustain an ultimate load factor of 3.75 g.
MRA.SYS.STRUCT.1.5	The structure shall sustain a minimum load factor of -1 g.
MRA.SYS.STRUCT.1.6	The structure shall sustain loads from landing gear.
MRA.SYS.STRUCT.1.7	The structure shall sustain at least 60 000 loading cycles.
MRA.SYS.STRUCT.1.8	The structure shall not yield under maximum load.
MRA.SYS.STRUCT.1.9	The structure shall not buckle under maximum load
MRA.SYS.STRUCT.1.10	The structure shall allow access for maintenance.
MRA.SYS.STRUCT.1.11	The structure shall not flutter under maximum loads at maximum speed.

7.2. Assumptions

The following assumptions are used for the structural design of the Cryo-V:

- The half-wing of the aircraft is split into a cabin-wing and an aft-wing segment, each idealised as a beam.
- It is assumed that the wing bends along the neutral axis of the airfoil, on a line parallel to the chord line.
- It is assumed that a single material is used for the structure, allowing to neglect strain compatibility and allowing more representative verification with literature [5, 63–65].
- Different loads are mainly born by different parts. For this simplified analysis it is assumed that specific parts carry exclusively their respective loads.
- It is assumed that bending loads are carried by the skin, the stringers and the spars forming a single cross-section for the stress analysis.
- Shear loads are assumed to be carried by the wing spars. This assumption leads to an over-estimation of the acting shear stress as some is carried by the skin. Including the skin would however require a more time consuming shear flow analysis coupled with the skins torsion loads. As this assumption does not compromise the safety of the design it is kept.
- Torsional loads are assumed to be carried by the skin sheet. This allows to consider the wing-beams as a closed cross-section and neglecting the multi-cell nature of a wing with spars.
- The loads in flight direction are neglected. The reason for that is that the ultimate load factor of 3.75 g happens along the normal vector of the planform during manoeuvres. In addition to that, considering the thrust to weight ratio of 0.18 from Chapter 6, the maximum expected loads in flight direction are only 4.8% of the ones perpendicular to the planform. Therefore the loads in flight direction are not analysed further.
- Considering the preliminary design phase and the limited verification and validation resources, the cross-section is simplified and assumed constant along the wing span apart from the chord length which reduces along the span for the aft-wing.
- The spars have a rectangular cross-section.
- The spars are placed at fractions of the chord line. In the cabin wing the spars are placed right in front and right after the passenger cabin.
- As the detailed stringer design is considered out of scope for this project, they are reduced to point-areas placed on the skin for the moment of inertia calculations. Considering their small size compared to the total cross-section their individual moment of inertia is negligible.
- The expected sheet thickness has an order of magnitude of millimetres and the expected cross-section height is around 2 meters, hence the thin-walled assumption is valid.
- Because at this stage of the design it is not possible to obtain a chordwise lift distribution, accurate chordwise center of gravity and accurate positioning of the shear center, it is assumed that the two first ones are collinear through the latter.

7.3. Methods

This section presents the method used to design and analyse the structure of the Cryo-V. It includes the goal of the methods, pressure vessel sizing and the load, cross-section and stress analyses. Fatigue is also considered, as well as the mass and Center of Gravity (CoG) computation.

7.3.1. Goal

The ultimate goal of the structural analysis is to obtain a representative weight estimation for the structure that complies with the requirements stated in Section 7.1. The multitude of input parameters describing the structure makes the inclusion of a full structural design optimiser in the total iteration program impossible. Therefore, a class II weight estimation following Raymer [25] is included in the iteration process and a more detailed structural analysis is performed after the iterative design.

7.3.2. Pressure Vessel

Considering that the pressurised cabin does not extend until the tip of the cabin wing and following the sizing method for oval fuselages presented in [11], the pressure vessel sizing can be done independently. The current layout does not allow for circular pressure vessels, therefore, a lower weight efficient pressure vessel is used and its thickness t is sized according to Equation 7.1 [11].

$$t = \frac{j\Delta_p R}{\sigma_{fatigue}} \quad (7.1)$$

The pressure difference Δ_p is computed for ISA conditions at FL400, assuming a cabin pressure equivalent of 6900 ft [66]; the safety factor j is assumed to be 1.5 [11]; and $\sigma_{fatigue}$ is the maximum stress amplitude after the required number of cycles. The radius R must be determined for each curve in the pressure vessel cross-section.

7.3.3. Load Analysis

The first step in the structural design of a wing structure is to set up the span-wise loading diagram. As stated in the assumptions, the analysis focuses on the forces acting in the vertical direction. The different masses are distributed on the span interval on which they occur and operational empty weight, fuel weight and payload weight distributions are added for a total weight distribution. A lift distribution for the considered configuration is also extrapolated from [63].

Because the wings are idealised as beams, it loads are analysed in the direction of the beams. This simplifies the analysis since the challenges concerning torsion and bending in swept wings are thus combined into one bending load in the sweep direction. Therefore, care must be taken when integrating the line loading over the beam direction, as the magnitude decreases but the length increases. Integrating once yields the applied shear load and integrating again the applied bending load. From the assumptions in Section 7.2, the only applied torsional load comes from the moment coefficient of the local airfoil.

Next, it is important to analyse the beam junction. Because the cabin and the aft beams, which represent the cabin wing and aft wing respectively, do not have the same sweep angle, bending loads at the root of the aft beam are distributed in both bending and torsion in the tip of the cabin beam. This critical point is shown as point B in Figure 7.1b. The same is true for the torsional loads at the root of the aft beam. A similar effect occurs due to the attachment of the winglet, which induces additional bending and torsion on the aft beam and is modelled as the resulting root moment and torque from the winglet beam. However, only one of the papers used for verification and validation includes usable results for this effect, meaning that it cannot be verified or validated rigorously. Therefore, the contribution from the winglet is neglected. This means that torsion and bending loads on the aft wing are underestimated, but considering the small size and area of the winglet and the symmetric airfoil chosen in Subsection 8.2.3, this contribution is negligible.

7.3.4. Cross-Sectional Analysis

The next step towards a stress analysis is to compute the cross-sectional properties at each beam station. The first parameter to be determined is the neutral axis of the airfoil, since from the assumptions it is considered to also be the neutral axis of the beam. This is done by discretising the airfoil in points, integrating the discretised areas and dividing by the total area to find the neutral axis. Then, the moment of inertia is computed in a similar way for the skin by integrating the point areas and their distance to the neutral axis squared. The moment of inertia of the spars can then be added, along with the sum of the Steiner term for the moment area of the stringers. The stringers are placed at regular chord interval on both the upper and lower surface of the skin.

For the shear stress analysis, the first moment area of the spars is computed by multiplying half of the

cross-sectional area with a quarter of the spar height. For a torsional stress analysis, the enclosed area of the cross-section is required, which is computed by summing the trapezoidal areas created by each set of four points on the airfoil.

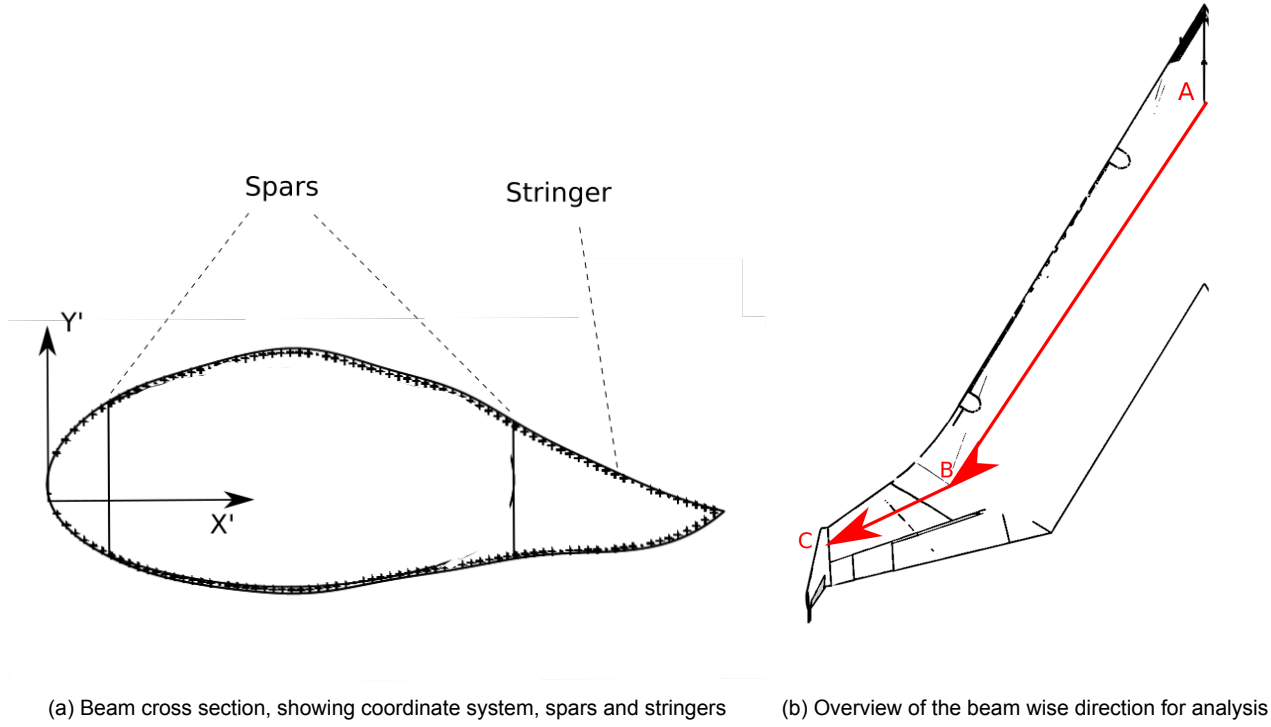


Figure 7.1: Overview of the structural analysis coordinate system

7.3.5. Stress and Buckling Analysis

For bending stress analysis, the flexure equation, Equation 7.2, is applied, assuming no load in the x direction. For the shear stress analysis, Equation 7.3 is used and for torsional stress, Equation 7.4 is applied. The total stress is computed using von Mises stress, calculated by Equation 7.5.

$$\sigma_{bending} = \frac{M_{x'} I_{y'y'} - M_{x'y'} I_{x'y'}}{I_{x'x'} I_{y'y'} - I_{x'y'}^2} \quad (7.2)$$

$$\tau_{shear} = \frac{VQ}{I_{x'x'} t_{spar}} \quad (7.3)$$

$$\tau_{torsion} = \frac{T}{2t_{skin} A_m} \quad (7.4)$$

$$\sigma_{total} = \sqrt{\sigma_n^2 + 3\tau^2} \quad (7.5)$$

In Equation 7.2, $I_{x'x'}$, $I_{y'y'}$ and $I_{x'y'}$ are the moments of inertia of the cross-section in the beam wise coordinate system, $M_{x'}$ is the bending load and x' and y' are the positions coordinates on the cross-section as shown in Figure 7.1a. For Equation 7.3, V is the shear load, Q is the area moment and t_{spar} is the spar thickness. For Equation 7.4, T is the torsion load, t_{skin} is the skin sheet thickness and A_m is the area enclosed by the cross-section. For the von Mises stresses in Equation 7.5, σ_n is the normal stress and τ is the shear stress. For the case of the wing skin, the normal stress is taken as the bending stress and the shear stress as the torsional stress, for the spar the normal stress is also the bending stress and the shear stress is taken as the spar shear stress.

The total stresses and critical stresses can be compared and the design parameters adjusted to reduce the maximum stresses in the skin sheet below the critical buckling stress computed from Equation 7.6 at ultimate load and keep the maximum shear stress below that of the material.

$$\sigma_{cr} = \frac{K_c \pi^2 E}{12(1 - \nu^2)} \left(\frac{t_{skin}}{b} \right)^2 \quad (7.6)$$

Considering that the stress in the skin is applied in a thin walled plate, buckling is critical. Using Equation 7.6, the critical buckling stress for a thin plate is obtained. In this equation, the buckling coefficient K_c is assumed to be 4.0 since the considered plate segment is simply supported by the ribs and stringers [67]. E represents the Young's modulus of the considered material, ν the Poisson ratio, t the sheet thickness and b the stringer pitch.

7.3.6. Fatigue Consideration

From the requirement **MRA.SYS.STRUCT.1.7**, the airframe should sustain 60 000 cycles. In order to meet that requirement, the maximum stress amplitude allowed by the main structure's material at that cycle count must be known for the considered material, which itself depends on the stress ratio. The stress ratio is computed using Equation 7.7 [68].

$$R_\sigma = \frac{\sigma_{min}}{\sigma_{max}} \quad (7.7)$$

For the pressure vessel, the cycle goes from maximum stress to zero stress when depressurised, therefore yielding a stress ratio of 0. The stress ratio of the wing structure is computed by taking the maximum stress at maximum load σ_{max} and the minimum stress at minimum load σ_{min} . The maximum and minimum loads are taken as the maximum loads in the two most extreme load cases considered. In case the maximum stress amplitude exceeds the materials fatigue stress, the structure's design parameters must be adjusted to lower the maximum stress amplitude.

7.3.7. Mass and Center of Gravity

As stated in the goals in Subsection 7.3.1, a class II estimation for structural mass is used in the iteration process. This estimation uses Raymer's fuselage mass equation for the cabin wing and the wing mass equation for the aft wing [25].

For the more detailed design, the total material volume is computed and multiplied by the material density. Because the design is still preliminary and neglects many other parts usually present in aircraft structures, such as rivets and reinforcements for cutouts, a contingency margin of 20% is added to account for the extra weight.

The centre of gravity is computed for each wing by determining the centroid in both chord and length direction. Then, the general structural CoG is computed by multiplying the CoG of the wings with their computed structural mass and dividing by the total structural mass.

7.4. Verification

The first step of verification is to visually check all formulae to ensure that they are correctly written and implemented. Then, unit tests are performed on each function in the design code. Each unit is tested for simple inputs for which the result can be computed analytically and the results of the unit are compared with manual calculations. After that, the units are tested for singularities, for example sweep values of 90° or length values of 0 are inputted, and the behaviour of the unit is observed. For conciseness the result of each unit test will not be presented. For the larger system verification test scenarios are set-up in the form of a wing-beam with a circular airfoil and input data as seen in Table 7.2. The three first scenarios are used to verify the stress computation, while the last input set is used to verify the CoG shift computation. The results of the stress calculation verification is shown in Table 7.3. The class II weight estimations are verified using data from the Airbus A320 [17] and Boeing B737¹ for both fuselage and wing weight, which will be used on the Cryo-V design for cabin wing and aft wing respectively as deduced from [25]. The torsion at the root of the aft wing, described in the methods, is verified using data from [5] and comparing the results for the torsion around the

¹URL <http://www.b737.org.uk/techspecs/detailed.html> [cited 09 June 2020]

7.5. Validation

cabin wing beam. The weight estimations, torsion calculation and CoG shift showing deviations within 10% and hence are considered verified.

Table 7.2: System test inputs for structural design verification

	Chord (m)	Beam Length (m)	Beam Sweep (deg)	Number of Spars (-)	Bending Loads (Nm)	Shear Loads (N)	Torsion Loads (Nm)
Scenario 1	1	10	0	0	1	1	1
Scenario 2	1	10	0	1	1	1	1
Scenario 3	2	10	0	1	1	0	0
Scenario 4	1	10	45	0	1	0	0

Table 7.3: System tests: stress deviation from manually computed values in percentage

	Moment of inertia (%)	Bending stress (%)	Shear stress (%)	Torsion stress (%)	Deflection (%)	Mass (%)
Scenario 1	0.1	0.1	-	0.07	0.1	1.2
Scenario 2	-0.2	0.2	0.1	0.1	2	0.1
Scenario 3	0.2	0.18	-0.1	0.1	0.2	0.11

7.5. Validation

After making sure that the computations yield correct results, it is important to check whether the method used is the right one to achieve the set design goals. Because no Flying-V type aircraft has been built, it is not possible to validate the method with existing aircraft. What can be done however is comparing it to existing papers dealing with the structural design of such aircraft. Four papers were found dealing with that subject, two from the same author dealing with the structure on a conceptual scale [5, 63] and two making use of Finite Element Modelling (FEM) [64, 65]. The goal of the structural design is to come up with a weight estimate for a structure able to carry the applied loads, therefore the validation process focuses on the comparison of weight estimates and maximum stress between the found studies and the method for the same input parameters. Those input variables can be found in the most detail in [64, 65] and are summarised in Table 7.4. Both input sets are run with the built method and a comparative of the main results is shown in Table 7.5. It must be noted that for the case of the FEM studies, an average stress result is presented neglecting local peaks. Additionally, [5, 63] do not present a full list of inputs and [63] does not present numerical values for stress and mass estimations, but considering they deal with the same aircraft with the same general specifications the results of [5] is still shown in Table 7.5.

Even though the result of the method lies within the range of estimations coming from the considered studies, the significant mass variation between the studies and the low amount of papers found show that making an accurate mass prediction for the structure of a Flying-V configuration is challenging. In conclusion, as the values resulting from the chosen method lie in the range of the values found from literature the method is considered validated, but it is recommended to reiterate the validation process once more data on the Flying-V configuration is available.

7.6. Structural Characteristics Determination

Following the aforementioned method, the structure of the aircraft can be designed. The process starts with a load analysis, followed by the design of the beams cross-section and ending with a stress and fatigue analysis. For this structural design aluminium AA2024T6 is chosen as material for its recyclability, isotropic properties and because it is a very commonly used material in aerospace structures [25].

7.6. Structural Characteristics Determination

Table 7.4: Structural analysis validation input parameters [64, 65]

		From [64]	From [65]
Wing area	(m ²)	883	895
Span	(m)	65	65
Cabin wing sweep	(deg)	64.48	-
Aft wing sweep	(deg)	37.85	-
Wing root chord	(m)	24	24
First kink location, span frac.	(-)	0.387	0.38
Second kink location, span frac.	(-)	0.629	0.6
MTOW	(kg)	260 000	260 000
Fuel weight	(kg)	70 000	97 065
Payload weight	(kg)	60 000	56 190
OEW	(kg)	130 000	106 745
Taper ratio	(-)	0.13	0.15

Table 7.5: Structural analysis validation results

	Maximum Stress (MPa)	Structural Mass (kg)
Method with inputs from [64]	94.2	85 743
Methods with inputs from [65]	98.7	84 179
Results from [64]	average 66-133	99 781
Results from [65]	no numerical value shown	58 457
Results from [5]	33	73 953

7.6.1. Load Cases

During operations, the aircraft will be subjected to a wide variety of loads. It is therefore important to identify the most critical load cases which will be used to size the structure. For the Cryo-V aircraft, two distinct critical load cases are identified.

- 1. Maneuvering at MTOW at ultimate load factor** The first load case includes the aircraft at MTOW maneuvering at ultimate load factor which is defined as 1.5 times the maximum load factor. As from **MRA.SYS.STRUCT.1.3** the maximum load factor is 2.5 g, the load factor for this load case is 3.75 g. Additionally the cabin is pressurized.
- 2. MTOW on ground** Considering the Flying-V configurations offers significant bending relief because of the mass being distributed along the wing, the concentrated load coming from the reaction forces of the landing gear should be considered for sizing.

The next step is to construct applied loading diagram for each load case, and determining the applied bending and shear force in the beam following the method presented in Section 7.3. The weight distribution is obtained by distributing the different weight elements shown in Table 7.6 on their respective half span length. It must be noted that in Table 7.6 the cabin wing element includes structural weight, furnishing and equipment weights. Results for loading for both load cases is shown in Figure 7.2 and the bending distributions in Figure 7.3. In the latter figure one can observe the effect of the analysis in beam direction and the effect of the sweep change at 13 m from the centerline explained in Section 7.3. Finally torque distribution is shown in Figure 7.4.

7.6. Structural Characteristics Determination

Table 7.6: Half span positions and masses of the different weight-elements considered in the load cases

	Passengers	Cargo	Fuel	Propulsion	Fuel Cells	Cabin Wing	Aft Wing
Start on half span (m)	0	11.5	0	0	0	0	14.2
End on half span (m)	11.5	14.2	14.2	4.88	0.9	14.2	18
Mass (kg)	18972	3860	4179	3918	5490	30193	5479

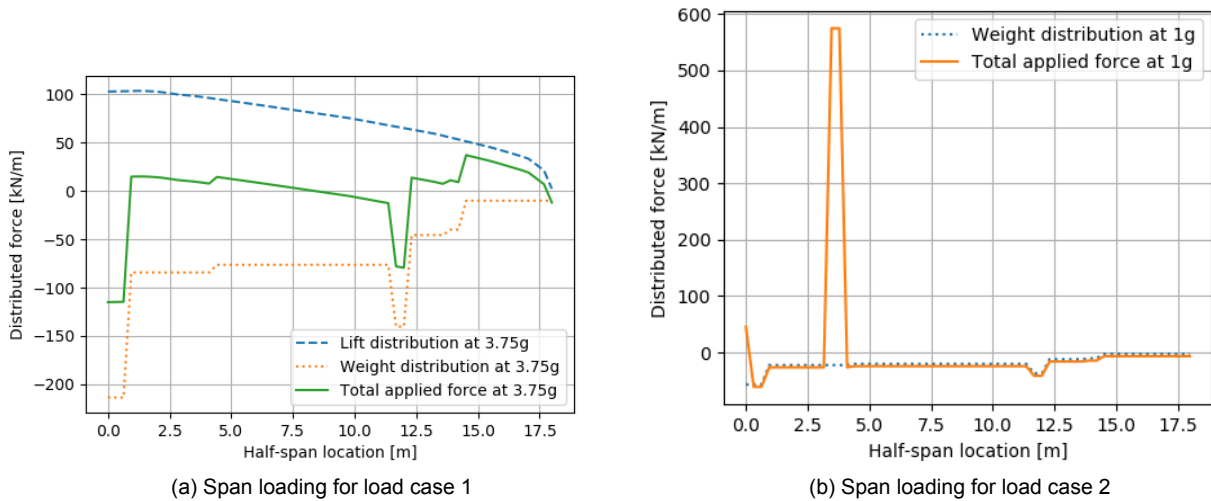


Figure 7.2: Applied loading on the wing in spanwise direction

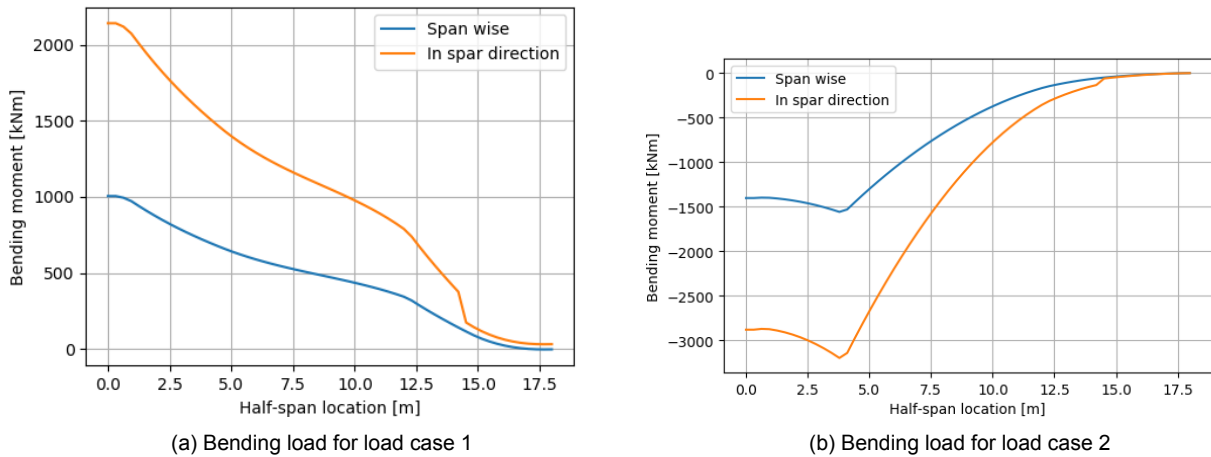


Figure 7.3: Bending loads on the wing in spanwise direction

7.6.2. Stress Analysis

In order to sustain those loads, different design parameters can be adapted. An iterative work is then performed to obtain a weight-efficient parameter combination which is shown in Table 7.7. Applying the method described in Section 7.3 to those parameters and the previously computed loads yields a maximum von Mises stress distribution in the skin shown in Figure 7.5 and in the spars in Figure 7.6. As can be observed the actual stress values are low as the most critical parameter is buckling, which is logical considering the small thickness of the skin compared to the overall cross-section.

7.6. Structural Characteristics Determination

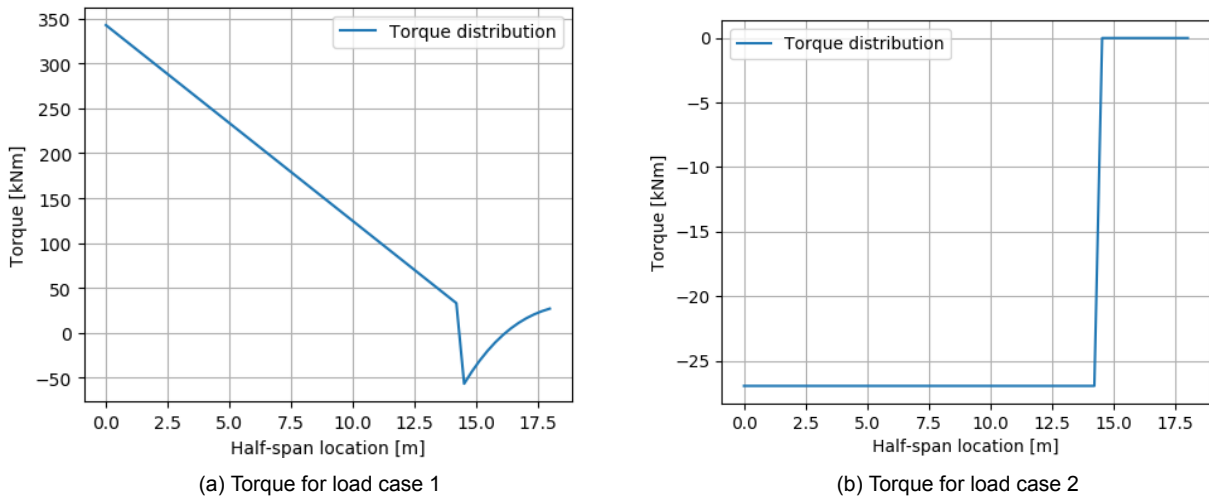


Figure 7.4: Internal torque on the wing in spanwise direction

Table 7.7: Cross-section design parameters

	Sheet Thickness (mm)	Spar Thickness (% spar height)	Spars Location (% chord)	Number of Stringers (-)	Stringer Area (mm ²)
Cabin wing	4	0.1	9 ; 69	150	60
Aft wing	3	0.2	25 ; 60	120	60

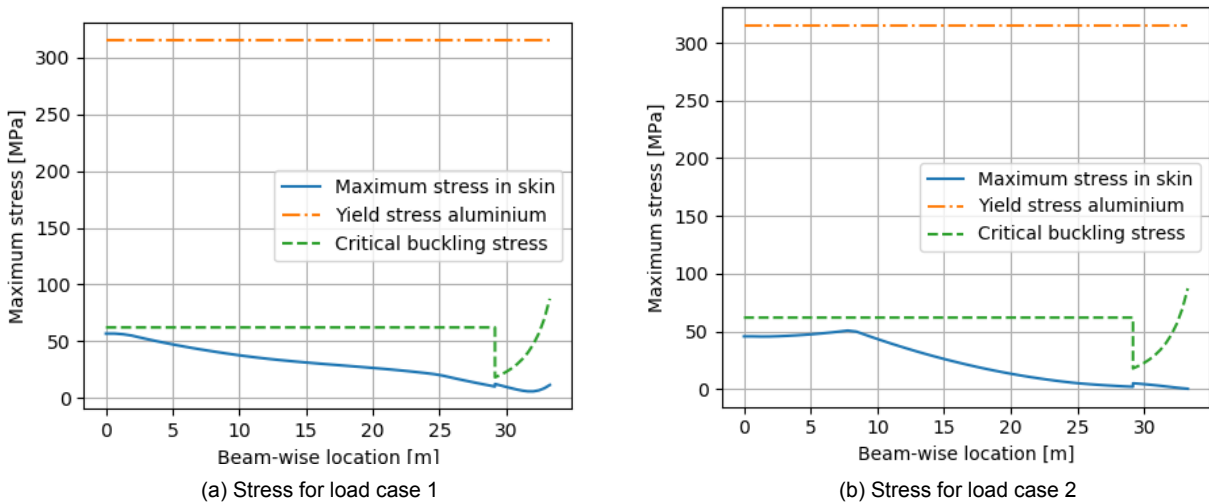


Figure 7.5: Maximum von Mises stress in the skin, measured in beam direction

7.6.3. Fatigue Considerations

As per requirement **MRA.SYS.STRUCT.1.2**, the structure shall sustain at least 60 000 cycles. To check for that the maximum stress amplitude and stress ratio must be computed, and using the S-N curve of AA2024T6 alloy the maximum fatigue stress can be found. Using as stress amplitude the maximum stress in 3.75 g load factor and the minimum stress as the maximum stress in the load case landed on ground, a stress amplitude of 51 MPa for the skin, 120 MPa for the spars and an average stress ratio of -0.6 can be found. The stress amplitude is defined as the average of the absolute values of the minimum and maximum stresses. Using the aluminium AA2024T6 curves ¹ assuming

7.6. Structural Characteristics Determination

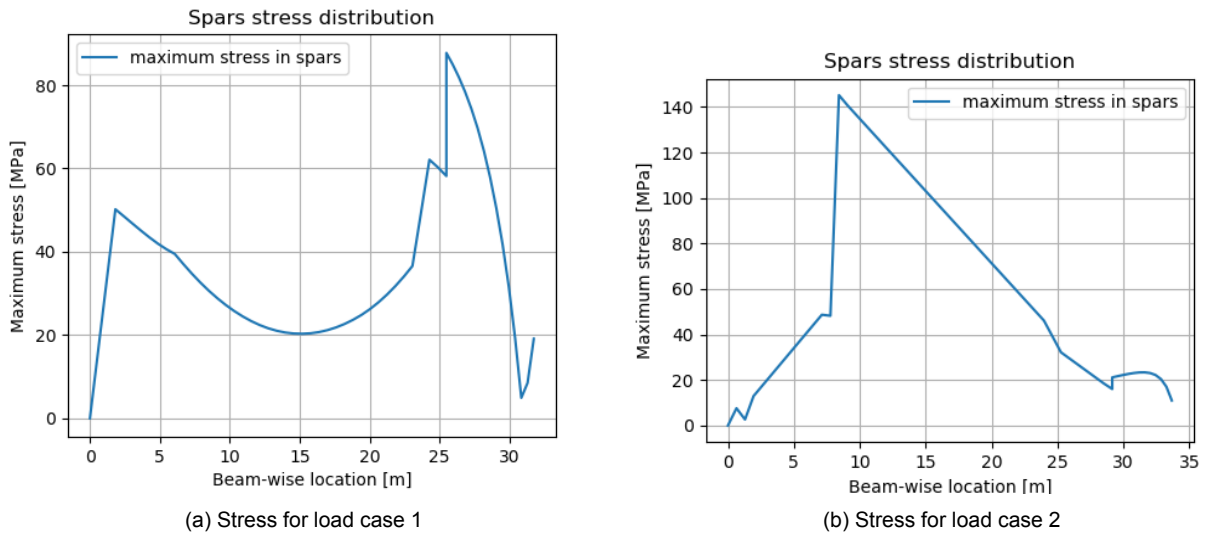


Figure 7.6: Maximum von Mises stress in the spars, measured in beam direction

100 000 cycles in order to have an operational margin a fatigue stress of 290 MPa is obtained. This is above the maximum expected stress amplitudes in both spars and skin, therefore fatigue of the structure is not a driving requirement.

7.6.4. Pressure Vessel Sizing

Another aspect of the structure is the pressure vessel. As explained in Section 7.3, the wall thickness is computed as function of the pressure difference, the radii of the pressure vessel and the fatigue stress of the material. The pressure difference is computed using the ISA pressures of the altitudes shown in Section 7.3, the fatigue stress is computed using S-N curves for AA2024T6 aluminium¹ assuming the same amount of cycles as the main structure but using a stress ratio of 0 as no compressive stresses are expected from pressurisation and depressurisation. This results in a fatigue stress of 250 MPa. The radii are computed by assuming a pressure vessel cross-section as shown in Figure 7.7. After applying a safety factor of 1.5, the resulting thicknesses are rounded to the nearest millimeter for production purposes. This yields a maximum pressure vessel thickness of 2 mm.

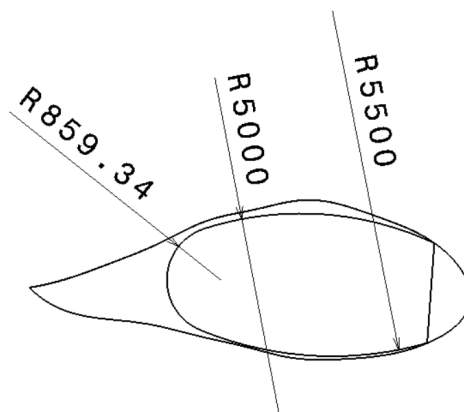


Figure 7.7: Pressure vessel radii in mm

¹URL https://icme.hpc.msstate.edu/mediawiki/index.php/Aluminum_2024-T3_Stress-Strain_and_Fatigue_Life_Data [cited 10 June 2020]

7.6.5. Mass Results

The structure being sized for the loads, it is possible to compute the total material mass needed based on the cross-sectional area, the length of the beams and the density of aluminium. It is clear that the structural mass is not exclusively composed out of material mass, as fasteners are needed to attach the parts together, reinforcements are needed at critical locations such as cutouts etc. Therefore a 20% mass margin is added to account for those extra masses which have not been designed for yet. This results in an estimated structural mass of 19.0 tonnes which is comparable to the corresponding class II weight estimation from Raymer [25] yielding 19.4 tonnes.

7.7. Material Characteristics

The choice of material is important for the structure, as each material and each alloy has particular properties.

7.7.1. Main Structure

The structural models assumptions limiting the analysis to isotropic materials, non-isotropic materials like unidirectional composites. This limitation can be worked around by assuming quasi-isotropic layup with properties ² shown in Table 7.8. It must be noted however that composite materials are not the favourite option as they are currently not recyclable. In addition to that, validation of the structural model could be done only with aluminium as no study involved other materials. In conclusion, aluminium alloys were the preferred options for the main structure.

There exists a variety of aluminium alloys, all with different mechanical properties. In the aerospace industry, the two most commonly used alloys are the 2024-t6 and 7075 [25] with the 2024-t6 selected for the main structure. The 7075 alloy is mainly used in high-strength applications. The mechanical properties³ of those alloys are shown in Table 7.8.

Table 7.8: Considered materials for structures & landing gear

		Aluminium AA2024-T6	Aluminium AA7075T6	Steel AISI 1025	Titanium Ti-6Al-4V	Quasi-Isotropic Carbon Fibre & Epoxy
Youngs modulus	(GPa)	72.4	71.7	205	113.8	70
Shear modulus	(GPa)	27.0	26.9	80	44	30
Yield strength	(MPa)	315	503	370	880	n.a.
Ultimate tensile strength	(MPa)	415	572	440	950	570
Shear strength	(MPa)	283	331		550	310
Density	(kg/m ³)	2780	2810	7858	4430	1600
Poisson ratio	(-)	0.33	0.33	0.29	0.342	0.1

7.7.2. Propulsion System

For the propulsion system, a specific component requires more attention in the choice of materials. The turbofan, with its high temperature, pressure and rotational speed, requires stronger and more heat resistant materials than aluminium. From [69], a commonly used material for the fan is titanium because of its high strength-to-mass ratio, corrosion and fatigue resistance. From the compressor to the exhaust the temperature increases significantly to 1000°C in the compressor to 1800°C in the combustion chamber. For those very high temperature and high strength applications nickel-based superalloys including some aluminums and titaniums must be used along with cooling techniques.

²URL http://www.performance-composites.com/carbonfibre/mechanicalproperties_2.asp [cited 11 June 2020]

³URL <http://www.matweb.com/search/PropertySearch.aspx> [cited 11 June 2020]

7.8. Compliance and Recommendations

Table 7.9: Summary of the structural design results

	Sheet Thickness (mm)	Spar Thickness (% spar height)	Spars Location (% chord)	Number of Stringers (-)	Stringer Area (mm ²)
Cabin wing	4	0.1	9 ; 69	150	60
Aft wing	3	0.1	25 ; 60	100	60
	Thickness (mm)	Max Stress Skin (MPa)	Max Stress Spar (MPa)	Structural Weight (kg ton)	Material
Pressure vessel	2	53	101	19.0	Aluminium AA2024T6

7.7.3. Other Components

The landing gear is an example of a subsystem which requires higher strength as they are required to sustain the whole take-off weight and the landing loads. Therefore according to [70] the most commonly used alloys in the landing gear subsystem are high-strength steel and titanium alloys.

7.8. Compliance and Recommendations

Considering the sizing process was done on basis of critical load cases flowing from the requirements, requirements **MRA.SYS.STRUCT.1.3**, **MRA.SYS.STRUCT.1.4**, **MRA.SYS.STRUCT.1.5**, **MRA.SYS.STRUCT.1.6**, **MRA.SYS.STRUCT.1.8**, **MRA.SYS.STRUCT.1.9** and **MRA.SYS.STRUCT.1.10** are automatically met. **MRA.SYS.STRUCT.1.1** and **MRA.SYS.STRUCT.1.2** are met as the pressure vessel is designed for those values with a safety factor. **MRA.SYS.STRUCT.1.7** was shown to be met because of the low stress amplitude in the skin sheet, which is caused by the buckling requirement being the most critical design aspect. **MRA.SYS.STRUCT.1.10**, **MRA.SYS.STRUCT.1.11** and **MRA.SYS.STRUCT.1.12** require more detailed design in order to be accurately computed and were therefore considered out of scope.

To conclude on the structural design of the Cryo-V airframe, it is possible to design a structure meeting the set requirement and achieving a reasonable weight. The Flying-V configuration offers significant advantages as the entire weight of the aircraft is distributed along the span which limits the bending moments from lift. This causes the second load case, on the ground at MTOW, to be more critical than in conventional airplanes as in that case the distributed mass will not relieve bending loads. Having a thick airfoil on a large chord length for the cabin wing also implies that this segment is naturally very stiff, therefore thin skin and spars can be used. However using such thin skin sheets on such large cross-section increase the risk for buckling which was shown to be the most critical aspect of the stress sizing. The result of this design is a skin thickness of 4mm for the cabin wing and 3mm for the aft wing, a spar thickness of 0.1% and 0.2% of the spar height respectively, 150 stringers for the cabin wing and 100 stringers for the aft wing. A summary of the results from the structural design is shown in Table 7.9.

Because of the high-level aspect of this structural design, a number of recommendations must be made for further design.

- As shown in the stress distributions in the stress analysis in Subsection 7.6.2, a sudden change in stress magnitude is observed at the junction of the two wings. This is due to the assumption that the wings are considered as beams. In reality there would be a smooth transition between the cabin wing and the aft wing which would smooth the stress curves.
- Because of the wing-beam assumption, the junction of the two wings is not analysed. However this location is important and could sustain significant stresses, it is therefore recommended to expand the analysis including that joint area.
- As no literature on a first order implementation of flutter could be found, this aspect was left out of this analysis. It is nonetheless an important part of safety to not experience excessive flutter during flight, therefore it is recommended to analyse the flutter of this airframe in future studies.
- All airframes include a number of cutouts for doors, windows and hatches. Each cutout is a weak

point in the structure which requires reinforcements which themselves increase the weight. It is recommended to analyse the weight increase due to the different cutouts required.

- As explained in Section 7.5, only few papers dealing with the structural design of a Flying-V aircraft were found, additionally two of those based their analysis on finite element analysis, making the validation of the method inconclusive. It is therefore recommended to reiterate the validation with additional papers or ideally with a physical model when it is available.
- For this design a unique material for the whole structure was assumed for simplicity of computations, it is however not optimal as a combination of different materials and alloys in different parts of the structure could be more efficient. As this method does not allow for multiple materials it is recommended to use a different method allowing multiple materials for future research.
- For the buckling analysis, the crippling stress of stringers was not investigated as they were assumed to be point-areas. It is therefore recommended to perform a more detailed design which would further detail the stringers.
- The assumption that the lift and weight vectors on the cross-section are colinear and going through the shear center can be avoided in future works if more accurate lift distributions and weight distributions are available and using a complete shear flow analysis on the cross-section.
- The natural frequency requirement was not investigated in this analysis, it is however important to make sure that no frequencies emitted by the propulsion system or any other subsystem damages the aircraft. It is therefore recommended to analyse this aspect in future works.



Stability and Controllability Design

"The basic concept of stability is simply that a stable aircraft, when disturbed, tends to return by itself to its original state (pitch, yaw, roll, velocity, etc.)." [25]

The principle of Stability and Controllability (S&C) is one of the fundamental characteristics of an aircraft. Therefore, this chapter presents the analysis of its most important components, including the three main degrees of freedom: longitudinal, lateral and directional. Furthermore, as in this stage of the design accurate data regarding the dynamics and inertia of the aircraft are not accurately defined, the dynamic S&C analysis is left for a later more detailed design stage, and only the static S&C is analysed. The longitudinal and lateral-directional aerodynamics are also assumed to be decoupled.

First the longitudinal S&C is presented in Section 8.1, then the lateral-directional S&C is presented in Section 8.2 and finally, a landing gear is designed for ground stability in Section 8.3.

8.1. Longitudinal Stability and Controllability

This section contains the considerations of S&C in the longitudinal direction, related to pitch movement. Subsection 8.1.1 first analysis the X-plot and Subsection 8.1.2 analysis the elevator design.

8.1.1. X-Plot

The X-plot determines the longitudinal stability of the aircraft. It shows the centre of gravity (CoG) range for which the current configuration is stable.

Functional Analysis - Longitudinal stability is an important factor in aircraft design and significantly influences the platform design. The two main considerations for longitudinal stability are stability and trimmability (controllability).

CS 25.171 General - The aeroplane must be longitudinally, directionally and laterally stable [...]. In addition, suitable stability and control feel is required in any condition normally encountered in service, if flight tests show it is necessary for safe operation.

The stability is mainly governed by stability derivative $C_{M\alpha}$, the change of moment with angle of attack. CS certification - § 25.171 states the stability requirement. This is established by having a $C_{M\alpha} < 0$. A safety margin of 0.05 is considered to ensure stability, thus $C_{M\alpha} < -0.05$. For trimmability moment equilibrium has to be possible for every desired flight phase. The main contributors to longitudinal S&C in conventional aircraft are the tail and elevator. In the Cryo-V the aft wing and elevon will play this role.

Method - In order to determine the longitudinal stability the aircraft is split up in two parts: 1) the fuselage lifting section; 2) the aft-wing lifting section as can be seen in Figure 8.1. This allows the construction of an X-plot with the aft-wing surface area as output. The X-plot plots the area ratio of the two lifting surfaces vs the CoG range of the aircraft and gives a clear overview of if/when the aircraft is longitudinally statically stable. There are two lines in the X-plot: a stability line and a controllability line.

The stability line (Equation 8.1) determines whether $\frac{dC_M}{d\alpha} < -0.05$. The controllability line (Equation 8.2) determines whether it is possible to trim the aircraft.

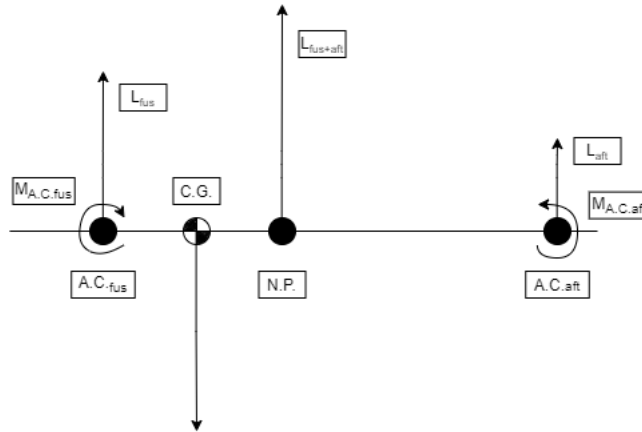


Figure 8.1: Simplified view of the Cryo-V stability centre

Stability

$$\bar{x}_{CoG} = \bar{x}_{ac_{fus}} + \frac{C_{L\alpha_{aft}}}{C_{L\alpha_{fus}}} \left(1 - \frac{d\varepsilon}{d\alpha} \right) \frac{S_{aft}l_{aft}}{S_{fus}\bar{c}} \left(\frac{V_{aft}}{V} \right)^2 - 0.05 \quad (8.1)$$

Controllability

$$\bar{x}_{cg} = \bar{x}_{ac_{fus}} - \frac{C_{m_{acfus+aft}}}{C_{L_{fus}}} + \frac{C_{L_{aft}}}{C_{L_{fus}}} \frac{S_{aft}l_{aft}}{S_{fus}\bar{c}} \left(\frac{V_{aft}}{V} \right)^2 \quad (8.2)$$

The position terms in the equations ($\bar{x}_{...}$) are the x position with respect to the MAC. $S_{...}$, $l_{...}$ and \bar{c} represent the wing area, tail position and MAC chord, respectively. The other parameters are aerodynamic derivatives and coefficients, determined by Chapter 5. The most critical controllability case is the landing configuration, when $C_{L_{fus}} = C_{L_{max}}$. In this case the only true unknown is the $C_{L_{aft}}$, the maximum negative C_L that can be created by the elevator. This is assumed to be -0.8 from control surface design found in Subsection 8.1.2.

Simplifications and Assumptions - All simplifications from Roskam are assumed in this calculation [71]. The main assumption that will have to be taken into account is the assumption displayed by Equation 8.3. The L_{aft} term represents the length between the aerodynamic center (AC) of the fuselage and that of the aft wing. This simplification is based on the AC of the main wing being significantly closer to the center of gravity, thus ignoring this distance for the moment equilibrium in the aft wing. This simplifies the mathematics and makes comparison possible. If the aft wing produces relatively too much lift, this assumption might become invalid. Checks are made to make sure this assumption stays valid.

$$L_{aft} = x_{n.p.} - x_{acwing} \quad (8.3)$$

Final Characteristics - Figure 8.2a shows the final aft wing configuration. The red centre of gravity range line displays the area ratio between aft wing and fuselage wing Sh/S of the Cryo-V and the range for which the aircraft is stable. The feasible design space is the whole area between the Stability and Control lines. The CoG range is found by means of a CoG-plot in Figure 8.2b, which shows the centre of gravity throughout the loading process. For the CoG range a stability margin of 2% is applied. In a traditional aircraft the horizontal stabiliser position and area would be changed to exactly fit the CoG Range in between the Stability and Control lines, to minimise the required horizontal stabiliser area (less mass and drag). However, the Cryo-V aft wing also provides other functions and is required to produce lift during cruise. This makes stability not a critical part of the aft wing. The horizontal red

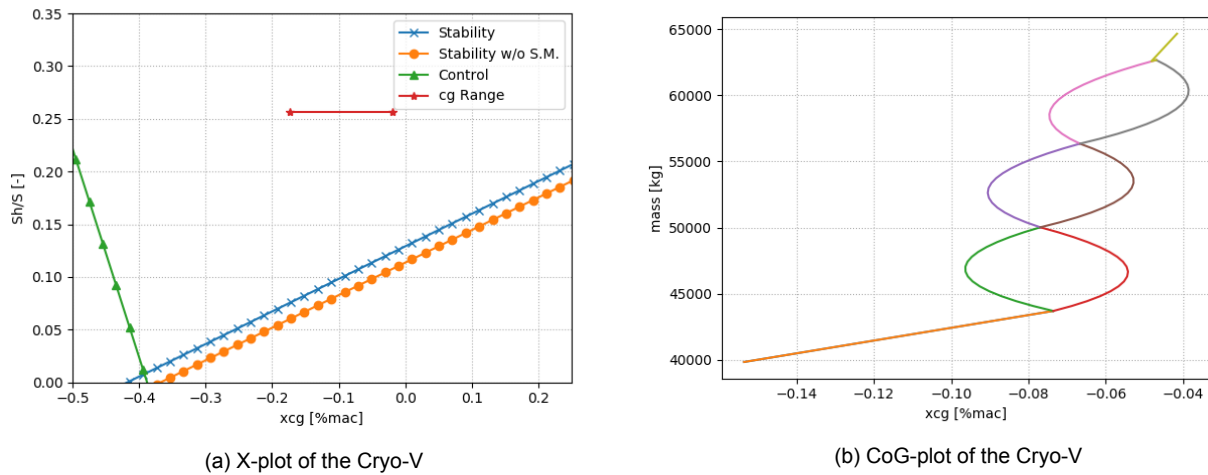


Figure 8.2: X-plot and CoG plot of the Cryo-V

starred line in Figure 8.2a represents the design of the aft wing and shows that it has a large stability margin and easily complies with the requirements.

8.1.2. Elevator Design

Following the longitudinal S&C analysis of the X-Plot, the elevator is analysed to fulfill additional pitch requirements.

Functional Analysis - Longitudinal control is provided by the elevator. This control surface governs **pitch manoeuvres**, including take-off rotation, longitudinal stabilising and initialising climb/descent. Pitch control is achieved by a difference in lift distribution caused by an elevator deflection, resulting in a pitch moment around the Center of Gravity (CoG). Pitch control needs to be effective for **all flight conditions**. Generally, take-off rotation is considered the limiting factor [72] for which the elevator is designed. CS-25 [21] contains a specific requirement regarding the angular take-off rotation acceleration. For the considered aircraft type, this results in a required angular acceleration $\ddot{\theta}_{req}$ of 9 deg/s^2 . Furthermore, the take-off rotation speed V_r is said to be in range of $1.1 - 1.3 V_S$, the stall speed [72], where $1.1 V_S$ is used in this analysis to ensure requirement compliance for all possible take-off rotation speed. An overview of the considered subsystem requirements is shown in Table 8.1.

Table 8.1: Elevator subsystem requirements

Elevator Requirements	
MRA.SYS.S&C.2.1	The elevator shall be designed for take-off rotation conditions.
MRA.SYS.S&C.2.2	The aircraft shall rotate at take-off with an angular acceleration of at least 9 deg/s^2 .
MRA.SYS.S&C.2.3	The elevator shall rotate at take-off with an airspeed of $1.1 V_S$.
MRA.SYS.S&C.2.4	The aft wing containing the elevator shall have a minimum lift coefficient of -0.9.
MRA.SYS.S&C.2.5	The aft wing elevator to chord ratio shall be smaller than 0.5.

Elevator Analysis - The elevator design is done using the method described in [72]. This method calculates the required lift force to be delivered by the part of the wing where the elevator is located, to ensure the required angular pitch acceleration during take-off rotation. This calculation is based on the dynamic moment equation around the Main Landing Gear (MLG) visually shown in Figure 8.3 and described by Equation 8.4,

$$\begin{aligned} \sum M_{MLG} = & -W dx_{MLG,CoG} + D dz_{D,MLG} - T dz_{T,MLG} + L_{f_{rw}} dx_{MLG,ac_{f_{rw}}} + M_{ac_{f_{rw}}} - L_{aft} dx_{ac_{aft},MLG} \\ & + m a dz_{MLG,CoG} = I_{yy_{MLG}} \ddot{\theta}_{req} \end{aligned} \quad (8.4)$$

where W is the MTOW, D the total drag force, T the maximum take-off thrust, $L_{f_{rw}}$ the lift of the fuselage wing, $M_{ac_{f_{rw}}}$ the moment around the aerodynamic center, L_{aft} the lift force of the aft wing, m the MTOW in kg, a the longitudinal acceleration and $I_{yy_{MLG}}$ the lateral moment of inertia (MOI) around the MLG all evaluated right before rotation at take-off. The distances $dx, z_{a,b}$ should be read as being the longitudinal/vertical distance calculated by $x_b, z_b - x_a, z_a$. As the MOI of the aircraft is not known, the lateral MOI of the Airbus A320 is used, equal to 3 092 400 kgm² [73]. As the calculations are checked to not deviate significantly by altering this value, they are considered to be sufficiently accurate for this design stage.

This is considered to be a valid assumption as the calculations are checked to not deviate significantly by altering this value.

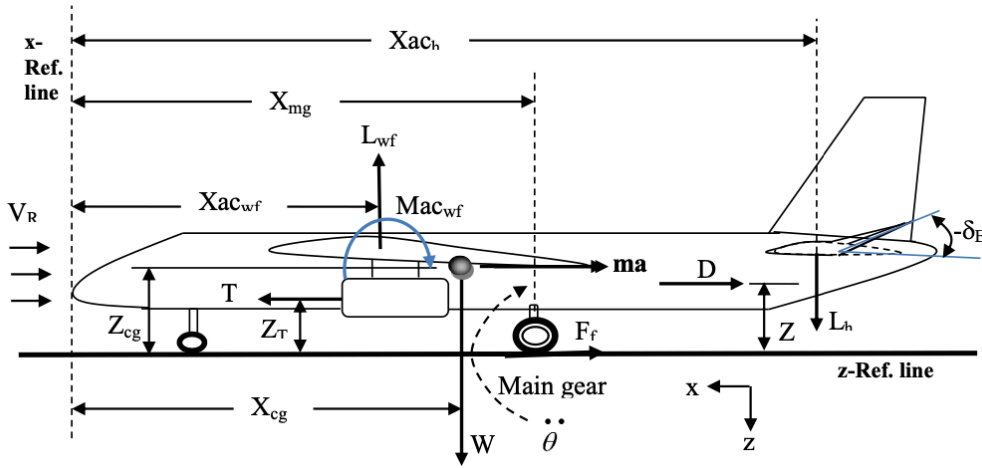


Figure 8.3: Forces and moments during take-off rotation [72]

Furthermore, the longitudinal acceleration a is calculated using Equation 8.5,

$$\sum F_x = T - D - F_f = m a \quad (8.5)$$

where F_f is the friction force calculated by $F_f = \mu N$, with μ being the dynamic friction force coefficient of a concrete surface (equal to 0.04) and N being the normal force on the ground, all evaluated right before rotation.

From the required lift force of the aft wing, the lift coefficient can be calculated using Equation 8.6, where it should be noted that this equation takes into account that the aft wing consists of a part containing the aileron, which has a fixed lift coefficient $C_{L_{aft,ail}}$ and respective wing surface area $S_{aft,ail}$; and the elevator, which has an adjustable lift coefficient $C_{L_{aft,elev}}$ and fixed respective wing surface area $S_{aft,elev}$.

$$C_{L_{aft,elev}} = \frac{2 L_{aft}}{\rho_0 V_r^2 S_{aft,elev}} - C_{L_{aft,ail}} \frac{S_{aft,ail}}{S_{aft,elev}} \quad (8.6)$$

Then, the estimated $C_{L_{aft,elev}}$ is used to find the elevator effectiveness τ_e using Equation 8.7,

$$C_{L_{aft,elev}} = C_{L_{\alpha_{aft}}} (\alpha_{aft} + \tau_e \delta_e) \quad (8.7)$$

$$\alpha_{aft} = \alpha_{LG} + \alpha_t - \epsilon_{aft} \quad (8.8)$$

where $C_{L_{\alpha_{aft}}}$ is the lift curve slope of the aft wing, δ_e the maximum upwards elevator deflection and α_{aft} the AoA of the aft wing calculated using Equation 8.8, where α_{LG} is the AoA of the aircraft due to the landing gear height, α_t the twist angle of the aft wing and ϵ_{aft} the downwash angle at the aft wing, assumed to be zero as stated previously.

Finally, the elevator to wing chord ratio is found using Figure 8.4, where the calculated elevator effectiveness gives the required control surface chord ratio.

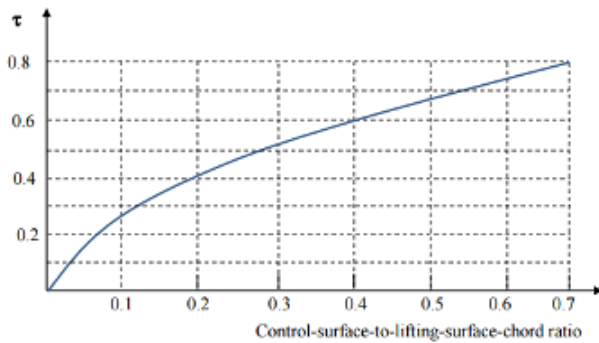


Figure 8.4: Control surface effectiveness graph [72]

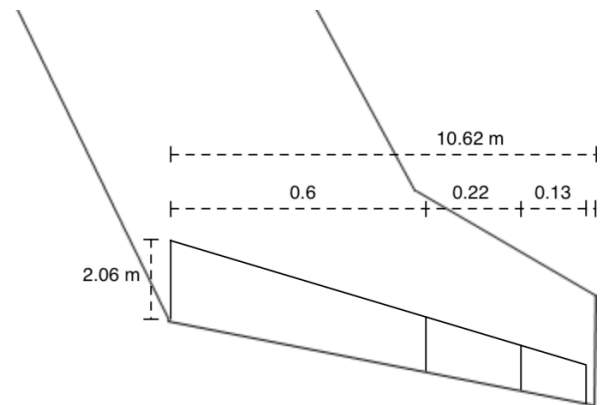


Figure 8.5: Aft wing control surfaces planform

Final Lay-Out and Characteristics - The described calculation method is included in the design integration code, explained in Chapter 4, which results in a final design complying with the elevator control requirements. The final elevator lay-out is visually shown in Figure 8.5, where the elevator spans from 0 to 0.82 fraction of the aft wing half span, corresponding to the left two control surfaces in the figure. Additionally, the elevator to chord ratio equals 0.4, which results in an elevator root chord of 2.06 m. It should be noted that centre control surface acts both as elevator and aileron, known as the elevon. Here, it is assumed that the elevon can be modelled both as an elevator and aileron individually.

Furthermore, Table 8.2 also contains the elevator characteristics, including the minimum lift coefficient for the aft wing containing the elevator and the calculated elevator effectiveness. These parameters are verified and validated in the paragraph below.

Table 8.2: Elevator final characteristics and planform

	Value	Unit		Value	Unit
Planform			Characteristics		
S_e	25.85	m ²	$\ddot{\theta}_{req}$	9	deg/s ²
$b_{/2e}$	8.71	m	$\delta_{e,max}$	-30	deg
c_e/c_{aft}	0.4	—	$C_{L_{aft,min}}$	-0.889	—
$b_{e,start}$	0.0	$b_{/2aft}$ m	μ_e	0.605	—
$b_{e,end}$	0.82	$b_{/2aft}$ m	α_{LG}	4	deg
S_e/S_{aft}	0.365	—	$I_{yy_{LG}}$	3 092 400	kgm ²

Verification and Validation - Before implementing the elevator analysis in the design integration code, it is ensured that the code runs without errors and is verified. As the elevator calculation depends on a large number of detailed parameters, including several force application locations and detailed aerodynamic parameters, using input parameters of another aircraft is not considered feasi-

ble for comparison. Therefore, use is made of an example calculation provided by the used design method [72] that provides all input parameters and the intermediate parameter values for a high-wing twin jet engine light utility aircraft. As this method is presented by a widely acknowledged aircraft systems design book, the example calculations are considered valid. By using the same input parameters, it is ensured that the main equations are implemented correctly. As the aft wing of the Cryo-V contains both the elevator and aileron, instead of just the elevator, Equation 8.6 differs from the method described in [72]. Therefore, this specific step is calculated by hand and checked for the output value of the code to be correct.

After implementing the elevator analysis in the design integration code, all input parameters for the elevator calculations are checked with the corresponding department to prevent parameter misconceptions. This includes communication with the aerodynamic department concerning wing planform and aerodynamic characteristics, structures and S&C department concerning the CoG location and propulsion department concerning the thrust.

Finally, the calculated elevator planform and characteristics are compared to the Airbus A320, shown in Table 8.3. It can be seen that no significant differences are present, resulting in the elevator analysis to be considered validated. Furthermore, it should be noticed that the minimum aft wing lift coefficient of the part containing the elevator equals -0.889, which is considerably smaller than -0.4, stated in [74] to be assumed for a conventional aircraft with a fixed tail. However, due to the absence of the significant downwash of the main wing, in combination with a downwards twist angle of 9.43 degrees, this minimum lift coefficient is considered acceptable. It should also be noted that the tail volume coefficient is significantly smaller than for conventional aircraft, caused by the Flying-V shape. This results in the need of larger control surfaces, which is also seen as a result compared to the Cryo-V, where both the chord ratio and aft wing surface area ratio increased.

Table 8.3: Validation of the elevator analysis compared to the Airbus A320

		A320	Cryo-V
Longitudinal Control Derivative [73]			
$C_{L\delta_e}$	(rad ⁻¹)	0.2297	0.40
Elevator Planform [72] ¹			
$\delta_{e_{max}}$	(deg)	-30	-30
S_e/S_{aft}	(-)	0.31	0.365
S_e/S_{ref}	(-)	0.078	0.074
c_e/c_{aft}	(-)	0.32	0.4
Tail volume coefficient	(-)	0.799	0.322

8.2. Lateral-Directional Stability and Controllability

This section contains the S&C in the lateral-directional direction, related to roll and yaw movement respectively. Subsection 8.2.1 first presents the aileron design method; Subsection 8.2.2 presents the vertical tail design method; and finally, Subsection 8.2.3 presents the rudder design method.

8.2.1. Aileron Design

Located next to the elevator is the aileron which is analysed to fulfill the roll requirements.

Functional Analysis - Lateral control is provided by the aileron. This control surface governs **roll manoeuvres**, which is achieved by a net pressure difference on the wing creating a roll moment L^* by deflecting the control surfaces located on both sides of the wing in opposite direction. Example

¹URL <https://booksite.elsevier.com/9780340741528/appendices/data-a/default.htm> [cited 20 June 2020]

of roll manoeuvres are coordinated, steady turns, crosswind landings (combined with rudder control) and spin recovery [72].

Roll control needs to be effective for **all flight conditions** and is generally designed for a steady roll rate P considering approach conditions [72]. This steady roll rate is taken from CS-25 [21] to be 30 degrees in 1.7 seconds. An overview of the considered subsystem requirements is shown in Table 8.4.

Table 8.4: Aileron subsystem requirements

Aileron Requirements	
MRA.SYS.S&C.3.1	The aileron shall be designed for approach conditions.
MRA.SYS.S&C.3.2	The aircraft shall have a steady state roll rate of at least 17.65 deg/s during approach.
MRA.SYS.S&C.3.3	The aft wing aileron to chord ratio shall be smaller than 0.5.

Aileron Analysis - The aileron design is performed using the method and equations described in [75] and [72], where the latter contains an example calculation. The roll control analysis is based on two phenomena: 1. roll rate and 2. roll damping.

The pressure differences resulting from deflecting the ailerons are caused by a change in local AoA. This effect increases when the aileron chord to wing chord ratio increases, which is captured by the aileron effectiveness τ in Figure 8.4, where its value is found for the used aileron to chord ratio. This pressure difference can be transferred to a rolling moment, of which the rolling moment coefficient $C_{L_{\delta a}^*}$ is expressed by Equation 8.9,

$$C_{L_{\delta a}^*} = \frac{2 C_{L_{\alpha}} \tau_a}{S_{ref} b} \int_{b_1}^{b_2} c(y) y dy \quad (8.9)$$

where the integration runs from the start of the aileron b_1 to the end of the aileron b_2 , $C_{L_{\alpha}}$ is the lift curve slope of the wing the ailerons are located on and $c(y)$ is the wing chord as a function of the spanwise location y .

For this integration, use is made of Equation 8.10, which describes the chordwise function of a conventional wing, that is rewritten to Equation 8.11, to allow wing segments that start at a spanwise location b_i not equal to zero to be analysed.

$$c(y) = c_r \left(1 + \left(\frac{\lambda - 1}{b/2} \right) y \right) \quad (8.10)$$

$$c(y) = c_r \left(1 + \left(\frac{\lambda - 1}{b^*/2} \right) (y - b_i) \right) \quad (8.11)$$

Due to the created roll rate, the aircraft experiences roll damping which is caused by a change in AoA due to the upwards and downwards motion of the wing. The roll damping coefficient $C_{L_P^*}$ is expressed by Equation 8.12, where the integration runs over the entire wing span. This results in the need of two separate integrations accounting for the different geometry and aerodynamic characteristics, as can be seen below.

$$\begin{aligned} C_{L_P^*} &= -\frac{4 (C_{L_{\alpha}} + C_{D_0})}{S_{ref} b^2} \int_0^{b/2} y^2 c(y) dy \\ &= -\frac{4}{S_{ref} b^2} \left[(C_{L_{\alpha}} + C_{D_0})_{frw} \int_0^{b/2, frw} y^2 c(y) dy + (C_{L_{\alpha}} + C_{D_0})_{aft} \int_{b/2, frw}^{b/2} y^2 c(y) dy \right] \end{aligned} \quad (8.12)$$

In above equation, $C_{L\alpha}$ is the lift curve slope and C_{D_0} the zero lift drag coefficient of the evaluated wing. Again use can be made of both equations Equation 8.10 for the first integration and Equation 8.11 for the second integration to calculate $C_{L_p^*}$.

Finally, the required steady state roll is calculated using Equation 8.13,

$$P = -\frac{C_{L\delta_a^*}}{C_{L_p^*}} \delta_a \left(\frac{2 V_{appr}}{b} \right) \tag{8.13}$$

where δ_a is the maximum aileron deflection and V_{appr} the approach speed.

Final Lay-Out and Characteristics - Above calculations are integrated in the design integration code, ensuring compliance with the aileron requirements. The final aileron lay-out is shown in Figure 8.5, including also the elevator. The aileron spans from 0.6 to 0.95 of the aft wing half span and has an aileron to chord ratio of 0.4, similar to the ratio of the elevator. It should be noted that the required chord ratio to fulfill the requirement is 0.23, however, as the control surfaces are connected to the rear spar of the aft wing the same chord ratio is used as required for the elevator resulting in better roll characteristics than required.

The part of the elevator and aileron that overlap is called the elevon, being the center control surface.

Finally Table 8.5 includes the characteristics, including the maximum aileron deflection and calculated roll moment coefficients, which are next verified and validated.

Table 8.5: Aileron final characteristics and planform

	Value	Unit		Value	Unit
Planform			Characteristics		
S_a	7.186	m ²	P	17.65	deg/s
$b_{/2a}$	3.72	m	$\delta_{a_{max}}$	25	deg
c_a/c_{aft}	0.4	—	τ_a	0.460	—
$b_{a,start}$	0.60	$b_{/2aft}$ m	$C_{L\delta_a^*}$	0.024	—
$b_{a,end}$	0.95	$b_{/2aft}$ m	$C_{L_p^*}$	-0.135	—
S_a/S_{aft}	0.100	—			

Verification and Validation - The same procedure is followed for the aileron verification and validation as for the elevator. Again, an example calculation is provided by the used method [72], giving all necessary input parameters for a land-based military transport aircraft and the calculated intermediate parameters. The calculations are implemented and checked using the example to make sure no mistakes are present. As the aileron is generally located on the main wing several modifications are necessary to the code to enable the evaluation of an aileron that is located on an aft wing, next to the elevator. This modification is performed by manually evaluating the integrals present in Equation 8.9 and 8.12 several times, to ensure no mistakes remain.

After implementing the aileron analysis in the main code it is ensured that all input parameters are consistent by communication with the respective departments. This step is less involved as with the elevator analysis as it only depends on aerodynamic and wing parameters.

Finally, the output values for the final design are compared to the Fokker 100A, Boeing 777-200 and the Airbus A320, shown in Table 8.6. It can be seen that no major differences exist resulting in the aileron analysis to be considered validated.

8.2. Lateral-Directional Stability and Controllability

Table 8.6: Validation of the aileron analysis compared to the Fokker 100A, Boeing 777-200 and the Airbus A320

	Fokker 100A	Boeing 777	A320	Cryo-V
Lateral Control Derivative [73]				
$C_{L\delta_a}$ (rad ⁻¹)	-	-	0.1127	0.164
Elevator Planform [72]				
$\delta_{a_{max}}$ (deg)	25	20	-	25
c_a/c_{aft} (-)	0.24	0.22	-	0.23

8.2.2. Vertical Tail Design

The vertical tail is indispensable in balancing any yaw moment. The most critical yaw moment should be considered for the vertical tail sizing. Logically, the required tail size should be determined for all manoeuvres and load cases ; the tail size for the most critical situation is chosen.

Functional Analysis - There are four main aspects to take into account: Crosswind, directional stability, engine failure and spin recovery.

Crosswind:

§25.237 "Wind velocities"- For landplanes and amphibians, a 90-degree cross component of wind velocity, demonstrated to be safe for take-off and landing, must be established for dry runways and must be at least 20 knots or 0.2 V_S .

The main design parameter for crosswind is the ability of the rudder to put the aircraft in the direction of the crosswind (crabbing) and back in line with the runway after drifting in the direction of the wind for a while. These considerations are treated in the rudder design section.

Engine Failure:

The requirement of the vertical tail sizing regarding an engine failure is as follows: The vertical tail shall provide lateral stability in case of engine failure at take-off. From JAR25:

25.147(a) It must be possible, with the wings level, to yaw into the operative engine and to safely make a reasonably sudden change in heading of up to 15° in the direction of the critical inoperative engine.

Lateral-Directional Stability:

Lateral-Directional Stability assures the aircraft returns to its original position when the equilibrium state is disturbed. This results in the requirement that $C_{n_{Beta}} > 0.0571 \text{ rad}^{-1}$, which represents yaw stability [76]. Roll stability should also be obtained ($C_{l_{Beta}} < 0$), but this is more influenced by the dihedral angle of the wing than the vertical tail [76].

Stall Recovery:

Stall recovery is traditionally more important for the design of smaller, general aviation aircraft than for larger commercial aircraft; for large aircraft the emphasis is more on avoiding stall. There are no EASA requirements regarding spin recovery for large commercial airliners. Furthermore, estimating Vertical tail and rudder requirements for stall recovery is considered to be out of scope for this design phase. Detailed estimates of the moments of inertia of the aircraft and estimates of the wake region during stall are required. Both of these elements aren't present at this phase. Therefore the rudder design might change when this mode is analysed.

Yaw Derivative With Respect to Sideslip Angle - The first step in vertical tail design is to determine stability coefficient C_{n_B} as this plays a role in all situations. Determination of C_{n_B} is complicated considering the unconventional form of the aircraft. Raymer gives multiple semi analytical and empirical relationships but they are valid for traditional fuselages and wings. Determining this coefficient through thorough analysis is relatively difficult and considered outside the scope of this project. As

no relevant estimation techniques could be found, Raymer’s formulas will be used, adding a safety margin of 1.2. Equation 8.14 estimates the $C_{n\beta}$ of the wing and Equation 8.15 estimates $C_{n\beta}$ of the fuselage. These two added together form $C_{n\beta_{A-h}}$ as portrayed in Equation 8.16.

$$C_{n\beta_w} = C_L^2 \left\{ \frac{1}{4\pi A} - \left[\frac{\tan \Lambda}{\pi A(A + 4 \cos \Lambda)} \right] \times \left[\cos \Lambda - \frac{A}{2} - \frac{A^2}{8 \cos \Lambda} + \frac{6(\bar{X}_{acw} - \bar{X}_{CoG}) \sin \Lambda}{A} \right] \right\} \quad (8.14)$$

$$C_{n\beta_{fus}} = -1.3 \frac{V_{fus}}{S_w b} \left(\frac{L_f}{W_f} \right) \quad (8.15)$$

Vertical Tail Design Method - The vertical is the most elemental aspect in lateral stability.

Engine failure:

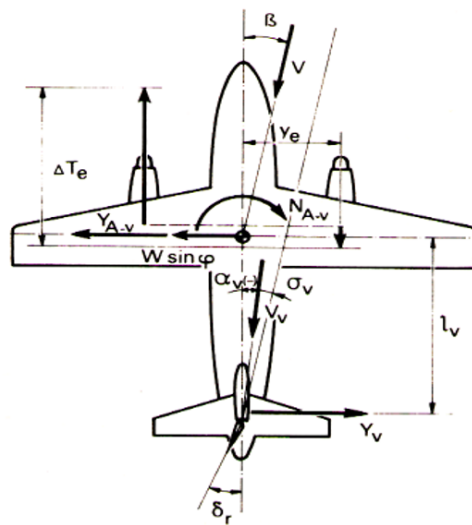


Figure 8.6: Free Body Diagram of an Aircraft with Engine Failure ⁴

$$n_v C_{y\beta_v} \left(\frac{S_v}{S} \right) = \frac{C_L \frac{y_e \Delta T_e}{l_v W} + \beta (C_{n\beta})_{A-h} \frac{b}{l_v}}{\tau_v \delta_r - (\beta - \sigma_v)} \quad (8.16)$$

In case of engine failure a yaw moment is created. Using Roskam’s method [71] it can be shown that moment equilibrium leads to equation 8.16 (Figure 8.6 ²). η_v is the dynamic pressure ratio, $C_{y\beta}$ is the lift curve slope of the vertical tail. y_e represents the moment arm of the engine, ΔT_e the force difference between both engines (thrust of operating+drag of failed engine). β is the sideslip angle, which in this case is 15 degrees due to CS requirement 25.147(a). The unknowns in this equation are the rudder parameters (T_v and δr) and σ_v . T_v and δr are treated in the rudder section. σ_v (crab angle) can be assumed to be 0 as the vertical tail is outside the wake of the aircraft, hence no interference is assumed to happen. From this equation the required vertical tail area S for engine failure can be determined.

For the Cryo-V in particular a complete engine failure of one side will be considered: a case when the main turbofan and all 4 distributed engines fail. The moment arm is y_e is determined by means of waited averages. However, such situation when all engines on one side fail is extremely unlikely since each electric fan is driven by a separate motor. Nonetheless, the most critical situation must be analysed.

²URL <https://brightspace.tudelft.nl/d21/1e/content/213478/viewContent/1474638/View>

Static Lateral-Directional Stability:

$$\frac{S_V}{S_W} = \frac{C_{N,\beta_{req}} - C_{N,\beta,F}}{-C_{Y,\beta,V}} \cdot \frac{b_W}{l_V} \tag{8.17}$$

Equation 8.17 represents the worked out form of the $C_{n_\beta} > 0.0571 \text{ rad}^{-1}$ requirement. It splits up $C_{n_{Beta}}$ in a fuselage/wing part ($C_{N,\beta,F}$) and the vertical tail contribution ($-C_{Y,\beta,V} \cdot \frac{l_V}{b_W} \cdot \frac{S_V}{S} = C_{n_{\beta_{vert.tail}}}$). The vertical tail area can now be determined.

Dynamic Lateral-Directional Stability:

Long vertical tails increase the later-directional coupling. Multiple shorter fins could be convenient in this respect. Cryo-V has relatively little lateral directional coupling because of reason.

Verification and Validation - It is important to verify and validate the calculation models used. Unit tests are performed to make sure the code has a correct output regarding the use of formulas. For certain values the code equations are manually computed and compared to code output. Verifying the code as a whole is more difficult since very little information is available on specific stability and control derivatives of existing aircraft. Hence, to validate the models, A320 and B777 parameters will be used as input and the tail surfaces will be compared ^{3 4 5}.

For the horizontal stabilizer, as the formulae are based on the Bachelor course of "Systems Engineering and Aerospace Design" ⁶, a worked out example for a conventional aircraft is used as verification of the code. The input values from this problem are used to generate the X-plot. Both plots showed the same results. ⁷.

Table 8.7: Vertical tail computation V&V using the Airbus A320 and Boeing 777 aircraft

		A320		B777		Difference
		computed	actual	computed	actual	
S_{aft}	(m ²)	29.35	31	-	-	-5.32%
$C_{N\beta}$	(-)	-0.76	-	-0.224	-	-
$S_{vert, \text{ stability}}$	(m ²)	25.86	21.50	57.49	53.23	14.14%
$S_{vert, \text{ engine failure}}$	(m ²)	35.21	21.50	49.71	53.23	28.57%

For both comparisons the aircraft is assumed to have a BAC 449 airfoil, which is the 737's root airfoil ⁸. No actual airfoils could be found. Deviations were expected due to the preliminary way of estimating C_{n_B} . Deviations can also partly be explained by the high level of uncertainty of A320 and B777 input data, as aerodynamic parameters had to be estimated (like the airfoil characteristics).

The horizontal stabilizer design code converges. This design process is also simpler than lateral stability design, hence this was expected. Uncertainties for the B777 were too high to make a fair assessment for this aircraft. The vertical tail area for both failure modes diverge more but that was expected.

Overall, the code seems to give a realistic, yet varying estimation of the tail area. As there are significant uncertainties in the validation data, it is hard to provide an accuracy level of the code, however

³URL <https://booksite.elsevier.com/9780340741528/appendices/data-a/table-4/table.htm> [cited 16 June 2020]

⁴URL <https://booksite.elsevier.com/9780340741528/appendices/data-a/table-1/table.htm> [cited 16 June 2020]

⁵URL <https://m-selig.ae.illinois.edu/ads/aircraft.html> [cited 16 June 2020]

⁶URL <https://brightspace.tudelft.nl/d21/1e/content/213478/viewContent/1474638/View> [cited 22 June 2020]

⁷URL <https://brightspace.tudelft.nl/d21/1e/content/213478/viewContent/1474579/View> [cited 16 June 2020]

⁸URL <https://m-selig.ae.illinois.edu/ads/aircraft.html> [cited 16 June 2020]

it can be used as a first order vertical tail estimate. A safety margin will be used as some parts of the code are shown to underestimate the required area.

8.2.3. Rudder Design

The rudder is a critical element in yaw control. It allows the pilot to control yaw motion and guarantee flight safety.

Functional Analysis - An initial rudder estimation is made in the engine failure lateral stability section as shown in Subsection 8.2.2. It now has to be checked whether this rudder can also provide equilibrium in crosswind conditions. The requirements for crosswind are treated in Subsection 8.2.2. Another function of the rudder is to enable a coordinated turn, but this is rarely critical for the design and is assumed to be able to perform this task at this design stage[72].

Method - To calculate the rudder requirement for crosswind first the sideslip angle has to be calculated. This is the resulting vector from aircraft speed V and crosswind U_1 .

$$\beta = \tan^{-1}\left(\frac{V}{U_1}\right) \quad (8.18)$$

In case of crosswind, moment equilibrium has to be obtained to keep the aircraft "in the wind". This is described by equation 8.19 and 8.20, being moment equilibrium in x and y directions, respectively. The two unknowns in the equation are sigma (see Figure 8.6 and the elevator deflection).

$$\frac{1}{2}\rho V_T^2 S b \left(C_{n_o} + C_{n_\beta}(\beta - \sigma) + C_{N_{\square R}} \delta_R \right) + F_w \cdot d_c \cos \sigma = 0 \quad (8.19)$$

$$\frac{1}{2}\rho V_w^2 S_S C_{D_y} - \frac{1}{2}\rho V_T^2 S \left(C_{y_o} + C_{y_\beta}(\beta - \sigma) + C_{y_{\square R}} \delta_R \right) = 0 \quad (8.20)$$

C_{D_y} represents the aircraft side drag coefficient, which is determined from literature. C_{n_β} is estimated by the method described in C_{n_β} and C_{y_β} is estimated according to equation 8.21. Here K_{12} is a constant dependent on aircraft type. F_w represents the force generated by the crosswind (Equation 8.22). $C_{y_{\delta R}}$ and $C_{n_{\delta R}}$ are the aerodynamic coefficients of the rudder determined by equations 8.23 and 8.24), where \bar{V} is the tail volume coefficient.

$$C_{y_\beta} = K_{12} C_{L_{av}} \left(1 - \frac{d\sigma}{d\beta} \right) \eta_V \frac{S_V}{S} \quad (8.21)$$

$$F_w = \frac{1}{2}\rho V_w^2 S_S C_{D_y} \quad (8.22)$$

$$C_{y_{\delta R}} = C_{L_{av}} \eta_V \tau_r \frac{b_R}{b_V} \frac{S_V}{S} \quad (8.23)$$

$$C_{n_{\delta R}} = -C_{L_{av}} \bar{V}_V \eta_V \tau_r \frac{b_R}{b_V} \quad (8.24)$$

The required rudder deflection is now computed and compared to maximum set value of 30 degrees. If the rudder is not feasible τ_r , the rudder effectiveness will be changed to fit the requirements. τ_r influences the part of the vertical tail that is used for the rudder (control surface to lifting surface chord ratio).

Verification - The rudder code is verified alongside the Verification and Validation procedures for the vertical tail. The control surface to lifting surface chord ratio output of the code is compared to an estimation of this ratio of the specific aircraft. For both aircraft the ratio is estimated within 0.1 of the actual ratio.

Final Lay-Out and Characteristics - The directional stability calculations show the engine failure case is critical. The resulting required vertical tail area is shown in Figure 8.7.

8.3. Landing Gear Design

This area is divided by two, because there are two winglets at the edges of both aft wings. Therefore, each winglet/vertical tail has an area of 18.45 m². A sweep angle of 30 degrees is applied in the iteration to delay flow separation. The aspect ratio of the vertical tail is 3, which is quite high for a vertical tail. Such high aspect ratio is implemented to minimise the aft wing area, on which the winglet has to be placed. To compensate for large tail height, a relatively thick NACA0016 airfoil is chosen, which has better stall characteristics than more traditional thin vertical tail airfoils and has a critical Mach number around the cruise Mach number. No taper ratio is used, this could be improved in the next design phase.

The required elevator effectiveness, τ_v , is 0.4 for the most critical case. This leads to a control surface to lifting surface chord ratio of 0.2; 20% of the vertical tail chord will be used for the rudder.

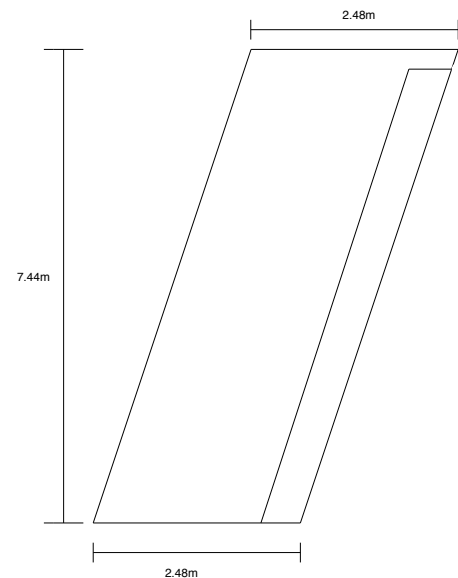


Figure 8.7: Vertical tail final dimensions

8.3. Landing Gear Design

In order to support the aircraft weight on the ground, absorb landing loads and provide stability on the ground, the Cryo-V must be equipped with landing gear. This section presents the functions performed by the landing gear, the selection of the tires, the positioning of the struts and finally verification and validation of the presented method.

8.3.1. Functional Analysis

The purpose of the landing gear is supporting the weight of the aircraft on the ground so the aircraft is capable of loading, ground manoeuvring like taxiing and take-off without any external structural support. The landing gear also prevents damage to the aircraft when a load is applied, for example cargo loading and touch-down during landing. The landing gear subsystem functions are explained and listed below, followed by a list of requirements in Table 8.8.

1. **Ground support** The landing gear shall be able to support at least the MTOW of the aircraft.
2. **Manoeuvring ability** The landing gear shall allow the aircraft to manoeuvre on the ground, including taxiing and towing.
3. **Shock absorption** The landing gear shall be able to absorb the shock during landing without any damage to itself and other parts of the aircraft.
4. **Protect the ground surface** The landing gear shall protect the ground surface.

Table 8.8: Landing gear subsystem requirements

Performance Requirements	
MRA.SYS.LG.1.1	The landing gear shall be able to support at least 64660 kg
MRA.SYS.LG.1.1	The landing gear shall provide mobility for the aircraft on the ground.
MRA.SYS.LG.1.1	The landing gear shall be able to absorb 306,000 J of kinetic energy.
MRA.SYS.LG.1.1	The landing gear shall protect the runway and taxiway with LCN = 50.
MRA.SYS.LG.1.1	The landing gear shall be able to retract into the airframe.
MRA.SYS.LG.1.1	The landing gear shall ensure the aircraft is stable during loading and turning.

8.3.2. Assumptions

Some assumptions are made during calculations:

1. **Number of nose wheels is 2** The number of nose wheels is assumed to be 2, as the Cryo-V is a narrow-body aircraft and most narrow-body aircraft are using two nose tires.
2. **Load fraction on nose gear is 15%** The nose gear is assumed to carry 15% of the take-off weight. The load fraction on nose gear (lf_{nlg}) is usually between 8% to 15% [31]. Due to the Flying-V configuration, the CoG location is more forward than in conventional aircraft, thus a larger number is assumed.
3. **Main landing gear absorbs the entire touch-down kinetic energy** It is assumed that the entire touch down kinetic energy is absorbed by the main landing gears. This is a conservative assumption as nose gear may also absorb some kinetic energy but it provides an extra safety margin to the landing gear design.
4. **The maximum rotation angle during take-off is 15 deg** The maximum value for pitch angle during take-off is assumed to be 15 deg [31].

8.3.3. Landing Gear Properties

Cryo-V is a medium range aircraft with a cruise speed of Mach 0.78. The retractable landing gear design is chosen, as the aerodynamic penalty for a non-retractable gear is greater than weight increment by a retractable gear due to aerodynamic losses. A tri-cycle arrangement is used as it is simple, reliable and widely used.

Tire Selection - As the number of nose tires is assumed to be 2, the number of main tires can be determined by Equation 8.25 as Cryo-V is a commercial aircraft [31].

$$N_{mw} = MLW/210,000 \quad (8.25)$$

where MLW is the maximum landing weight. N_{mw} is rounded to the nearest multiple of 4 with a minimum of 4. With the numbers of tires and load on each gear, the static load applied to each tire in kg can be calculated:

$$p_{nw} = MTOW \cdot lf_{nlg}/N_{nw} \quad (8.26)$$

$$p_{mw} = MTOW \cdot (1 - lf_{nlg})/N_{mw} \quad (8.27)$$

As the Cryo-V should be able to access all the airports that A320 can, the Load Classification Number (LCN), which determines the pressure on the tarmac, is chosen to be 50. The tire pressure can be obtained from Figure 8.8, which is about 12 kg/cm². From Figure 8.9, several tires can be selected based on the static load applied to the tire.

Shock Absorber - The landing gear is supposed to absorb the kinetic energy vertically. Total vertical kinetic energy can be calculated by Equation 8.28. The energy absorbed by the landing gear absorber is defined by Equation 8.29 [12]:

$$E_t = 0.5 W_L/g \cdot w_t^2 \quad (8.28)$$

$$E_t = N_{mw} P_m N_g (\eta_t s_t + \eta_s s_s) \quad (8.29)$$

Where p_m is the maximum static load per tire, N_g is the Landing gear load factor which is 1.5 according to FAR 25 [12]. η_t and η_s are the energy absorption efficiency for tire and absorber, respectively. $\eta_t = 0.47$ and $\eta_s = 0.80$ for the oleo-pneumatic absorber which is used on A320. s_t is the maximum

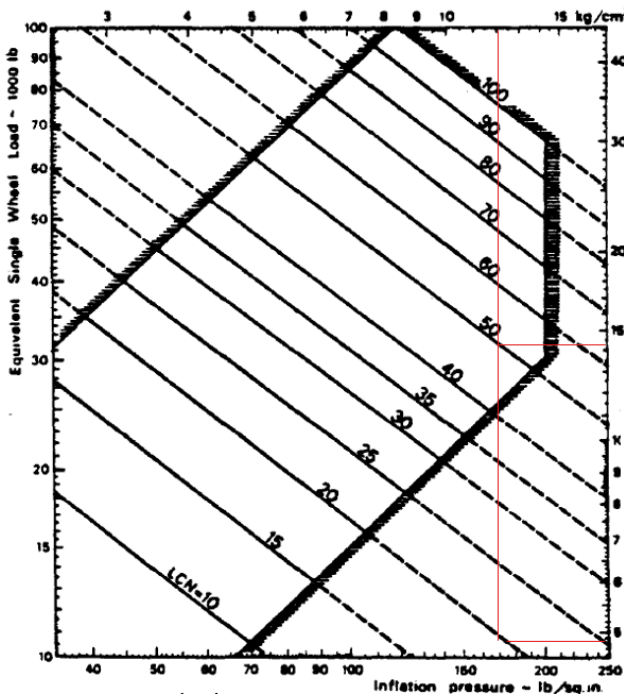


Figure 8.8: Tire pressure

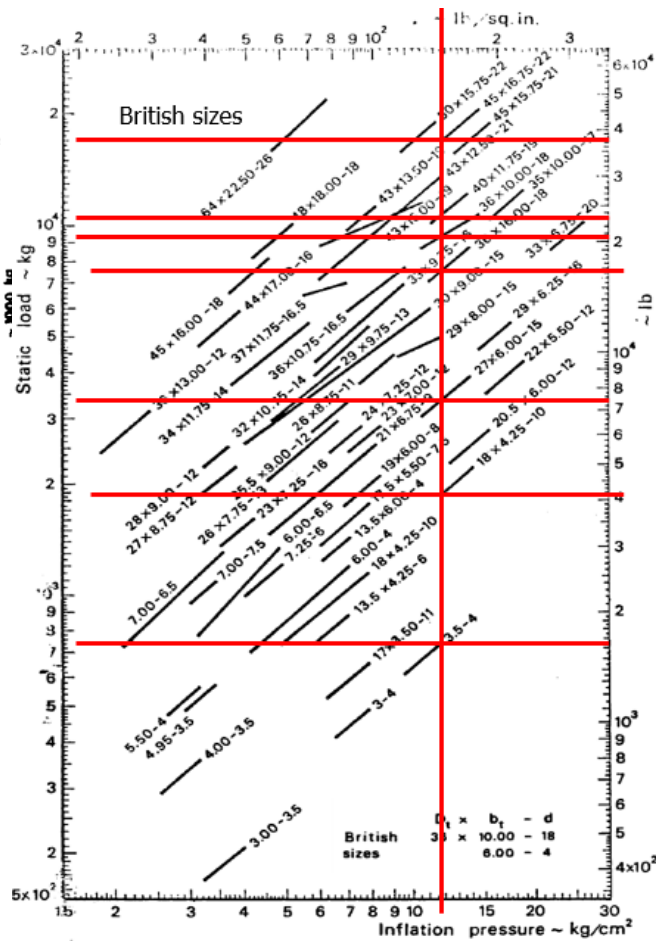


Figure 8.9: British tire dimensions

allowable tire deflection determined by Equation 8.30, where D is the outer diameter and LR is the Loaded Radius, which is given by the selected tire.

$$s_t = (D - 2 * LR) / 12 \tag{8.30}$$

With all the values in Equation 8.29, the length of the absorber can be calculated with one additional inch added as safety margin [12]. The diameter of the oleo-pneumatic absorber can be estimated by the following equation:

$$d_s = 0.041 + 0.0025(P_m)^{0.5} \tag{8.31}$$

The same type of absorber will be used for the nose landing gear to save on maintenance costs. A strut is added to the main landing gear to prevent damage from longitudinal loads, like friction, and it also works as the retracting mechanism. For the nose landing gear, the concerning load will be in lateral direction as there is only one nose gear.

8.3.4. Landing Gear Position

The most important function of the landing gear is supporting the aircraft. The aircraft will perform loading, turning and other manoeuvring acts on the ground. There are several scenarios that should be taken into the consideration for landing gear positions to ensure the aircraft is stable in all conditions.

Longitudinal Tip-Back - During take-off, the aircraft will rotate nose up and tail down. The CoG location will shift aft. If the CoG location shifts longitudinally behind the main gear, the aircraft will tip back. To prevent this, the angle between the line passing through CoG. and main landing gear and the

vertical line through main landing gear should be larger than 15 deg. This leads to a minimum value of the longitudinal position of the main landing gear. Due to the elevator sizing in Subsection 8.1.2, the maximum value is also known. After the main landing gear position is known, the nose landing gear position can be calculated with $l_{f_{nlg}}$ and the balance of the aircraft which means the moments generated by supporting forces from nose and main landing gear are zero around the CoG.

The storage of landing gear is also important for aerodynamic performance. The landing gears are retracted into the trailing edge of the cabin wing. The main landing gear span will be lower than the nose gear and satisfies the airport operation requirements in Section 11.1. Therefore, the lateral position of the main landing gear (y_{mlg}) is related to the longitudinal position (x_{mlg}).

Lateral Tip-Over - To avoid tip-over due to CoG lateral movement during ground turning, the span between two main landing gear should be large enough to keep the CoG in between. This gives a minimum value of the lateral position of the main landing gear, which can be calculated by Equation 8.32 with a minimum value of $\Psi = 55$ deg. In the equation, the l_n and l_m are the longitudinal distance of nose and main landing gear to the nose tip at cockpit. And h_{cg} is the height of the CoG to the ground.

$$y_{mlg} > \frac{l_n + l_m}{\sqrt{\frac{l_n^2 \tan^2 \Psi}{h_{cg}^2} - 1}} \quad (8.32)$$

h_{cg} is the sum of aircraft CoG to the bottom skin of the cabin wing and height of landing gear. The maximum rotation angle is 15 deg, so the main landing gear should be high enough to avoid the tail wing scraping the runway. With the total aircraft length (L_{ac}) and the main landing gear position, the height of the main landing gear can be calculated. As for the nose landing gear, it should be taller than the main landing gear as the aircraft should have a pitch angle for take-off mentioned in Subsection 8.1.2. The length of nose landing gear can be computed with position main landing gear and the ground pitch angle requirement due to the take-off requirement.

8.3.5. Final Design of the Landing Gear

With all the calculations and assumptions made, the landing gear subsystem is determined and shown in Table 8.9:

Table 8.9: Landing gear subsystem final values

		Nose Landing Gear	Main Landing Gear
Height	(m)	2.80	2.30
Longitudinal position	(m)	9.03	15.55
Lateral position	(m)	0	3.46
Tires			
Nr. of tires	(-)	2	4
Outer diameter	(m)	0.91	1.14
Inner diameter	(m)	0.46	0.56
Width	(m)	0.41	0.43
Absorber			
Length	(-)	0.30	0.43
Diameter	(m)	0.14	0.14

8.3.6. Verification and Validation

For verification and validation of the landing gear subsystem, first code unit tests are performed. As most of those are calculations with formulas, it is verified by comparing the function outputs and manual calculation in Excel. After unit tests, subsystems test are done by comparing data computed by the code with A320 inputs and actual data. For example, the landing gear position test comparisons are shown in Table 8.10. The results are slightly different due to the different $l_{f_{nlg}}$ used.

Table 8.10: System test: A320 actual landing gear positions and computed positions

		A320	Code Results	
			$l_{g_{nlg}} = 8\%$	$l_{g_{nlg}} = 15\%$
x_{nlg}	(m)	5.07	5.30	6.41
x_{mlg}	(m)	17.71	17.63	17.33
y_{mlg}	(m)	3.80	3.72	4.22

Validation is done by manual drawing and data comparison, as the Flying-V configuration is relatively new. The tire selected is manually compared with other aircraft, which have a similar MTOW. As for gears positions, they are validated by manual drawings conforming the possibility of the shape and the outcome of calculations.

8.4. Recommendations

As stated in the introduction of this chapter, dynamic S&C is not considered in this analysis. Phugoid motions, short period oscillations and Dutch roll are all examples of important dynamic stability characteristics. However, to analyse these stability modes, the moment of inertia and (especially for Dutch Roll) all stability derivatives have to be known. There is a large uncertainty in estimating stability derivatives, even more so for unconventional aircraft, and an accurate moment of inertia is not computed in this design stage. Therefore, the computation of these parameters and the subsequent dynamic S&C analysis is left for the next design stage.

For lateral stability it is recommended to do a linearised stability derivative analysis, using for example AVL, as the stability derivatives are now estimated using empirical methods. This may underestimate the vertical tail size.

For the landing gear, further analysis for the strut and the retracting mechanism should be performed during the next design stage. Fairing and storage space in the trailing edge for main landing gear is also necessary for the retracting system.

Furthermore, as the control surface calculations are based on simplified equations for conventional aircraft, a CFD analysis will have to be performed to serve as an accurate method of verification. This also includes checking the validity of decoupling the longitudinal and lateral aerodynamics, which may be problematic due to the unconventional Flying-V shape.

Aircraft Configuration

This chapter presents the aircraft configuration. The final sizing results and aircraft configuration are presented in Section 9.1. The main aircraft systems and their integration are described in Section 9.2 and Section 9.3, respectively. Finally, a sensitivity analysis is performed and it is explained in Section 9.4 before presenting the manufacturing, assembly and production plan in Section 9.5.

9.1. Final Sizing and Configuration

After the iterative process described in Section 4.2 has converged to a final design, the configuration can be thoroughly described. The two fuselage, V-Shape, configuration is shown in Figure 9.1. This configuration enables the total area to be used much more efficiently than conventional aircraft. The cabin area of the Cryo-V including cockpit, cargo hold and space for fuel makes up roughly 80% of the total area whereas the A320 fuselage makes up roughly 40% of the total area [77]. The side view of the Cryo-V is shown in Figure 9.7.

Cabin Layout - To determine the required area for the cabin, an optimal cabin configuration had to be determined. A single aisle 3 by 3 seating arrangement, as shown in Figure 9.2, provides most efficient use of space as the length of the cabin does not exceed the inner wing length. A Twin-aisle configuration was deemed unfeasible due to the large increase in chord length this encompasses. To ensure maximum comfort while using minimal space, a seat pitch of 0.81 m and a seat width 0.51 m were applied. This is the same seat pitch as a regular A320 economy class but a higher seat width, which is usually around 0.43-0.46 m [77]. In the cabin layout as shown in Figure 9.1, two toilets have been added. However the airliner has the option to include one or two extra lavatories in the extra space. This space can also be used as extra galley/stowage room or a bar/lounge area. Two front exits, two aft exits and two middle exits were implemented where the middle exits do not require open space. Spacing for the crew and galleys are implemented to the front of the aircraft. This configuration gives a total cabin area of 159 m².

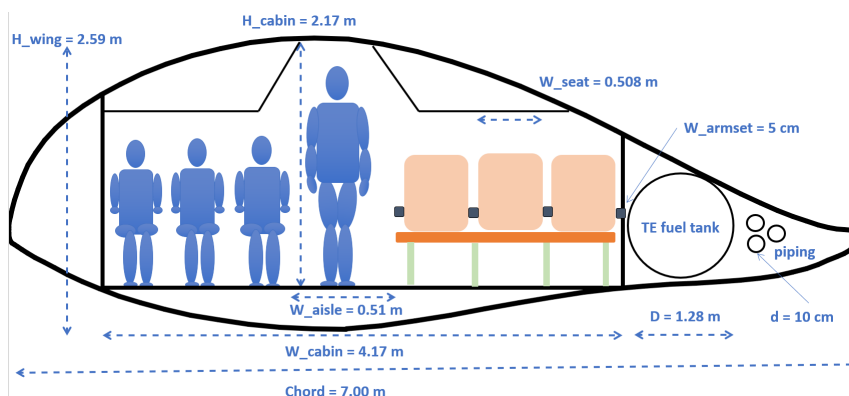


Figure 9.2: Cross-section of Cryo-V cabin

9.1. Final Sizing and Configuration

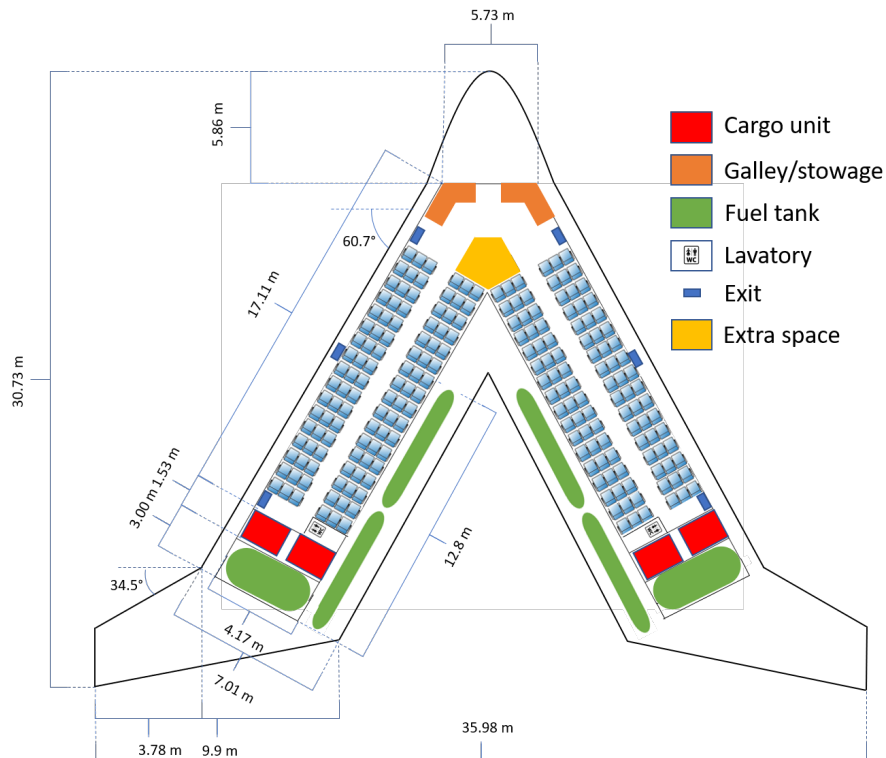


Figure 9.1: Topview of the Cryo-V configuration

Cargo Hold - As the cabin is placed within the airfoil, there is not enough space to place the cargo units directly underneath the cabin. The most forward position for the cargo units to be placed is directly behind the cabin. Two LD3-45 containers are placed on each side which can be perfectly fitted within the cabin, as shown in Figure 9.3. These four containers provide a total cargo volume of 18 m^3 and have a required cargo hold area of 12.8 m^2 .

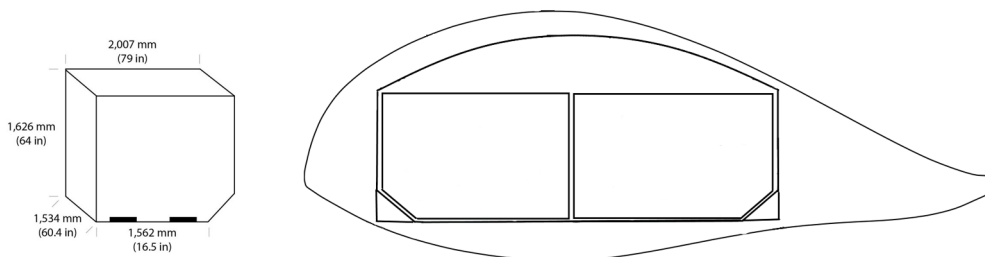


Figure 9.3: Cross-section of cargo hold and LD3-45 dimensions ¹

Fuel Tanks - The Cryo-V uses a hybrid propulsion system with liquid hydrogen as fuel. Liquid hydrogen is approximately four times less dense than kerosene, hence relatively large tanks are required. This space is accounted for in the back of the aircraft and the trailing edge. As the fuel has a relatively low mass compared to the cabin and cargo, the tanks can be placed in the most aft position. As shown in Figure 9.1, the fuel tanks are positioned in the trailing edge as much forward as possible to ensure a most forward centre of gravity. There are two tanks in both trailing edge areas to avoid structural problems, for example bending of tanks, and to provide redundancy in case there is a malfunction in fuel system. The space in front of these fuel tanks is used for the main landing gear.

¹URL https://www.aclairshop.com/container_specs.php [Cited 19 June 2020]

Landing Gear - Figure 9.4 shows the landing configuration of the aircraft, the CoG range and the OEW centre of gravity. The landing gear position is a compromise between tip over/CoG requirements and the requirement to be able to rotate the aircraft on take-off. Thus the landing gear positions is varying with the CoG position to ensure the aircraft is stable on the ground. After take-off the main landing gear is stored between the cabin and the trailing edge.

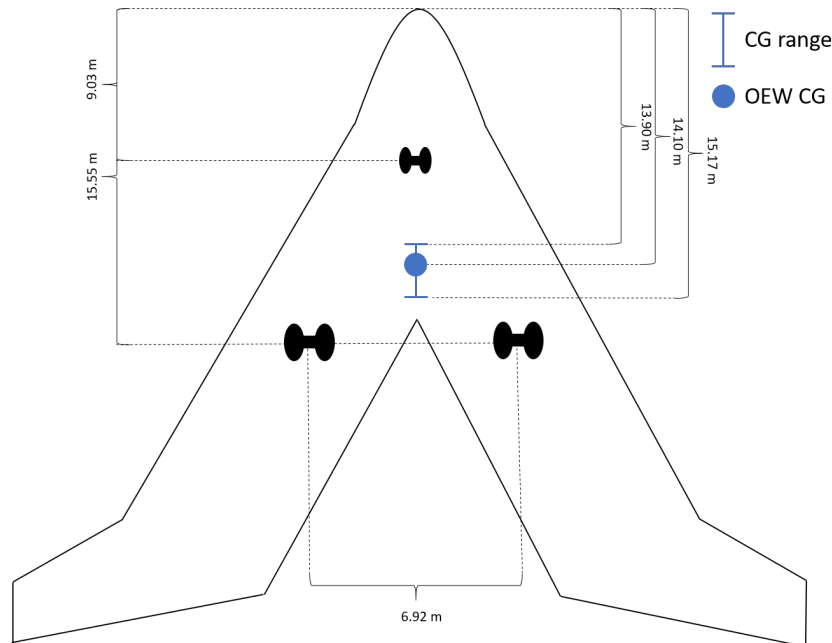


Figure 9.4: Landing gear positioning and CoG range

Hybrid Propulsion System Integration -

The Cryo-V propulsion system consists of 2 turbofan engines and 8 DEP units powered by fuel cells. The propulsion system layout is shown in Figure 9.5. 33% Of the fuel cell volume is located within the turbofan, allowing for optimal performance during cruise. However, an additional 67% of fuel cell volume is located in a fairing on top of but partially integrated in the wing. These fuel cells are placed relatively close to the turbofans in order to reduce the friction losses. Because the fuel cells should be provided with high pressure and hot air at any time, the propulsion system is equipped with a battery pack and electric heaters. These heaters are used to activate the fuel cells before take-off by provision of high temperature air. Furthermore, the heaters are also implemented for redundancy in case failure occurs during flight, whenever turbofans cannot provide the fuel cells with sufficiently hot air.

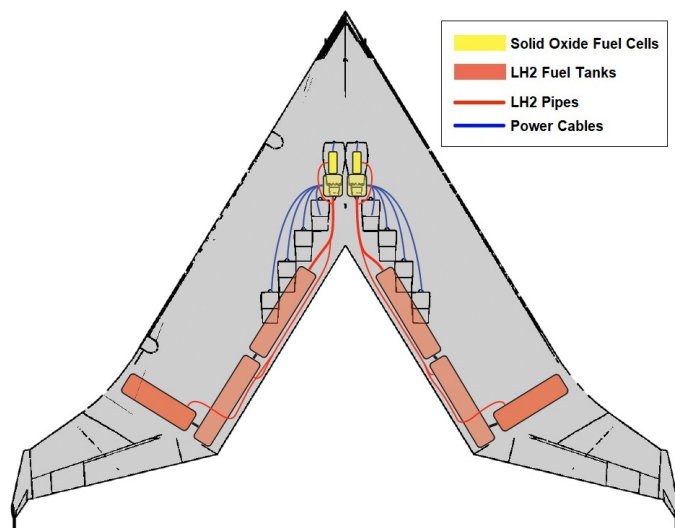


Figure 9.5: Propulsion system layout

Control Surfaces - No high-lift devices are present. Flaps are not feasible for this configuration due to placement constraints. Slats and other leading edge devices are feasible, but do not offer enough extra lift to justify the noise pollution they emit.

9.2. Aircraft System Characteristics

The lateral stability of the aircraft is ensured by the vertical tail integrated winglet (Figure 9.7). It counteracts any yaw moments created in operation and ensures the aircraft returns to equilibrium positions when disturbed. An in-depth explanation is provided in Section 8.2.

Furthermore, the aft wing contains three control surfaces, as shown in Figure 9.6, with the elevator, elevon and aileron running from the base to the tip, respectively. For final dimensions and characteristics the reader is referred to Figure 8.5 and Chapter 8, respectively.



Figure 9.6: Aft wing control surfaces

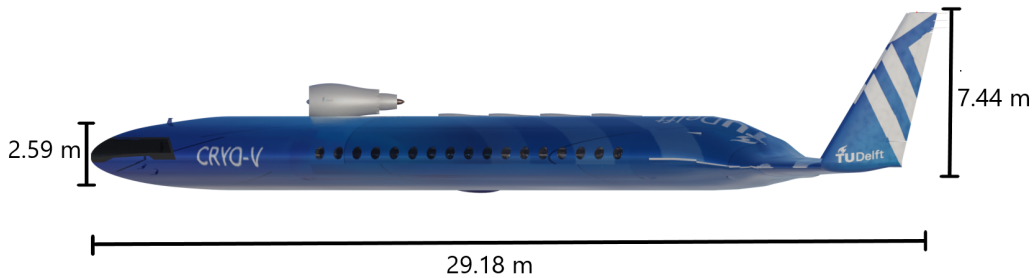


Figure 9.7: Cryo-V side view and dimensions

9.2. Aircraft System Characteristics

For the functioning and support of the subsystems described in Chapter 5 to Chapter 8, the following aircraft systems and their interactions are considered.

Fuel System - The fuel system is described in Figure 9.8. This shows how the fuel cells and the turbofans receive both their required inputs, liquid hydrogen and air, as well as how the electric engines receive electric power. Also one can see that from the fuel cells reaction, the resulted water is first used to transport heat to the turbofan system before being discarded by exhaust. The extra heat is used to provide heat to the cabin. For further description of the fuel system and its integration with the propulsion system refer to Chapter 6.

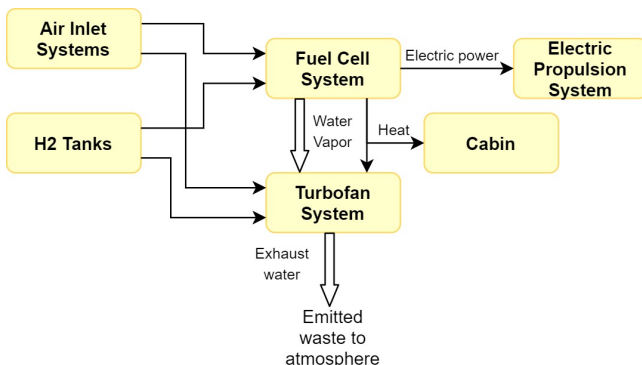


Figure 9.8: Fuel system block diagram of the Cryo-V

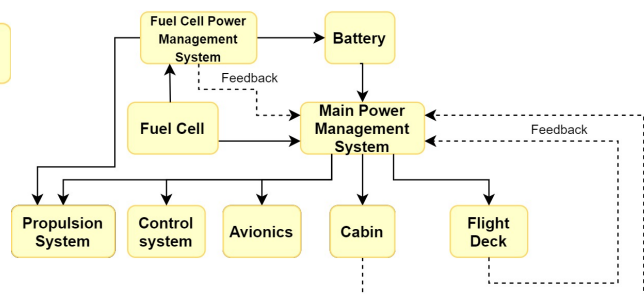


Figure 9.9: Auxiliary electric power block diagram of the Cryo-V

Auxiliary Electric Power System - The auxiliary electric power system is described in Figure 9.9 showing how the electric power provided by the fuel cells is managed to also provide power for the required non-propulsive electric systems.

Hydraulic System - The used hydraulic system is described in Figure 9.10. This is a simple feedback loop where the pilot, or auto-pilot, exerts an external loading force through an actuator, which in turn returns a feedback force for monitoring of the input.

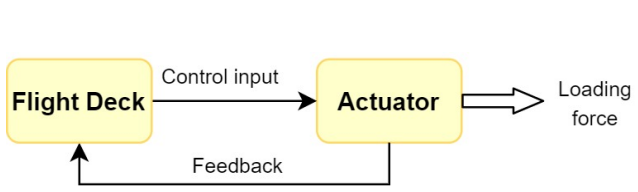


Figure 9.10: Hydraulic system block diagram of the Cryo-V

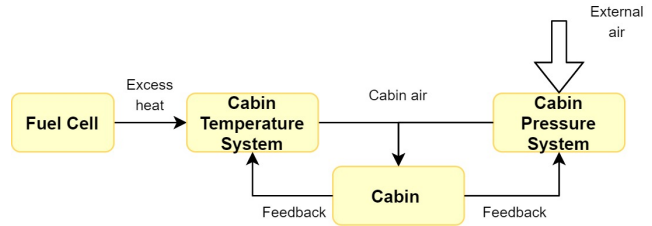


Figure 9.11: Cabin environmental control block diagram of the Cryo-V

Cabin Environment Control - The cabin environment control system controls the atmospheric conditions inside the aircraft and is described in Figure 9.11. The system is able to maintain a comfortable environment for the passengers and crew by controlling the temperature with the excess heat from the fuel cell, and the pressure through a pressurisation system using the outside air.

External Environment Control - The external environment control system allows for the aircraft to measure and adapt for the outside conditions. This is described in Figure 9.12. Here one can see how the flight and atmospheric measurements are relayed to the flight deck for which it then can be used to control the aircraft's external actuators.

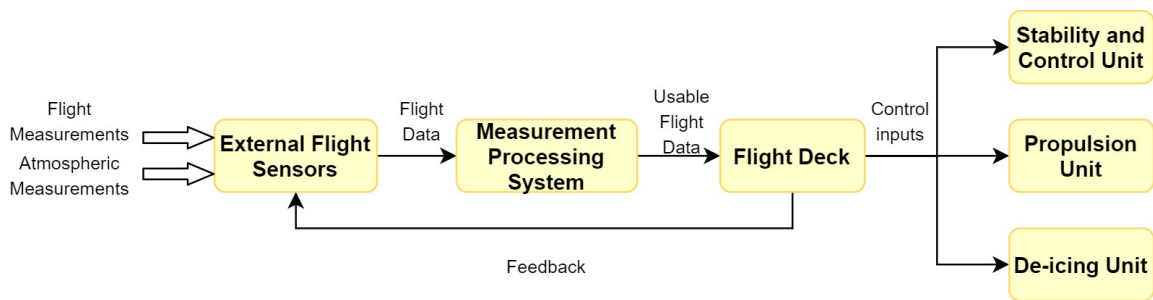


Figure 9.12: External environment control block diagram of the Cryo-V

9.3. System Integration

The communication flow and data handling block diagram shows the way data is processed to and within the aircraft. Figure 9.13 shows how data is collected by the aircraft and gives an overview of how this is processed inside the system.

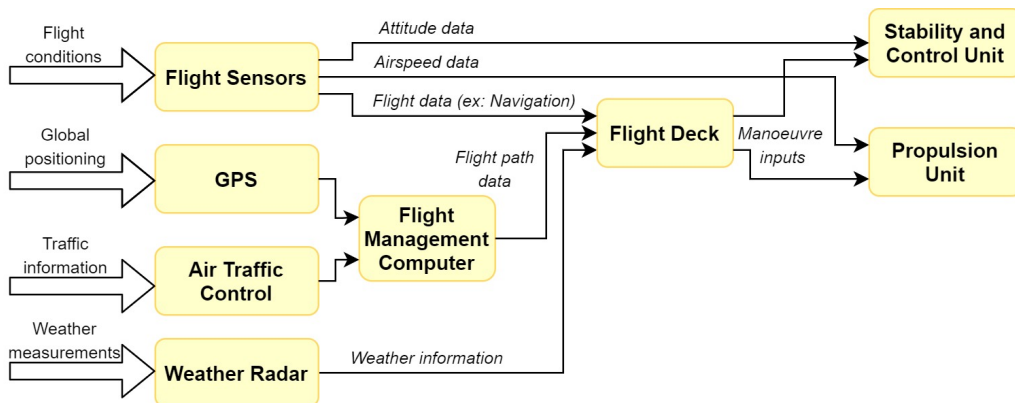


Figure 9.13: Communication flow and data handling block diagram of the Cryo-V

9.4. Sensitivity Analysis

The hardware and software block diagrams are shown in Figures 9.14 and 9.15. These diagrams illustrate the relations and interactions among systems and their components.

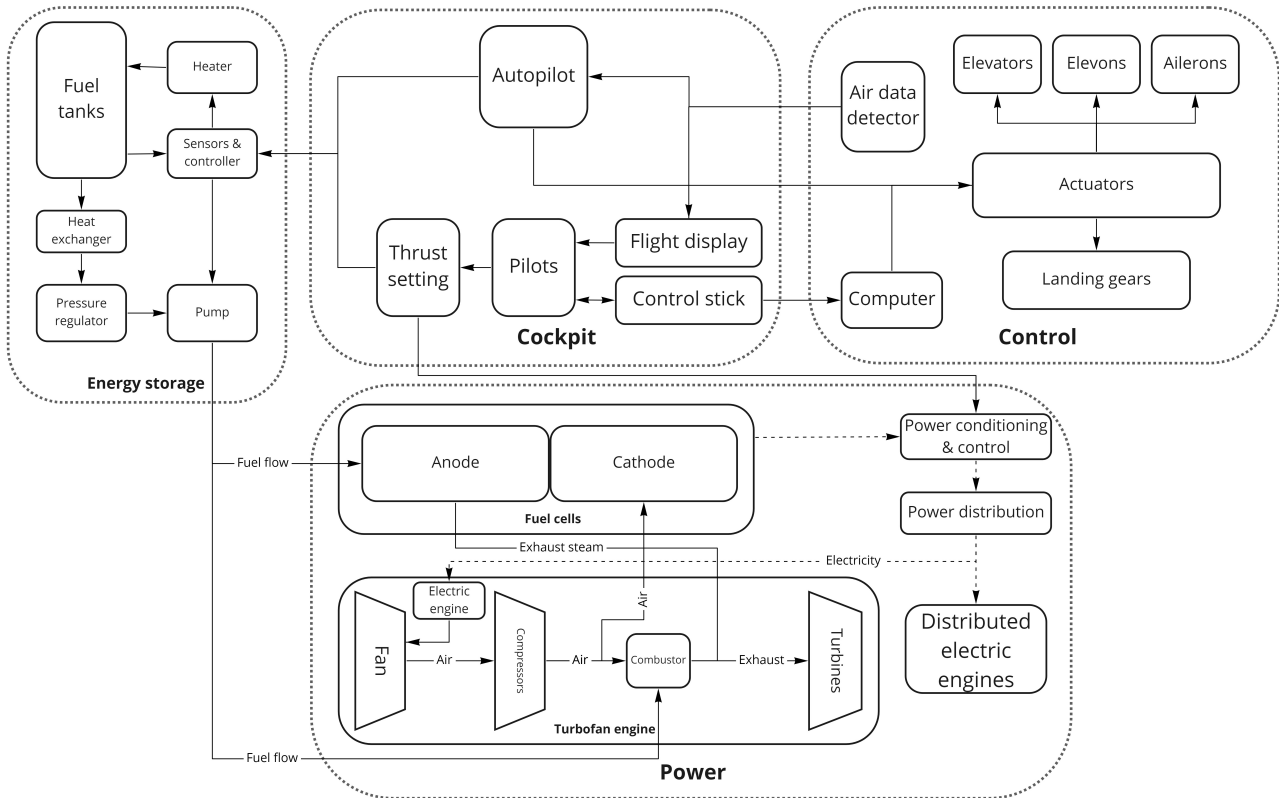


Figure 9.14: Hardware block diagram of the Cryo-V

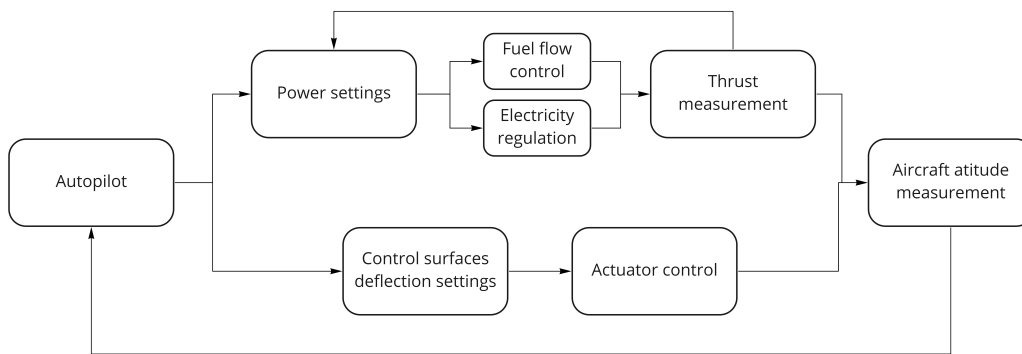


Figure 9.15: Software block diagram of the Cryo-V

9.4. Sensitivity Analysis

In an iterative process such as the design of the Cryo-V, it is important to ensure that the final design is analysed for changes in design or response parameters. The influence of these input parameters is established with a sensitivity analysis, where all parameters are varied within their contingency margins, or as far as the model allows. The design is characterised using five main parameters: the maximum take-off weight *MTOW*, the approach and lateral noise *AppAircraftNoise* and *LatAircraftNoise*, the NO_x emissions *NOxEmissions* and the manufacturing cost *mc*. These response variables are considered to be driving in the design, since many factors have an influence on their value and they are vital to fulfilling the requirements.

Two different sensitivity analyses are performed. The first analysis focuses on the effect of the optimisation parameter. Figure 9.16 shows the results of optimisation for *MTOW*, *NOxEmissions*,

9.4. Sensitivity Analysis

LatAircraftNoise and *AppAircraftNoise*, using the *MTOW* optimisation as a benchmark. The *mc* optimisation is not included for clarity as it closely resembles the *MTOW* results. As is clear, due to limitations of the optimiser, an optimisation for *AppAircraftNoise* results in a cheaper, quieter and slightly lighter design, at the cost of producing only 0.5% more NO_x . The optimal *AppAircraftNoise* design is, therefore, presented in this report, but it is recommended that future work focus on developing an optimisation function that incorporates multiple, weighted response variables.

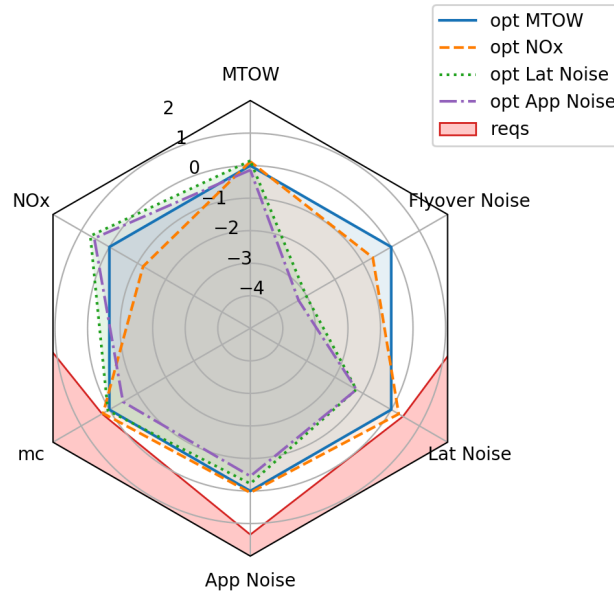


Figure 9.16: Optimisation for different response variables using opt MTOW as a benchmark

The second sensitivity analysis is performed by varying each input parameter and running a single round of optimisation for this new result. The same iterative parameters are used as in the main optimisation, except for the sensitivity parameter being analysed. The iterative parameters are allowed to change by a maximum of 5% to ensure that all aircraft stay close to the original design. An optimisation process within the sensitivity analysis is not optimal, but it is necessary given the number of interrelated variables. Changing only one parameter can quickly lead to unfeasible results if all other variables also remain constant, which does then not provide useful results for the sensitivity analysis.

The optimisation procedure results in the sensitivity graphs not always going through the origin. This is because the final design is the result of numerous rounds of optimisation, whereas the aircraft configurations shown in the sensitivity analysis only go through a single round and cannot, therefore, be expected to be as refined. The jumps in the data are also a result of the optimisation: if more optimisation rounds were used, the graphs would become smoother. The recommendation is therefore in future design phases to simplify and document all major input parameter connections such that the influences can be better monitored.

Cruise Speed - The cruise speed sensitivity analysis is shown in Figure 9.17a. The result is unusual, since a reduction in cruise speed increases all output parameters, most notably the NO_x emissions, MTOW and manufacturing cost. The reasoning behind this behaviour is most likely due to thrust, rather than electric power, being the limiting factor during cruise. Since the fuel cell weight is determined for cruise at a lower altitude, the increase in thrust for a higher cruise speed does not lead to a heavier aircraft. Therefore, only the fuel consumption increases with speed, but this effect seems to be small due to the large lift-to-drag ratio of the Cryo-V and when compared with the decrease in total flight time.

The NO_x emissions are very sensitive to changes in cruise speed. This is because the MTOW increases, which has a large effect on the thrust required on take-off and during climb. Since 98% of NO_x emissions are produced in the take-off and climb phases, an increase in turbofan thrust and

9.4. Sensitivity Analysis

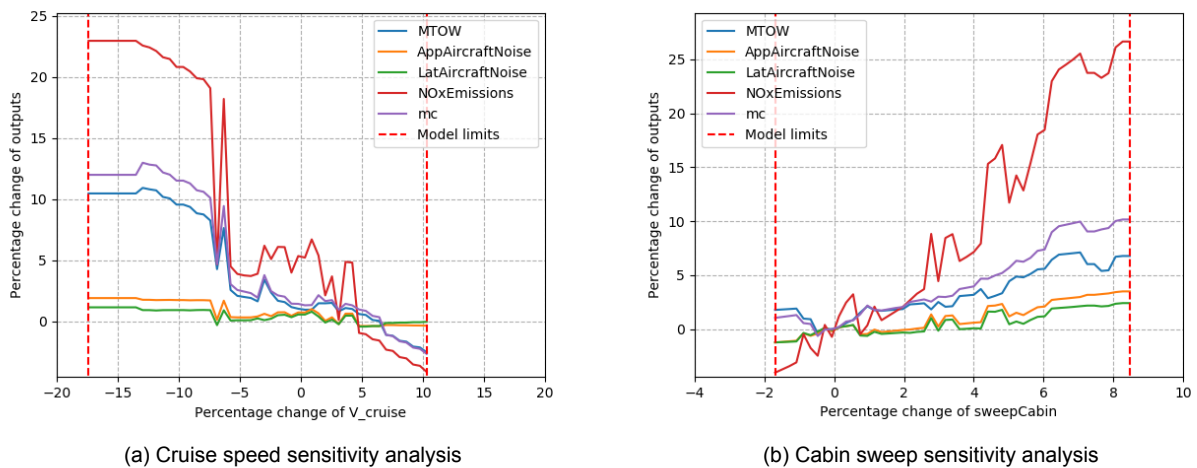


Figure 9.17: Cruise speed and cabin sweep sensitivity analyses

therefore internal temperature leads to a larger amount of emissions and a high sensitivity to MTOW. This effect can be seen in the other analyses as well. The manufacturing cost is also related to a large amount to the MTOW and the parameters linked to that value, such as the total surface area, structural mass and take-off thrust. The change of the cost is therefore in line with the change of the MTOW.

It is important to note that while increasing the cruise speed seems to be a feasible way to decrease emissions, cost and MTOW, other factors must be analysed. Above Mach 0.8, a 3% increase, compressibility effects have a much larger influence on the design and a number of the methods and models used may no longer be valid. In future design phases, it is recommended to analyse faster cruise speeds in more detail, as this could improve the performance of the Cryo-V further.

Cabin Sweep Angle - The cabin sweep angle sensitivity analysis is shown in Figure 9.17b. The result is expected, since a smaller sweep angle increases the maximum C_L of the aircraft, improving aerodynamic performance and resulting in a lower stall speed. There is a lower limit for the sweep angle due to stability, controllability and volume constraints, since smaller sweep angles reduce the size of the aft wing and reduce the space available in the cabin. This is because the maximum wingspan is limited to 36m to conform with airport operations. An upper limit to the sweep is also present for stability reasons, since the OEW centre of gravity location moves aftwards with increasing sweep angle. This limit is reached at around a 9% increase.

As with the cruise speed analysis, the NO_x emissions are sensitive to the sweep angle, predominantly due to the increase in thrust required at take-off for lower C_L values at higher sweep angles. The noise is decreased for lower sweep angles due to the decreased stall and therefore approach speeds, as well as the reduced thrust. It is clear that the cabin sweep is an important parameter in the design of the Cryo-V that must be monitored carefully if any changes are made.

Range - The range sensitivity analysis is shown in Figure 9.18a. This graph clearly shows the advantage of cryogenic hydrogen as a form of energy storage in aircraft. Increasing the range by 20% only increases the MTOW by about 4% due to the small increase in fuel mass. The cost is predominantly affected by the MTOW and increases in a similar fashion, whereas the noise remains essentially constant. The NO_x emissions also increase with range, but are again fairly sensitive without more optimisation. However, the magnitude of the NO_x emissions change is small. The range is therefore not a driving input parameter for the design and can be increased fairly easily, improving the flexibility and versatility of the design.

Cruise Altitude - The cruise altitude sensitivity analysis is shown in Figure 9.18b. The results of the sensitivity analysis are expected, since at higher altitude, the density of the air and therefore the

9.4. Sensitivity Analysis

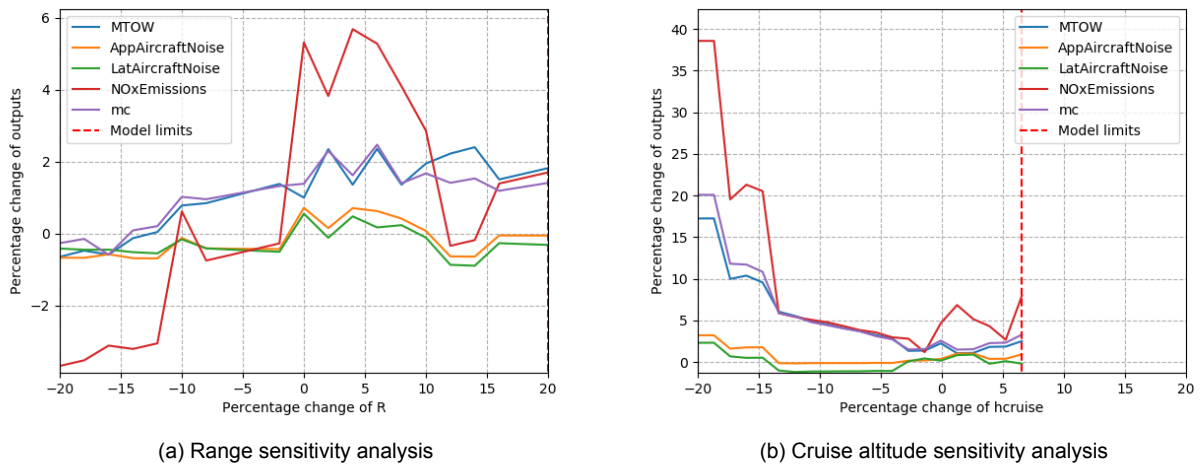


Figure 9.18: Range and cruise altitude sensitivity analyses

drag reduces, which decreases the cruise power and fuel mass. This effect seems to outweigh the reduction of available thrust until 0%, or FL400, after which the design variables plateau. Below -15%, or FL340, the values diverge sharply. This is most likely due to a stability requirement no longer being met, for which a substantially different aircraft configuration is required. The aircraft noise is fairly constant above -15%. Clearly, optimising the aircraft to fly at high altitude is beneficial for the design.

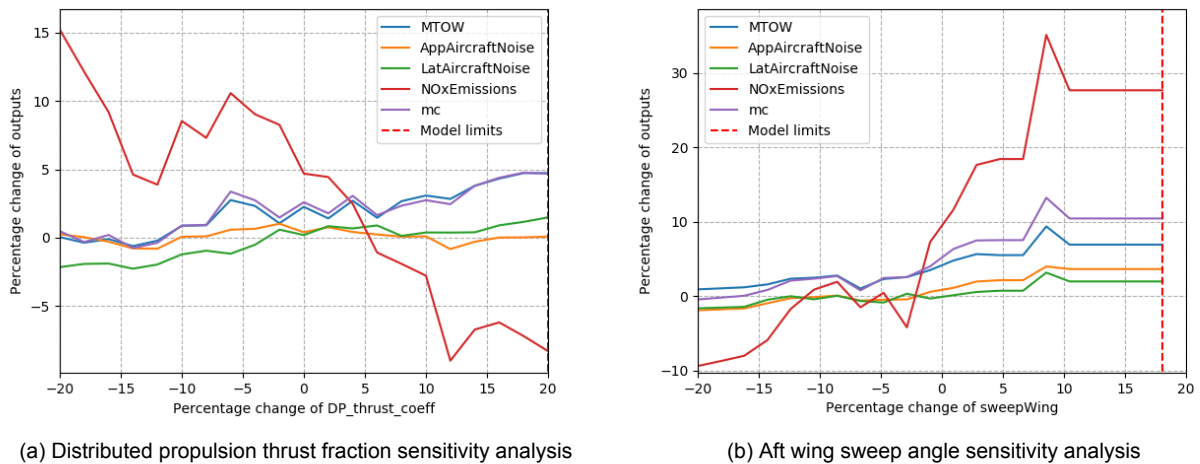


Figure 9.19: Distributed propulsion thrust fraction and aft wing sweep angle sensitivity analyses

Distributed Propulsion Thrust Fraction - The distributed propulsion thrust fraction sensitivity analysis is shown in Figure 9.19a. The results of this analysis show that, for this aircraft design, turbofans have a higher specific mass than the fuel cell system. This is not a correct, general statement, but because the Cryo-V is designed to also be able to fly at maximum cruise speed at the off-design altitude of FL300, the fuel cell mass has a much larger effect and an increase in the amount of thrust produced by the distributed electric propulsion leads to an increase in MTOW and therefore also manufacturing cost. However, as expected, increasing the thrust fraction decreases the NO_x emissions substantially, since less fuel is burnt at lower temperatures. The approach noise is constant, whereas the lateral noise increases due to the lower effectiveness of the distributed propulsion shielding than for the turbofans.

Aft Wing Sweep Angle - The aft wing sweep angle sensitivity analysis is shown in Figure 9.19b. Similarly to the cabin sweep angle, reducing the sweep of the aft wing results in an increase in the

maximum C_L , which improves aerodynamic performance and therefore has a reduction effect on all design variables. The NO_x emissions is again very sensitive to changes in the sweep angle, mostly due to the increase in MTOW, which can be seen in the similar pattern. The other variables seem to plateau at lower than the chosen aft sweep angle, showing that further reduction is less interesting. Most likely, this is due to controllability requirements, since these stipulate a minimum aft wing area.

9.5. Manufacturing, Assembly, and Production Plan

A production flow diagram is shown in Figure 9.20. Raw materials are shown in green boxes, manufactured individual parts in yellow boxes, assembled systems in blue boxes and the final Cryo-V in purple box.

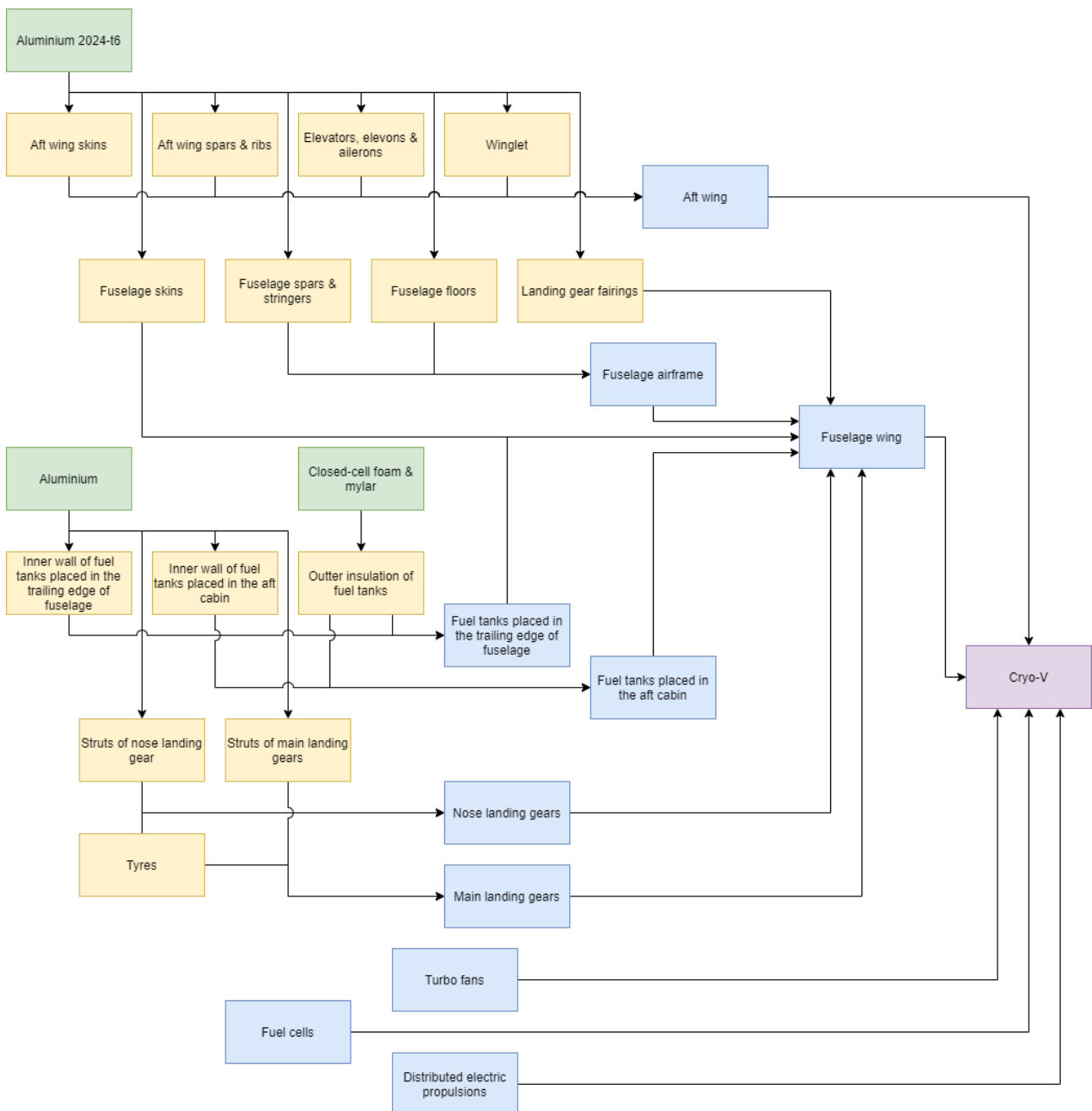


Figure 9.20: Production plan flow diagram of the Cryo-V

Aircraft Performance Analysis

This chapter analyses the performance of the Cryo-V compared to the Airbus A320. Section 10.1 analyses the weight, Section 10.2 the flight characteristics and Sections 10.3 and 10.4 analyse the greenhouse gas and noise emissions. Finally, Section 10.5 presents the allocation of resources and contingency management.

10.1. Weight Analysis

Weight is a crucial parameter for overall aircraft performance. It is, therefore, important to keep track of how the weight changes during iteration. Once a final configuration is selected, a final weight breakdown can be created.

10.1.1. Take-Off Weight Breakdown

The iteration process results in a mass breakdown as shown in Figure 10.1. The numerical values for the computed mass groups are shown in Table 10.1, where the contingency margins presented in Section 10.5 are applied. The take-off weight MTOW, the empty weight OEW and the fuel weight M_F are given a contingency of 10%, the propulsion system mass M_{PS} and fuel system mass M_{FS} are given a contingency of 15% and the payload mass M_{PL} is given a contingency of 5%. Those results are compared to the corresponding A320 data [17] and it can be observed that the Cryo-V is expected to have a smaller take-off weight, although its propulsion system is heavier. This is due to the drastic reduction in fuel weight.

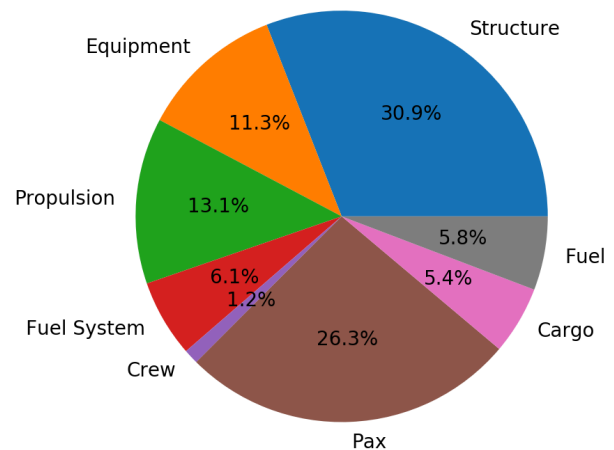


Figure 10.1: Cryo-V MTOW breakdown, in % of MTOW

Table 10.1: Class II+ mass group results, including contingency margins

	MTOW (kg)	OEW (kg)	M_{PS} (kg)	M_{FS} (kg)	M_{PL} (kg)	M_F (kg)
min	64 883	40 573	7998	3726	21 690	3761
Cryo-V calculated	72 092	45 081	9409	4384	22 832	4179
max	79 301	49 589	10 820	5042	23 974	4597
A320 (6150 km) [17]	78 000	42 100	4760	-	13 500	22 400

10.1.2. Empty Weight Breakdown

Next to the top-level weight breakdown, the operational empty weight is investigated in more detail. This breakdown allows the differentiation of the propulsion system mass, fuel system mass, structure mass, landing gear mass and fixed equipment mass. It should be noted that for an airliner, the crew is considered part of the operational empty weight. The operational empty weight breakdown is shown in Table 10.2.

Table 10.2: Class II+ operational empty weight breakdown

	Mass (kg)	% of OEW
Structure	19 362	43.0
Propulsion System	9409	20.9
Fuel System	4384	9.7
Landing Gear	2937	6.5
Fixed Equipment	8152	18.1
Crew	837	1.8
Total	45 081	100

10.2. Flight Characteristics

This section presents the performance and flight characteristics of the Cryo-V and a comparison to the Airbus A320. The payload/range diagram as well as climb performance diagrams are used for direct comparison.

10.2.1. Payload/Range Diagram

Figure 10.2 shows the payload/range diagram of the Cryo-V aircraft variants and the Airbus A320. The advantage of using a lighter fuel and the versatility of the Cryo-V become immediately clear. It is important to note that, unlike the Airbus A320, no spare fuel capacity is provided in the Cryo-V design: Extra range is gained only by the reduction of the aircraft mass due to a smaller payload. All graphs exclude 5% reserve fuel.

The Cryo-V achieves a 6150 km range at Mach 0.78 with full payload at its optimal design altitude of FL400, as well as a ferry range of 9100 km. At a lower altitude of FL300, the Cryo-V only achieves a full payload range of 3260 km at Mach 0.76 due to the increased drag at lower altitude. However, this performance is comparable to the Airbus A320 for short-haul flights.

The diagram also shows the performance of the Cryo-V XLR, the extra long-range variant, which replaces the cargo compartments with extra fuel tanks. The Cryo-V XLR can take the full number of passengers 8280 km and has a ferry range of 12 600 km. Since the electric engines and fuel cells are sized for cruise at FL300, the Cryo-V XLR can also be flown at higher Mach numbers at the cost of range. This variant is included in the diagram to show the flexibility of the Cryo-V design and the possibility for a family of aircraft.

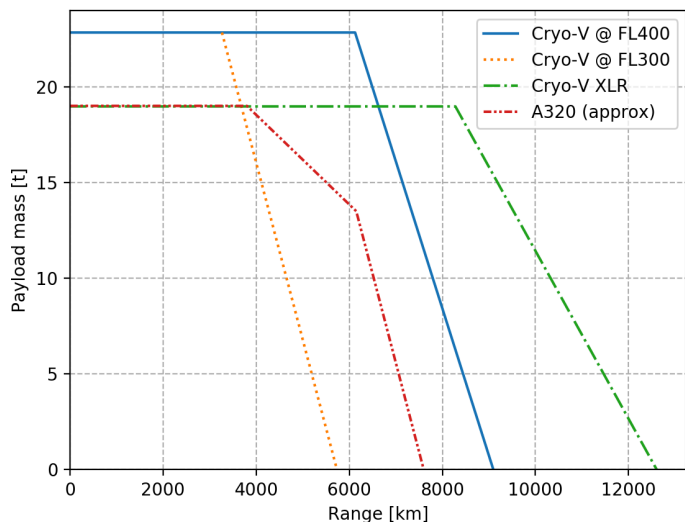


Figure 10.2: Payload/Range diagram of the Cryo-V

10.2.2. Climb Characteristics

To be competitive, the Cryo-V must be able to climb at least as well as the Airbus A320 to nominal cruise altitudes. Figure 10.3 shows the climb rate and gradient performance of the Cryo-V at MTOW compared to the Airbus A320 ¹. "Cryo-V max" shows a 100% thrust setting for both the turbofans and DEP, whereas "Cryo-V nom" shows for the turbofans an 85% thrust setting to 3000 ft followed by a 70% thrust setting, and a 100% thrust setting for the DEP. Since 95.6% of NO_x emissions are produced during take-off and climb (see Section 10.3), a reduction in turbofan thrust setting has a large effect on production rates and nominal climb rates are, therefore, preferred. The turbofan thrust values are calculated using GSP 11.

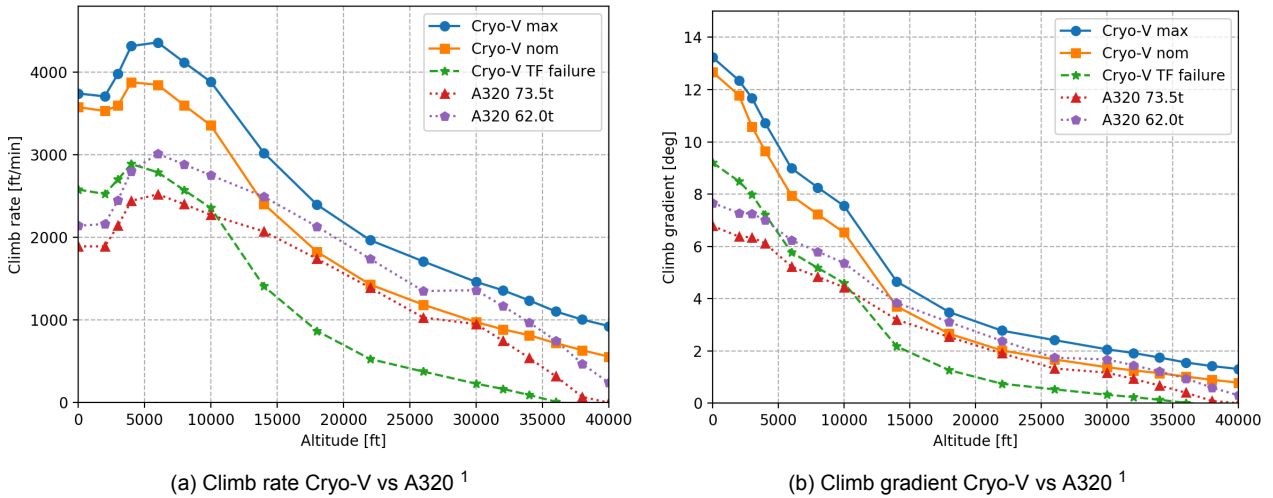


Figure 10.3: Climb rate and gradients Cryo-V vs Airbus A320 ¹

The Cryo-V shows improved performance at low altitude compared with the Airbus A320. However, in order to reach acceptable climb rates at altitudes above FL300, the airspeed is decreased by 25 m/s compared to the Airbus A320. However, the effect of this reduction in speed is determined to be negligible, as shown by the difference in time and distance in Figure 10.4. The Cryo-V nominal climb is directly comparable with the Airbus A320 at 62 t in Figure 10.4, whereas the maximum Cryo-V climb is a large improvement to the Airbus A320.

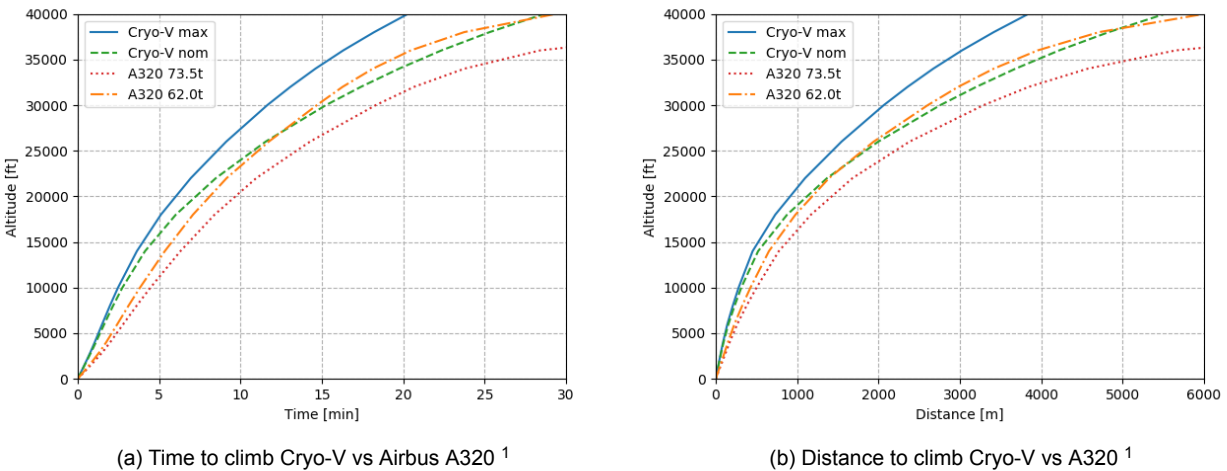


Figure 10.4: Climb time and distance Cryo-V vs Airbus A320 ¹

¹URL https://www.eurocontrol.int/sites/default/files/library/015_BADA_Aircraft_Performance_Summary_Tables.pdf [cited 16 June 2020]

10.3. Emission Characteristics

The Flightpath 2050 requirements stipulate that CO₂ emissions must be reduced by 75% and NO_x by 90% compared to the Airbus A320. This corresponds to a limit of 17 249 kg CO₂ and 8.923 kg NO_x per maximum range, maximum payload trip. As LH₂ is the only fuel carried, no CO₂ is produced. However, due to combustion, a small amount of NO_x is formed. In addition, conversion of LH₂ leads to the production of water vapour, which needs to be further investigated as well.

10.3.1. NO_x Emissions

Combustion occurs at high temperatures in the turbofans, which induces the formation of NO_x. Using a model provided by NASA [78], NO_x formation in gas turbines can be approximated by Equation 10.1. EINO_x expresses how many grams of NO_x is formed per kilogram of fuel burned.

$$EINO_x = 30 \cdot (p_3)^{0.594} \cdot \exp\left(\frac{T_3}{350}\right) \cdot FAR^{1.6876} \cdot (100 \cdot \Delta p/p)^{-0.56} \quad (10.1)$$

In this equation, p_3 is the combustion chamber inlet pressure in psi, T_3 is the combustion chamber inlet temperature in °F, and $\Delta p/p$ is the pressure drop in the combustion chamber as a percentage. Units should carefully be converted to avoid errors. The model can be applied to the combustion of LH₂ by using Equations 10.2 and 10.3, where ϕ_{H_2} is the hydrogen equivalence ratio and T_4 is the combustion chamber outlet temperature in °F.

$$\phi_{H_2} = 7.1 \cdot 10^{-5} \cdot (T_4 - T_3)^{1.157} \quad (10.2)$$

$$FAR_{H_2} = \phi_{H_2} \cdot 0.0292 \cdot 2.55 \quad (10.3)$$

The model is verified using the simulation software GSP 11 [41]. In Figure 10.5, EINO_x is shown versus flight altitude, corresponding to the nominal climb performance of the Cryo-V, as introduced in Subsection 6.4.6. Maximum EINO_x occurs during take-off at 32.17 g/kg, while cruise EINO_x is estimated at 1.69 g/kg. By including the NO_x prediction model in the turbofan thermodynamic model described in Subsection 6.4.3, the EINO_x can be predicted. It is concluded that the model shows a slight, constant overestimation of emissions, but stays within a margin of 25%. The prediction model is, therefore, still verified and included in the class II iteration, because it will ensure that the NO_x requirement is met due to overestimation.

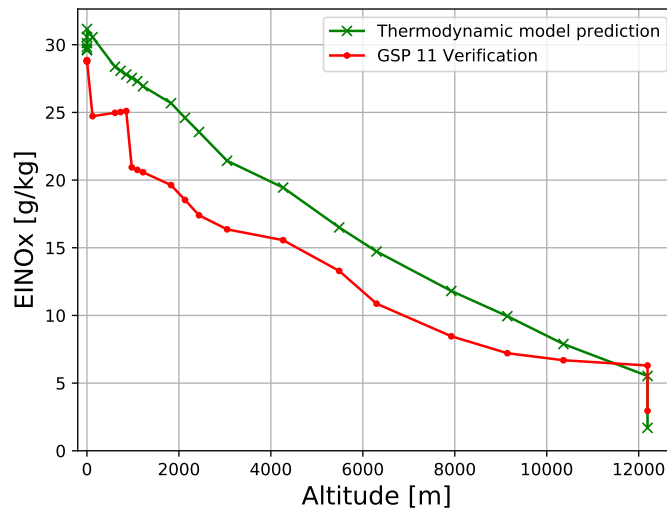


Figure 10.5: EINO_x in g/kg for the Cryo-V turbofans during nominal climb performance

A more global flight emission profile is shown in Figure 10.6, where NO_x emissions are plotted against flight time. A flight altitude profile is included for visualisation. It is clear that most NO_x is produced during take-off and climb, while constant emissions of 0.0135 g/s of NO_x are formed during cruise. Cruise flight only contributes 4.39% of the total emissions. By integrating the emission rate over flight time, total emissions are calculated and normalised, and are provided in Table 10.3

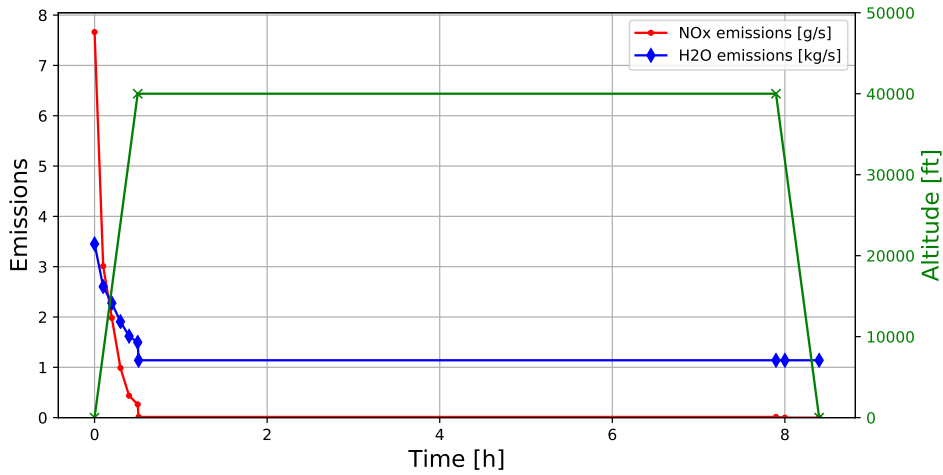


Figure 10.6: Emission profile of the Cryo-V during various flight phases

Table 10.3: Total emissions of the Cryo-V, including a comparison to the Airbus A320

	LTO Cycle (kg)	Cruise (g/s)	Total - Max Range (kg)	Comparison to A320
NO _x	7.839	0.0135	8.200	-90.8%
H ₂ O	3538	1212	35 816	+33.1%
CO ₂	0	0	0	-100%

10.3.2. H₂O Emissions

During conversion of H₂ in both the turbofans and the fuel cells, H₂O is produced. The amount of water vapour is calculated as follows:

$$M_{H_2O} = \frac{2 \cdot m_H}{m_O} \cdot M_F = 9 \cdot M_F \quad (10.4)$$

As shown in Figure 10.6, peak H₂O emissions occur during take-off and climb. However, the majority of water vapour is produced during cruise, due to the constant rate of 0.547 kg/s. Total emissions are calculated, normalised, and provided in Table 10.3.

Although reduction of H₂O emissions is not a requirement, the additional climate impact is nevertheless investigated. Compared to the Airbus A320 [17], about 33.1% more H₂O is produced, assuming 1.24 kg of H₂O is produced per kg of kerosene [79]. Considering this is still a small increase in emissions, and the fact that no H₂O requirement has to be met, it is concluded the Cryo-V induces no significant extra climate impact due to H₂O emissions compared to the Airbus A320.

For H₂O emissions, two different impact mechanisms are distinguished. First, water vapour is considered as a greenhouse gas itself. However, this effect is negligible compared to the second mechanism², that water vapour released at altitude evolves into Aircraft Induced Cloudiness (AIC). This

²URL <https://lae.mit.edu/2019/11/08/new-study-finds-aviation-emissions-impacts-on-air->

can only happen in layers that are supersaturated and sufficiently cold [15]. A technique described by Mannstein [80] uses atmospheric data to predict these layers and changes the cruise altitude by 2000-4000 ft in order to prevent the formation of AIC. It is highly recommended that these techniques are investigated in future design stages to further reduce the climate impact of the Cryo-V.

10.3.3. Effect of H₂O in Combustion Chamber

As a result of the integration of SOFCs and turbofans, a constant flow of gaseous water is directed through the combustion chamber, where the steam-to-air ratio is 0.117 during cruise. This effect is investigated in order to eliminate any potential threats to reaching the emission requirements. In addition, potential benefits of combustion chamber water injection are explored.

According to Benini [81], water injection in combustion chambers of small turbojets reduces thermal NO_x formation by decreasing the flame temperature during combustion. Injection of steam shows the same results to a slightly lesser extent. Experiments on a small turbojet showed a 16% reduction in NO_x emissions when water was injected, and 8% for steam injection, when fuel consumption remained unchanged. This reduction was achieved for a water/steam mass flow of 200% of the fuel mass flow.

Gonca [82] also investigates combustion of different biofuels with steam injection. It is concluded that due to the higher specific heat of the fuel-air mixture in the combustion chamber, adiabatic combustion temperature diminishes, which decreases the formation of NO_x and CO.

For the outcome of the class II iteration, it is assumed that steam injection in the combustion chamber has negligible effect on fuel consumption, but may potentially lower the actual NO_x emissions. It is highly recommended that research on H₂ combustion and steam injection is conducted during further design phases.

10.3.4. Altitude Effects

The choice to fly at a cruise altitude of FL400 instead of FL300 is justified by numerous reasons as explained in Section 9.4. Additionally, the climate impact at different altitudes is investigated. A study conducted by Dallara and Kroo [15] shows the effect of altitude on climate impact by different species. In Figure 10.7, the forcing factor for long- and short-living O₃ (caused by NO_x) as well as aircraft induced cloudiness (AIC) is shown. The forcing factor is related to radiative forcing, which is directly related to global warming [83]. By choosing to fly at FL400, the climate impact forcing factor of the species caused by NO_x increases by 30% for short-lived ozone and by 96% for long-lived ozone. However, as the requirements are based on the Airbus A320 performance, which cruises most economically at FL370 ft³, the increase in climate impact is negligible, when the 90.4% reduction of NO_x emissions is taken into account.

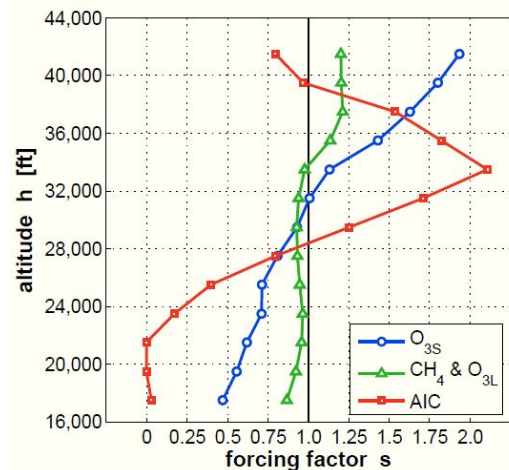


Figure 10.7: Radiative NO_x forcing factor and induced cloudiness versus altitude [15]

For AIC, on the other hand, the forcing factor is reduced by 57% when flying at FL400 instead of FL300. Considering that the largest share of total climate impact of the Cryo-V is caused by the emission of H₂O, flying at FL400 is a justified strategy to further lower the climate impact for the Cryo-V.

quality-to-be-larger-than-on-climate/ [cited 19 June 2020]
³URL [https://www.airliners.net/aircraft-data/airbus-a320/23#:~:text=A320%2D200%20%2D%20Max%20cruising%20speed,\(454kt\)%20at%2037%2C000ft.](https://www.airliners.net/aircraft-data/airbus-a320/23#:~:text=A320%2D200%20%2D%20Max%20cruising%20speed,(454kt)%20at%2037%2C000ft.) [cited 19 June 2020]

10.4. Noise Characteristics

This section provides an overview of the noise emissions of the Cryo-V and the mitigation methods used to meet the requirements.

10.4.1. Noise Regulations and Requirements

Currently, noise regulations for civil aircraft are set by international standards. ICAO set these standards in the form of chapters with a cumulative noise limit [84]. In 2001, the chapter 4 limit was introduced and all new civil aircraft built after the introduction have to satisfy this limit. The Airbus A320-211, which is used as the reference aircraft for noise, has a cumulative noise of 277 EPNdB and meets chapter 4 regulations⁴. The metric used for these chapters is the effective perceived noise level (EPNL), which is explained in Subsection 10.4.2.

The Flightpath 2050 goals aim to have a 65% noise reduction, which can be understood in many different ways. However, it is generally understood as a 65% perceived volume reduction, which can be translated into a 15 dB sound pressure level reduction⁵, shown in Table 10.4. The aviation industry translates this into a 15 EPNdB reduction for each certification measurement point, explained in Subsection 10.4.2 [22].

Table 10.4: EPNL noise requirements and reference noise levels⁶

		A320	Cryo-V
Lateral	(EPNdB)	93.7	78.7
Approach	(EPNdB)	96.0	81
Flyover	(EPNdB)	85.6	70.6

10.4.2. Noise Assessment

Noise Metric - To measure the effect created by aircraft noise, the Effective Perceived Noise Level (EPNL) is used. This metric requires the instantaneous sound pressure level for each of the 24 one-third octave bands for each 0.5 second increment of time during the noise measurement of 10 seconds⁷. These are then converted to the Perceived Noise Level (PNL) which is corrected for tone and duration [85]. The conversion from sound pressure level to effective perceived noise level is outside the scope of this project. A substantial amount of data is required for each noise source which is typically only accessible by aircraft companies. Therefore, this project considers the A-weighted maximum sound pressure level (LA_{max}) for each noise source instead of the EPNL.

The A-weighting serves as a filter for frequencies that are less sensitive to the human ear and puts extra emphasis on the frequencies of 1-5 kHz, to which people are most sensitive [86]. Therefore, the noise within this spectrum is amplified to a certain degree. If the LA_{max} for a particular noise source cannot be acquired, the Overall Sound Pressure Level (OASPL) is estimated and converted to LA_{max}.

The reference aircraft noise is converted from EPNL to LA_{max} by means of the available noise-power-distance data acquired from the ANP database⁸. This data translates the EPNL requirements into the LA_{max} requirements as specified in Table 10.5. Some assumptions had to be made for this

⁴URL <https://www.easa.europa.eu/domains/environment/easa-certification-noise-levels> [cited 17 June 2020]

⁵URL https://www.acousticalsurfaces.com/soundproofing_tips/noise_reduction.htm [cited 17 June 2020]

⁶URL <https://www.easa.europa.eu/domains/environment/easa-certification-noise-levels> [Cited 17 June 2020]

⁷URL https://www.law.cornell.edu/cfr/text/14/appendix-A_to_part_36 [cited 17 June 2020]

⁸URL <https://www.aircraftnoisemodel.org/> [cited 17 June 2020]

conversion. The ANP database provides the L_{Amax} and EPNL at different thrust levels and different heights directly underneath the flightpath. However, the lateral certification point is measured at 450m distance from the flightpath laterally. For the conversion at this point, the directivity factor is ignored. The other major assumption is that the difference between EPNL and L_{Amax} of the Airbus A320 corresponds to the same difference for the Cryo-V. In reality, different maximum sound pressure levels may arise as the sound pressure may vary substantially across the frequency range.

Table 10.5: L_{Amax} noise requirements and reference noise levels

		A320	Cryo-V
Lateral	(dBA)	86.4	71.4
Approach	(dBA)	86.1	71.1
Flyover	(dBA)	71.7	56.7

Assessment Location - The positions for which the noise levels are estimated at are in compliance with the regulations and are as shown in Figure 10.8. The approach case is defined as 120.5 m straight below the aircraft in landing conditions, which is equivalent to 2300 m from the landing point with a 3° descent path. The flyover case is conservatively assumed to be at 500 m below the aircraft, corresponding to 2-3 km from the airfield at a typical 10 to 15 deg take-off angle⁹. Finally, the lateral case is assumed to be 450 m from the centre line of the runway when the aircraft is 60.96 m above the ground after take-off¹⁰.

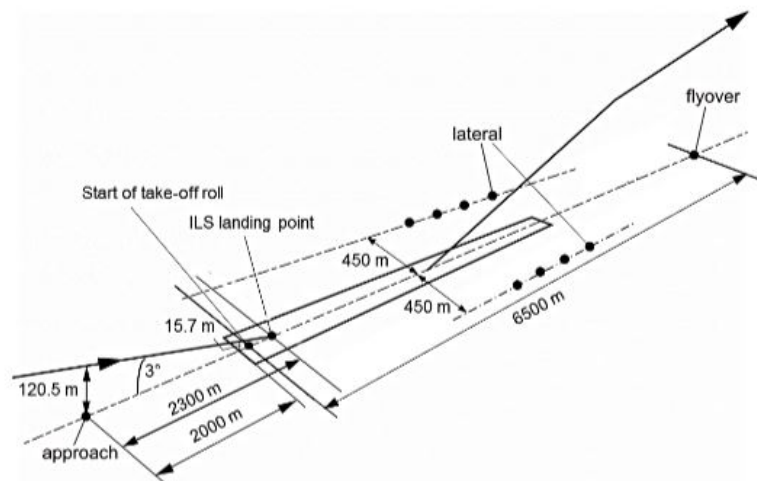


Figure 10.8: Location of noise assessment points

10.4.3. Noise reduction

To calculate the total noise reduction of the Cryo-V design it is needed to estimate noise emissions from multiple noise sources. Then shielding and noise reduction technologies are implemented and their effects are evaluated.

Preliminary Turbofan Engine Noise Estimate - As a starting point for the engine noise estimation, the take-off noise (L_{Amax} at 200 ft directly underneath flightpath) is plotted as a function of take-off thrust, as shown in Figure 10.9. These values are derived from the NPD data provided by the

⁹URL <https://www.bangaloreaviation.com/2009/05/typical-takeoff-and-climb-angles-of-all.html> [cited 17 June 2020]

¹⁰URL <https://www.aircraftnoisemodel.org/> [cited 17 June 2020]

ANP database ¹¹. As engine noise is the dominant noise source during take-off [87], it can be derived from this plot.

The turbofan engine noise is computed by using the thrust produced by the turbofan engines at take-off. This gives an initial estimate of 98.9 dBA for the total aircraft noise, at 200 ft. The jet noise and fan noise is derived from the noise source ranking provided by [87]. This ranking is shown in Figure 10.10. The estimated jet and fan noise at 200 ft for the turbofans at take-off are 97.9 dBA and 89.9 dBA respectively. Here shielding is not taken into account yet. This corresponds to a 79.2 dBA fan noise and 72.2 dBA jet noise at 454 m distance, which is the distance of the lateral measurement point.

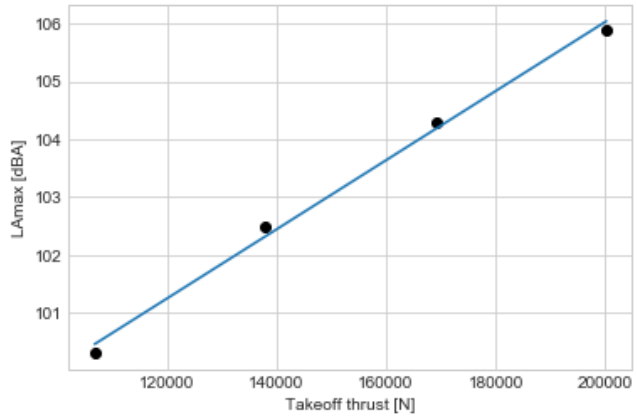


Figure 10.9: L_{Amax} (dBA) as a function of take-off thrust (N)

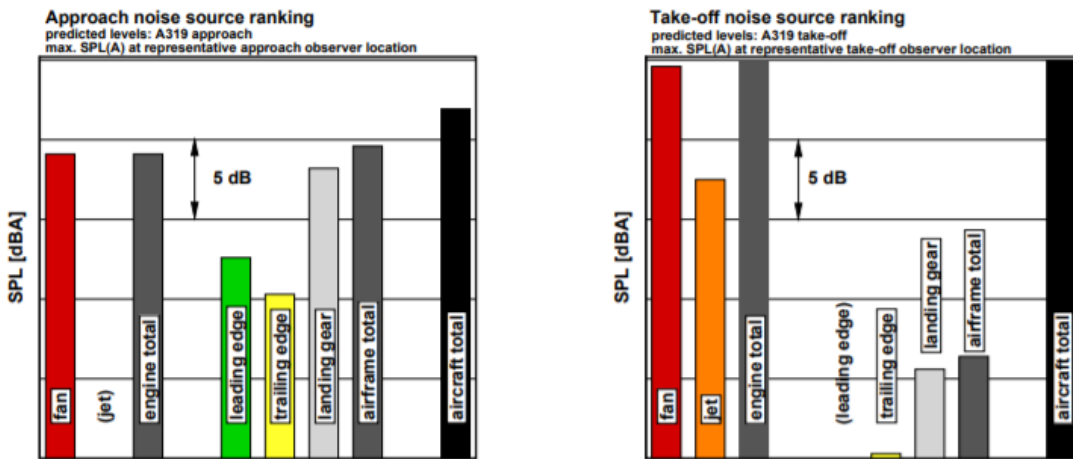


Figure 10.10: Noise source ranking of the A319 at approach and take-off [87]

By applying Equation 10.5, the total turbofan engine noise can be computed to be 80.0 dBA. There are more accurate methods of determining the jet noise and fan noise, such as those described in Lighthill's acoustic analogy [88] for jet noise and the method given in Heidmann's paper [89] for fan noise. Lighthill's acoustic analogy provides a method for determining the difference in jet noise between a reference aircraft and the designed aircraft. However, for this method multiple parameters such as the exhaust jet velocity are required which are missing for the reference aircraft. Heidmann's method also requires certain parameters for the turbofan engines which have not yet been defined. Therefore, the more general method of determining the engine noise as a function of thrust is chosen.

$$L_{p,total} = 10 \log \left[\sum_{s=1}^N 10^{\frac{L_{p,s}}{10}} \right] \quad (10.5)$$

Initial DEP Noise Estimate - For the distributed electric propulsion system the same method is used for a starting point noise estimate. The dominant noise source for the electric propulsion system was found to be the fan. The motor noise only starts to play a role for very small engines with a shaft power of 1 MW or less [90]. The total Cryo-V DEP has a shaft power of 3.36 MW, thus the motor noise can be neglected. The jet noise is dependent on V_j^8 which is substantially lower than the jet

¹¹URL <https://www.aircraftnoisemodel.org/> [cited 17 June 2020]

velocity of the turbofan engine [91]. Literature shows the difference in noise of the A320 using regular turbofan engines and a distributed electric propulsion system as a function of number of engines [92]. Eight electric engines give a noise reduction of 3 dB compared to the conventional propulsion system for fixed take-off thrust. When applying the same method as the turbofan engines to account for the thrust reduction, the DEP is estimated to have a L_{Amax} of 86.5 dBA at 454 m distance. This is considerably high compared to the turbofan engine noise but since fan noise is mainly forward propagated noise, shielding can have a big effect on the noise if the engines are placed near the trailing edge. Furthermore, the designed blade tip speed is 0.85 Mach which does not increase the inlet duct noise comparing to slower tip speeds as found by Heidmann [93].

Shielding - The engine positioning used by the Cryo-V allows for part of the engine noise to be attenuated by engine shielding. This allows for a noise reduction at all three noise assessment locations as shown in Figure 10.11:

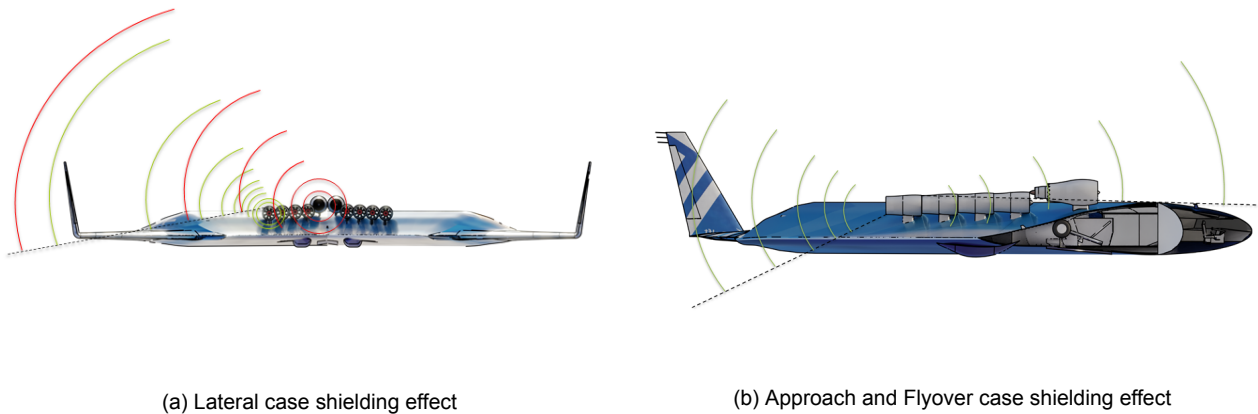


Figure 10.11: Representation of the engine shielding effect for the Cryo-V

To determine the noise reduction due to engine shielding from the wing the barrier shield method applied for aircraft wing [94] was used. This method consists of the following steps:

1. Compute path length difference with: $\delta = \pm(|A| + |B| - |d|)$, where d is the direct sound ray and $(A + B)$ is the shortest path over the edge. For this the wing is considered a simple swept rectangle.
2. Compute Fresnel number with : $N = \frac{2\delta f_i}{c_\infty}$, where f_i is the take centre frequency of 1000 Hz and c_∞ is the reference speed of sound of 343 m/s
3. Determine sound attenuation per edge with:

$$A_{tti} = \begin{cases} 20 \log \frac{\sqrt{2\pi N}}{\tanh \sqrt{2\pi N}} + 5.0, & \text{for } N \geq 0 \\ 20 \log \frac{\sqrt{2\pi N}}{\tan \sqrt{2\pi |N|}} + 5.0, & \text{for } -0.2 \geq N < 0 \\ 0, & \text{for } N < -0.2 \end{cases} \quad (10.6)$$

4. Combine to find total attenuation with: $A_{tt_{tot}} = -10 \log \Sigma 10^{(-A_{tti}/10)}$

This method was then applied for the lateral, approach, and flyover cases to find the resultant attenuation due to shielding for the turbofan and distributed propulsion system. The results are shown in Table 10.6:

Table 10.6: Engine noise reductions achievable due to shielding for the Cryo-V

	Approach	Lateral	Flyover
Attenuation distributed propulsion (dB)	30.49	13.28	24.18
Attenuation turbofan (dB)	28.53	12.19	22.22
Total engine attenuation (dB)	26.39	9.69	20.08

Landing Gear Noise - As shown in Figure 10.10, the landing gear is the dominant airframe noise source at approach. Therefore to reach the approach noise requirement, the landing gear noise must decrease considerably. This can be achieved in multiple ways. First the approach velocity and approach angle are considered. The landing gears have a cluster of aerodynamic noise sources, which intensities are dependent on the local flow velocity to the 6th power [95]. Thus by reducing the approach velocity, the landing gear noise can be decreased significantly. Furthermore the approach angle has an effect on the distance to observer at approach. The noise level the observer perceives is also dependent on the distance squared. However, since the approach certification measurement point has a fixed approach angle of 3 deg, changing the approach angle is considered as a final option. An estimate of one of the landing gears overall sound pressure level, depending on these parameters and the wheel diameter, is provided by Fink [96]:

$$OASPL = 60 \log\left(\frac{1.94V}{194}\right) + 20 \log\left(\frac{D}{r}\right) + 10 \log(10^{12.5}) \quad (10.7)$$

Here V is the flow velocity in front of the landing gear in knots, D is the wheel diameter in inches and r is the distance to observer in meters. Normally the strut noise is also included in the equation but at approach this can be ignored since the measurement point is directly underneath the flightpath [96]. This gives a nose landing gear OASPL of 78.1 dB. For the main landing gear the flow velocity is assumed to be 20% lower due to flow disturbance [97]. This gives a total landing gear OASPL of 81.1 dB. As a rule of thumb for airframe noise the LAm_{ax} can be assumed to be 4.6 dB lower than the OASPL with a standard deviation of 1.3 dB [96].

Other Airframe Noise - To determine the rest of the noise contribution linked to the airframe, the airframes clean noise contribution as well as the (if relevant) leading and trailing edge High Lift Devices (HLDs), empirical data from Fink's [96] work was used. During design optimisation becomes apparent whether leading edge or trailing edge HLDs are required. It could be that to meet the approach requirement, the approach velocity must decrease substantially which can be achieved by HLDs. However, these do produce extra noise. If the landing gear noise requirement can only be met by applying HLDs, an optimal balance between landing gear noise and HLD noise must be found.

The clean airframe noise is estimated as a function of airspeed, based on flyover levels of aerodynamically very clean airframes [96] resulting in the following interpolation:

$$OASPL_{\text{Clean airframe}} = 31.3 + 0.667 \cdot V - 2.15 \cdot 10^{-3} \cdot V^2 \quad (10.8)$$

Where 13 dB is added if the design includes leading edge high lift devices. For trailing edge devices the noise level is modelled with the following equation [96]:

$$OASPL_{\text{Trailing edge device}} = 112 + 10 \log\left(\frac{S_f \cdot \sin(\delta_f)^2}{r^2}\right) + 60 \log\left(\frac{V \cdot 1.94}{100}\right) \quad (10.9)$$

which are then corrected for speed and distance to determine the noise levels at each assessment case. The same conversion to LAm_{ax} can be applied as for the landing gear noise. As the approach

velocity has a substantial influence on the approach noise, the design is optimised in the iteration process to minimise this parameter. The final design has an approach velocity of 71 m/s compared to 80 m/s of the A320 [87].

Additional Noise Reduction Technologies

To further reduce the noise levels of the Cryo-V further techniques and technologies have been included in the design. These are as follows:

- **Swept stators:** Rotor stator interaction noise has proven to be a dominant noise source considering fan noise. It is caused by periodic cutting of rotor wakes by the stator vanes. By implementing a certain sweep to the stators a fan noise reduction of 3 dB can be achieved [98].
- **Over rotor acoustic treatment:** While acoustic lining on the inlet walls have already been applied to existing engines, a new method of passive noise reduction has been introduced by NASA. A metal foam material known as Haynes 25, can be applied on the fan rotor to provide additional noise reduction. Studies show that this acoustic treatment has the potential to reduce the fan noise further by roughly 4 dB [99].
- **Higher Bypass ratio:** As previously mentioned, the jet noise is dependent on V_j^8 [88]. One factor that has an effect on the jet velocity is the bypass ratio. As less air passes the combustion chamber, enhanced mixing of the flows and a decrease in jet velocity is achieved [100]. In the estimation method for the turbofan engines the same engine dimensions as for the CFM56, which is the engine of the A320, were assumed. These engines have a bypass ratio of 6¹², whereas the Cryo V turbofan engines have a bypass ratio of 8 during take-off. This results in a jet noise decrease of 1 dB [100].
- **Chevrons:** Another design alteration that has an influence on the jet noise is the addition of chevrons to the trailing edge of the exhaust nozzle. The tooth-saw shapes at the end of the nacelle cause axial vorticity of the exhaust flow and therefore improve the mixing of jet flow which results in lower jet velocity [101]. Chevrons are expected to provide a 2.5 dB jet noise reduction.
- **Electric engine phase control:** This technology involves syncing the rotational frequency of the different electric engines in the distributed propulsion such that part of the noise which is emitted by the latter is "cancelled" out. From literature this is estimated to result in a 6 dB reduction of electric engine noise [102].
- **Reduction of landing gear cavities:** Cavities present in current landing gear designs emit cavity tonal noise contributing the aircraft annoyance. Studies show that the removal of these cavities can reduce the landing gear noise with 2 dB [103].
- **Landing gear hub caps:** The cavity present at the wheel hub and rim of the landing gear is also prone to emitting noise. Covering these cavities with a hub cap is found to be able to reduce the landing gear noise levels with 6.1 dB [104].

10.4.4. Results and compliance

Combining the noise estimation and reductions in Subsection 10.4.3 results in Table 10.7 which can be posed to verify the designs compliance with the requirements. The approach angle has not been changed to reach the approach requirement. However, if in a later design stage additional noise reduction were to be required, it would be an effective option.

¹²URL <https://www.safran-aircraft-engines.com/commercial-engines/single-aisle-commercial-jets/cfm56/cfm56-5b> [cited 18 June 2020]

Table 10.7: Cryo-V final noise levels, including a comparison to the Airbus A320

		Approach	Lateral	Flyover
A320 noise	(dBA)	86.1	86.4	71.7
Design requirements	(dBA)	71.1	71.4	56.7
Cryo-V	(dBA)	69.8	70.1	50.4
Compared to A320	(dBA)	-16.3	-16.3	-21.3

10.4.5. Verification and Validation

To assure that the noise estimations made are adequately correct for this stage of design the following verification and validation has taken place, a 5 dB margin is considered satisfactory for each noise source.

Initial Turbofan Engine Estimation - To verify the turbofan engine noise assessment, the fan noise was estimated using a different approach. Equation 10.10 is an empirical equation which computes the fan noise power level as a function of rated motor power (kW) and discharged volume (m³/s). the -10 constant is applied to take into account the axial fan ¹³. The Sound Power Level (SPWL) can be converted to Sound Pressure Level (SPL) using Equation 10.11. Here Q_d is the directivity factor which is assumed to be 1, corresponding to sound being transmitted in full sphere propagation. By comparing both methods at 120 m distance, a difference of 4 dB was found. To verify the assumption of the possibility to apply noise source ranking to estimate jet noise and fan noise from [87], data for different reference aircraft are compared. A NASA paper provides noise source ranking at cutback for a medium range, twin engine aircraft [105]. This gives a difference in jet and fan noise of 7 dB which is in line with the 8 dB difference used in the engine noise estimation.

$$PWL_{fan} = 94 + 20\log(S) - 10\log(Q) - 10 \quad (10.10)$$

$$SPL = PWL - \left| 10\log\left(\frac{Q_d}{4\pi r^2}\right) \right| \quad (10.11)$$

Initial DEP Noise Estimation - To verify results obtained from initial DEP noise estimation another estimation method is used from a different NASA study from 2016 [106] that investigates electric motor noise and compares it to fan noise at flyover, approach and take-off. In order to verify lateral noise obtained during take-off, focus is placed on finding take-off fan noise using the method presented.

For conventional motors the sound power level can be calculated as shown in Equation 10.12 [106]. Sound power level depends on shaft power in kW, rotational velocity ω in RPM and conformal surface area of fan S_c .

$$PWL = 27 + 10\log(P) + 15\log(\omega) + 10\log(S_c) \quad (10.12)$$

Then sound power level is converted to sound pressure level by using Equation 10.11. The study provides measurements of fan noise as compared to motor noise for both 13 MW and 1 MW motor. The results are extrapolated to find that for Cryo-V DEP motor fan noise is 17 dB higher than motor noise. Hence, the fan noise per engine is calculated to be 68 dB by using Equation 10.12 and adding the difference in fan noise based on the model. By applying Equation 10.5 the total fan noise for eight electric fans is 89 dB based on the model.

¹³URL https://www.engineeringtoolbox.com/fan-noise-d_61.html [cited 18 June 2020]

However, the accuracy of the model shall be carefully considered. The authors of the experiment state that the uncertainty of the method is high and newer motors can provide 5 to 10 dB noise reduction [106]. Considering that Cryo-V is a design for the future, it is safe to assume that newer and more silent motors indeed can be used. Then the model predicts lateral take-off SPL of 79 to 84 dBA.

All of the values obtained from the model are in the same range of magnitude as the value found for DEP noise estimation which is 86.5 dBA, at the lateral measurement point. The SPL derived from the NASA model [106] without assuming use of newer motor is 2.4 dB higher than the Cryo-V DEP noise estimate. Considering the average noise reduction for newer motors (-7.5 dB) - the verification model suggests a 5 dB lower value. Discrepancies of the results from used models are within the achievable uncertainty margin, hence the calculation of DEP sound pressure level is verified.

Shielding - For verification of the engine shielding attenuation the results from the method obtained in Subsection 10.4.3 are compared to the results from Equation 10.13 based on a method using correction factors to the Fresnel Number obtained from [94, 107].

$$A_{tt} = 10 \log \left(\frac{\sqrt{2\pi N}}{\tanh \sqrt{2\pi N}} \right) + 5 - 10 \log \left(1 + \frac{N}{N_{side1}} + \frac{N}{N_{side2}} \right) \quad (10.13)$$

Where N is the Fresnel Number of the longest edge and N_{side} are the Fresnel Numbers of the side edges. The computed Fresnel Number were verified by checking their behaviour (positive/negative) corresponded to what is described in [94] when a different shielding case was inputted.

The results show that the shielding estimations are reliable as shown in Table 10.8.

Table 10.8: Engine shielding method verification

		Approach		Lateral		Flyover	
		Verification	Computed	Verification	Computed	Verification	Computed
Distributed Propulsion	(dB)	31.20	30.49	13.28	13.28	24.89	24.18
Turbofan	(dB)	29.41	28.53	12.19	12.19	23.10	22.22

For validation, in [94] the results from the method described with Equation 10.13 were compared to results from the NASA Aircraft Noise Prediction Program (ANOPP) where it was found that the results differ slightly for high frequencies. However for this stage of the design only the frequency spectrum between 1000 Hz and 5000 Hz was considered, for which the computed results followed the experimental results. Therefore the shielding results can be considered reliable.

Landing Gear Noise - A tool developed by another team, investigating the same topic, was acquired which estimates the nose landing gear noise [108]. This tool estimates the sound pressure level across a wide frequency range which is then integrated to determine the overall sound pressure level. Implementing the parameters of the Cryo-V into this tool gives an OASPL of 79.9 dB for the nose landing gear. This gives a difference of 1.8 dB. For the main landing gear the same method can be applied. Therefore the landing gear noise estimate is verified.

Total Aircraft Noise - For the final verification of the total aircraft noise, the final results for cumulative noise were compared to literature. Studies [7] estimate the cumulative noise reduction from BWB designs to be of the order of 41.6 dBA to phase 4 aircraft. From the estimations made in Subsection 10.4.2 and Subsection 10.4.3 the current cumulative estimation for the Cryo-V design compared to the phase 4 aircraft is 54 dBA. Both results are of the same order of magnitude and the higher reduction of the Cryo-V can be explained by the use of electric propulsion, in contrary to high-bypass turbofans, and the more extensive addition of noise reduction technologies. This estimation is accurate enough to be used at this stage of the design however further validation for the particular case would still be required.

Design maturity	Contingencies (%)																		
	Mass budget					Power budget				Energy budget		Emissions		Noise			Costs budget		
	MTOW	OEW	Propulsion	Payload	Fuel	Turbofan power	DEP power per unit	On-board systems	Endurance	Range	CO ₂	NO _x	Lateral	Flyover	Approach	Development	Production	Operations	
Conceptual estimates	15	15	20	7	15	20	20	30	15	10	0	15	30	30	30	30	20	30	
Final conceptual design	10	10	15	5	10	10	15	20	10	5	0	10	20	20	20	20	10	20	
Detailed design	7	7	10	5	7	7	10	10	7	5	0	7	15	15	15	10	8	10	
Manufacturing	5	5	5	5	5	5	5	5	5	5	0	5	10	10	10	5	5	5	
Flight tests	3	3	3	3	3	3	3	3	3	3	0	3	5	5	5	0	0	3	
Final product	0	0	0	0	0	0	0	0	0	0	0	0	0	0	0	0	0	0	

Figure 10.12: Budget breakdown and contingencies of the Cryo-V

10.5. Resource Allocation and Budget Review

Budget estimation and contingency management are crucial components of every design project. It is vital to understand the developing accuracy of all parameters and methods used to obtain a successful result. With increasing design maturity, the accuracy increases and, therefore, the contingencies can be lowered. This can be managed using budgets. Mass, power, energy, emissions, noise and cost are considered the most significant budgets for the Cryo-V and are shown in Figure 10.12. The contingency margins presented depend on the budget considered and on the specific design phase, adapted from [109].

Range, endurance and payload mass are set as top level design requirements and therefore require an accurate estimation. During class II, the design focuses on mass estimation and it is, therefore, assumed that the contingency can be lowered to 10%. For the power budget, there is more uncertainty since the on-board systems power is estimated using empirical relations. Furthermore, the DEP power depends on many factors, such as fan efficiency and flow conditions, that could not be accurately implemented in the iteration. Production costs are considered to be measured to 10% accuracy, while development and operations cost to 20% because less data is available. The noise prediction models used are still fairly general at the conceptual design level and are, therefore, also given a 20% contingency.

Operations and Logistics

The Cryo-V is characterised by its unconventional shape. In order to be competitive with the Airbus A320 or similar aircraft, the Cryo-V has to meet a number of operational requirements as presented in Section 2.2. In this section, aircraft operations are investigated, and the benefits and challenges that come with the Cryo-V design are presented.

11.1. Airport Operations

Ground Operations - To be able to service at least the same amount of airports the Airbus A320 can [17], the Cryo-V has to be classified as a type 4C aircraft by the ICAO ¹. From this classification, dimensional requirements of wingspan being less than 36 m (**MRA.SYS.PERF3.7**) and main landing gear span being less than 9 m (**MRA.SYS.PERF.3.8**) arise. In addition to this, turnaround time should be less than 45 minutes (**MRA.SYS.PERF.3.9**) for competitiveness with the Airbus A320 [110]. These dimensional constraints are implemented in the design, to make sure the requirements are met. The turnaround time requirement is less specific, which is why extra analysis on ground operations is performed.

According to [110], 25 minutes are typically reserved for passenger boarding, in this time no alternative activities such as cleaning or catering can be performed. It is thus of great importance that boarding is a smooth and time-efficient process. It is concluded that the unconventional shape of the aircraft is no reason for longer boarding time. When two boarding bridges are used, each hull structure can be boarded at the same time, as visualised in Figure 11.2, and total boarding time could be reduced to 20 minutes due to less aisle interference [110]. Other boarding strategies can be utilised by the airline operator, for efficient time-management and further reduction of turnaround time.

Another driving parameter in turnaround time is accessibility for ground crew. As the Cryo-V consists of two connected, passenger carrying hull structures, the access points for ground crew are selected carefully. Ground crew takes care of cargo, fuel, galley service, potable & waste water, electric power, and push-back before take-off. In Figure 11.1, these access points are shown, along with a typical layout during gate position operations. It is concluded that no extra vehicles or services are required during gate operations, compared to the Airbus A320. Approximately the same number of access points for cargo, fuel and galley service are present. The main difference is in the lateral symmetry of fuel tanks and cargo holds, where the Airbus A320 has front and aft compartments. Especially the port side cargo loader should be carefully selected, as it is located next to the aft boarding bridge. Sufficient access is available for fuel trucks, and fuel tanks could be reached from both lateral sides of each tank. According to [111], it is possible to fuel a hydrogen aircraft the size of the Cryo-V at gate position in approximately 20 minutes in total. A turnaround timeline is provided in Figure 11.2. Compared to conventional aircraft, boarding time is reduced from 25 to 20 minutes, because of the multiple boarding bridges granting access to both hull structures. Refuelling time is increased from 10 to 20 minutes, to provide a safe margin allowing for uncertainties in future infrastructure and fuelling equipment. Cargo loading is reduced from 12 to 8 minutes, to account for the reduction in cargo

¹URL https://www.skybrary.aero/index.php/ICAO_Aerodrome_Reference_Code [cited 19 June 2020]

11.2. LH₂ Logistics

weight compared with conventional aircraft. It is concluded that the turnaround time requirement is met, and sufficient working space is available for ground crew in order to achieve this.



Figure 11.1: Gate position layout of the Cryo-V

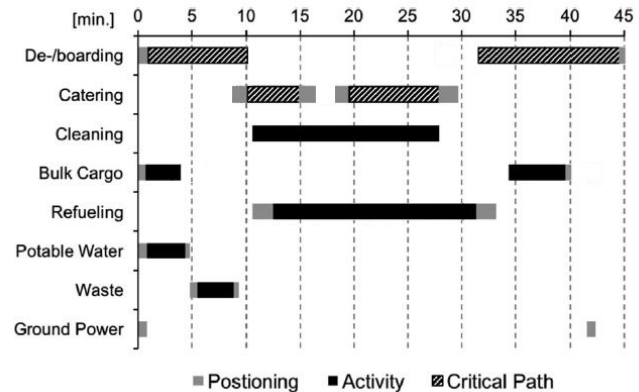


Figure 11.2: Turnaround timeline for the Cryo-V, adapted from [110]

Flight Operations - Another important parameter regarding competitiveness of the Cryo-V is the range it can operate at. As discussed in Subsection 10.2.1, the range of the Cryo-V carrying 200 passengers is 6150 km. For comparison, for the same amount of passengers the Airbus A320 can only fly 3800 km [17]. Based on [23], the average trip length of the Cryo-V is expected to be 1500 km. In Figure 11.3, the maximum range of the Cryo-V is shown, compared to the Airbus A320, with Schiphol as base airport and maximum payload (200 pax). In addition, the astonishing range of 8280 km of the Cryo-V XLR option is provided as well.

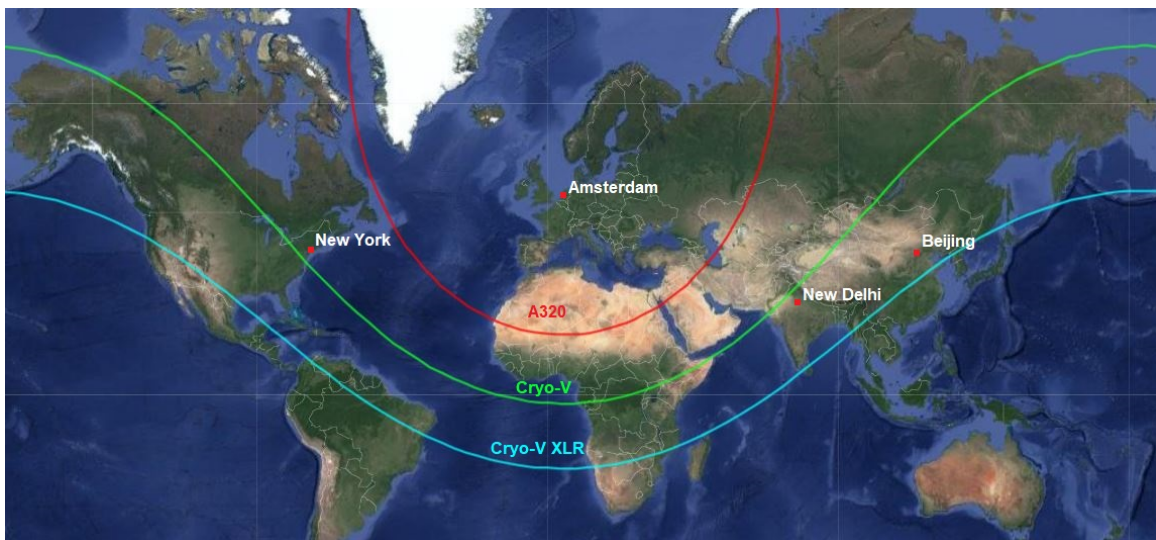


Figure 11.3: Range of the Airbus A320 and Cryo-V, departing from Amsterdam, for maximum payload (200 pax).

11.2. LH₂ Logistics

As LH₂ is the energy source of the Cryo-V, a new challenge arises. Conventional aircraft use petroleum-based fuels, and infrastructure is fully focused on this fuel. Hydrogen supporting infrastructure for large scale usage is still lacking, but some solutions are already present.

Existing solutions are mainly focused on short-range transport. Nowadays, up to 50 000 L of LH₂ can be transported by road trucks². This is a promising short-term solution, especially because a number

²URL <http://www.hydroville.be/en/waterstof/hoe-transporteer-je-waterstof/> [cited 19 June 2020]

of major airports in the world is already located within 60 km from a LH₂ liquefaction plant [14]. On top of that, conversion of natural gas pipelines could allow for LH₂ transportation to the airport. Larger amounts of LH₂ are already being transported by tanker ships, but the feasibility to supply airports this way in the near-future should be questioned, as a lot of new infrastructure is required. Ultimately, based on current expectations, LH₂ will be produced on the airport itself in the future. This option becomes feasible if more aircraft start using LH₂.

To adapt to the lacking infrastructure immediately in the near future, the Cryo-V will be supported by LH₂ carrying road trucks. Trucks can carry up to 50 000 L of LH₂ which corresponds approximately to a maximum range trip of the Cryo-V. This way, impact on road traffic is negligible. In addition to that, because of the road transport being short-range only, climate impact from transportation is insignificant. As soon as more aircraft start using LH₂ as a fuel, pipeline transportation becomes more feasible and is highly recommended.

Optimally, LH₂ would be produced at the airport, where electricity could be produced in a green way, and water is highly available. Such a plant would supply all hydrogen powered vehicles at the airport. Road traffic is not impacted this way, and climate impacts caused by transportation are reduced. Only when demand is sufficient, construction of such a plant would be economically interesting, and theoretically feasible. In 1987, it was already investigated if a pilot plant producing 30 tonnes of LH₂ per day could be built at Zurich Airport [112]. Conclusion of this research was that for economical reasons construction would be unfeasible. However in the near future demand could rise and costs could drop quickly. The influence of the Cryo-V alone on global infrastructure might not be large enough to achieve this, but if demand rises in the future, on-site production of LH₂ is highly recommended.

11.3. End-of-Life Procedures

A typical aircraft can generally operate for 20 to 25 years. After this time, its components start to show wear to a level economically unfeasible to maintain³. Furthermore, as aircraft technology experiences rapid improvements, a newly build aircraft will be likely to operate at lower cost and with better efficiency. Furthermore, they generally have improved passenger comfort levels, which attributes to airlines having to renew their fleet to remain or become more competitive.

Once an aircraft has reached its operational End-of-Life (EoL), care should be taken to limit environmental waste as much as possible. Possible strategies include reusage of components or parts, recycling of materials, incineration of waste and land-fill. The first two strategies results in waste regaining value as a new product and lowering the need of raw material extraction. The later two strategies are characterised as invaluable waste, as they both dispose the material. Incineration does have a less significant environmental impact than land-fill as it does not include material dumping [113].

Value Regaining - EoL solutions are governed by economic incentives. When considering decomposing an aircraft for value regaining, a structural material or part can either be recycled or reused. As cleaning, repairing, re-certifying and selling components for reuse generally consists of 90-95% of the total regained value [114], reuse of parts is maximised during aircraft disassembling. From the aircraft components, the engine is considered to be the most valuable part. Furthermore, the landing gear, electrical power units, flight controls and navigation system are other valuable parts for reuse, making up around 70% of airframe value, excluding the engines [114]. Any remaining material, mainly the wing box and aircraft skin, is then recycled making up the remaining part of the regained value.

There are several associations that operate using this principle, some of which are Aircraft Fleet Recycling Association (AFRA)⁴ and Aircraft End of Life Solutions (AELS)⁵. These associations are specialised in disassembling and dismantling aircraft to maximise the value through repairing, re-certifying and reusing components, as well as recycling. As the Cryo-V is mainly built out of commonly

³URL <https://www.proponent.com/aircraft-recycling/> [cited 21 June 2020]

⁴URL <https://afraassociation.org> [cited 17 June 2020]

⁵URL <https://aels.nl> [cited 17 June 2020]

used metallic materials, it is expected that these organisation can easily deal with the dismantling and maximising the value regaining of the Cryo-V.

Invaluable Waste - Any remaining material, that cannot be reused or recycled is then left for either incineration or land-fill. The main components ending up for land-fill is the cabin interior, including textiles and fibre lining [113]. As current aircraft increase the use of fibrous materials, the invaluable waste is expected to increase, as reusing or recycling of these materials is considered challenging if not impossible [113]. As the Cryo-V uses commonly used metals, this problem does not occur resulting in less invaluable waste ending up as land-fill. Finally, as a recommendation for the next design stage containing the detailed cabin interior, careful attention is required to limit the land-fill materials as much as possible, encouraging innovative solutions as presented for example by KLM, reusing worn uniforms of stewardesses to create interior cabin seating and carpets ⁶.

Estimated Value Regaining Target - Calculating an accurate recycling percentage requires some detailed structural EoL characteristics which is often considered confidential [113]. Therefore, an estimation is made based on available aircraft EoL solutions. In 2008, Airbus conducted an EoL project called PAMELA [113], where an Airbus A300 was dismantled. This project resulted in 85% of reuse/recyclability with the product being used either in the same industry or in another field, and 15% of the material weight ending up as land-fill [113], mostly consisting of cabin interior. Nowadays valuable weight regaining percentages go up to 90% ^{7 8}. As the Cryo-V increases the use of commonly used metals, the non-recyclable/reusable part is expected to decrease, resulting in an estimated value regaining target of **more than 90%**.

11.4. RAMS aspect

RAMS stands for Reliability, Availability, Maintainability and Safety; It assesses these aspects over the life cycle of the aircraft to assure a safe and available product. The four aspects are discussed below.

11.4.1. Reliability

To accurately estimate the complete reliability of the aircraft, the reliability of each individual component is required. This is not possible at this design stage. Therefore the reliability of the A320 (99.6% [27]) is taken as benchmark. The reliability of certain subsystems is estimated and compared to estimate the reliability of the Cryo-V.

Structural Reliability - "The fusion of the wing and fuselage results in a more distributed load over the span of the aircraft. This can result in a simplified structure with fewer high stress concentrations. Even though the pressurisation of the fuselage might lead to structural complications, the structural reliability of the Cryo-V should be higher than that of the Airbus A320." [3]

Control Surface Reliability - "The Cryo-V uses elevons and does not use flaps. Both these factors reduce the number of (hydraulic) parts required compared to the Airbus A320. This will lead to an overall increase in reliability.

These two factors and the fact that an APU is not necessary increase the Reliability of the Aircraft. As no detailed design has been performed and no precise data is available, the increase in reliability due to these factors will be 1% with respect to the A320 as a first order estimate. This estimation should be revised and further worked out in the next design phase.

For all other subsystems except power and propulsion (non propulsive electrical, avionics, landing

⁶URL <https://klmtakescare.com/en/content/new-cabin-interior-sustainable-design-> [cited 21 June 2020]

⁷URL <https://www.airbus.com/company/sustainability/environment/product-responsibility.html#Rec> [cited 21 June 2020]

⁸URL <https://www.greenaironline.com/news.php?viewStory=866> [cited 21 June 2020]

gear etc.) a constant reliability is assumed with respect to the A320. These parts of the Cryo-V are relatively standard, thus comparably reliable as these parts on the A320.

Propulsion - The In-Flight Shutdown (IFSD) rate of the CFM56 engines of the A320-200 equals 0.003 (or 1 failure every 333 333 flight hours)⁹. This equals a reliability of 99.9995 percent. The same reliability will be assumed for the Cryo-V turbofans. According to the electric aircraft symposium of 2015¹⁰ electrical engines with all their components (wiring, circuits, storage etc.) can be expected to have similar reliability as a traditional turbofan (even though the electrical motor itself is much more reliable [115]). So the assumption is made every extra distributed engine will have a reliability of 99.9995 percent.

A 2009 study found the average failure rate of SOFC is around the order of 10⁻⁶ per cycle[116]. This is also taken into account for the Cryo-V.

Another important factor in the reliability of Cryo-V is the cryogenic storage and especially the pumps and valves of the system. A more recent study from the journal of energy science and engineering found a failure rate of 5.19 × 10⁻⁴ of liquid hydrogen fuel cells in mobile applications [117]. This takes into account the whole energy storage and conversion from tank storage to electrical power. This figure will be used for the Cryo-V as a conservative estimate, as the reliability is expected to improve in future applications.

Estimation - As the total Reliability is the product of the reliability of its components, the new reliabilities can be multiplied with the overall A320 reliability of 99.6%. The two turbofans are already regarded in the original value, so only the distributed propulsion and structural/control reliability changes are regarded. This leads to an overall reliability of 99.54% . Slightly less than the A320.

$$R_{tot} = \prod_{i=0}^N R_i \tag{11.1}$$

11.4.2. Maintainability

As described in the midterm report [3], the Cryo-V will adhere to the so called "ABC" check system. The checks are in ascending order regarding effort and man hours required. The *A* check is the most routine and relatively quickest inspection, where for example visual structural inspections are performed, hydraulics are lubricated and emergency systems are inspected. The *B* check is disregarded for the Cryo-V, as many modern aircraft do [118]. Instead the *B* check tasks are divided between *A* and *C* checks. In the *C* check individual components are inspected. This makes it a much more time and labour intensive procedure. Finally the most intensive maintenance procedure is the *D* check. Here large parts of the aircraft are taken apart and are overhauled. Intervals and duration can be found in Table 11.1. Further explanations can be found in the Midterm Report [3].

Table 11.1: Cryo-V maintenance checks [118]

Maintenance Checks	Flight Hour Intervals	Duration
A Check	750 (750 cycles or 4 months)	6-24 hours
C Check	7500 (7500 cycles or 24 months)	1-2 weeks
D Check	6/12 years	2 months

11.4.3. Availability

The availability of an aircraft depends on both the reliability or Mean Time to Failure (MTTF) and the maintainability or Mean Time to Repair (MTTR): The MTTF indicates how often an aircraft fails, the

⁹URL <https://www.cfmaeroengines.com/press-articles/now-thats-a-reliable-engine/> [cited 9 June 2020]

¹⁰URL <https://www.avweb.com/ownership/electric-aircraft-reliability-not-so-simple/> [cited 10 June 2020]

MTTR indicates the time it takes to repair it.

$$\text{Availability} = \frac{\text{MTTF}}{\text{MTTF} + \text{MTTR}} \quad (11.2)$$

When analysing availability also non-scheduled maintenance, which includes failures, have to be taken into account. The range of repair times is large, as some failures, like a windscreen failure, can be fixed in half an hour and some, like engine failure, can take weeks. It can be assumed an average non-scheduled failure takes as much time as an A-check; approximately 24 hours [118].

As stated in the Midterm report [3], "to calculate availability, one period from C to C check, which consists of 7500 flight hours (Total MTTF), is taken. The average flight length of an Airbus A320 is 1:49 hours, even though it can fly significantly longer ¹¹. This results in 4120 flights." With a reliability of 99.54%, approximately 19 flights will have an operational failure during or before flight. This results in a total MTTR of 152 lost flight hours, assuming the plane flies 8 hours a day. Scheduled downtime will be ± 2 weeks or 112 lost flight hours for the C checks and 10 days or 80 lost flight hours for the A checks. This results in an availability of 95.61% (Equation 11.2).

11.4.4. Safety

Safety is closely related to technical risk, so the main elements and contingencies are treated in the Technical risk Chapter 14. Potential safety hazards are summarised here. The Cryo-V design involves preventive measures for the listed risks and they shall be implemented during the detailed design process.

Cryo-V Critical Safety Concerns

Strong Gusts Vulnerability - The Flying-V concept has, due to its blended form, a relatively low wing loading. This makes the aircraft vulnerable to gusts and stability problems. This is partly compensated by a larger vertical tail.

Explosion Hazard - Hydrogen is very flammable and a tank leakage in a confined space may cause an explosion hazard. Hence, strong insulation, pressure relief valves and venting system are installed.

Fire Hazard - Electric propulsion units work at high voltages and fuel cells operate at high temperature inside turbofans. Both can cause potential fire hazard.

Integrated Engine Risks - Integrated engines on top of the wing pose a risk to the structural integrity of the wing/fuselage when catastrophic failure occurs.

¹¹URL <https://www.flightglobal.com/airbus-begins-tests-to-extend-service-life-of-a320-family/78350.article> [cited 15 May 2020]

Life Cycle Assessment

A Life Cycle Assessment (LCA) is a useful tool to evaluate the Environmental Impact (EI) of a product, process or system based on material in and outflows over its life time. This enables better understanding of these material flows and their influence on receiving ecosystems. LCAs are generally performed using a standardised methodology prescribed by the International Organisation for Standardisation (ISO) in ISO 14040 and 14044 ¹, which allows for reliability and transparency. Here a distinction between four phases is made ²:

- | | |
|------------------------------|---|
| 1. Goal and Scope | This phase defines the purpose, scope (boundaries), functional unit and intended audience of the LCA. |
| 2. Inventory Analysis | This phase identifies and measures material in and outflows of the considered processes. |
| 3. Impact Assessment | This phase categorises the material flows identified in the previous phase to environmental impacts using well defined methodologies. |
| 4. Interpretation | This phase organises results from previous phases to present a comprehensible output used for decision making. |

Due to time limitation, performing a full LCA is outside the scope of this project. Instead, use is made of performed LCAs of the Airbus A320 [23, 119, 120] and A330 [121], which analyses life cycles that are applicable to general aviation and can therefore be adopted to the LCA of the Cryo-V. The created LCA for the Cryo-V is first created for the Airbus A320 to serve as verification and validation of the method, after which the inventory analysis is modified to present the Cryo-V. Finally, the presented EI comparison between both aircraft is based on two different inventory analysis but the same impact assessment calculation method.

12.1. Goal and Scope

As the main goal of this analysis is to obtain an overview of EI compared to the Airbus A320, it is ensured that the life cycles covered are similar to the ones in the performed LCAs. The considered life cycles between those LCAs are similar, but only differ for the EoL cycle, as both [23, 119] do not include it, whereas [120, 121] do. However, the later two LCAs both conclude this phase to have a negligible effect on the final EIs. Also, because accurate values for EoL solutions are often shielded by companies [113], it is decided to not include the EoL cycle in this LCA. This results in the identification of cycles presented below, where the scope ranges from the extraction of raw materials up to dispersion into receiving ecosystems covering manufacturing/production and aircraft/airport operations.

Manufacturing Cycle - The manufacturing cycle includes processing and extracting raw materials, manufacturing components from these materials and transporting them to final assembly.

¹URL <https://www.iso.org/home.html> [cited 11 June 2020]

²URL <https://www.pre-sustainability.com/sustainability-consulting/lca-methodology-basics> [cited 11 June 2020]

Flight Operational Cycle - The flight operational cycle includes Landing and Take-Off (LTO) cycles, cruise phase and airport operations.

Fuel Production Cycle - The fuel production cycle covers the production from cradle to gate. This includes raw material extraction, transport of these raw materials, hydrogen production and transportation to the airport.

A commonly used functional unit for LCAs of transportation methods is *Passenger Kilometre* (PKM) [122]. This unit allows for normalising the LCA results to enable comparison. To compute this value, use is made of the average flight distance flown by the Cryo-V, equal to 1500 km as stated in Chapter 11; and a seat load factor of 0.815 [120]. Furthermore an operational life time of 22 years is used, equivalent to the Airbus A320 [23].

12.2. Inventory Analysis and Impact Assessment

This section presents the identification and measurements of the material in and outflows and converts these material flows to EIs for the considered life cycles.

12.2.1. Manufacturing Cycle

As explained previously, the manufacturing cycle consist of three processes: 1. material usage, 2. component manufacturing and 3. transportation to assembly.

For the **material usage**, a material breakdown structure is composed from the Cryo-V subsystem design, shown in Table 12.1. This presents the materials used for the main structural components of the Cryo-V. Each material has its own environmental characteristics, as some materials require more energy intensive manufacturing processes, are less available or impact other ecosystems more than others. To assess these EI for all used materials, use is made of the Ecoinvent database in combination with Idemat [123], where access was obtained from Delft University of Technology. Both database contain a large number of materials and processes that are analysed using the ReCiPe midpoint category method [28], resulting in a list of quantified EI for a given amount of material use or process. A thorough explanation of all EI and its considerations is presented in [28]. These EI obtained from Ecoinvent are assessed for the same scope as in this LCA, from cradle to gate or cradle to grave. All materials shown in Table 12.1 are listed in Ecoinvent from which the total EI of the material usage process are found.

For the **component manufacturing process**, use is made of [122], which presents a simplified method to calculate the EI of this process based on the amount of seats in the manufactured aircraft. For each seat it is said that 2640 kg of CO₂, 1.97 kg of NO_x and 23 540 kg of H₂O is produced, which can be converted to ReCiPe EI by use of a conversion table provided by [122]. These calculations are based on information published by Airbus and are very simplified. Because this process is found to minimally affect the final results [122] and no significant differences exist in the manufacturing process of the Cryo-V and the Airbus A320, the method is adopted in the LCA.

Finally, to include the **transportation to assembly** it is found that 16 700 tn km of air transport and 13 700 tn km of road transport is needed for the Airbus A320 assembly [120]. To convert this method and weight of transportation to EI use is made of the Ecoinvent database, which contains specific data regarding air and road transport. Here it is assumed that the transportation of manufactured parts to final assembly is the same for the Cryo-V.

12.2.2. Flight Operational Cycle

This life cycle is further split into: 1. LTO cycles, 2. cruise flight and 3. airport operations.

For the **LTO cycles** use is made of the calculated emissions of the Cryo-V as explained in Section 10.3. This resulted in a total of 7.839 kg of NO_x and 3538 kg of H₂O emissions. To convert this

12.3. Interpretation

Table 12.1: Structural material breakdown of the Cryo-V

Structural Part	Material	Weight (kg)		Material	Weight (kg)
Fuselage/Wing	Aluminium	13 883			
Aft Wing	Aluminium	5479			
Engines	Aluminium	1561		Aluminium	23 556
	Nickel	174		Steel	6893
	Titanium	329		Titanium	329
	Others	19		Nickel	174
Landing Gear	Aluminium	100		Polyurethane	1106
	Steel	2500		Zirconia Cermet	879
	Others	337		Yttria	55
Fuel Tanks	Aluminium	2533		SDLM	165
	Polyurethane	1106		Others	516
	Others	160		Total	33 672
Fuel Cells	Steel	4393			
	Zirconia Cermet	879			
	Yttria	55			
	SDLM	165			
Total		33 672			

to ReCiPe EI use is made of the conversion table provided by [122].

The **cruise flight** is analysed in the same way, where from Section 10.3 it is found that the NO_x emissions are equal to 0.0585 g/km and the H₂O emissions to 5.256 kg/km. By using the average flight distance of 1500 km the total emissions are found to be 0.088 kg of NO_x and 7884 kg of H₂O. To convert this to EI use is made of the conversion table provided by [122].

Finally, the **airport operations** turned out to be less straight forward to include as an elaborate airport operational study would be necessary. Therefore, it is chosen to use the EI of this process from [23], that include the EI of airport production. As this phase is considered to remain constant for the Cryo-V and the Airbus A320 this is assumed to be justified.

12.2.3. Fuel Production Cycle

As the Cryo-V uses LH₂ as fuel, the fuel production cycle changes significantly compared to the Airbus A320. Therefore, care should be taken to investigate this cycle into more detail. The Ecoinvent database does include the production of kerosene, however it does not contain the production of hydrogen fuel. Instead, use is made of a documented LCA of hydrogen production methods [124]. Current and future hydrogen production methods are evaluated by modelling the required processes using the Ecoinvent database and present ReCiPe EI of the production of 1 kg hydrogen of various production methods. Based on the amount of hydrogen the Cryo-V uses for an average flight, the EIs of the fuel production cycle are modelled for various production methods which can then be compared to each other, as well as to the fuel production of the Airbus A320.

12.3. Interpretation

Several EIs are analysed by using the ReCiPe method. However, in the aircraft industry the main focus is on the climate change EI as this becomes very dominant when burning fossil fuels, shading the other EIs. It has been identified that the aircraft operational phase contributes for 80 - 90% to the total climate change EI, and the remaining percentage by the fuel production process [122]. The manufacturing cycle, airport operations and EoL cycle are all found to contribute minimally to the total

climate change [23, 119, 121].

As the Cryo-V moves entirely from burning fossil fuels to LH₂, the emissions are drastically changed by eliminating CO₂ entirely and reducing other harmful emissions significantly, as shown in Table 10.3. This results in a significant reduction of the climate change EI of the Cryo-V, resulting in other processes in the aircraft life cycle to have a more significant effect on the overall sustainability.

12.3.1. Climate Change Environmental Impact

As stated above, a significant change in climate change is achieved as shown in Figure 12.1a, where the flight operational cycle is drastically reduced to only contain the aircraft operations impacts. This graph also shows that the fuel production EI is increased from 18.9 g of CO₂ eq. PKM to 26.5 g of CO₂ eq PKM, however, this is heavily depended on the used hydrogen production which is discussed in Subsection 12.3.3. Furthermore, from Figure 12.1b it is clear that the climate change of the manufacturing cycle is reduced by 48%, however, as the EI of this phase only occurs once and is normalised over the entire life cycle, the final contribution is negligible when considering the functional unit PKM.

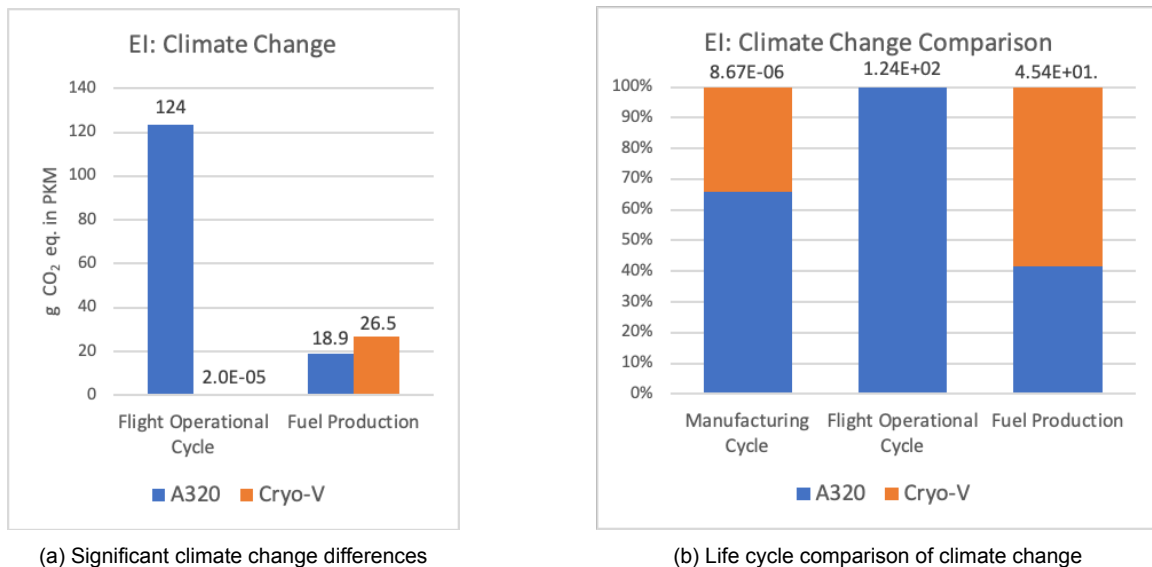


Figure 12.1: Comparison of the climate change environmental impact between the Airbus A320 and the Cryo-V

12.3.2. Material Environmental Impact

As air travel continues to grow, aircraft demand is expected to follow. On the short term, the EIs are mainly caused by the manufacturing cycle, which should therefore not be ignored, even though this assumption can be made considering the entire life cycle of the aircraft, as stated above. From Figure 12.1b, it is shown that the climate change impact of the manufacturing cycle is reduced compared to the Airbus A320. This reduction is further analysed in Figure 12.2 and 12.3 where the EIs are categorised for the materials used.

The main differences between the materials used on the Airbus A320 and the Cryo-V is the elimination of Carbon Fibre Reinforced Polymers (CFRP) for the Cryo-V and the increase in usage of aluminium. As shown in Figure 12.2a the largest EI are caused by the usage of CFRP, even though only 3345 kg is used. This shows the large EI CFRP has, which is entirely eliminated for the Cryo-V.

Furthermore, as the Cryo-V integrates fuel cells which are not used on the Airbus A320, the EI of those materials on the total material usage EI is analysed. Figure 12.3 presents the EI of the materials used, where Aluminium is not displayed to increase readability. From this figure it becomes clear that the EI of these additional materials do not affect the overall EI of the material usage phase, mainly due to the small amount used.

12.3. Interpretation

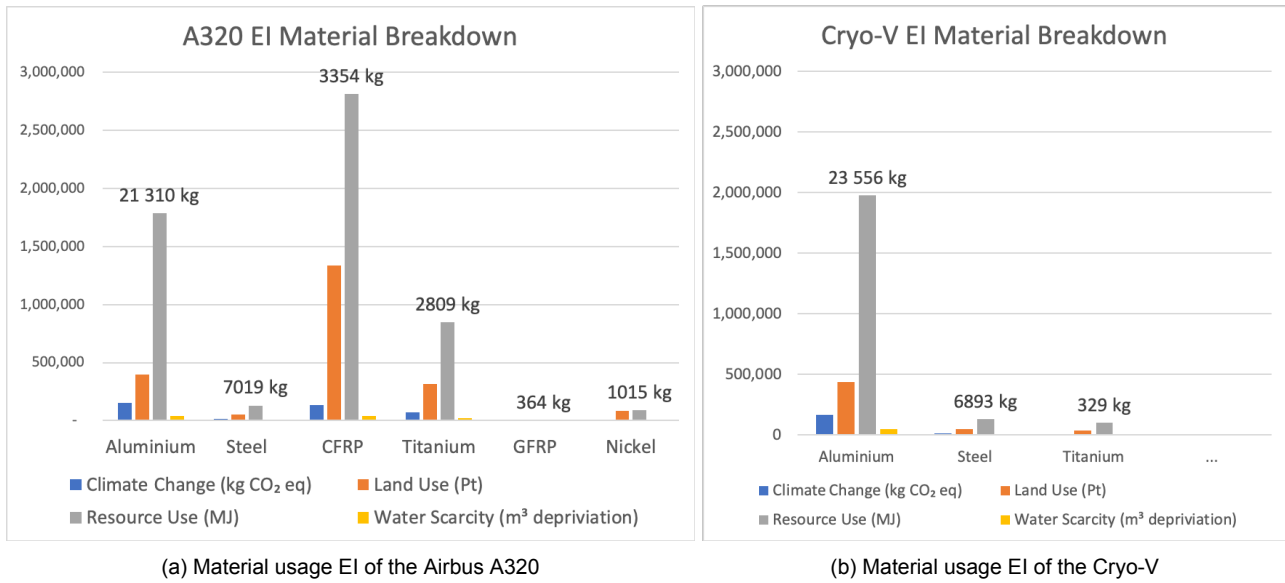


Figure 12.2: Environmental impact of the material usage of the Cryo-V and A320, including a material breakdown

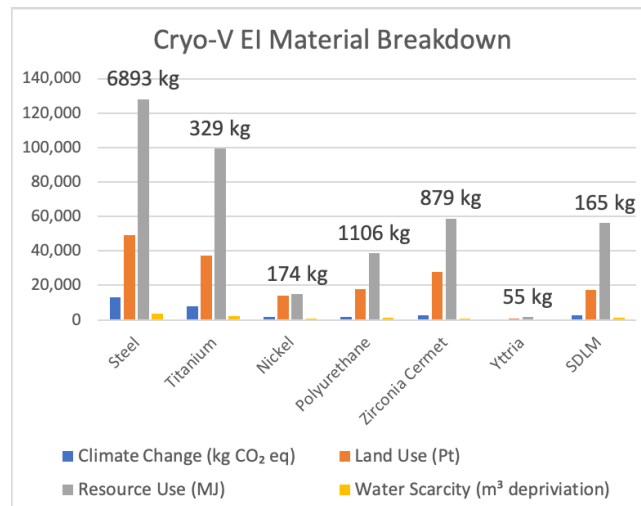


Figure 12.3: Environmental impact of the Cryo-V, not showing aluminium

12.3.3. Fuel Production Environmental Impact

Finally the fuel production cycle is analysed for its EI. Hydrogen can be produced using several methods and is in general a more energy intensive process than kerosene production [124]. This energy can come from both renewable and non-renewable sources which significantly affect the EI of the fuel production methods.

Currently, most hydrogen is produced using Steam Methane Reforming (SMR) which uses non-renewable energy sources [124]. Hydrogen can also be produced using electrolysis, which is generally said to be more environmental friendly [124]. Current electrolysis technologies are the Proton Exchange Membrane (PEM) and the Solid Oxide Electrolysis Cell (SOEC), which can use both renewable and non-renewable energy sources. From [124] it is found that the least EI are caused by the SOEC using wind energy, which is used to model the fuel production EI of the Cryo-V, as shown in Figure 12.4a. The fuel production EI when using SOEC with non-renewable energy, PEM with wind energy and the SMR methods are shown in Figure 12.4b, where also the EI of the kerosene production of the Airbus A320 is shown as baseline. This comparison clearly shows that the fuel production EI of the Cryo-V has the potential to greatly increase the EI compared to the Airbus A320. Therefore, it has to be ensured the hydrogen is produced by electrolysis with renewable energy.

12.4. Verification and Validation

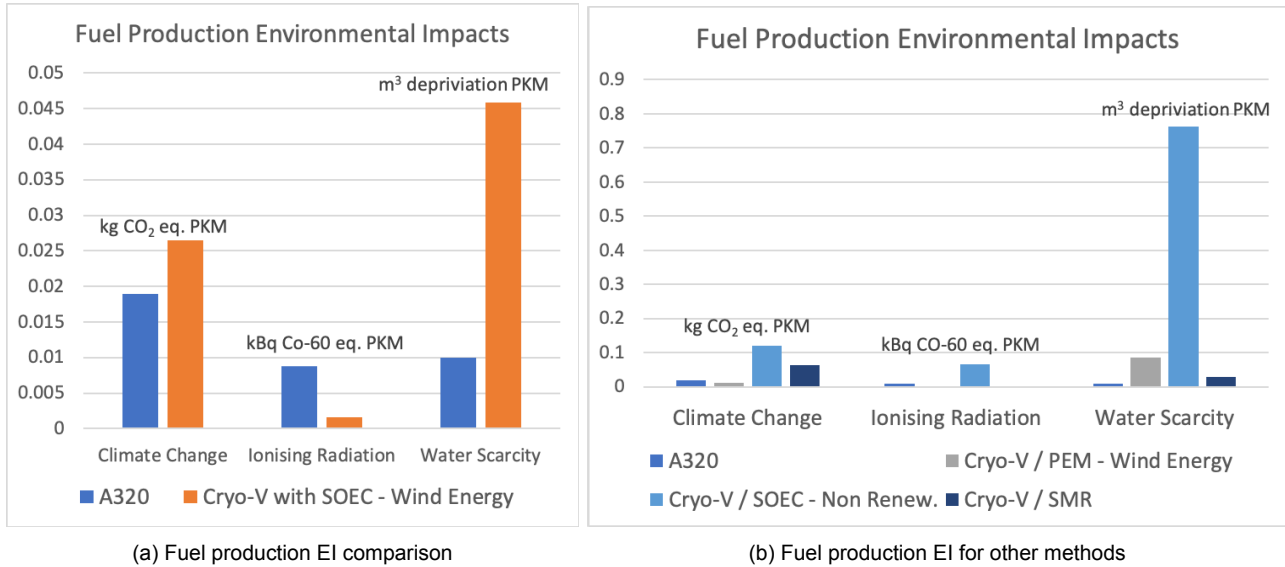


Figure 12.4: Fuel production EI comparison between the Airbus A320 and the Cryo-V

12.3.4. Final Considerations and Recommendations

As a final note, due to the significant reduction in the climate change EI, it no longer shadows the other EI. Looking at Figure 12.4a it is shown that water scarcity is increased compared to the Airbus A320 and new non-metallic materials are introduced in the Cryo-V which potentially affect the environment differently. Therefore, a more detailed look is recommended at other EI than climate change in the next design phase.

Furthermore, the EoL cycle is ignored in this LCA due to the lack of available data. In the next design phase a detailed case study should be conducted to identify the percentages of valuable and non-valuable waste for all used materials, which can then be integrated in the LCA by lowering the manufacturing cycle EI as resource extraction is reduced by recycling or reuse.

12.4. Verification and Validation

As the presented LCA uses a simplified method combining well documented LCAs, care should be taken that the obtained results are accurate and valid. LCAs are a recent discovery, resulting in little information to be available. At the time this report is written, the most complete LCA is that of the Airbus A330 from Lopes [121]. Following this report, two Master Thesis perform a similar LCA on the Airbus A320, [23, 119] Jemiolo and Lewis, respectively. Furthermore, Scholz et al [122] presents a very simplified LCA method on the Airbus A320 and Howe et al [120] present another short LCA on the Airbus A320, but rather uses Eco-Indicator 99 as EI categories instead of the ReCiPe method, making comparing EI difficult. All these LCA use a software called Simapro to convert the material flows to EI and do not document about this conversion. Therefore, the main focus of this V&V is on the conversion between material flows to EI, where both a combination of a simplified conversion is used from Scholz et al [122] and direct documentation of material/process EI of the Idemat database as previously described.

The used inventory analysis material flows for the Airbus A320 LCA is presented in Table 12.2. These material flows are then converted to EI using the methods described in Section 12.2.

12.4.1. Environmental Impacts

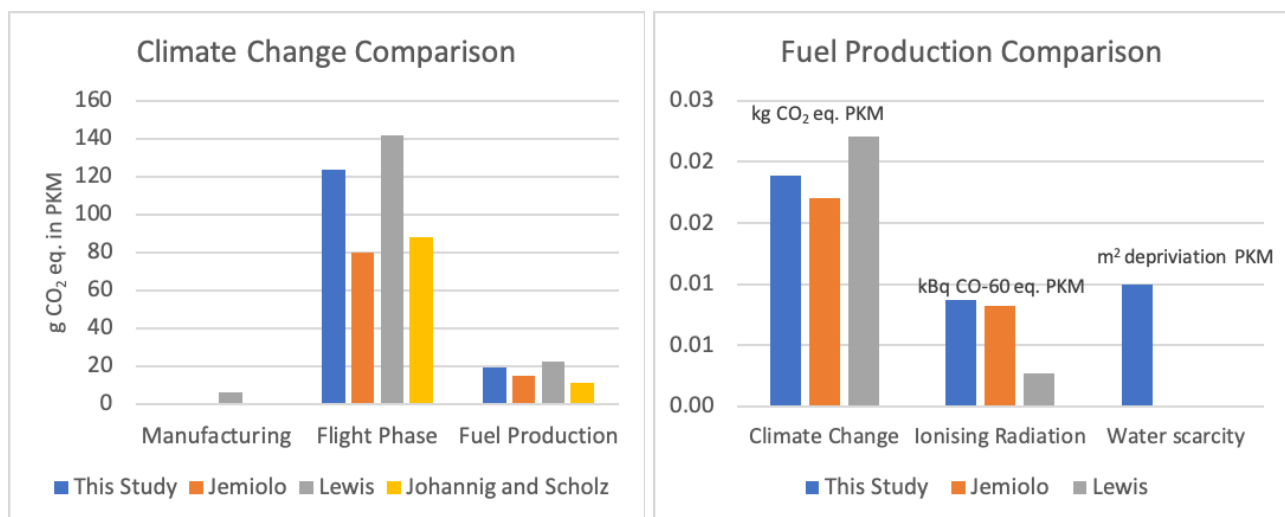
From Figure 12.5a it becomes clear that values differ between studies, which is mainly caused by a difference in the functional unit PKM. Therefore, the calculated climate change can be considered

12.4. Verification and Validation

Table 12.2: Inventory analysis for the Airbus A320

Manufacturing Cycle	
Material Usage	[121] presents a structural breakdown of the A330, and [119] justifies to linearly estimate these values for the A320. For this, the OEW of 120 000 kg and 41 310 kg is used of the A330 and A320 respectively.
Component Manufacturing	[122] presents and estimate for material flows which is used.
Transportation of Components	[120] presents and estimation of the transportation masses and distances for the A320.
Flight Operational Cycle	
LTO Cycle	[119] estimates the mass of fuel burned for the A320.
Cruise Phase	[119] estimates the mass of fuel burned for the A320.
Airport Operations	No material flows are identified; the direct EI are used obtained from [23].
Fuel Production Cycle	
Fuel Production	The mass of fuel is calculated by summing up the LTO and cruise phase.

valid as the output is comparable to the considered studies. Looking at Figure 12.5b it becomes clear that both the calculated climate change and ionising radiation EI correspond to the considered studies, however, the water scarcity EI is seen to deviate an unacceptable level. This implies that some misconception exists between this EI. As the other two EI are shown to be correct it is expected that there exists a misconception for the water scarcity which may be caused by a thoroughly revision of the ReCiPe EI in 2016³, where both considered LCA are written before that. This is further justified by considering Figure 12.4, where a comparable water scarcity EI is shown between the calculation method and the hydrogen production LCA [124] being a recently conducted LCA.



(a) Climate change verification and validation for the Airbus A320

(b) Fuel production EI comparison for the Airbus A320

Figure 12.5: Environmental impacts verification and validation for the Airbus A320, using comparative studies

Finally, Lopes [121] is the only LCA showing a material breakdown for the EI of the manufacturing cycle. However, since this LCA was written in 2010, comparison between other EI than climate change is not possible due to the significant change in ReCiPe EI definition from 2016, presented above. By using the same material component weight of the Airbus A330 provided by Lopes [121] and modifying the PKM calculation for the Airbus A330, the material breakdown EI calculation is considered correct as the calculated climate change EI is equal to 5.17×10^{-9} kg CO₂ eq. PKM compared to the 5.90×10^{-9} kg CO₂ eq. PKM from Lopes [121].

³URL <https://www.rivm.nl/en/life-cycle-assessment-lca/downloads> [cited 20 June 2020]

Economic Analysis

Economic analysis is performed to make sure that Cryo-V aircraft can successfully enter the market with its own advantages. Aircraft cost breakdown is presented in Section 13.1. It is followed by market analysis in Section 13.2 providing a vision on what position Cryo-V will take in the future market. Finally, return on investment and operational costs are estimated in Section 13.3.

13.1. Cost Breakdown

The cost for Cryo-V can be divided into two parts, recurring cost and non-recurring cost. Development cost, which are spent during the design phase, are non-recurring cost. Production costs are recurring cost that are spent in the actual manufacturing of the aircraft. The aircraft is divided into several top-level structures for development and production shown in Figure 13.1. Both development and manufacturing costs contain the wing, empennage, fuselage, landing gear, engine, system and payload costs, while final assembly cost includes manufacturing cost only.

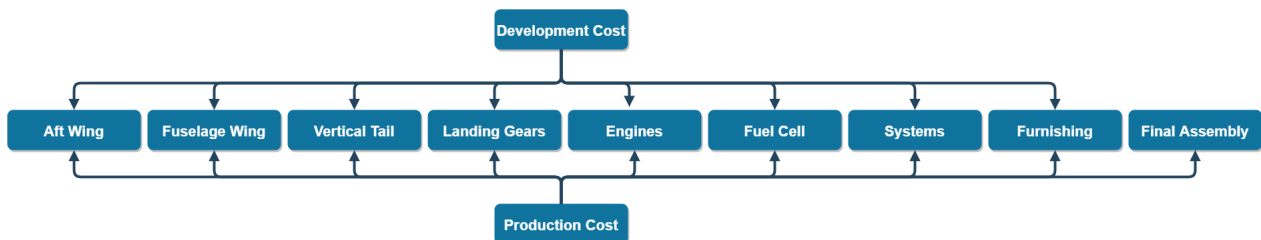


Figure 13.1: Cost breakdown for Cryo-V design and production

13.1.1. Development Cost

The development cost includes engineering cost and tool cost for the development process. They take different proportions in the development process, which are indicated in the first row in Table 13.1. The original cost units are \$/lb in 2002, which is converted to \$/kg in 2020 shown in Table 13.1 [2]. The development cost for fuel cell is part of the system development cost as it is an additional system comparing to conventional aircraft.

13.1.2. Manufacturing Cost

Similarly, the costs of manufacturing are listed in Table 13.2. It contains the costs for labours, material used and other costs including tools, jigs, etc. The fuel cells are listed separately as the price does not scale with MTOW [116]. There are several types of fuel cell, and the price ranges from 50 USD/kW to 5000 USD/kW, 1544 USD/kW are used in the cost analysis based on the number of fuel cell units produced per year in industry ¹. As the power density is 2.5 kW/kg, the cost for fuel cell is 3860 USD/kg.

¹URL https://www.energy.gov/sites/prod/files/2016/07/f33/fcto_battelle_mfg_cost_analysis_pp_chp_fc_systems.pdf [cited 20 June 2020]

13.1. Cost Breakdown

Table 13.1: Development costs per kg in USD 2020

	Engineering (\$/kg)	Manufacturing (\$/kg)	Tool Design (\$/kg)	Tool Fabrication (\$/kg)	Support (\$/kg)	Total (\$/kg)
Percentage	40%	10%	10.5%	34.8%	4.7%	100%
Aft Wing	22 437	5608	5890	19520	2635	56 090
Vertical Tail	65 991	16 499	17 322	57 412	7753	164 976
Fuselage Wing	40 606	10 151	10 660	35 330	4770	101 516
Landing Gear	3160	791	829	2749	370	7898
Engines	10 998	2749	2888	9569	1291	27 494
Systems	43 409	10 853	11 394	37 765	5099	108 520
Furnishing	13 618	3404	3574	11 849	1601	34 045

With these values, the production cost can be evaluated based on the mass of each subsystem of the aircraft. [3]

Table 13.2: Manufacturing costs per kg in USD 2020

	Labour (\$/kg)	Material (\$/kg)	Other (\$/kg)	Total (\$/kg)
Percentage	41%	33%	26%	100%
Aft Wing	1926	645	278	2850
Vertical Tail	5105	1531	737	7373
Fuselage Wing	2148	601	310	3059
Landing Gears	338	310	51	699
Engines	784	288	114	1186
Systems	996	288	146	1430
Furnishing	1281	316	187	1784
Final Assembly	183	13	9	206
Fuel Cell	-	-	-	3860

13.1.3. Costs Results

With the estimated subsystem masses computed in Section 10.1, the total cost can be estimated. The final development cost is 3.3 billion EUR and the production cost is 98.8 million EUR (111 million USD) per aircraft. The production cost is lower than expected, this is because of the Flying-V design which has the fuselage inside the wing. The production cost breakdown is shown in Figure 13.2.

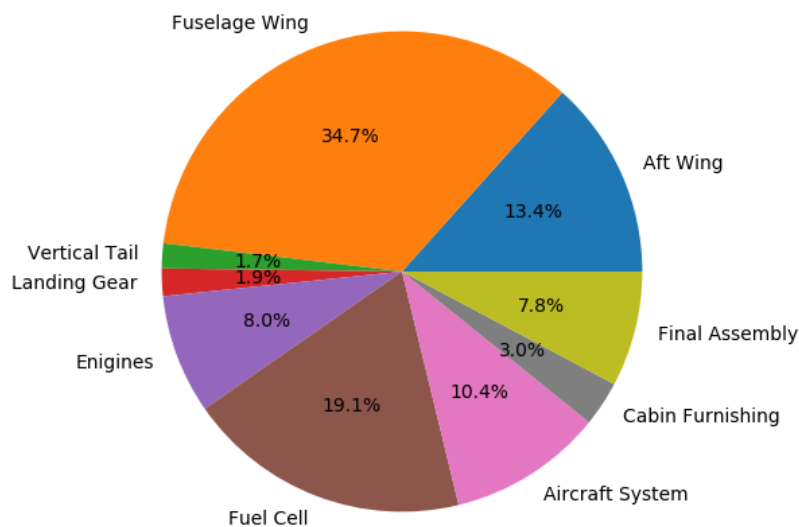


Figure 13.2: Production cost breakdown pie chart

13.2. Market Analysis

This section presents market analysis results by investigating current market in Subsection 13.2.1 and by analysing market dynamics in Subsection 13.2.2. The results of market analysis are carefully assessed in the design process of the Cryo-V.

13.2.1. Current Market

An investigation for the current aircraft market is done with the information from Planespotters and DVB bank – a specialist in finance of international transportation [125]. Figure 13.3a shows proportions of different types of medium range aircraft from different manufacturers with a total number of 23 885 aircraft delivered to customers.

There are two giants - Airbus and Boeing which take about 73% of the market combined. Another two medium-sized manufacturers Bombardier and Embraer cover about 20% of the market. From the pie chart, it is shows that the market share proportions of these four companies stay relatively constant over time. Therefore, the current market for medium range aircraft is relatively stable. It will be difficult to introduce a new aircraft and take over part of current market share. The table shows the trend of old aircraft from Fokker and McDonnell Douglas being replaced by new aircraft with more seats [2].

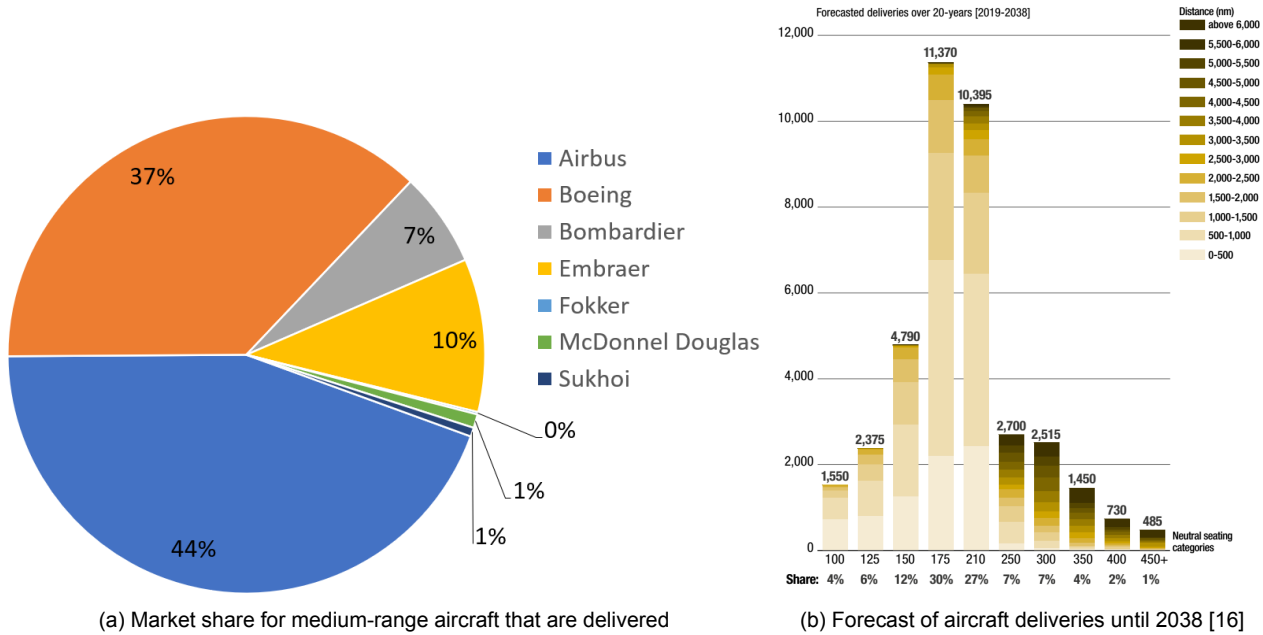


Figure 13.3: Medium range aircraft market share and forecast

13.2.2. Market Dynamics

The need for air traffic will keep increasing the following decades as the global population is growing and middle class population is expanding. According to the Airbus GMF 2019 [16], the air traffic growth per year is about 4.3%. The market in 2050 will be two to three times bigger than the current market. As the climate regulations are getting stricter, there is also a lot of old aircraft that need to be replaced by newer aircraft which is more climate friendly. The air traffic pair between Aviation Mega-City (AMC) and Secondary City (SC) is increasing dramatically in the past few years [16], which creates a new market for medium range aircraft like the Cryo-V. This can be seen in Figure 13.3b, which shows the forecast of aircraft deliveries until 2038. As shown in Figure 13.3b, the highest demand is for aircraft with 175 seats or 210 seats. For aircraft of such size, medium range aircraft are the most common in aircraft with around 200 seats.

13.3. Return on Investment and Operational Profit

Return on Investment (ROI) is a measure for efficiency of a project by measuring the amount of return based on the investment. A ROI is done for Cryo-V as it is using a new revolutionary design, from financial aspect, it shows the feasibility and potential profit of this design.

13.3.1. Operating Cost

The operating cost covers costs such as crew, fuel, maintenance, insurance and airport services². These costs vary for airlines, airport and fluctuating fuel price. Therefore, the operational cost estimation provided comes with a relatively large uncertainty margin. However, it still reflects the expectation of the cost in the Midterm Report [3]. Table 13.3 shows the partitions of operating cost which comes to 2415 EUR/hr (2711 USD/hr). This operating cost is estimated based on a typical 6 hr flight with a 6150 km range. For passenger service cost, it is calculated by average cost per passenger per mile (RPM). The price for LH2 is 1.4 USD/kg which is lower than the current hydrogen price, as the cost of hydrogen is expected to drop by 60% by 2030³.

Table 13.3: Cryo-V operating cost in USD

	Value	Unit	Total (USD)
Crew	600	USD/hr	3600
Fuel	400	USD/hr	3831
Aircraft service cost	800	USD/operation	800
Traffic service cost	15	USD/pax	3060
Passenger service cost	0.015	USD/per rpm	344
Maintenance	660	USD/hr	3960
Others	100	USD/hr	672
Average cost per hour			2711

Maintenance Cost Increment - As the Cryo-V is using a Flying-V configuration, the inspection and maintenance costs will be higher than for conventional aircraft. Moreover, the aircraft is using a fuel cell, which adds an additional cost component. This also leads to increment in maintenance. The basic maintenance cost are obtained by calculating the average maintenance cost for A320 with data from Planet⁴. In the operating cost calculation, the maintenance cost increased by 10% due to the Flying-V design and usage of fuel cell. The final operating cost is lower than the typical operating cost of A320. One reason of this is the high gravimetric energy density of liquid hydrogen, thus lower cost of the fuel. Although the maintenance cost is higher than that for the A320, the total operating cost is almost the same to A320 as the fuel cost is much lower by using liquid hydrogen. Thus the requirement for operating cost and maintenance can be considered as satisfied.

13.3.2. Operational Profit

The operational profit for airlines is the difference between ticket income and the operating cost. The average ticket price per km in Europe is about 14.14 USD/km⁵. With an assumed seat occupancy rate of 75% and operating cost of 2711 USD/hr, the operating profit for airline is about 15 440 EUR/hr.

²URL https://www.planestats.com/bhsn_2014dec [cited 18 June 2020]

³URL <https://blog.ballard.com/fuel-cell-price-drop> [cited 18 June 2020]

⁴URL https://www.planestats.com/bhsn_2014dec [cited 18 June 2020]

⁵URL <https://www.finder.com/ranked-the-cost-of-air-travel-in-80-countries> [cited 18 June 2020]

13.3.3. Return on Investment

In order to analyse the potential return on investment it is required to estimate aircraft market price of Cryo-V and market characteristics.

Aircraft Market Price - Aircraft market price can be calculated by Equation 13.1 using the 101 million USD costing A320 as reference aircraft. ⁶.

$$AMP = \left(0.7358 \left(\frac{seats}{seats_{ref}} \right)^{1.91} + 0.427 \cdot \frac{range}{range_{ref}} \right) * Price_{ref} \quad (13.1)$$

With 180 seats and a 6112 km maximum range for the A320, the estimated aircraft market price for the Cryo-V is 117.6 million EUR.

Market Volume - Figure 13.3b shows the future aircraft delivery forecast until 2038. The potential competitors for the Cryo-V are the aircraft with 150 to 250 seats. Airbus predicts an annual growth of the aircraft market of 4.3% [16]. The COVID-19 pandemic will influence aircraft demand, so a conservative 90% of the original forecast is assumed. With these numbers, the total number of medium range aircraft with 150 to 250 seats is expected to be 50 534.

Market Share - Figure 13.3a shows the current market share of medium range aircraft. Airbus and Boeing take 39% and 34% of the market, respectively. Other manufactures only takes 27%. Some of these are old aircraft like McDonnell Douglas and Fokker. Aircraft from Bombardier and Embraer have a relatively low seat capacity. As the Cryo-V provides more seats while obtaining a lower operating cost, the market share for future delivery can be high. However, the list price (AMP) is significantly higher than the A320, which may reduce the number of aircraft sold due to budget concern of airlines. Thus the final market share for future delivery until 2050 are assumed to be 20%.

Return on Investment - ROI can be calculated by Equation 13.2, where *DC* and *MC* are development cost and manufacturing cost, respectively. *N* is the total number of aircraft sold. The profit per aircraft sold is multiplied by 0.9 due to the possible cost for delivery and storage.

$$ROI = \frac{(AMP - MC) * N}{DC + MC * N} * 100\% \quad (13.2)$$

The total estimated delivery until 2050 is 10 100 aircraft. Assuming that the number of aircraft for the first delivery is 5 aircraft and the annual increment ratio is 25% of previous year. The final ROI is about 17% which is higher than the average Airbus ROI.

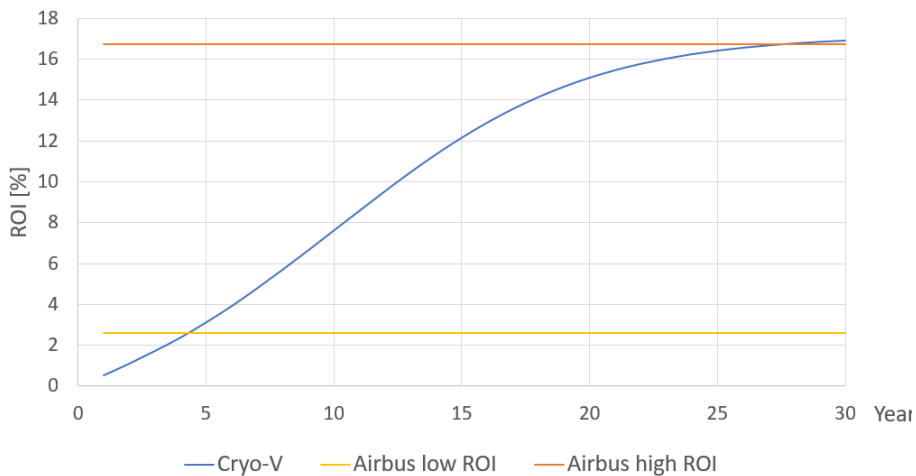


Figure 13.4: Return on Investment for the Cryo-V

⁶URL <http://www.airbus.com/content/dam/corporate-topics/publications/backgrounders/Airbus-Commercial-Aircraft-list-prices-2018.pdf> [cited 18 June 2020]

13.3.4. Competition

The Cryo-V will face a competition with many existing and future medium range aircraft and strong market position is essential for further development.

Aircraft Cost in Current Market - Table 13.4 shows a cost comparison with other medium range aircraft. Unit cost is the delivery price of the aircraft. Operation cost includes the crew, fuel and other operation related cost ⁷. Unit cost per seat and operational cost per kg per hour (OC/PL) are the two main factors that are taken into the consideration. Unit cost per seat is a rough expectation for profit gained by the entire aircraft life time regardless of maintenance. OC/PL indicates the operational efficiency of the aircraft.

Table 13.4: Cost detail of dominant aircraft in the market

	Unit cost (million USD)	Max Seats (1 class)	Unit cost per seat (million USD)	Operation Cost (USD/hr)	Max. Payload (kg)	OC/PL (USD/kg/hr)
A320	101	180	0.56	5042	19 900	0.25
B737-800	106	189	0.56	4652	20 540	0.23
A321	118.3	220	0.54	3078	25 300	0.12
A319	92.3	156	0.59	2933	17 700	0.17
B737-700	89.1	149	0.60	4492	17 554	0.26
Average	101.34	179	0.57	4039	20 199	0.20
Cryo-V	-	-	0.66	-	-	0.11

The unit cost per seat of the Cryo-V is 0.66 million which is 16 % higher than average. The OC/PL is 0.11 USD/kg/hr which is 45 % lower than average. This makes the aircraft more competitive in a financial aspect.

Cryo-V meets the requirements from Flightpath 2050 with significantly lower noise emission and air pollution. The design range of 6150 km is relatively large compared to other competitor aircraft, which provides more possibilities to airline operations. Moreover, the Cryo-V is largely recyclable, which is a selling point. Emissions, noise and recycling aspects are expected to play increasingly larger roles in the market during the coming years [2].

13.3.5. SWOT Diagram

At last, a SWOT diagram is constructed to give an overview of Cryo-V regarding its strengths, weaknesses, opportunities and threats, it is shown in Figure 13.5.

Strengths	Weaknesses
-57.2 dB noise reduction -100% CO ₂ emission reduction Low climate impact Recyclable	More expensive than A320 Onsite hydrogen production Higher structural complexity
Opportunities	Threats
Fast growing market Stricter environmental law	COVID-19 pandemic Economical crisis Strong competitors like Airbus Conservative industry for radical design

Figure 13.5: SWOT diagram of Cryo-V for market

⁷URL https://www.planestats.com/bhsn_2014dec [cited 18 June 2020]

Risk Analysis

Risk analysis is an integral part of the design process. Multiple technical risks were managed throughout the conceptual design phase and a risk management strategy is developed for the next design phases. These aspects are presented in this chapter.

14.1. Technical Risk Management

Multiple different risk events can occur during design process and operations. To organise the risk management and not to miss any high risks, the risks are split into four major categories - production (index P) risks, operational (O) risks, external (E) risks and detailed design (D) phase risks.

Production Risks - account as a major risk group, especially considering that a lot of different parties are involved (workforce transportation, financial considerations) and production phase is the most significant development phase after the design is finished. Risk events like accidents, employee strike and others need to be assessed carefully. Production timeline and budgets must be assigned attentively by including the contingencies as well.

Operational Risks - are the risks which can happen during the aircraft operations. Many of the operations risks were listed in the Midterm Report [3] and they were considered in the design. Main operational risks are listed in Table 14.1 for which attention should be addressed during the detailed design phase. The design of all specific detailed components shall be reliable.

Furthermore, aircraft shall be operated according to operational procedures as explained in Chapter 11. Multiple ground operations risks shall be assessed during the detailed design phase and also during operations of the aircraft. Cryo-V operations shall be compatible with airports.

External and Market Risks - cannot be controlled by the design team and they can cause major problems in the development process. These events are more difficult to predict, however they should be managed carefully by applying risk mitigation strategies because market risks can prevent the production of the aircraft. Some of the external risks are associated with the availability and cost of hydrogen. Current trends suggest that hydrogen is becoming more and more available and also less expensive, however there is no guarantee that these trends will continue in the future. From the other hand, if the hydrogen becomes widely available Cryo-V will face a strong competition in the market.

Design Risks - shall be assessed before entering the detailed design phase as well. Cryo-V requirement compliance matrix is provided in Table 15.1 which shows which requirements are met. However, new requirements might appear during detailed design phase which will need to be satisfied. A lot of assumptions were made during conceptual design, hence there is a risk that some of the assumptions might not be valid and that can possibly cause major problems in the detailed design phase. One of the consequences might be that the aircraft turns out to be under-designed and it cannot be certified. Currently these risks were mitigated by applying extensive verification and validation procedures for the design. Nonetheless, the conceptual design estimates include uncertainty of around 10-15%. During the detailed design phase there is a risk that the design is on a verge of not meeting some of the requirements if the assumptions used turn out to be incorrect.

14.1. Technical Risk Management

Table 14.1: Summary of main technical risks

Risk Event	Mitigation/Contingency Plans
Production Risks	
P1 Production cost is too high	Contingencies are applied for cost planning, if a minor component is too expensive - design a simpler model.
P2 Accident during production	Work in factories shall be well organised, transportation safe. Include cost contingencies for small accidents.
P3 Production is too complex	Complexity of production is considered for Cryo-V design, if a specific part is still too complex to produce, redesign needs to be performed for that part.
P4 Delay due to unconventional design	Production shall be planned including unexpected delays, specific production plan is made for all subsystems.
P5 Production process is not sustainable	Extensive production plan is made and sustainability assessment is considered together with use of recyclable materials. If the activities are non-sustainable they shall be changed as quickly as possible.
P6 Employee strike	Employees shall receive satisfying wages and work in a safe environment.
Operational Risks	
O1 Maintenance not performed regularly	Maintenance schedule is made and presented in Chapter 11. Operational procedures shall be strictly followed.
O2 Refuelling risks (leakage, crew safety)	Fuelling process shall be performed according to airport operations, fuel pipes shall be insulated, the contact with skin must be prevented.
O3 Hydrogen explosion or tank bursting	Foam insulation layer, venting system and pressure relief valves are implemented to prevent these risk events from happening. Tank should be tested for boil-off rate and the insulation characteristics, fuel system shall be tested in laboratory conditions.
O4 Incorrect aircraft loading procedure	Landing gear is sized and positioned such that no tip-over happens during different loading procedures. To satisfy lateral stability and prevent roll-over - passenger, cargo and fuel loading must be performed according to ground operations
O5 Ground collision	Ground operations are performed in low speed. Landing gear is placed and sized such that no roll-over happens in low speeds. Fuel tank is designed such that it can withstand minor impacts as foam and aluminium structure is used.
O6 Actuators not working	Emergency generator and redundancy in actuators are implemented. The aircraft is able to perform emergency landing without HLDs
O7 Inoperative engine	Eight electric fans and two turbofans are installed on Cryo-V aircraft, hence there is a sufficient redundancy in an event of engine failure. Yaw controllability is satisfied by using two rudders on both vertical tails, aircraft is able to glide to perform landing.
External & Market Risks	
E1 Hydrogen remains expensive or gets more expensive	Cryo-V plane is designed to run specifically on hydrogen, hence this risk must be accepted.
E2 Low availability of hydrogen	This risk must be accepted. If there is a situation that hydrogen is available only in a specific part of the globe, then Cryo-V should attempt entering the market of that region.
E3 Competition in market increases significantly	Market is analysed including competitor assessment, strong marketing strategy shall be developed. If possible - improve the main selling points, like reducing the GHG emissions, noise and operational costs even more to make the design more competitive in the market.
Design Risks	
D1 Wrong assumption used	All of the assumptions used in conceptual design phase are carefully assessed and design is verified and validated in both subsystem and system levels. Redesign of a subsystem will be needed if an invalid assumption is used.
D2 Requirement not met	All requirements are validated and compliance is shown in requirements compliance matrix. If a certain requirement is not met, negotiation with the client will be needed.
D3 Strong crosswinds and gusts	Cryo-V design has two large vertical tails, design for controllability involves analysis of 90 degree wind conditions described. If crosswinds are higher than the specified maximum conditions, landing or take-off must be abandoned.
D4 Certification is unsuccessful	Cryo-V design is verified to be compatible with all CS-25 requirements, such as inoperative engine, strong gusts, bad weather conditions, etc. If a certification test is failed, redesign on a subsystem or system level would be needed.
D5 Underdesigned aircraft	Cryo-V design involves safety margins for subsystems and aircraft design is verified and validated on conceptual level. If the aircraft is underdesigned, redesign and budget reallocation shall be considered.

14.1. Technical Risk Management

The main risks together with their mitigation plans are shown in Table 14.1. Each risk is evaluated in terms of likelihood and the potential impact and displayed in the risk map shown in Figure 14.1. The probabilities are ranked from *very low* to *very high*. For example, *high* probability means that the risk event is likely to happen during operations or next phases of development. Impacts are ranked from *insignificant* to *catastrophic*. For example, a *major* impact leads to major consequences and major redesign activities.

Pre-mitigation and post-mitigation risk maps are shown in Figure 14.1 and Figure 14.2, respectively. High risks are displayed on the red background in the top right corner, low risks on the green background on the lower left corner, while the risks of medium significance are displayed on a yellow background in the middle part of the map.

As shown in Figure 14.1, detailed design risks, production cost and some of the operational risks are evaluated as high risks mainly due to their major impacts on the development. However, by implementing prevention and risk mitigation strategies the potential impacts of these risks are lowered as well as the likelihood of these risk events.

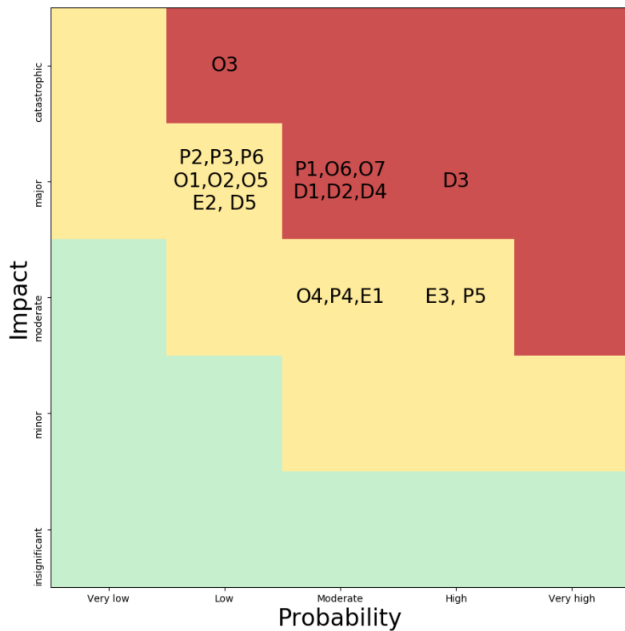


Figure 14.1: Risk map

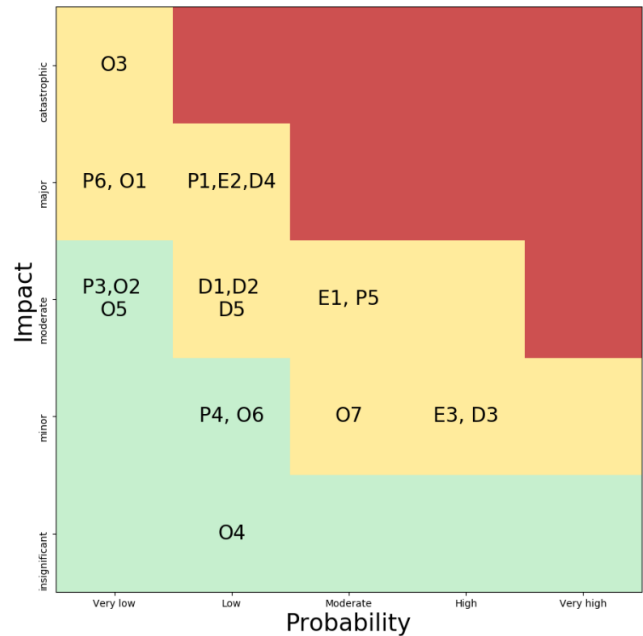


Figure 14.2: Post-mitigation risk map

Compliance With Requirements

With this design stage closing to its end, it is important to check whether all the requirements presented in Section 2.2 are still met. This is done through the compliance matrix in Section 15.2. But before that a short feasibility analysis is performed to determine whether some requirements are out of scope, unfeasible or changed.

15.1. Feasibility Analysis

Some requirements are deliberately chosen to not be met. **MRA.SYS.OP.2.2**, cargo volume, is reduced to improve the efficiency of the aircraft. Market research also showed only the 18 m² is typically used in the aircraft. The cruise altitude, **MRA.SYS.PERF.1.4**, cruise altitude, is deliberately changed to fly more efficiently and have a lighter aircraft.

MRA.SYS.OP.1.1, reliability, is estimated to not reach the operational reliability. This occurs due to the high complexity of the fuel system, leaving more room for failure. The difference is however small and not seen as catastrophic for the design.

Requirement **MRA.SYS.SUST.5.1**, a carbon neutral life cycle, was not feasible as the requirement was too ambitious. This also requires the production processes and airline operations to be carbon neutral, which is out of the hands of the preliminary designer. The aircraft's reduction in gas emissions is deemed sufficient.

All requirements indicated as blue are either partly satisfied or have to be analysed further. **MRA.SYS.PERF.4** about stability needs further analysis, because dynamic stability is not taken into account. Also some stability derivatives were estimated in an empirical way, requiring more analysis/wind tunnel testing. The same is true for **MRA.SYS.OP.REG.1.1**, CS25. This is a very extensive authority regulation document, so not all of these regulations could be taken into account regarding available time.



Other requirements have not been taken into account for this design phase yet. **MRA.SYS.OP.COST.1.2**, maintenance costs, greatly depends on the conditions the aircraft flies in and the airline maintenance policy. This is also to be further analysed.

Overall most requirements have been satisfied. The requirements that have not been satisfied or have partly been satisfied are not deemed critical to reach the project objective statement. The Cryo-V significantly reduces gas emissions and noise, while still being close to the Airbus A320 operational aspects.

15.2. Compliance Matrix

Table 15.1: Requirement compliance matrix

		Cryo-V	Margin	Compliant
Performance Requirements				
MRA.SYS.PERF.1.1	The aircraft shall have a minimum range of 6150 km.	6150	0	Yes
MRA.SYS.PERF.1.3	The aircraft shall have a minimum cruise speed of 830 kph.	830	0	Yes
MRA.SYS.PERF.1.4	The aircraft shall have a cruise altitude of 30 000 ft.	40 000	+10 000	Partly Satisfied
MRA.SYS.PERF.1.5	The aircraft shall have a minimum endurance of 6 h under standard conditions.	7:44	+1:44	Yes
MRA.SYS.PERF.4	The aircraft shall be stable in all flight conditions.	-	-	No complete analysis
MRA.SYS.PERF.7.1	The aircraft shall obtain an initial maximum climb rate at sea level at standard conditions of 3000 ft/min.	3550	+550	Yes
MRA.SYS.PERF.10.6	The aircraft shall have a maximum take-off distance of 2100 m at sea level at standard atmospheric conditions on a concrete runway.	2100	0	Yes
MRA.SYS.PERF.11.6	The aircraft shall have a maximum landing distance of 1500 m at sea level at standard atmospheric conditions on a concrete runway.	1031	-469	Yes
Sizing Requirements				
MRA.SYS.OP.1.6	The aircraft shall be designed for a load factor of 2.5.	2.5	0	Yes
MRA.SYS.OP.1.7	The aircraft shall be designed to withstand gust loads of 20 kts.	20	0	Yes
MRA.SYS.OP.2.2	The aircraft shall have a cargo volume of 25 m ³ .	18	-7	No
MRA.SYS.OP.2.4	The aircraft shall have a capacity of 200 passengers.	200	0	Yes
MRA.SYS.OP.3.1	The aircraft shall be able to operate from a type 4C Aerodome.	4C	-	Yes
MRA.SYS.PERF.10.10	The aircraft shall have a maximum take-off weight of at most 78 000 kg.	72 092	-7908	Yes
Regulation Requirements				
MRA.SYS.OP.REG.1.1	The aircraft shall be certified to EASA CS25 standard.	-	-	No complete analysis
MRA.SYS.PERF.12.7	The aircraft shall qualify for an ETOPS-180 min rating.	-	-	Yes
Operation Requirements				
MRA.SYS.OP.1.1	The aircraft shall have an operational reliability of 99.6%.	99.54%	-0.06%	No
MRA.SYS.OP.1.2	The aircraft shall perform at least 60 000 cycles or 120 000 flight hours.	100 000	+40 000	Yes
MRA.SYS.OP.7.1	The aircraft shall be integrate-able in the global infrastructure.	-	-	Yes
Cost Requirements				
MRA.SYS.OP.COST.1.2	The aircraft's maintenance costs shall on average be less than 800 USD per flight hour.	-	-	Partly Satisfied
MRA.SYS.OP.COST.1.3	The aircraft's operational costs shall on average be less than 2800 USD per flight hour.	2415	-385	Yes
MRA.SYS.OP.COST.1.4	The aircraft's production cost shall be less than 100 million EUR.	98.8 million	-1.2	Yes
Sustainability Requirements				
MRA.SYS.SUST.1.0	The aircraft shall have a cumulative noise reduction of 45 dBA for all three certification levels.	-53.9	-8.9	Yes
MRA.SYS.SUST.1.1	Lateral/full power reference noise shall be lower than 71.4 dBA.	69.8	-1.6	Yes
MRA.SYS.SUST.1.2	Approach reference noise shall be lower than 71.1 dBA.	70.1	-1.0	Yes
MRA.SYS.SUST.1.3	Flyover reference noise shall be lower than 56.7 dBA.	50.4	-6.3	Yes
RA.SYS.SUST.4.0	The aircraft shall comply with gas emission reductions as stated in Flightpath 2050.	-	-	Yes
MRA.SYS.SUST.4.1	The aircraft shall emit at most 17 249 kg CO ₂ during flight.	0	-17 249	Yes
MRA.SYS.SUST.4.2	The aircraft shall emit at most 8.923 kg NO _x during flight.	8.200	-0.723	Yes
MRA.SYS.SUST.5.0	The aircraft shall have a lower environmental impact than the Airbus A320.	-	-	Yes
MRA.SYS.SUST.5.1	The entire life cycle shall have a lower environmental impact on climate change than 142 g CO ₂ eq PKM.	26.5	-115.5	Yes
MRA.SYS.SUST.5.6	The aircraft shall be at least 75% recyclable.	>90%	15%	Yes

 Partly satisfied or to be further analysed
 Not Satisfied

Conclusion and Recommendations

This chapter concludes the report and, in Section 16.2, offers recommendations for future design and development work regarding the Cryo-V and its use.

16.1. Conclusion

The Cryo-V design demonstrates that meeting the Flightpath 2050 requirements whilst remaining competitive with existing aircraft is challenging, but theoretically possible. To meet the emissions requirements, it is clear that hydrogen propulsion is the only viable long-term solution. Although bio- and synthetic fuels could arguably be considered carbon neutral if their entire lifecycle is analysed, these fuels will, when used on their own, not meet the NO_x requirements. Based on the emissions analysis performed in this report, it is even questionable whether the Cryo-V would have met the NO_x requirements if it had employed a biofuel / hydrogen fuel cell hybrid propulsion system due to the higher EINO_x.

However, hydrogen fuel cell propulsion is not without its caveats. As previous designs and prototypes have shown, hydrogen fuel cells on their own can provide propulsion for general aviation and short-range passenger aircraft. However, for aircraft equivalent to or larger than the A320, a second form of energy conversion, such as combustion, is required to prevent the aircraft from becoming much larger and heavier and, therefore, no longer competitive.

Furthermore, hydrogen propulsion is unequivocally tied to an unconventional aircraft configuration. The reduction in drag achieved by the planform of the Cryo-V is absolutely essential to limit the amount of hydrogen that must be carried for a given range. Although possible, powering an Airbus A320 with hydrogen would not be an optimal solution due to the large hydrogen tanks required, which would inevitably limit the payload capacity.

Noise reduction is also tied to unconventional aircraft configurations. Compared to emissions reduction, noise is more difficult to estimate accurately. However, based on the noise analysis presented in this report, engine shielding and the approach speed are found to be crucial parameters. It is, therefore, assumed that conventional aircraft configurations will not be able to meet the Flightpath 2050 noise requirements. The A320 is comparatively already a quiet aircraft and, although more reduction is feasible, for example by optimisation of the landing gear, the resulting design will not achieve the required reduction. Simply converting the aircraft to electric propulsion will also not lead to a sufficient design, even after reduction such as engine phasing, due to the lack of shielding. Using a BWB or Flying-V planform allows shielding to be maximised to achieve a large reduction in noise emissions.

Further reduction can be achieved by modifying operational procedures. Although the Cryo-V is designed to meet the noise reduction requirements at a conventional, 3° approach angle, this could be improved at higher angles. This should also be taken into account in new aircraft designs, as it presents a challenge for existing aircraft.

The Cryo-V project was completed successfully, notwithstanding the uncertain circumstances surrounding it. The majority of the project management tools described in this and previous reports were

used effectively throughout, which meant that the project was rarely at risk of falling behind schedule. Some elements of the mandated systems engineering process were found not to be useful for the team for this project, but their use has improved the team's understanding of their potential use cases in future projects. Overall, the Design Synthesis Exercise has allowed the team to make use of all skills acquired in the Bachelor programme and gain a deeper understanding of the challenges and opportunities surrounding silent, clean and green aviation.

16.2. Recommendations

Further research and analysis is required to prove the feasibility of the Cryo-V design. First and foremost, the novel, hybrid hydrogen combustion / fuel cell propulsion system needs to be analysed in more detail. The overall hybrid design is not limited to the Cryo-V and could be a potential solution even for existing aircraft, in conjunction with conventional turbofans, to reduce emissions. For this purpose, a more thorough thermodynamic analysis and prototypes would be necessary. Furthermore, the fuel cell model presented in this report is rudimentary and should be improved or replaced by a CFD analysis and prototype test. The start-up procedure and the emergency battery-electric heating system discussed in this report should also be investigated for feasibility. To further improve the design, the possibility of energy recovery during descent and landing could be analysed.

Liquid hydrogen refuelling is not considered in this report, but is critical for safety and operations at the airport. The fuel purge and pressure relief system should also be further analysed in all flight conditions to minimise risks. A detailed boil-off model would be necessary to complete this step and validate the fuel tank design presented in this report.

The Cryo-V planform and its inspiration, the Delft University of Technology Flying-V, have potential to dramatically decrease emissions and fuel consumption, even for existing propulsion designs. Since the Flying-V design is at a later stage of development than the Cryo-V at the time of writing, it is recommended that cryogenic hydrogen propulsion is analysed also for the Flying-V. The use of distributed propulsion as a boundary layer ingestion system is not considered in this report and could be of use to decrease the required power and noise emissions further. A detailed thrust model would be necessary for this analysis.

For noise reduction, it is recommended that future work validates the results presented in this report with physical tests using prototypes as well as more detailed analyses. Research should be conducted into the possibilities of modifying operational procedures, such as a higher approach angle, to reduce the impact of airports on surrounding neighbourhoods and businesses. A more detailed analysis of the noise production of the planform itself would also be beneficial and could be optimised.

On a global scale, it is recommended that research is continued into hydrogen fuel cell technology in aviation. Consortia and working groups such as EUROCAE WG-80 and the Hydrogen Council of Europe already help to create safety standards and design and procedural guidelines for the use of hydrogen, spanning multiple company and country boundaries. Close interaction between airports, hydrogen suppliers and local governments is key to preparing for the hydrogen supply chain required for aircraft such as the Cryo-V and investigating the possibilities of on-site production or conversion of existing pipelines.

Overall, it is recommended that focus be firmly placed on reducing the aviation industry's impact on the environment as part of a green recovery from the COVID-19 pandemic. This can be done at the European and national level with new initiatives and projects within CleanSky or national stimulus packages, but also at the company or individual level. Sustainability is, after all, everyone's responsibility.

Bibliography

- [1] J. Aalders, E. Daugulis, S. van Dalen, T. Francotte, Y. Laar, L. Megill, M. Shi, S. de Vilder, F. Vossen, and Z. Wu. Silent and Climate-Neutral Medium-Range Aircraft, Project Plan. Unpublished. Delft University of Technology. course: AE3200-II, 2020.
- [2] J. Aalders, E. Daugulis, S. van Dalen, T. Francotte, Y. Laar, L. Megill, M. Shi, S. de Vilder, F. Vossen, and Z. Wu. Silent and Climate-Neutral Medium-Range Aircraft, Baseline Report. Unpublished. Delft University of Technology. course: AE3200-II, 2020.
- [3] J. Aalders, E. Daugulis, S. van Dalen, T. Francotte, Y. Laar, L. Megill, M. Shi, S. de Vilder, F. Vossen, and Z. Wu. The Cryo-V Aircraft, Midterm Report. Unpublished. Delft University of Technology. course: AE3200-II, 2020.
- [4] ACARE Flightpath. 2050-Europe's vision for aviation. *Advisory Council for Aeronautics Research in Europe*, 2011.
- [5] J. Benad. Design of a commercial aircraft for high-subsonic speed as a flying wing configuration. March 2015.
- [6] C. Chen et al. Assessment on critical technologies for conceptual design of blended-wing-body civil aircraft. *Chinese Journal of Aeronautics*, March 2019.
- [7] Y. Guo, C. L. Burley, and R. H. Thomas. On noise assessment for blended wing body aircraft. In *52nd Aerospace Sciences Meeting*, page 365, 2014.
- [8] D. Schiktanz and D. Scholz. Box wing fundamentals - an aircraft perspective. *DGLR*, 2009.
- [9] R. Martínez, E.O. Pérez, and J.F. Palacin. Historical evolution of air transport productivity and efficiency. 2005.
- [10] EASA. ICAO aircraft engine emissions databank [online database], 2019. [cited 18 May 2020].
- [11] R. Vos and M. Hoogreef. *Semi-Analytical Weight Estimation Method for Fuselages with Oval Cross-Section*. American Institute of Aeronautics and Astronautics (AIAA), April 2013.
- [12] J. Roskam. *Airplane Design. Pt. 4. Landing gear and Systems*. Roskam Aviation and Engineering, 1985.
- [13] Airbus S.A.S. Maintenance planning document. *Airbus SAS, Blagnac, Toulouse*, 2005.
- [14] C. Stiller and P. Schmidt. Airport liquid hydrogen infrastructure for aircraft auxiliary power units'. In *18th World Hydrogen Energy Conference (WHEC 2010)*, Essen, Germany, 2010.
- [15] E. Dallara and I. Kroo. Aircraft design for reduced climate impact. pages 1–20, January 2011.
- [16] Airbus S.A.S. Global market forecast: Cities, airports & aircraft. 2019.
- [17] Airbus S.A.S. Airbus A320 aircraft characteristics airport and maintenance planning. *Airbus SAS, Blagnac, Toulouse*, 2020.
- [18] M. Basner, C. Clark, A. Hansell, J. Hileman, S. Janssen, K. Shepherd, and V. Sparrow. Aviation noise impacts: State of the science. *Noise & Health*, 19:41–50, March 2017.
- [19] M. Basner, A. Samel, and U. Isermann. Aircraft noise effects on sleep: DLR research and application. December 2006.
- [20] A. Correia, J. Peters, J. Levy, S. Melly, and F. Dominici. Residential exposure to aircraft noise and hospital admissions for cardiovascular diseases: Multi-airport retrospective study. *BMJ (Clinical research ed.)*, volume 347:page 5561, October 2013.
- [21] European Aviation Safety Agency (EASA). Acceptable means of compliance for large aeroplanes cs–25. *Amendment 24*, 2020.
- [22] R. J. Astley. Can technology deliver acceptable levels of aircraft noise? In *Inter-Noise and Noise-Con Congress and Conference Proceedings*, volume 249, pages 2622–2633. Institute of Noise Control Engineering, 2014.
- [23] W. Jemiolo. Life cycle assessment of current and future passenger air transport in Switzerland. Master's thesis, University of Nordland, 2015.
- [24] John D. Anderson. *Aircraft Performance and Design*. Tata McGraw-Hill, 2010.
- [25] D. P. Raymer, American Institute of Aeronautics, and Astronautics. *Aircraft design : a conceptual approach*. American Institute of Aeronautics and Astronautics, 2012.
- [26] N. Jørgensen. The Boeing 777: Development life cycle follows artifact. *Roskilde University, Department of Computer Science, Roskilde, Denmark*, 2006.
- [27] Airbus. A320 family: The most successful aircraft family ever, March 2020.
- [28] M. A. J. Huijbregts, Z. J. N. Steinmann, P. M. F. Elshout, G. Stam, F. Verones, M. D. M. Vieira, A. Hollander, M. Zijp, and R. Van Zelm. A harmonized life cycle impact assessment method at midpoint and endpoint level. *Report 1: characterization, Bilthoven, Netherlands*, 2016.
- [29] E.J. Cramer, J.E. Dennis, P.D. Frank, R.M. Lewis, and G.R. Shubin. Problem formation for multidisciplinary optimization. *SIAM Journal on Optimization*, 4(4):754–776, 1994.
- [30] A. B. Lambe and J. R. R. A. Martins. Extensions to the design structure matrix for the description of multidisciplinary design, analysis, and optimization processes. *Structural and Multidisciplinary Optimization*, 46:273–284, 2012.
- [31] F. Oliviero. *Aerospace Design and Systems Engineering Elements II AE2111-II aircraft part*. Delft University of Technology, 2018.
- [32] J. Larminie and A. Dicks. *Fuel Cell Systems Explained*. John Wiley & Sons Ltd, Chichester, England, 2003.

- [33] M. Ni and T. S. Zhao. *Solid Oxide Fuel Cells - From Materials to System Modeling*. Royal Society of Chemistry, 2013.
- [34] A. Himansu et al. Hybrid solid oxide fuel cell/gas turbine system design for high altitude long endurance aerospace missions. *Fourth International Conference on Fuel Cell Science, Engineering and Technology*, 2006.
- [35] A. Leonide. *SOFC Modelling and Parameter Identification by means of Impedance Spectroscopy*. PhD thesis, Karlsruher Institut für Technologie, Karlsruhe, Germany, 2010.
- [36] K. Zheng, K. Xie, S. Shen, and S. Wang. Numerical modeling and parametric analysis of solid oxide fuel cell button cell testing process. *International Journal of Energy Research*, 43(7), 2019.
- [37] M. Delgado Gosálvez, J. van Ham, S. Joosten, D. Juschus, G. Nieuwerth, T. van Pelt, L. Smit, M. Takken, Y. Wang, and T. Ziere. Green flying. Technical report, Delft University of Technology, 2018.
- [38] A. Purushothaman Vellayani. Fuel cell systems ME45100 introduction. 2019.
- [39] A. Musa, A. Agina, and M. Talbi. Operating conditions on the performances of SOFC. *ICREPQ'12*, 2012.
- [40] J.P. van Buijtenen, Visser W.P.J., S. Shakariyants, and F. Montella. Gas turbines, propulsion and power, AE2203, 2011.
- [41] National Aerospace Laboratory NLR. *GSP 11 User Manual*, 11.4.6.0 edition, February 2016.
- [42] P. Van den Bossche, F. Vergels, J. Van Mierlo, J. Matheys, and W. Van Autenboer. Subat: An assessment of sustainable battery technology. *Journal of Power Sources*, 2005.
- [43] S. Stuckl. *Methods for the Design and Evaluation of Future Aircraft Concepts Utilizing Electric Propulsion Systems*. PhD thesis, Technical University of Munich, 2015.
- [44] C. Pernet et al. Integrated fuel-battery hybrid for a narrow-body sized transport aircraft. *Aircraft engineering and aerospace technology*, page 4, October 2014.
- [45] J. Zamboni. A method for the conceptual design of hybrid electric aircraft. Master's thesis, Delft University of Technology, 2018.
- [46] T. Hermann et al. Dependency of machine efficiency on the thermal behavior of induction machines. *Machines*, 8(9):3, 2020.
- [47] N.H.M. van den Dungen. Synthesis of an aircraft featuring a ducted-fan propulsive empennage. Master's thesis, Delft University of Technology, 2017.
- [48] L. Veldhuis. *Propeller Wing Aerodynamic Interference*. PhD thesis, Delft University of Technology, June 2005.
- [49] A. Jasudavissu. Optimization of a ducted fan propulsion system for a single engine aircraft. Master's thesis, Ryerson University, Toronto, Canada, 2007.
- [50] Y. Jin et al. Modeling of ducted-fan and motor in an electric aircraft and a preliminary integrated design. *SAE International Journal of Aerospace*, October 2008.
- [51] E. Torenbeek. *Synthesis of Subsonic Airplane Design*. Delft University Press, 1982.
- [52] K.W. Mort. Performance characteristics at zero angle of attack for several fan blade angles. Technical report, NASA, 1965.
- [53] C. Winnefeld, T. Kadyk, B. Bensmann, U. Krewer, and R. Hanke-Rauschenbach. Modelling and designing cryogenic hydrogen tanks for future aircraft applications. *Energies*, 11(1):105, 2018.
- [54] J.S. Ciaravino. Study of hydrogen as an aircraft fuel. *Naval Postgraduate School Monterey, California*, 2003.
- [55] G.D. Brewer. *Hydrogen Aircraft Technology*. CRC Press, Boca Raton, FL, United States, 1991.
- [56] D. Verstraete. *The Potential of Liquid Hydrogen for long range aircraft propulsion*. PhD thesis, Cranfield University, 2009.
- [57] P. Hendrick et al. Hydrogen fuel tanks for subsonic transport aircraft. *International Journal of Hydrogen Energy*, 2010.
- [58] A. Avots, U. Cabulis, and M. Kirpluks. Rigid polyurethane foam thermal insulation protected with mineral intumescent mat. *AUTEX Research Journal*, page 5, December 2014.
- [59] I. Tapeinos. *Multi-Spherical Composite-Overwrapped Cryogenic Fuel Tanks for Hypersonic Aircrafts*. PhD thesis, Delft University of Technology, 2019.
- [60] Airbus. *Flightdeck and Systems Briefing for Pilots*, 1998.
- [61] T. Okura. Materials for aircraft engines. 2015.
- [62] L. Periklis. Development of a preliminary weight estimation method for advanced turbofan engines. 2014.
- [63] J. Benad. The Flying-V, a Commercial Aircraft Configuration for Commercial Passenger Transport. 2015.
- [64] L. v d Schaft. *Development, Model Generation and Analysis of a Flying V Structure Concept*. PhD thesis, Delft University of Technology, 2017.
- [65] M. Claeys. Flying-V and reference aircraft structural analysis and mass comparison. Master's thesis, Delft University of Technology, 2018.
- [66] Elwood H. Hunt, Dr. Don H. Reid, David R. Space, and Dr. Fred E. Tilton. Commercial airliner environmental control system. 2011.
- [67] J. Melkert and C. Rans. Buckling, AE2135-I structural analysis & design. 2018.
- [68] W.D. Callister and D.G. Rethwisch. *Materials Science and Engineering*. John Wiley & Sons (Asia) Pte Ltd, 2014.
- [69] R. Storm, M. Skor, K.D. Lisa, T. Benson, and C. Galica. *Pushing the envelope: A NASA Guide to Engines*. 2007.
- [70] A.P. Mouritz. 3 - materials and material requirements for aerospace structures and engines. In *Introduction*

- to *Aerospace Materials*, pages 39 – 56. Woodhead Publishing, 2012.
- [71] J. Roskam. *Airplane Design. Pt. 1. Preliminary Sizing of Airplanes*. Roskam Aviation and Engineering, 1985.
- [72] M. H. Sadraey. *Aircraft design: A systems engineering approach*. John Wiley & Sons, 2012.
- [73] T. Mutluay. The development of an inertia estimation method to support handling quality assessment. Master's thesis, Delft University of Technology, 2015.
- [74] F. Oliviero. Requirement analysis and design principles for a/c stability & control (part 2). PowerPoint presentation. Delft University of Technology. course: AE3211-I, 2020.
- [75] F. Oliviero. Aircraft aerodynamic analysis - mobile surfaces of the wing. PowerPoint presentation. Delft University of Technology. course: AE2111-II, 2019.
- [76] D. Scholz. *Empennage Sizing*. Hamburg University of Applied Science, May 2017.
- [77] Airbus. Aircraft characteristics airport and maintenance planning. Technical report, 2005.
- [78] K. Kundu, C. J. Marek, and T. D. Smith. Low emission hydrogen combustors for gas turbines using lean direct injection. *41st AIAA/ASME/SAE/ASEE Joint Propulsion Conference and Exhibit*, 2005.
- [79] M. Palocz-Andresen. *Decreasing Fuel Consumption and Exhaust Gas Emissions in Transportation*. Springer, Hamburg, Germany, 2013.
- [80] H. Mannstein, P. Spichtinger, and K. Gierens. A note on how to avoid contrail cirrus. *Transportation Research Part D*, 10, 2005.
- [81] E. Benini, S. Pandolfo, and S. Zoppellari. Reduction of no emissions in a turbojet combustor by direct water/steam injection: numerical and experimental assessment. *Applied Thermal Engineering*, volume 29, 2009.
- [82] G. Gonca. Investigation of the influences of steam injection on the equilibrium combustion products and thermodynamic properties of bio fuels (biodiesels and alcohols). *Fuel*, 144:244–258, 2015.
- [83] D.S Lee et al. Aviation and global climate change in the 21st century. *Atmospheric Environment*, 43, 2009.
- [84] N. Dickson. Aircraft noise technology and international standards. 2015.
- [85] A. Depitre. Noise certification workshop. November 2006.
- [86] R. Bennett and K. Pearsons. Handbook of aircraft noise metrics. April 1981.
- [87] E. L. Bertsch. *Noise prediction within conceptual aircraft design*. PhD thesis, DLR, 2013.
- [88] M. Lighthill. On sound generated aerodynamically. i. general theory. *Proceedings of The Royal Society A: Mathematical, Physical and Engineering Sciences*, 211:564–587, March 1952.
- [89] M. Heidmann. Interim prediction method for fan and compressor source noise. *NASA Tech Memo X-71763*, July 1975.
- [90] D. Huff, B. Henderson, and E. Envía. Motor noise for electric powered aircraft. May 2016.
- [91] A. Synodinos, R. Self, and A. Torija. Framework for predicting noise–power–distance curves for novel aircraft designs. *Journal of Aircraft*, 55, August 2017.
- [92] A. Synodinos, R. Self, and A. Torija. Preliminary noise assessment of aircraft with distributed electric propulsion. June 2018.
- [93] M. Heidmann. Interim prediction method for fan and compressor source noise. Technical report, NASA, 1979.
- [94] F.H.V. Dewitte. Aircraft noise shielding assessment: The creation of software tool to predict aircraft noise shielding. Master's thesis, Delft University of Technology, 2016.
- [95] W. Dobrzynski. Almost 40 years of airframe noise research: what did we achieve? *Journal of aircraft*, 47(2):353–367, 2010.
- [96] M.R. Fink. Airframe noise prediction method. Technical report, FAA, 1997.
- [97] M. Pott-Pollenske, W. Dobrzynski, H. Buchholz, S. Guérin, G. Saueressig, and U. Finke. Airframe noise characteristics from flyover measurements and prediction. May 2006.
- [98] R. Woodward, D. Elliott, C. Hughes, and J. Berton. Benefits of swept and leaned stators for fan noise reduction. *AIAA Journal of Aircraft*, 38:1130–1138, January 2001.
- [99] D. Huff. Noise reduction technologies for turbofan engines. January 2006.
- [100] N. Antoine and I. Kroo. Optimizing aircraft and operations for minimum noise. In *AIAA's Aircraft Technology, Integration, and Operations (ATIO) 2002 Technical Forum*, page 5868, 2002.
- [101] M. Gorji-Bandpy and M. Azimi. Technologies for jet noise reduction in turbofan engines. *Aviation*, 16:25–32, March 2012.
- [102] K.A. Pascioni, S.A. Rizzi, and N.H. Schiller. Noise reduction potential of phase control for distributed propulsion vehicles. January 2019.
- [103] R. Merino-Martinez, E. Neri, M. Snellen, J. Kennedy, D. Simons, and G. Bennett. Analysis of nose landing gear noise comparing numerical computations, prediction models and flyover and wind-tunnel measurements. June 2018.
- [104] M. Wanga, D. Anglanda, and X. Zhang. The noise generated by a landing gear wheel with hub and rim cavities. ,” *Journal of Sound and Vibration*”, vol. 392, 2017.
- [105] H. Kumasaka, M. Martinez, and D. Weir. Definition of 1992 technology aircraft noise levels and the methodology for assessing airplane noise impact of component noise reduction concepts. July 1996.
- [106] D. Huff, B. Henderson, and E. Envía. A first look at electric motor noise for future propulsion systems. April 2016.

- [107] A. Ghiacc. Excess attenuation: Barriers of finite length. Technical report, University of Bologna, 2012.
- [108] R. Merino-Martinez, E. Neri, M. Snellen, J. Kennedy, D. Simons, and G. Bennett. Multi-approach study of nose landing gear noise. *Journal of Aircraft*, January 2020.
- [109] R. J. Hamann and M. J. L. van Tooren. *Systems Engineering & Technical Management Techniques Part II. Lecture notes*. Delft University of Technology, 2006.
- [110] M. Schmidt. A review of aircraft turnaround operations and simulations. *Progress in Aerospace Sciences 92 (2017) 25-28*, 2017.
- [111] G. Brewer and R. Morris. Study of fuel systems for LH2-fueled subsonic transport aircraft. Technical report, NASA, 1978.
- [112] I. J. H. Energy. Hydrogen in air transportation. Feasibility study for Zurich airport, Switzerland. *Int J Hydrog Energy*, 12(8):571–585, 1987.
- [113] E. Asmatulu, M. Overcash, and J. Twomey. Recycling of aircraft: State of the art in 2011. *Journal of Industrial Engineering*, volume 2013, 2013.
- [114] IATA. *Optimize the realization of residual value from aircraft decommissioning*, 1st edition edition, 2018.
- [115] M. Villani, G. Tursini, P. Fabri, and L. Castellini. High reliability permanent magnet brushless motor drive for aircraft application. May 2012.
- [116] R. Clague. *The Probability of Failure of Solid Oxide Fuel Cells by the Integrated Modelling of Multiple Physical Processes*. PhD thesis, Imperial College London, South Kensington, London, 2009.
- [117] F. Uhrig, J. Kader, and K. Mueller. Reliability of liquid organic hydrogen carrier-based energy storage in a mobility application. *Energy Science & Engineering*, 8(6), 2020.
- [118] H. Kinnison and T. Siddiqui. *Aviation Maintenance Management*. McGraw-Hill, 2nd edition, 2011. p.122-168.
- [119] T. Lewis. A life cycle assessment of the passenger air transport system using three flight scenarios. Master's thesis, Norwegian University of Science and Technology, 2013.
- [120] S. Howe, A. J. Kolios, and F. P. Brennan. Environmental life cycle assessment of commercial passenger jet airliners. *Transportation Research Part D: Transport and Environment*, 19:34–41, 2013.
- [121] J. V. de O. F. Lopes. Life cycle assessment of the airbus A330-200 aircraft. *Instituto Superior Tecnico Universidade Tecnica de Lisboa, Portugal*, 2010.
- [122] A. Johanning and D. Scholz. *A first step towards the integration of life cycle assessment into conceptual aircraft design*. Deutsche Gesellschaft für Luft-und Raumfahrt-Lilienthal-Oberth eV, 2014.
- [123] J. Vogtländer. Idemat2020 & EI v3-5. Database. Delft University of Technology, 2019.
- [124] A. Mehmeti, A. Angelis-Dimakis, G. Arampatzis, S. J. McPhail, and S. Ulgiati. Life cycle assessment and water footprint of hydrogen production methods: from conventional to emerging technologies. *Environments*, 5(2):24, 2018.
- [125] A.M. Casanova, B. van Leeuwen, C. Capelle, S. Finn, and S. Guo. An overview of commercial aircraft 2018 - 2019. DVB Bank SE Aviation Research (AR), 2017.